CELL BASED BIOSENSORS USING MICROELECTRODES

A DISSERTATION
SUBMITTED TO THE DEPARTMENT OF
ELECTRICAL ENGINEERING
AND THE COMMITTE ON GRADUATE STUDIES
OF STANFORD UNIVERSITY
IN PARTIAL FULFILLMENT OF THE REQUIREMENTS
FOR THE DEGREE OF
DOCTOR OF PHILOSOPHY

David A. Borkholder

November, 1998

To my wife and my parents
whose love and support have made this possible.

I certify that I have read this dissertation and that in my opinion it is fully adequate, in scope and quality, as a dissertation for the degree of Doctor of Philosophy.

_____

Gregory T.A. Kovacs (Principal Advisor)

I certify that I have read this dissertation and that in my opinion it is fully adequate, in scope and quality, as a dissertation for the degree of Doctor of Philosophy.

_____

David A. Stenger (Associate Advisor)

I certify that I have read this dissertation and that in my opinion it is fully adequate, in scope and quality, as a dissertation for the degree of Doctor of Philosophy.

_____

Stephen P. Boyd

Approved for the University Committee on Graduate Studies:

_____

ABSTRACT

Instruments for the study of living cells have historically been of significant importance for such things as basic neuroscience and cell biology. More recent work has included extending the use of cell based sensors to pharmaceutical screening, environmental monitoring, and toxin detection. While there are a variety of different measurement techniques, microelectrode arrays provide a simple interface for monitoring the electrical activity and impedance characteristics of populations of cultured cells over extended periods. The cell / sensor interface is created as cells attach directly to planar electrode structures. With excitable cells, both intrinsic and stimulated electrical activity has been directly monitored in this way. Impedance techniques have also been used to monitor such things as cellular adhesion, motility and proliferation of both electrically active and non-electrically active cell types.

For this work, a 36 element array of platinized platinum electrodes was packaged and used as a substrate for the culture of neurons, cardiac and glial cells. Electrical activity from a spontaneously beating syncytium of cardiac cells was monitored and analyzed in detail. Power spectral density analysis was used as a means of identifying the class of ionic channel affected by pharmacological compounds or toxins. Impedance

measurements on neurons and glial cells were targeted towards measuring changes in cellular membrane conductance in addition to cellular adhesion and motility.

This thesis describes the basic cell theory relevant to measurement of electrical activity and cellular impedance. Classical measurement techniques are compared to planar microelectrode array technologies. New packaging technologies and systems developed for both electrical activity and impedance measurements are described along with pharmacological data for neurons, cardiac and glial cells. The practicality of using microelectrode based sensor technologies for monitoring the activity of cultured cells is discussed.

ACKNOWLEDGEMENTS

If a man does not make new acquaintances as he advances through life, he will soon find himself left alone; one should keep his friendships in constant repair.

Samuel Johnson

There are so many people who have been involved in the creation of this work. Some have been intricately involved in the technical details while others have enriched my life in other ways. If I neglect to mention your name, you know who you are and how you have helped me through this process, and I thank you.

I would like to thank my advisor, Prof. Gregory Kovacs for his friendship, enthusiasm, energy, and undying spirit. He has been a great mentor, developing in me the ability to think both critically and creatively. This work would not have been possible without his guidance and support, and I am truly grateful. Greg always worked to promote me as an individual and include me in the planning aspects of collaborations and grant writing. I appreciate the broad exposure he worked to provide and the career building growth he has fostered. I look forward to continued interactions and collaborations with Greg in the future.

My associate advisor, Dr. David Stenger, has played a critical role in the formulation and execution of this research. His experience and insights were invaluable as I struggled to grasp the biological aspects of this work. I wish to thank him for his significant

technical discussions, and your friendship. I will truly miss our daily interactions. I would especially like to thank Derek DeBusschere who is taking over the cell based sensor work. After several years of working alone, I finally had someone I could discuss experiments with, develop protocols, etc. on a daily basis. I greatly appreciated his intelligence, his engineering competence, and all of our stimulating discussions. I look forward to continued friendship and future collaborations.

I would also like to thank Heather and Eric Kent who, while not being involved with any of this research, have helped to keep me sane during the process. Thanks for being my surrogate family; sharing special times and holidays when my family was so far away. Your friendship and support have been greatly appreciated.

I want to thank my mother and father for teaching me the value of hard work, honesty and integrity. For making the sacrifices which allowed me to attend college and for their endless love and support. Without all you have done for me, I would not be finishing this doctorate today. From my heart I thank you for everything.

And finally, my wife Robin. Thank you for supporting me through the bulk of my graduate work; for being my best friend, for making me laugh and remember the important things in life, for raising my spirits when experiments were getting me down, and most of all, for your love.

CONTENTS

Appendix D   HSPICE MODEL OF A BULLFROG ATRIAL CELL   223

LIST OF TABLES

LIST OF ILLUSTRATIONS

Chapter 1   INTRODUCTION

That particular day's work, I think, had all the elements that one could wish for. The new apparatus seemed to be misbehaving very badly indeed, and I suddenly found that it was behaving so well that it was opening up an entire new range of data. I'd been bogged down in a series of very unprofitable experiments and here suddenly was the prospect of getting direct evidence instead of indirect, and direct evidence about all sorts of problems which I had set aside as outside the range of the techniques that one could use... it didn't involve any particular hard work, or any particular intelligence on my part. It was one of those things which sometimes just happens in a laboratory if you stick apparatus together and see what results you get.

A.L. Hodgkin, 1977

1.1   Objectives and Goals

The study of cellular function and response has been used for decades to better understand the workings of the body. As technology has advanced, the capabilities and sensitivity of cellular studies have greatly improved. Current techniques allow for examination of single cell electrical characteristics either *in vivo* (within the body) or *in vitro* (outside of the body) via glass micropipette or wire microelectrodes [Kandell, et al., 1991; Standen, et al., 1987]. More recent advances allow for populations of cells to be examined simultaneously [Wise, et al., 1970; Thomas, et al, 1972; Edell, 1986, Gross et al., 1995] thereby permitting researchers to gain better insight into the functionality and interconnectivity of cellular networks. These same technologies may also offer the opportunity to utilize living systems in different sensor applications.

The use of living cells as sensor elements provides the opportunity for high sensitivity to a broad range of biologically active substances which affect the electrochemical response of a cell. These biologically relevant signals can be directly measured using

1

microelectrodes which provide a stable, non-invasive interface for monitoring populations of cells. The potential uses for such cell based sensors include environmental monitoring (chemical/biological warfare agents, groundwater contamination, etc.), pharmaceutical screening, drug discovery and basic neuroscience.

This work will focused on the development of cellular measurement systems based on extracellular *action potential* (the intrinsic electrical activity in a cell) monitoring and *impedance* measurements where the electrical characteristics (capacitance and conductance) of the cellular membrane are examined. Electrode arrays utilizing new packaging techniques will be developed to act as the substrate for the culture of anchorage dependent cell types. The action potential system will be used to see if changes in the action potential *shape* due to pharmacological manipulation can be monitored using extracellular electrodes, and determine if the AP characteristics can be used to extract important information about the cellular response. The ultimate goal of this study is the development of techniques which would allow the action of an unknown agent to be deduced by the measured cellular response.

The impedance system will be developed to measure cellular membrane properties (capacitance and conductance) and monitor changes due to the action of pharmaceuticals or toxins. Modeling of the cell/electrode interface will be performed to optimize the electrodes for sensing changes in these membrane characteristics. The ultimate goal of this study is to show that the membrane properties of cultured cells can be monitored using extracellular microelectrodes.

1.2   Overview of Cultured Cell Systems
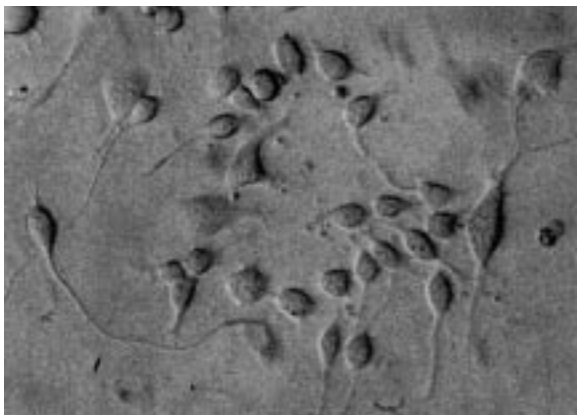
Figure 1.1:   Neurons cultured on a glass substrate.

At the beginning of this century the culture of living tissue *in vitro* was established as a viable technique for examining the properties of different cell types without the limitations or reliance on a living host organisms for cell maintenance [Harrison, 1907; Carrel, 1912]. These first examples of tissues maintained outside the body were actually *organ cultures* where a sample of tissue is cultured,

maintaining many of the features it exhibits *in vivo*. As the field of tissue culture developed, researchers began to disaggregate the tissue samples to obtain separated cells which could be cultured as an adherent monolayer (anchorage dependent cells) or as a cell suspension directly in the culture media. This evolved into the field of *cell culture* where individual cells are obtained from tissue, primary cell cultures or clonal cell lines and cultured. While cultured cell systems are not identical to those found *in vivo*, they do allow study of animal cells without the complications of systemic variations due to the normal physiology of the animal or stresses induced by invasive experimental procedures. In addition, they offer the opportunity to easily expand the applications of animal cells beyond the basic sciences to *hybrid biosensor* (sensors utilizing a biological element in conjunction with a more standard transducer, e.g. electrodes) applications. All of the procedures and systems described herein will utilize *cell cultur*e as opposed to any other type of *tissue culture*.

As mentioned above, the field of cell culture has historically utilized cells obtained directly from the original tissue, from an existing culture of primary cells, or from clonal cell lines. In each case, the cells are dispersed by a combination of enzymatic, mechanical, and/or chemical disaggregation. While cell lines can be genetically engineered to provide greater control over their characteristics, the cultured cell systems described herein will be limited to primary cell (embryonic chick myocardial and mouse astrocyte) and clonal cell (NG108-15: a hybrid combination of *neuroblastoma* (sarcoma of nervous system origin) and *glioma* (tumor composed of neuroglia) cells) line cultures.

Regardless of the cell type, maintenance of the living culture requires precise control of temperature, pH, ion concentrations, total solution osmolality, O_2 and CO_2 which constitute the *physiochemical* environment. However, the poorly defined (but well controlled) *physiological* environment (growth factors, hormones, etc.) is also critical and often requires supplementation of the media with serum or other compounds derived from living organisms which cannot be synthetically produced. Variation of any or all of these parameters can greatly influence cellular health as well as the development and proliferation of individual cells. Thus, culture of living tissue is as much an art as a science, making expansion to hybrid sensor technologies a non-trivial task.

1.3 Cultured Cell Systems as Sensors

Electrical activity in living cells is responsible for much of the complex behavior of organisms. Sensory processing, cardiac function, muscle control, thought, etc. are all partially controlled and regulated by the electrical activity and response of different cells in the body. While there are a plethora of different cell types, the fundamental mechanisms for electrical activity are quite similar. Structurally, cells are composed of a lipid bilayer membrane enclosing an intracellular ionic solution. This membrane contains numerous proteins, receptors, ionic channels, and ionic pumps which are responsible for maintaining the ionic concentrations within the cell and the intracellular potential relative to the extracellular.

Ionic channels are the most obvious fundamental excitable element in the membrane of excitable cells. There are many different types of channels that allow passage of different ionic species (Na^+, K^+, Ca^{2+}, Cl^-, etc.) and are gated by different mechanisms (voltage gated, second messenger protein cascades, etc.). The opening and closing of these channels shapes the electrical response of the cell as will be described in Chapter 2. Modulation of the ionic channel properties via toxin or pharmacological manipulation can be detected by changes in the electrical signature of the cell being monitored, making cells excellent candidates for use in broad specificity sensors.

1.3.1 Measurement of Cellular Activity and State

Electrical activity of cultured cells has classically been studied using micropipette or microwire electrodes. The cells to be monitored are located in a dish placed on a microscope stage, and micromanipulators are used to position the recording electrode (micropipette or microwire). Several different techniques are used (see Figure 1.2) depending on the electrode type and what is to be measured. To directly measure the transmembrane potential, an *intracellular* recording (relative to a distant reference electrode) of the action potential (AP) is made by carefully inserting a micropipette electrode through the membrane (which forms a tight seal to the electrode). While this method allows for a large signal ($\approx$ 100 mV) to be recorded, it also suffers from a mechanically fragile connection which makes long term recordings extremely difficult. Additionally, in some cases the damage caused by impalement of the cell compromises the intracellular ionic composition, which in turn can affect the intrinsic AP firing rate [Breckenridge, et al., 1995]. Thus, non-invasive recordings may in some instances provide a better indication of the true endogenous activity of the cultured cells.

4
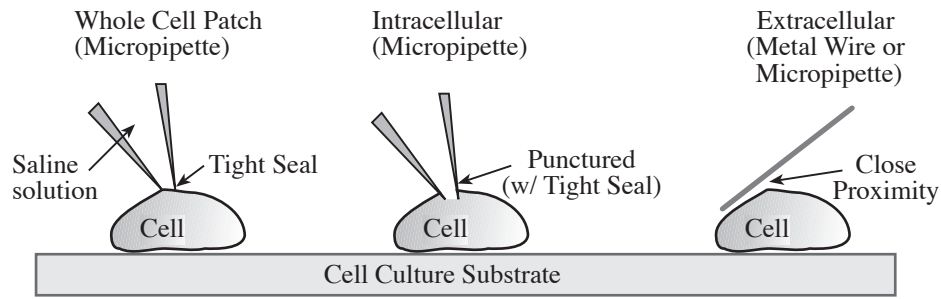
Figure 1.2: Classical electrical activity recording techniques. For intracellular recordings and monitoring of membrane impedance characteristics a micropipette is brought into contact with a cell and a light suction is applied forming a tight seal. This is known as the "whole cell patch" technique. The micropipette can be inserted through the membrane to directly measure the intracellular voltage for "intracellular" recordings. For "extracellular" recordings a micropipette or microwire is positioned in close proximity to the cell.

The micropipette can also be brought into contact with the cell membrane with a light suction applied to form a seal. This *whole cell patch* allows for measurement of the transmembrane potential (when the electrode is connected to a high input impedance amplifier) without compromising the interior composition of the cell. Additionally, it allows for observation of currents flowing through a small patch of membrane and determination of the impedance characteristics. There are several variations on this technique which allow different cellular characteristics to be examined. These are outlined in detail in [Nicholls, et al., 1992]. As with the impaled electrode technique, this also suffers from an instable interface which limits the duration of the experiment.

The final classical technique for monitoring the electrical properties of cultured cells involves moving a micropipette or microwire positioned in close proximity to the cellular membrane to record the *extracellular* AP. This signal is on the order of tens to hundreds of microvolts relative to a distant reference electrode immersed in the culture media. While this passive monitoring technique does not adversely affect cellular function, it is limited due to the significantly smaller AP amplitude as well as a recorded signal shape which is vastly different from the actual transmembrane potential. This will be described in detail in Chapter 2.

All of the classical techniques described above relied on optical observation of the cells for micropositioning of a recording electrode, significant human interaction, and resulted in fragile interfaces that limited the duration of the recordings which could be obtained. To improve the possibilities for long term recordings from cultured cell

networks *in vitro*, efforts have been made to bring the cells to the sensor. Planar microelectrode arrays have been used as a substrate for the culture of cells since the early 1970s, with successful monitoring of action potentials from single cells and networks of cells, as well as measurement of the impedance of the cell/electrode system as will be described in later sections. These advancements expand the possible uses of cultured cell networks beyond basic neuroscience and cell biology to hybrid biosensor systems.

While there are other ways to non-invasively monitor the electrical activity and/or physiologic state of cultured cells (see review by Bousse, 1995) such as voltage sensitive fluorescent dyes and the pH of the culture media, these suffer from limitations. Voltage sensitive dyes require photoillumination which can be toxic to the cells under study. This phototoxicity limits the time over which the electrically active cells may be monitored [Chien and Pine, 1991]. Additionally, the inclusion of the dye in the media results in conditions variant from the normal state of the culture, and unknown pharmacological effects may be of concern [Salzberg, et al., 1977]. Measurement of the culture media pH may be an indicator of general physiologic state for any cell type (electrically active or not), but for sensing applications it is a relatively nonspecific detector since changes in metabolism can be due to a wide variety of biological responses [Parce, 1989; Baxter, et al., 1994]. For these reasons, this work was focused on non-invasive monitoring of extracellular potentials and cellular impedance using microelectrodes.

1.3.2 Requirements for Cell Based Sensors

When developing a system for monitoring the extracellular action potential or cellular impedance of anchorage dependent cell types, it is necessary to design with many criteria in mind: biocompatibility, maintenance of the physiochemical environment (temperature, pH, etc.), maintenance of sterility during cell growth and sample introduction, methods of sample introduction, a transducer for monitoring the desired electrical signal, low signal path parasitics, electronics for extraction of the electrical signal, and packaging which facilitates insertion of the cell culture system in to the measurement electronics while protecting the living system from the external environment. These requirements often trade off against each other and require compromise for the best overall solution.

Biocompatibility is perhaps the most important consideration when developing a cell based biosensor. If biocompatible materials are not employed through the design, the sensing element (the cells) will not survive to perform the initial signal transduction required. While biocompatibility generally means not having a toxic, harmful, or otherwise deleterious effect on biological function, there are varying degrees dependent on

the application. Chronic studies where foreign materials are in contact with living tissue require a more diligent effort for the determination of biocompatibility than do acute studies where the tissue is in contact with the materials for a short duration. Cell culture for hybrid biosensor applications falls somewhere in between, depending on the application area. For all of the work presented herein, the requirements are for acute studies only (those where cells are cultured for less than one week).

All materials that contact the cellular system (comprising the cells and culture media) must be biocompatible as described above. This includes the substrate, electrodes, chamber housing, adhesives, sealants, tubing, valves, and pumps. Biocompatibility was determined for most materials by culturing the cells of interest with the cells themselves or the culture media in direct contact with the material to be tested. If the cells appeared "normal" under optical inspection and proliferated as expected, the material was deemed biocompatible for the acute studies presented herein.

The other aspects of biosensor development (electrode array design, packaging, electronics, etc.) will be examined in detail in Chapter 3 and Chapter 4.

1.4   History of Planar Arrays for Cultured Cell Systems

Planar microelectrode arrays for cultured cell studies generally consist of a substrate of glass, plastic or silicon (which allows inclusion of active circuitry in close proximity to the cells) over which a conductor (gold, platinum, indium-tin-oxide, iridium, etc.) is deposited and patterned. An insulating layer (photoresist, polyimide, silicon dioxide, silicon nitride, etc.) is

Figure 1.3: Conceptual drawing of a cultured cell coupled to a microelectrode.

deposited over the conducting electrodes and interconnects and then removed in regions over the electrodes to define the recording sites. Cells are cultured directly on this surface and contact the exposed conductor at the deinsulated recording sites. Depending on the size of the electrodes and the cells, recordings of electrical activity or impedance can be from a single cell or populations of cells. Each electrode site is generally connected to the input of a high input impedance, low noise amplifier (with or without AC coupling capacitors) to allow amplification of the relatively small extracellular signals.

1.4.1 Action Potential Measurements

Figure 1.4: Microelectrode array cross-section. Nickel was patterned on top of a glass substrate and gold plated. A photoresist insulation layer was then deposited and patterned to define the electrode and bondpad sites. A glass ring was affixed with bee's wax to form the culture chamber. Finally, platinum black was deposited electrochemically on the exposed electrode locations. After [Thomas, et al., 1972].

In 1972, C A. Thomas, et al. described the first use of a microelectrode array for extracellular recording from electrically active cells cultured *in vitro* [Thomas, et al., 1972]. They utilized gold plated nickel electrodes on a glass substrate passivated with patterned photoresist. A glass ring was affixed to the substrate with bee's wax to form a culture chamber containing microelectrodes of known spacing and size. Thomas also utilized the techniques of Gesteland and Robinson [Gesteland, et al., 1959; Robinson, 1968] to lower the electrode impedance by deposition of platinum

black on the recording sites. Embryonic chick heart cells were cultured in this chamber, adhering to the substrate and microelectrodes. Electrical activity was recorded extracellularly from the contracting heart cells simultaneously from many electrodes. This parallel, non-invasive technique for monitoring a population of cells *in vitro* has been the focus of significant research in the decades that followed.

Building from the structure and techniques of Thomas, numerous researchers have utilized microelectrode arrays to examine a wide variety of cell types under a plethora of conditions. Gross developed a microelectrode array almost identical to that of Thomas (except he employed a laser deinsulated, polymer passivation), using it to record extracellular electrical responses from explanted neural tissue (brain ganglia from the snail *Helix pomatia*) [Gross, et al., 1977; Gross, 1979]. The first extracellular recordings from dissociated neurons (superior cervical ganglia of neonatal rats) were reported in 1980 by Pine, who was the first to use silicon dioxide rather than an organic photoresist film to electrically insulate the interconnects [Pine, 1980]. Additionally, Pine combined the traditional method of intracellular recording with a glass micropipette inserted through the cell membrane, with extracellular recording with a metal microelectrode. This was an important simultaneous experiment for validation of the extracellular technique and

calibration of the recorded extracellular signal for comparison to the relatively large body of literature available on intracellular recordings. However, significantly more work was required to understand the true relationship between the intracellular and extracellular signals as will be described later.

Gross continued his research, expanding to dissociated neuron cultures in 1982 with mouse spinal neurons [Gross, et al., 1982]. However, the systems as developed made visualization of cells positioned over a microelectrode difficult since the metals were opaque and inverted microscopy was being utilized. To address this problem, Gross developed a microelectrode array employing indium tin oxide (ITO) electrodes which were both conductive and transparent [Gross, et al., 1985]. While the ITO structures did allow for optical observation of the cultured neuronal network and displayed no toxicity effects on the cells, the increased electrode impedance (4 to 5× higher than similarly sized gold electrodes) resulted in reduced signal to noise for the recorded APs. Nevertheless, Gross, et al. successfully recorded action potentials from cultured neurons utilizing the ITO microelectrodes, thereby verifying their utility in applications where visual observation is more important than signal-to-noise ratio. In 1993 they used the same ITO electrode structures to stimulate monolayers of cultured neuronal networks [Gross, et al., 1993].

The utilization of planar microelectrode arrays in the general form described above for cultured cells studies was continued by numerous research groups examining many different cell types over the years that followed [Novak, et al., 1986; Drodge, et al., 1986; Eggers, et al., 1990; Martinoia, et al., 1993; Maeda, et al., 1995]. Eventually researchers began to expand the capabilities of the simple planar array systems. Beginning in 1984 several investigators successfully stimulated *and* recorded from embryonic chick myocytes cultured on planar microelectrode arrays [Israel, et al., 1984; Israel, et al., 1990; Connolly, et al., 1990]. Beginning in 1990, Jimbo and Kawana moved beyond stimulation of cultured myocytes to selective excitation of neuron cell bodies (mouse and chick dorsal root ganglion cells) by stimulation of neurites guided to a stimulation site [Jimbo and Kawana, 1990; Jimbo and Kawana, 1992]. The neurites were guided to the stimulation sites (pairs of ITO electrodes) by microchannels in the PMMA passivation layer. The elicited response was recorded from neurites with the stimulating electrodes and from the cell body using a pipette electrode in the standard whole cell patch configuration. This was the first demonstration of this type of dendrite stimulation and of potential importance for many neuronal network studies. In 1933, this same group simultaneously recorded electrical activity and intracellular calcium concentration (via fluorescent dyes) using

similar electrode structures and cultured rat cortical neurons [Jimbo, et al., 1993]. This system allowed verification of electrical activity using optical techniques in conjunction with the electrical.
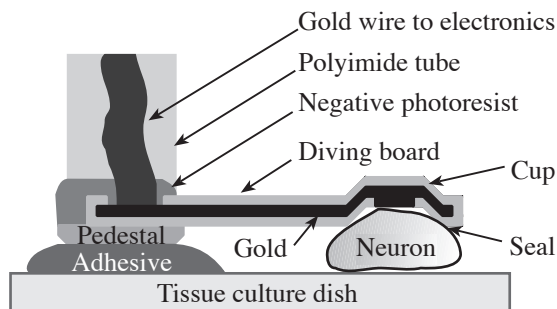
Figure 1.5: Diving board electrode structure in contact with a cell. The electrode was designed to provide a stable high impedance seal similar to those obtained with traditional glass micropipettes. After [Regehr, et al., 1988].

There have been attempts at making microelectrodes that can hold cells in place while maintaining a tight seal between the cell and the electrode (similar to that obtained with a glass micropipette used for patch-clamp studies of individual cells). This requires a three dimensional structure whereby the electrode can be positioned *over* the cell rather than the cell growing over the microelectrode (classical case). In 1988 Regehr, et al. described such a device whereby a "diving board" structure was glued into the bottom of a standard cell culture dish as depicted in Figure 1.5 [Regehr, et al., 1988]. By creating a recessed electrode surrounded by a cup with silicon dioxide exposed where the device contacted the cell, Regehr, et al. sought to simulate the material and surface conditions which allow high impedance seals to be obtained with glass micropipettes while simultaneously eliminating the mechanically unstable interface inherent when using micromanipulators to control positioning of glass micropipettes. While both stimulation and high signal-to-noise ratio (SNR) action potential recording capability were obtained with this electrode structure, it required manual placement of the electrode directly over an individual cell. Thus, use of this type of electrode structure requires the added complexity justifies the improved signal quality. For the majority of applications, the need for accessing a multiplicity of cells far outweighs the desire for greatly improved SNR. Additionally, the structures as described and implemented make reuse a difficult task.

There have been other attempts at improving SNR by modified electrode structures. Lind, et al. performed finite element analysis modeling of the extracellular action potential for cells surrounded by extracellular fluid, positioned over an extracellular electrode, over an electrode in a groove and over an electrode in a cubic pit [Lind, et al., 1991]. The result was a significant improvement (over 700%) in signal strength as the extracellular space was confined by the external structures (groove and pits). Unlike the diving board

structure of Regehr, et al., these changes in electrode structure allowed populations of cells to be simultaneously monitored with greatly improved signal strength. These modeling results have been experimentally verified using neurons from the snail *Lymnaea stagnalis* cultured over electrodes positioned in the bottom of a 10 *μ*m wide, 1 *μ*m deep groove [Breckenridge, et al., 1995].

In 1991, Fromhertz, et al. utilized an integrated transistor as the sensing element in place of the previously used bare metal electrodes. Using a silicon substrate and standard integrated circuit fabrication technologies, Fromherz, et al. developed the system described in Figure 1.6 whereby a single neuron was coupled to the bare gate (no metal) of a p-channel field-effect transistor [Fromherz, et al., 1991]. Single dissociated cells (Retzius cells from leech *Hirudo medicinalis*) were manually placed over the transistor
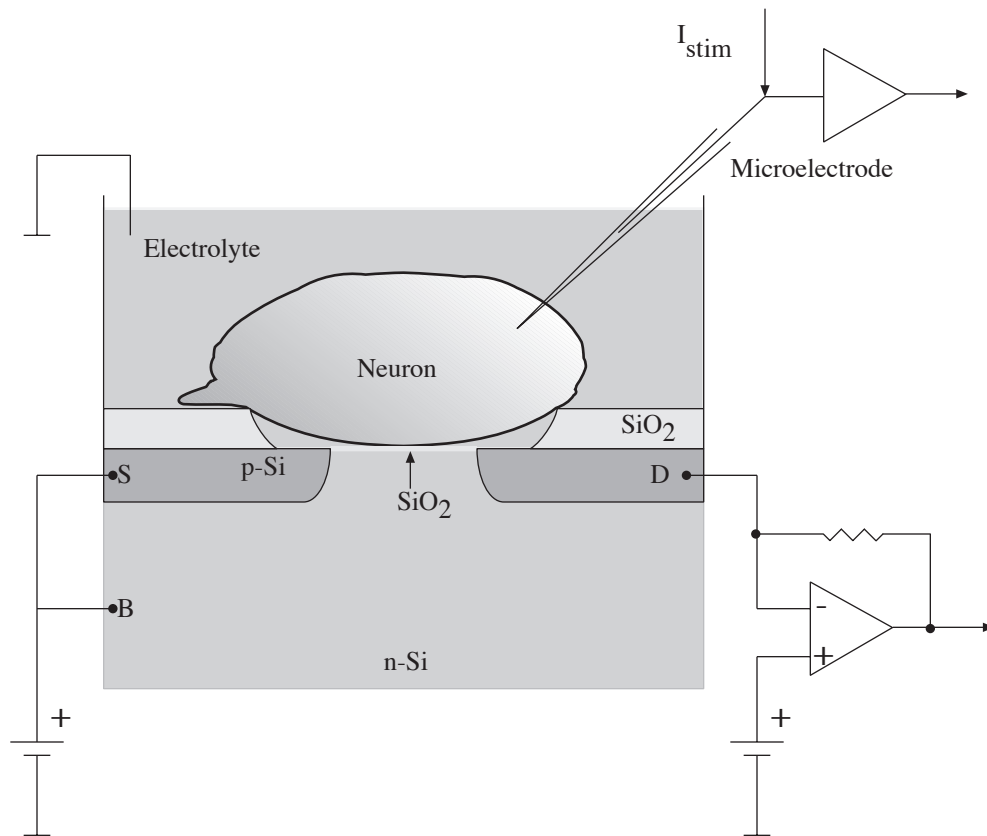
Figure 1.6: Neuron-Si junction. A neuron is attached to the gate oxide of a silicon field effect transistor. The electrolyte is maintained at ground potential while the source (S) and bulk silicon (B) are held at positive bias voltages.The source (S) to drain (D) current is monitored by a current to voltage converting amplifier. The micropipette electrode impaling the neuron is used to stimulate the cell (via current injection) and monitor the transmembrane potential using a voltage follower. After [Fromhertz, et al., 1991].

using a glass pipette and a stereomicroscope. A glass micropipette was inserted through the cell membrane and used to stimulate the cell and monitor the intracellular voltage. Changes in the I-V characteristics of the field-effect transistor were correlated to cell activity. Similar systems were utilized to explore the physical characteristics of the neuron-silicon junction using an array of transistors positioned below the neuron [Fromherz, et al., 1993] as well as capacitive stimulation of the neuron through a thin oxide layer [Fromherz, et al., 1995]. While these demonstrations did not utilize cultured cells, there is no reason why the technology could not be expanded to those types of studies to provide direct electronic to cell coupling without an intermediate metal electrode. However, this technology requires significantly more complex fabrication, biasing of the culture media in the recording chamber relative to the source of the transistor, and may suffer from limited lifetime and sensor drift due to ionic species migrating through the thin oxide layer comprising the gate of the transistor. For these reasons, technologies discussed and explored herein will be limited to those employing metal microelectrodes.

The measurement of extracellular action potentials using microelectrode arrays has been described in detail above. While many of the cited papers discussed how the recorded extracellular signal correlated to the intracellular AP, no simulation work had been performed. Beginning in 1991, Grattarola, et al., used an electrical equivalent model of the cellular membrane coupled to a microelectrode and the circuit simulator SPICE to model the extracellular signals. They found the signal amplitude was dependent on the coupling of the cell to the substrate and that the signal shape represented a time derivative of the intracellular signal. The order of this time derivative varied depending on the coupling of the cell to the electrode, the electrode characteristics and the parasitics of the system [Grattarola, et al., 1991; Grattarola and Martinoia, 1993; Bove, et al., 1995]. This will be discussed in detail in Chapter 2 where the mathematics of the recorded signal are described in detail.

While researchers have been using extracellular microelectrodes for decades to monitor the electrical activity of cultured cells, work examining the effects of chemical stimuli has been limited to a few groups. In 1986, Gross and colleagues were the first to examine changes in *spike trains* (spontaneous, rhythmic firing of action potentials) from networks of cultured neurons, as the composition of the media was changed [Drodge, et al., 1986]. They examined the effect of changing $MgCl_2$ concentration and the addition of strychnine on the firing rate and rhythmic bursting characteristics of mouse spinal monolayer cell cultures. In the years that followed, Gross, et al. continued to experiment

with numerous pharmaceuticals to examine the effect on the rhythmic bursting of neuronal networks in culture [Gross, et al., 1992; Rhoades and Gross, 1994, Gross and Schwalm, 1994; Gross, et al., 1995]. Their results indicate that changes in rhythmic bursting could be used for pharmaceutical screening or toxin sensing applications.

Three other groups have examined the effect of chemical changes in the culture media on an electrically measurable response using extracellular microelectrode arrays. In 1990, Israel, et al. monitored changes in the conduction velocity of spontaneous APs in cultured chick myocytes due to acidification of the culture media [Israel, et al., 1990]. Maeda, et al., replicated some of the work of Gross by monitoring the sensitivity of developing networks of neurons (firing rate and conduction velocity) to changing extracellular magnesium concentrations [Maeda, et al., 1995]. Mohr, et al. also examined changes in spike activity, but for cultured aggregates of embryonic chick myocardial cells [Mohr, et al., 1995; Mohr, et al., 1996]. For these experiments, the cardiac cells were cultured for four days in suspension allowing aggregates of up to 500 cells to form. These aggregates were transferred to the planar microelectrode array and allowed to adhere for one to two hours. Electrical activity was then monitored and the spike train response to the digoxin (a Na^+/Ca^{2+} ATPase antagonist) was observed.

While Gross, et al. have done extensive work with cultured networks of neurons and spike train changes due to pharmacological manipulation, and others have examined different chemical effects, no work has been reported in the literature where changes in the *shape* of the extracellular AP in response to biologically active agents has been observed. This work will focus on monitoring changes in the action potential shape due to the action of pharmaceuticals and toxins. The use of any observed shape changes for pharmaceutical screening and toxin detection will be explored.

1.4.2 Impedance Measurements

Since the advent of suitable instrumentation, the electrical properties of biological material have been studied. Impedance techniques have been used to study organs in the body [Dijkstra, et al., 1993], explanted neural tissues [Cole and Curtis, 1939; Hodgkin and Huxley, 1952], whole blood and erythrocytes [Fricke and Morse, 1926; Fricke and Curtis, 1935], cultured cell suspensions [Schwan, 1957], bacterial growth monitoring [Hause, et al., 1981], and anchorage dependent cell cultures [Giaever and Keese, 1984]. While all but the latter are not directly related to this research, there is a great deal of relevant information regarding the characteristics of biological material to be obtained from those studies. Most significant are the frequency dependent dielectric properties of biological

materials which yield insight into the expected behavior within different frequency ranges. This is examined in more detail in Chapter 2.

There are two main groups which have previously studied the impedance characteristics of anchorage dependent cultured cell lines; that of Giaever and Connolly. Giaever was the first to monitor the impedance of populations (20 to 80) of cultured cells using electrodes significantly larger than the cells to be studied. In 1984 he described a system where standard polystyrene tissue culture dishes were modified to include a large reference electrode (2 cm^2) and 4 smaller electrodes (3 × 10^{-4} cm^2) as outlined in Figure 1.7 [Giaever and Keese, 1984]. Giaever and Keese cultured human lung fibroblasts (WI-38 and WI-38/VA-13) cells on the modified cell culture dishes and applied an AC voltage through a resistor to a single small electrode in the dish. The result was a near constant current source which enabled the impedance to be determined by measurement of the resulting voltage. Using a lock-in amplifier, they were able to observe the effects of cell proliferation (impedance increase) as well as micromotion of the cells (fluctuations in observed impedance). This was the first demonstration of a system capable of monitoring proliferation and motion of a population of cells cultured *in vitro*.
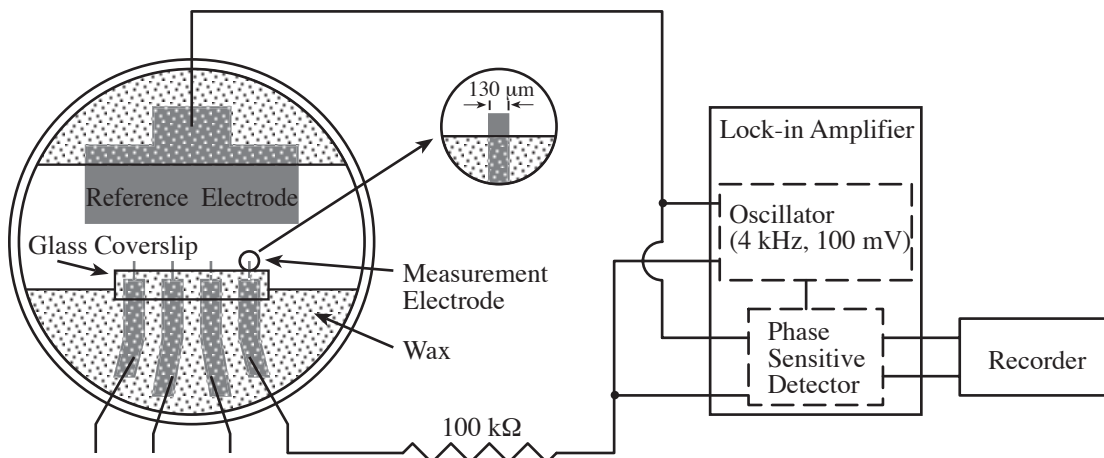
Figure 1.7: Impedance measurement system. A standard polystyrene tissue culture dish was used as the substrate for fabrication of gold electrodes. Varnish-insulated copper wires were soldered to the gold electrodes using indium. A glass coverslip was attached to the dish with wax such that the tips of the four small electrodes were exposed. The exposed copper wire, gold electrode surfaces were then covered over with wax to insulate them from the culture media. Cells were cultured in this tissue culture dish allowing measurement of electrode/cell impedance with the connected lock-in amplifier. Later modifications to the design of the electrical tissue culture dish included the used of photoresist in place of the wax utilized above and the creation of six independent wells allowing for multiple experiments on the same substrate. After [Giaever and Keese, 1984].

Giaever and Keese continued their work in the years that followed, examining the effects of different proteins on cell adhesion, spreading, and motility [Giaever and Keese, 1986; Mitra, et al., 1991]; a mathematical model of cell motion (determined to be fractional Brownian motion) [Giaever and Keese, 1989]; the use of this impedance method in cell based sensor applications [Keese and Giaever, 1990; Giaever and Keese, 1992; Keese and Giaever, 1994]; the effect of different factors (temperature, glucose, CO_2, etc.) on the micromotion observed over time in a stable culture [Lo, et al., 1993; Lo, et al., 1994]; and the morphological response of cells to pulsed ac fields [Ghosh, et al., 1994]. The complexity of the applications and analysis of the impedance measurements continued to increase as they gained insight into the limits of this technique. They began to explore other cell types including macrophages [Kowolenko, et al., 1990], bovine pulmonary microvessel endothelial cells (BPMVEC) and bovine pulmonary artery endothelial cells (BPAEC) [Tiruppathi, et al., 1992], and human umbilical vein endothelial cells (examining focal adhesion) [Moy, et al., 1996].

Giaever, et al. also showed this impedance technique was capable of resolving cellular movement at the nanometer level, something which previously was impossible using conventional time lapse microscopy [Giaever, and Keese, 1991; Giaever and Keese, 1993]. Thus, not only were they able to non-invasively monitor the activity of a population of cells, they successfully expanded the limits and capabilities of conventional techniques. In 1993 Giaever and his colleagues successfully used their electrodes to perform *electroporation* (formation of small transient pores in a cellular membrane by application of a transmembrane voltage) on transformed human lung fibroblasts (WI-38/VA-13) and in real time monitored the changes in impedance which resulted [Ghosh, et al., 1993]. Electroporation is commonly used to insert foreign material (generally plasmids or other genomic material) into a cell which would normally be excluded by the cell membrane. The system developed by Giaever, et al.was able to create the pores and then monitor their closure over time via impedance measurements. This was the first method for electroporation studies which allowed the observation and monitoring of this phenomenon for a population of cells.

The techniques and instrumentation of Giaever and Keese continued to be used by other researchers to examine more complex cellular responses such as the morphological effects of prostaglandin E_2 on cultured orbital fibroblasts from patients with Graves ophthalmopathy [Smith, et al., 1994; Wang, et al., 1995], the effects of pSV2-neo plasmid on NIH 3T3 cell motion [Pei, et al., 1994], and the role of nitric oxide in endothelin induced migration of endothelial cells [Noiri, et al., 1997]. They developed a full model

for MDCK (Madine-Darby canine kidney epithelial) cells which allowed determination of the distance between the basal cell surface and the substrate as well as the capacitance of the apica, basal, and lateral cell membranes [Lo, et al., 1995]. These values had been difficult, if not impossible to obtain previously.

Thus, the methods developed by Giaever and Keese were shown to be extremely useful for examining the attachment, spreading and motion of cultured cell populations. Detailed models made the determination of such things as cell/substrate separation and membrane capacitance values possible. The effect of different agents on the mitosis, motility, and morphology of the cultured cells was demonstrated in numerous cases. They were also able to successfully observe the motion of a single cell positioned on the electrode (with greatly decreased signal-to-noise ratio).

Connelly, et al. also used the methods of Giaever and Keese with a few modifications. In 1989 they fabricated electrodes on a standard Petri dish [Connolly, et al., 1989] as was outlined in Figure 1.7 for Giaever, et al. The only modification was the addition of a glass ring around the electrode area (to contain the cell culture media) and the insertion of a permeable, cellulose nitrate membrane to separate the culture dish into two sides, each with two measurement electrodes. This configuration allowed culture of cells in one side of the dish while "control" electrodes without cells were maintained in the other half of the dish. Using this system and electronic equipment similar to that employed by Giaever, et al., Connelly and colleagues were able to monitor the attachment, spreading and movement of BHK (baby hamster kidney fibroblasts) and MDCK cells while simultaneously monitoring changes in the control electrode impedance which was exposed to the same cell culture medium through the permeable membrane. This represented an advancement of the Giaever technique since a true control test on bare electrodes was possible.

Using the same electronic equipment as described above, Connelly, et al. also examined the impedance characteristics of individual BHK cells using smaller electrodes fabricated on glass substrates [Connelly, et al., 1989]. The basic fabrication process involved deposition and patterning of gold electrodes (10 μm wide), interconnects and bondpads. Silicon nitride (1 μm) or polyimide (4 μm) was then deposited over the electrode array to act as an insulating layer. This passivation layer was then patterned with grooves 8 μm wide to open over the electectrode areas (bondpads were deinsulated at the same time). Thus, the active electrode area was (8 × 10 μm); small enough to be covered by a single cell. Platinization was utilized to reduce the electrode impedance. Measurement of cultured BHK cells revealed fluctuations of 10 to 20% not observed on

the control electrodes. These fluctuations were attributed to cell motility with no further analysis performed.

For measurement of action potentials extracellularly, it is desirable to improve the seal at the cell/electrode junction [Tank, et al., 1986]. Thus, in 1991, the work of Connelly's group continued in an effort to deduce cell/electrode interface characteristics for development of a better understanding of extracellular action potential measurements [Lind, et al., 1991]. Surface roughness effects on cell adhesion were examined by looking at smooth gold electrodes, rough platinized gold electrodes, and gold electrodes roughened by dry etching. Lind, et al. found a definite improvement in BHK cell/electrode adhesion (on large area electrodes) for the platinized electrode case, but they were not sure if it was due to the roughness or some electrochemical difference. Trials using the roughened gold electrodes were inconclusive. Experiments using neurons from the brain of the snail *Lymnaea stagnalis* (single neurons were manually placed over an individual $10 \times 10 \ \mu$m microelectrode) revealed a relatively small increase in the initial measured impedance without the cell (5%). In 1995, the work was continued using *Lymnaea* neurons [Breckenridge, et al., 1995]. Impedance measurements were performed both before and during cell culture and estimates of the cell to substrate seal impedance were made. These impedance values were then correlated with the recorded extracellular action potentials, revealing a directly proportional relationship. As the seal impedance increased, the extracellular signal strength did as well, thereby verifying that the seal impedance is indeed critical for improved SNR.

Recently, impedance studies of anchorage dependent cultured cells have been performed by three other groups using different electrode structures. In 1995 Hagedorn, et al. utilized a perforated silicon membrane structure to examine the motion of fibroblasts cultured on the surface [Hagedorn, et al., 1995]. As shown in Figure 1.8, the upper and lower electrolytes were separated by the silicon membrane so that current flowing from electrode 1 to electrode 2 passed through the pore. Given large electrodes, the 10 μm diameter pore could be made to dominate the measured impedance.

Hagedorn, et al. monitored the motion of cultured 3T3 and L929 mouse fibroblasts using this technique. They claimed to be able to distinguish between cell and filopodia movement, but there was little convincing evidence presented. In addition to looking at a single electrode with a single pore, Hagedorn, et al. also examined arrays of pores while maintaining the two electrode structure shown in Figure 1.8. Thus, the experiment was similar to that of Giaever, et al. where populations of cells were responsible for the measured impedance. Hagedorn concluded that the array resulted in a significant decrease
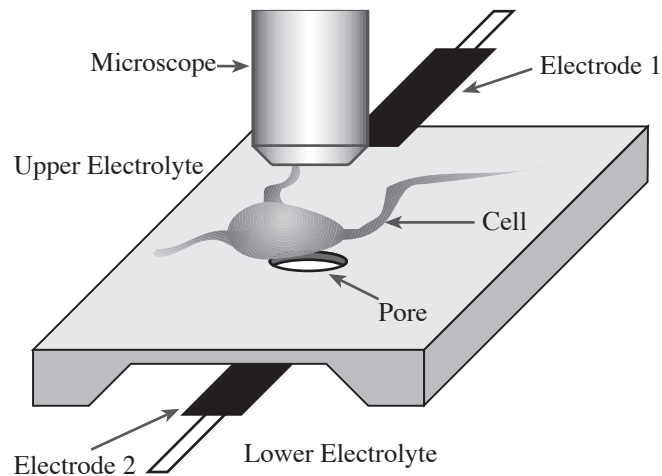
Figure 1.8:   Impedance measurement chamber. The upper and lower electrolytes were separated by a Si-membrane. The platinum electrodes were approximately 15 mm² in area. This silicon chip was manually assembled in a test fixture which contained the electrolyte and maintained the temperature at 37°C. Changes in impedance were observed as cells moved over, around and through the pores. After [Hagedorn, et al., 1995].

in signal strength (as is to be expected since all pore impedances were in parallel for this case).

This technology failed to offer any significant advantages over the techniques of Giaever, et al. and Connolly, et al. The only convincing argument the authors made on its behalf was that the silicon membrane was inert and therefore charge transfer reactions were not a concern. However, Giaever, et al. has shown that there are no deleterious effects from the applied voltages used in their system. Additionally, the technique of Hagedorn et al., while allowing measurements of single cells (as did the Connelly work), did not allow for measurement and monitoring of cell attachment. It also gave little information about cell proliferation.

The one possible advantage to the silicon membrane structure which was not mentioned by Hagedorn, et al. is the possibility for applying suction to the backside and forming a tight seal to a cell, similar to a patch clamp. It is possible that this would allow for a greater sensitivity of the measurements to changes in cell membrane properties with a reduced dependence on cell motility.

In 1996, Wegener, et al. described an electrode system similar to that of Giaever, et al. which utilized a voltage divider technique for determination of the unknown impedance across a range of frequencies (1 Hz to 10 kHz) [Wegener, et al., 1996]. They measured the

transepithelial and transendothelial resistances of cell monolayers consisting of primary cultured endothelial cells isolated from porcine brain microvessels, epithelial cells from porcine choroid plexus and MDCK cells. The cells were cultured directly on gold electrodes and such things as cell proliferation and total cellular impedance were monitored. Their results were consistent with those of Giaever, et al.

In 1997, Ehret, et al. described an interdigitated electrode structure with electrodes of 50 μm in width separated by 50 μm in a 5 mm x 5 mm active area [Ehret, et al., 1997]. While they successfully monitored the spreading, attachment and morphology of CV-1 (fibroblasts derived from the kidney of a male adult African green monkey) and LS 174T (epithelial cells derived from a human colon adenocarcinoma) cells, the results were almost identical to those of Giaever, et al. Ehret did show that cellular membrane destruction by toxic concentrations of cadmium over time could be detected, thereby confirming the potential use of this technique for toxicology studies.

In summary, the work of Giaever, Connelly, Ehret, Wegener and Hagedorn has shown that microelectrodes of various sizes and structure can be used to monitor the spreading, attachment and motion of a plethora of different cell types over a wide range of frequencies. The effects of different culture media, pharmacological compounds and toxins have been observed. In many cases, the capacitance of the cell membrane, cell/substrate separation, and cell/cell separation can all be monitored and determined. While all of these measurements provide biologically relevant information, there is still a need to examine the membrane properties of cultured cells. In particular, the effects of different compounds on the ionic channels of populations of cells cultured *in vitro*. To date, this has not been reported in the literature. The research presented herein will explore the use of extracellular microelectrodes for monitoring changes in cellular membrane properties due to pharmacological manipulation.

1.5 Overview of this Thesis

This thesis has already described the historical background of action potential and impedance measurements on cultured cell systems. These form the basis upon which this research was built. The following chapters will begin by describing the theory of cellular function with emphasis placed on cellular construction, cellular adhesion, motility, the basis of the action potential, and membrane impedance properties. The anticipated cellular response to external stimuli will be explored with respect to both action potential and cellular impedance modulation. Details on the specific cell types employed in this research and mechanisms for modulation of their cellular properties for the general classes of toxins and pharmaceuticals used will be discussed in the relevant action potential and impedance data chapters (Chapter 6 and Chapter 7 respectively).

Chapters 3 and 4 will focus on the design, theory and fabrication of a hybrid biosensor system. The basic theory of microelectrodes for extracellular action potential measurement and impedance monitoring will be discussed along with material considerations for the substrate and passivation. The fabrication process will be described including final packaging details. Instrumentation for monitoring the action potential and measuring cellular impedance will be discussed in detail in Chapter 5.

The experimental methods employed for testing the biosensor systems, including protocols for the culture of NG108, chick myocardial and astrocyte cell types will be described. Chapter 6 will focus on the measurement of extracellular action potentials from spontaneously beating chick myocardial cells and their response to pharmaceutical and toxic agents. Changes in the *shape* of the AP will be described as well as a possible method for deducing the action of an unknown, pharmacologically active agent. Chapter 7 is devoted to impedance measurements on individual cells using microelectrodes. Models of the cell/electrode interface will be presented along with theoretical optimized electrode geometries for monitoring changes in cell membrane conductance. Responses to pharmaceuticals and toxins will be presented along with data correlated to cell motility.

The thesis will conclude with a discussion of the utility of the whole cell based hybrid biosensors developed herein, and the limitations of the action potential and impedance based systems. Possible directions for future research will be explored.

References

Baxter, G.T., Bousse, L.J., Dawes, T.D., libby, J.M., Modlin, D.N., Qwicki, J.C. and Parce, J.W.,
"Microfabrication in silicon microphysiometry," *Clinical Chemistry*, 40(9):1800-1804 (1994).

Bousse, L., "Whole cell biosensors," *The 8th International Conference on Solid-State Sensors and
Actuators*, June 25-29, Stockholm, Sweden, 2:483-486 (1995).

Bove, M., Grattarola, M., Martinoia, S. and Verreschi, G., "Interfacing cultured neurons to planar substrate
microelectrodes: characterization of the neuron-to-microelectrode junction", *Bioelectrochemistry
and Bioenergetics*, 38:255-265 (1995).

Breckenridge, L.J., Wilson, R.J.A., Connolly, P., Curtis, A.S.G., Dow, J.A.T., Blackshaw, S.E. and
Wilkinson, C.D.W., "Advantages of using microfabricated extracellular electrodes for in vitro
neuronal recording", *Journal of Neuroscience Research*, 42:266-276 (1995).

Carrell, A., "On the permanent life of tissues outside the organism", *J. Exp. Med.*, 15:516-528 (1912).

Chien, C.B., and Pine, J., "Voltage-sensitive dye recording of action potentials and synaptic potentials from
sympathetic microcultures," *Biophys. J.*, 60:697-711 (1991).

Chien, C.B., and Pine, J.," An apparatus for recording synaptic potentials from neuronal cultures using
voltage-sensitive dyes," *J. Neuroscience Methods*, 38:93-105 (1991).

Cole, K.S. and Curtis, H.J., "Electrical impedance of Nitella during activity," *Journal of General Physiology*,
22(1):37-64 (1939).

Cole, K.S. and Curtis, H.J., "Electrical impedance of the squid giant axon during activity," *Journal of
General Physiology*, 22(5):649-670 (1939).

Connolly, P., Clark, P., Dow, J.A.T., Curtis, A.S.G., Lind, R. and Wilkinson, C.D.W., "Extracellular
electrodes for monitoring cell cultures," Institute of Physics Short Meeting Series No. 21 (IOP
Publishing, UK) (1989).

Connolly, P., Clark, P., Curtis, A.S.G., Dow, J.A.T. and Wilkinson, C.D.W., "An extracellular microelectrode
array for monitoring electrogenic cells in culture," *Biosensors and Bioelectronics*, 5(3):223-234
(1990).

Dijkstra, A.M., Brown, B.H., Leathard, A.D., Harris, N.D., Barber, D.C. and Edbrooke, D.L., "Clinical
applications of electrical impedance tomography," *Journal of Medical Engineering and Technology*,
17(3):89-98 (1993).

Drodge, M.H., Gross, G.W., Hightower, M.H. and Czisny, L.E., "Multielectrode analysis of coordinated,
multisite, rhythmic bursting in cultured CNS monolayer networks," *J. Neuroscience Methods*,
6(6):1583-1592 (1986).

Edell, D.J., "A peripheral nerve information transducer for amputees: long-term multichannel recordings
from rabbit peripheral nerves," *IEEE Trans. Biomed. Eng.*, BME-33:203-214 (1986).

Eggers, M.D., Astolfi, D.K., Liu, S., Zeuli, H.E., Doeleman, S.S., McKay, R., Khuon, T.S. and Ehrlich, D.J.,
"Electronically wired petri dish: a microfabricated interface to the biological neuronal network," *J.
Vac. Sci. Technol.*, B8(6):1392-1398 (1990).

Ehret, R., Baumann, W., Brischwein, M., Schwinde, A., Stegbauer, K. and Wolf, B., "Monitoring of cellular behaviour by impedance measurements on interdigitated electrode structures," *Biosensors and Bioelectronics*, 12(1):29-41 (1997).

Fricke, H. and Morse, S., "The electric resistance and capacity of blood for frequencies between 800 and 4.5 million cycles," *J. General Physiology*, 9:153-167 (1926).

Frick, H. and Curtis, H.J., "The electric impedance of hemolyzed suspensions of mammalian erythrocytes," *J. Gen.eral Physiology*, 18:821-836 (1935).

Fromherz, P., Offenhäusser, A., Vetter, T. and Weis, J., "A neuron-silicon junction: a retzius cell of the leech on an insulated-gate field-effect transistor," *Science*, 252:1290-1293 (1991).

Fromherz, P. Müller, C.O. and Weis, R., "Neuron transistor: electrical transfer function measured by the patch-clamp technique," *Physical Review Letters*, 71(24):4079-4082 (1993).

Fromherz, P. and Stett, A., "Silicon-neuron junction: capacitive stimulation of an individual neuron on a silicon chip," *Physical Review Letters*, 75(8):1670-1673 (1995).

Gesteland, R.C., Howland, B., Lettvin, J.Y. and Pitts, W.H., "Comments on microelectrodes," *Proc. IRE*, 47:1856-1862 (1959).

Ghosh, P.M., Keese, C.R. and Giaever, I., "Monitoring electropermeabilization in the plasma membrane of adherent mammalian cells," Biophys. J., 64:1602-1609 (1993).

Ghosh, P.M., Keese, C.R. and Giaever, I., "Morphological response of mammalian cells to pulsed ac fields," *Bioelectrochemistry and Bioenergetics*, 33:121-133 (1994).

Giaever, I. and Keese, C.R., "Monitoring fibroblast behavior in tissue culture with and applied electric field," *Proc. Natl. Acad. Sci.*, 81:3761-3764 (1984).

Giaever, I. and Keese, C.R., "Use of electric fields to monitor the dynamical aspect of cell behavior in tissue culture," *IEEE Transactions on Biomedical Engineering*, BME-33(2):242-247 (1986).

Giaever, I. and Keese, C.R., "Fractal motion of mammalian cells," *Physica D*, 38:128-133 (1989).

Giaever, I. and Keese, C.R., "Micromotion of mammalian cells measured electrically," *Proc. Natl. Acad. Sci.*, 88:7896-7900 (1991).

Giaever, I. and Keese, C.R., "A morphological biosensor for mammalian cells," *Nature*, 366:591-592 (1993).

Giaever, I. and Keese, C.R., "Toxic? Cells can tell," *Chemtech*, February:116-125 (1992).

Grattarola, M., Martinoia, S., Massobrio, G., Cambiaso, A., Rosichini, R. and Tetti, M., "Computer simulations of the responses of passive and active integrated microbiosensors to cell activity", *Sensors and Actuators*, B4:261-265 (1991).

Grattarola, M. and Martinoia, S., "Modeling the neuron-microtransducer junction: from extracellular to patch recording", *IEEE Transactions on Biomedical Engineering*, 40(1):35-41 (1993).

Gross, G.W., Rieske, E., Kreutzberg, G.W. and Meyer, A., "A new fixed-array multi-microelectrode system designed for long-term monitoring of extracellular single unit neuronal activity *in vitro*," *Neuroscience Letters*, 6:101-105 (1977).

Gross, G.W., "Simultaneous single unit recording *in vitro* with a photoetched laser deinsulated gold multimicroelectrode surface," *IEEE Transactions on Biomedical Engineering*, BME-26(5):273-279 (1979).

Gross, G.W., Williams, A.N. and Lucas, J.H., "Recording of spontaneous activity with photoetched microelectrode surfaces from mouse spinal neurons in culture," *J. Neuroscience Methods*, 5:13-22 (1982).

Gross, G.W., Wen, W.Y. and Lin, J.W., "Transparent indium-tin oxide electrode patterns for extracellular, multisite recording in neuronal cultures," *J. Neuroscience Methods*, 15:243-252 (1985).

Gross, G.W., Rhoades, B. and Jordan, R., "Neuronal networks for biochemical sensing," *Sensors and Actuators B*, 6:1-8 (1992).

Gross, G.W., Rhoades, B.K., Reust, D.L. and Schwalm, F.U., "Stimulation of monolayer networks in culture through thin-film indium-tin oxide recording electrodes, *J. Neuroscience Methods*, 50:131-143 (1993).

Gross, G.W. and Schwalm, F.U., "A closed flow chamber for long-term multichannel recording and optical monitoring," *Journal of Neuroscience Methods*, 52:73-85 (1994).

Gross, G.W., Rhoades, B.K., Azzazy, H.M.E. and Wu, M.C., "The use of neuronal networks on multielectrode arrays as biosensors," *Biosensors and Bioelectronics*, 10:553-567 (1995).

Harrison, R.G., "Observations on the living developing nerve fiber," *Proc. Soc. Exp. Biol. Med.*, 4:140-143 (1907).

Hagedorn, R., Konstanze, L.Z., Richter, E., Hornung, J. and Voigt, A., "Characterization of cell movement by impedance measurements on fibroblasts grown on perforated Si-membranes," *Biochemica et Biophysica Acta - Molecular Cell Research*, 1269(3):221-232 (1995).

Hodgkin, A.L. and Huxley, A.F., "A quantitative description of membrane current and its application ot conduction and excitation in nerve," *J. Physiol.*, 117:500-544 (1952).

Hause, L.L., Komorowski, R.A. and Gayon, F., "Electrode and electrolyte impedance in the detection of bacterial growth," *IEEE Transactions on Biomedical Engineering*, BME-28(5):403-410 (1981).

Israel, D.A., Barry, W.H., Edell, D.J. and Mark, R.G., "An array of microelectrodes to stimulate and record from cardiac cells in culture," *American Journal of Physiology*, 247:H669-H674 (1984).

Israel, D.A., Edell, D.J. and Mark, R.G., "Time delays in propogation of cardiac action potential," *American Journal of Physiology: Heart and Circulatory Physiology*, 27(6):H1906-H1917 (1990).

Jimbo, Y. and Kawana, A., "Electrical stimulation of cultured neural cells by planar electrode array," *Annual International Conference of the IEEE Engineering in Medicine and Biology Society*, 12(4):1741-1742 (1990).

Jimbo, Y. and Kawana, A., "Electrical stimulation and recording from cultured neurons using a planar electrode array," *Bioelectrochemistry and Bioenergetics*, 29(2):193-204 (1992).

Jimbo, Y., Robinson, H.P.C. and Kawana, A., "Simultaneous measurement of intracellular calcium and electrical activity from patterned neural networks in culture," *IEEE Transactions on Biomedical Engineering*, 40(8):804-810 (1993).

Kandel, E.R., Schwartz, J.H. and Jessell, T.M., *Principles of Neural Science*, Appleton and Lange, Norwak, Connecticut (1991).

Keese, C.R. and Giaever, I., "A whole cell biosensor based on cell-substrate interactions," *Annual International Conference of the IEEE Engineering in Medicine and Biology Society*, 12(2):500-501 (1990).

Keese, C.R. and Giaever, I., "A biosensor that monitors cell morphology with electric fields," *IEEE Engineering in Medicine and Biology*, June/July:402-408 (1994).

Kowolenko, M., Keese, C.R., Lawrence, D.A., and Giaever, I., "Measurement of macrophage adherence and spreading with weak electric fields," *Journal of Immunological Methods*, 127:71-77 (1990).

Lind, R., Connolly, P., Wilkinson, C.D.W., Breckenridge, L.J. and Dow, J.A.T., "Single cell mobility and adhesion monitoring using extracellular electrodes," *Biosensors and Bioelectronics*, 6:359-367 (1991).

Lind, R., Connolly, P. and Wilkinson, C.D.W., "Finite-element analysis applied to extracellular microelectrode design," *Sensors and Actuators*, B3:23-30 (1991).

Lo, C.M., Keese, C.R. and Giaever, I., "Monitoring motion of confluent cells in tissue culture," *Experimental Cell Research*, 204:102-109 (1993).

Lo, C.M., Keese, C.R. and Giaever, I., "pH changes in pulsed CO2 incubators cause periodic changes in cell morphology," *Experimental Cell Research*, 213:391-397 (1994).

Lo, C.M., Keese, C.R. and Giaever, I., "Impedance analysis of MDCK cells measured by electrical cell-substrate impedance sensing," *Biophysical Journal*, 69:2800-2807 (1995).

Martinoia, S., Bove, M., Carlini, G., Ciccarelli, C., Grattarola, M., Storment, C. and Kovacs, G., "A general-purpose system for long-term recording from a microelectrode array coupled to excitable cells," *J. Neuroscience Methods*, 48:115-121 (1993).

Maeda, E., Robinson, H.P.C. and Kawana, A., "The mechanisms of generation and propogation of synchronized bursting in developing networks of cortical neurons," *J. Neuroscience*, 15(10):6834-6845 (1995).

Mitra, P., Keese, C.R., and Giaever, I., "Electrical measurements can be used to monitor the attachment and spreading of cells in tissue culture," *BioTechniques*, 11(4):504-510 (1991).

Mohr, A. Finger, W., Föhr, K.J., Nisch, W. and Göpel, W., "Performance of a thin film microelectrode array for monitoring electrogenic cells in vitro, "*The 8th International Conference on Solid-State Sensors and Actuators*, Stockholm, Sweden, June 25-29, 2:479-482 (1995).

Mohr, A. Finger, W., Föhr, K.J., Göpel, W. Hammerle, H. and Nisch, W., "Performance of a thin film microelectrode array for monitoring electrogenic cells in vitro," *Sensors and Actuators B-Chemical*, 34(1-3):265-269 (1996)

Moy, A.B., Engelenhoven, J.V., Bodmer, J., Kamath, J., Keese, C., Giaever, I. and Shasby, S., "Histamine and thrombin modulate endothelial focal adhesion through centripetal and centrifugal forces," *Journal of Clinical Investigation*, 97(4):1020-1027 (1996).

Nicholls, J.G., Martin, A.R. and Wallace, B.G., *From Neuron to Brain*, Sinauer Associates, Inc., Sunderland, Massachusetts (1992).

Noiri, E., Hu, Y., Bahou, W.F., Keese, C.R., Giaever, I. and Goligorsky, M.S., "Permissive role of nitric oxide in endothelin-induced migration of endothelial cells," *Journal of Biological Chemistry*, 272(3):1747-1752 (1997).

Novak, J.L. and Wheeler, B.C., "Recording from the *aplysia* abdominal ganglion with a planar microelectrode array," *IEEE Transactions on Biomedical Engineering*, BME-33(2):196-202 (1986).

Parce, J.W., Owicki, J.C., Kercso, K.M., Sigal, G.B., Wada, H.G., Muir, V.C., Bousse, L.J., Ross, K.L., Sikic, B.I. and McConnell, H.M., "Detection of cell-affecting agents with a silicon biosensor," *Science*, 246:243-247 (1989).

Pei, Z., Keese, C.R., Giaever, I., Kurzawa, H. and Wilson, D.E., "Effect of the pSV2-neo plasmid on NIH 3T3 cell motion detected electrically," *Experimental Cell Research*, 212:225-229 (1994).

Pine, J., "Recording action potentials from cultured neurons with extracellular microcircuit electrodes," *J. Neuroscience Methods*, 2(1):19-31 (1980).

Regehr, W.G., Pine, J. and Rutledge, D.B., "A long term in vitro silicon-based microelectrode-neuron connection," *IEEE, Trans. Biomed. Eng.*, 35:1023-32 (1988).

Rhoades, B.K. and Gross, G.W., "Potassium and calcium channel dependence of bursting in cultured neuronal networks," *Brain Research*, 643:310-318 (1994).

Salzberg, B.M., "Optical recording of neuronal activity in an invertebrate central nervous system: simultaneous monitoring of several neurons," *J. Neurophysiology*, 40(6):1281-1291 (1977).

Schwan, H.P., "Electrical properties of tissue and cell suspensions," *Advances in Biological and Medical Physics*, Edited by Lawrence, J.H. and Tobias, C.A., Academic Press, New York, 5:147-209 (1957).

Smith, T.J., Wang, H.S., Hogg, M.G., Henrikson, R.C., Keese, C.R. and Giaever, I., "Prostaglandin E_2 elicits a morphological change in cultured orbital fibroblasts from patients with Graves ophthalmopathy," *Proc. Natl. Acad. Sci.*, 91:5094-5098 (1994).

Standen, N.B., Gray, P.T.A. and Whittaker, M.J. eds., "Microelectrode techniques," *The plymouth workshop handbook*, Company of Biologists, Cambridge (1987).

Tank, D.W., Cohan, C.S. and Kater, S.B., "Cell body capping of array electrodes improves measurements of extracellular voltages in microcultures on invertebrate neurons," *IEEE Conf. on Synthetic microstructures*, Airlie House, Arlington, Virginia, IEEE, New York (1986).

Thomas, C.A. Jr., Springer, P.A., Loeb, G.E., Berwald-Netter, Y. and Okun, L.M., "A miniature microelectrode array to monitor the bioelectric activity of cultured cells," *Exp. Cell Res.*, 74:61-66 (1972).

Tiruppathi, C., Malik, A.B., Del Vecchio, P.J., Keese, C.R., and Giaever, I., "Electrical method for detection of endothelial cell shape change in real time: assessment of endothelial barrier function," *Proc. Natl. Acad. Sci.*, 89:7919-7923 (1992).

Wang, H.S., Keese, C.R.,Giaever, I. and Smith, T.J., "Prostaglandin E_2 alters human orbital fibroblast shape through a mechanism involving the generation of cyclic adenosine monophosphate," *Journal of Clinical Endocrinology and Metabolism*, 80(12):3553-3560 (1995).

Wegener, J., Sieber, M. and Galla, H.J., "Impedance analysis of epithelial and endothelial cell monolayers cultured on gold surfaces," *J. Biochem. Biophys. Methods*, 32(3):151-170 (1996).

Weis, R., Müller, B. and Fromherz, P., "Neuron adhesion on a silicon chip probed by an array of field-effect transistors," *Physical Review Letters*, 76(2):327-330 (1996).

Wise, K.D., Angell, J.B. and Starr, A., "An integrated circuit approach to extracellular microelectrodes," *IEEE Trans. Biomed. Eng.*, BME-17:238-246 (1970).

Chapter 2   THEORY OF CELLULAR FUNCTION AND RESPONSE

Every animal appears as the sum of vital units, each of which bears in itself the complete characteristics of life.

Rudolf Virchow, 1858

2.1 Introduction

Cell biology cannot be fully understood without knowledge and understanding of biochemistry, metabolism, molecular biology and genetics. However, a full exploration of these profoundly interesting and intriguing fields is both beyond the scope of this work and the knowledge of the author. Thus, this chapter will focus on the basics of cellular function as it relates to electrical activity in cells, cellular membrane impedance characteristics, and cell adhesion and motion for animal cells. The specifics of these functions will be explored in detail where necessary for an understanding of the signals and responses characterized in these studies.

The chapter will begin with a discussion of cellular construction; the materials that comprise the membrane, transmembrane proteins that allow transfer of ions through the membrane, and proteins that provide both structural support and allow cell movement. The mechanisms responsible for cellular adhesion to solid substrates will be explored along with the protein functions underlying cellular *motility* (cell movement). The role of different ionic channels in establishing a potential across the cell membrane will be discussed, as will modulation of this potential with changing membrane properties. This basic information will be used to understand *action potentials* (the intrinsic electrical activity of cells) and how changes in the cellular membrane can affect them. This will be important when interpreting changes in the measured action potentials (APs) due to pharmacological manipulation in Chapter 6. The ionic channels not only affect the

transmembrane potential, but also the electrical impedance characteristics of the cellular membrane. This will be discussed along with a basic electrical model of the membrane. For measurement of this impedance using extracellular electrodes (as will be discussed in later chapters), cellular adhesion and motility can greatly impact the result. Thus, an understanding of the mechanisms responsible for these phenomena is critical for interpretation of the measured impedance and development of appropriate control experiments as is described in Chapter 7.

2.2   Cellular Construction

Cells consist of a lipid bilayer membrane surrounding an intracellular fluid containing numerous organelles (mitrochondrion, nucleus, endoplasmic reticulum, lysosomes, etc.). This membrane is the most significant portion of the cell as it relates to this research. The impedance characteristics may best be described as mostly capacitive with a slight resistive component due to channels that allow transmembrane transport of specific ions. Perhaps the most interesting property of this semipermeable membrane is that the permeability can be varied by *voltage* or *ligand* (molecule to molecule binding) gating of the ion channels. This is what forms the basis of an action potential.

Proteins are actively at work in almost all cellular functions and have been shown to play a significant mechanical role in both *mitosis* (cell division) and *motility* (cell motion). Two proteins of interest are actin and tubulin which help to form the basic physical structure of the cell upon which the membrane is built.

2.2.1 Phospholipids, Proteins and the Plasma Membrane
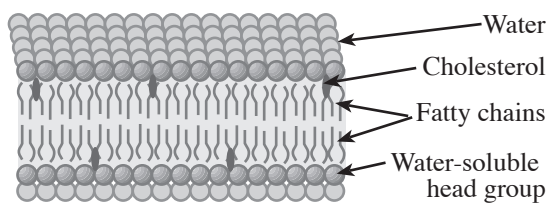
Figure 2.1: Phospholipid bilayer. Cell membranes consist of a sheet of aligned fatty molecules with water-soluble head groups at both ends. One side becomes the outside of the cell membrane while the other becomes the inside. Cholesterol molecules provide some rigidity to this fatty double layer. After [Lodish, et al., 1995].

Biological membranes are constructed from molecules containing long fatty chains with a charged head group (mainly charged phosphates) making one end water soluble. These molecules spontaneously orient themselves to form a double layer with the fatty ends of two molecules coming together. As shown in Figure 2.1, this results in a layer having a fatty interior with the

28

outer, electrically charged head groups in contact with the surrounding water. This *phospholipid bilayer* is generally about 7.5 nm thick and can fold to form an enclosed shell with water on both the inside and the outside. This is the basic structural building block of the cellular membrane, constructed so that the cell may survive in an aqueous environment while maintaining the independent intracellular cytoplasm. While this fatty double layer serves this purpose well, it does not provide much physical strength. Cholesterol molecules interspersed in the layer provide some rigidity, but most cellular stability is achieved through a network of proteins both inside and outside the cell membrane. It is these proteins that constitute the framework which gives the cell its shape and allows control of motion, transport of molecules, and adhesion to surfaces.

Proteins are the major macromolecules in the cell and are responsible for a variety of cellular functions. While there are many different kinds of proteins, they may be classified into two groups; the *integral proteins* which pass through the cell membrane and the *peripheral proteins* which stud the inside and outside of the membrane. On average, proteins constitute approximately 50% of the mass of the cellular membrane and are responsible for approximately seven different cellular functions. There are proteins that provide structural integrity to the cell membrane, proteins which function as pumps to actively transport ions across the cell membrane (as will be discussed later, this is important for

Figure 2.2: Transport across a pure phospholipid bilayer. The membrane is permeable to small nonpolar (hydrophobic) molecules such as O_2 and N_2 as well as small uncharged polar molecules such as urea and ethanol. It is slightly permeable to water and completely impermeable to large uncharged, and charged polar molecules as well as ions. Integral (transmembrane) proteins allow transport of these other substances. After [Lodish, et al., 1995].

development of a transmembrane potential), and proteins that operate as carriers to transport substances within the cell. There are integral proteins that form ion channels, receptor proteins that bind neurotransmitters and hormones, enzyme proteins which

catalyze reactions at the membrane surface, and glycoproteins which function in antibody processing and are responsible for cellular adhesion to surfaces [Ganong, 1993]. Most of these will be discussed with special attention given to those proteins responsible for transport of substances across the cell membrane and those responsible for the structural integrity of the membrane and adhesion to surfaces. An understanding of the function of these proteins is important for interpreting the results of pharmacological manipulation on the recorded action potential and measured cellular impedance.

The cellular membrane is truly a remarkable structure. While gases (small non-polar molecules), small uncharged polar molecules, and water are able to diffuse directly through the phospholipid bilayer (see Figure 2.2), transmembrane transport of ions and charged and uncharged polar molecules requires the presence of integral proteins. As shown in Figure 2.3, this transport can be accomplished by several different methods. There are protein pumps that harness the energy of adenosine triphosphate (ATP) hydrolysis to move specific ions across the cell membrane against their electrochemical gradient at a rate of 1 to 10^3 ions/s. These pumps maintain the relatively low calcium and sodium ion concentrations inside the cell relative to the extracellular environment, and are responsible for the transport of Na^+ and K^+ against their concentration gradients to establish the resting membrane potential as will be described in more detail in Section 2.5.2.

There are channel proteins that form a protein-lined passageway across the membrane through which water or specific types of ions can move along their chemical concentration or electrical gradients. These channels can be either always-open (as is the case for some K^+ channels), or gated, with the state (open or closed) being determined by the transmembrane potential (voltage-gated) or by binding of a ligand (often a neurotransmitter, hormone, intracellular Ca^{2+}, cyclic AMP, or G proteins) to the channel (ligand-gated). When open, these channel proteins allow 10^7 to 10^8 ions/s to travel across the cell membrane.

Another group of proteins that allow transmembrane transport of material are known as the transport proteins. In contrast to the channel proteins, these transporters bind a single (or a few) ion(s) (or molecule(s)) at a time and then undergo a conformational change. Thus, only one (or a few) ion(s) can be transported across the membrane at one time, making the process relatively slow. Only 10^2 - 10^4 ion/s are transported through any given channel. The transport proteins fall into three groups as shown in Figure 2.3. The *uniporter* allows diffusion of a single type of ion or molecule down its concentration gradient, while with both *symporters* and *antiporters*, the movement of one type of molecule or ion against its concentration gradient is coupled to movement of a different type of ion (or molecule) down its electrochemical gradient. In the case of symporters, both substances travel in the same direction; for antiporters, they move in opposite directions.
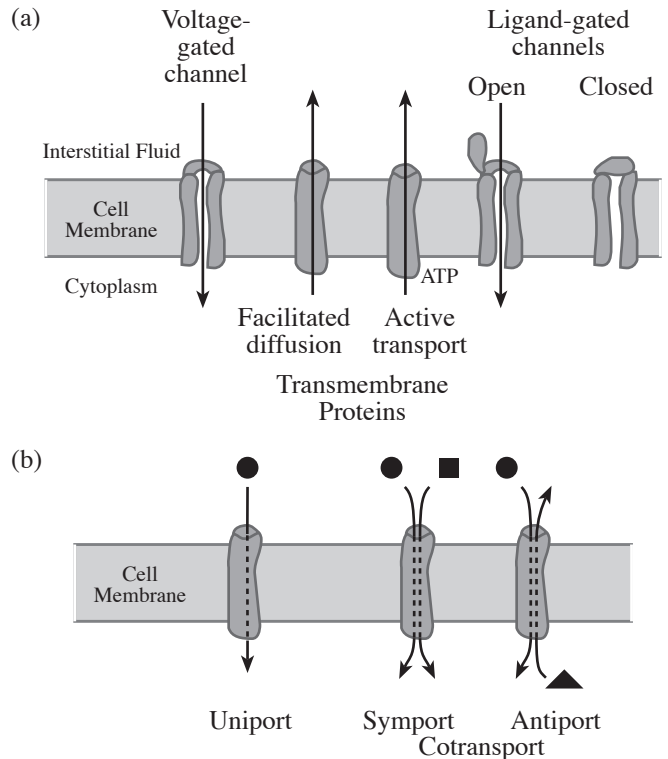
Figure 2.3: Transmembrane transport proteins. (a) The three major classes of transport proteins. Ion channels facilitate the movement of specific ions down their (electro)chemical gradients, while pumps utilize ATP hydrolysis to move specific ions across the cell membrane against their (electro)chemical gradients. The transporters facilitate movement of specific small molecules (glucose, amino acids, etc.) or ions (Na^+, H^+, etc.) across the cell membrane. (b) The three groups of transporters. Uniporters (also shown in (a)) transport one type of ion or molecule (black circle) down its electrochemical gradient. With both symporters and antiporters, movement of a specific ion(s) or molecule(s) (black circle) against its concentration gradient is coupled to movement of another ion(s) or molecule(s) transported in the same direction (square) or the opposite direction (triangle) against an (electro)chemical gradient. After [Ganong, 1993].

The membrane isolates the living cell from its environment while allowing transmembrane transport of the necessary ions and molecules using integral proteins as

described above. However, other substances known as *structural proteins* are equally important. These proteins are responsible for determining cellular shape, adhesion and movement as is described below.

2.2.2 Structural Proteins and the Cytoskeleton

The cytoskeleton is a cohesive meshwork of protein filaments which allows movement of the cell, shaping of the cellular membrane, and intracellular transport of different substances. It consists of three types of structural protein filaments (actin filaments, microtubules, and intermediate filaments) that may be distinguished by their diameter and their chemical properties as is discussed below.

The protein actin is the most abundant and versatile of the cytoskeletol proteins involved in motility. Almost all actin based motility functions are governed by the polymerization and depolymerization of actin filaments (also known as microfilaments). As shown in Figure 2.4, in the presence of salt, actin monomers are *activated* (transformed to a form active in polymerization) and form *nucleating seeds*: small clusters of actin monomers which allow the filament to begin assembly. Actin monomers bind onto the ends of the growing filament, with the rate of polymerization and depolymerization governed by simple kinetic equations dependent on the concentrations of monomer and filaments as well as their respective activation energies. As will be discussed later, there are compounds that interfere with both the polymerization and depolymerization processes which may be used to control cell motility.

Individual actin filaments organize themselves (via actin cross-linking proteins) into actin bundles and actin networks, both of which provide a structural framework which supports the cell membrane. The bundles consist of closely packed arrays of parallel actin
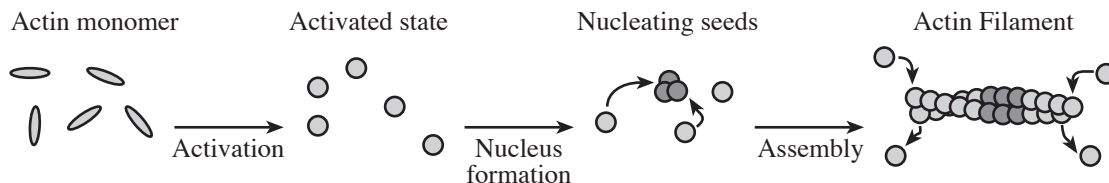
Figure 2.4: *Actin polymerization. Actin monomers bind salt and undergo a conformational change to a form active in polymerization. These activated monomers bind together to form clusters which act as nucleating seeds for the assembly of filaments. Activated monomers bind to the actin filament continuing growth. Depolymerization occurs by removal of individual monomer units from the chain. After [Bray, 1992].*

filaments (each filament approximately 8 nm in diameter) and generally protrude from the cell surface. These actin bundle projections create fingers of membrane; *microvilli* and *filopodia*. The microvilli present on cells are responsible for transport of nutrients from the surrounding media into the cell or tissue. These are not of great significance for the cells studied herein. The filopodia, however, are responsible for attaching cells to solid surfaces and are of significant importance to this work. They generally extend from the cell body at the edge of moving or spreading cells, establishing a stable contact to the underlying surface at the leading edge of the cell. As a cell migrates, there is an active zone of actin polymerization at the leading edge which alters the shape of the cellular membrane. The polymerized actin filaments crosslink to form bundles which project out from the leading edge of the cell and make contact with the substrate. The role of actin in cell movement and attachment are discussed in more detail in Section 2.4 and Section 2.3 respectively.

In the cell interior, the actin filaments fan out and become part of a network of filaments. This network consists of loosely packed, crisscrossed (often at right angels) actin filaments. Actin networks may be further divided into two types: a two-dimensional web associated with the plasma membrane and a three-dimensional structure extending through the cytosol. For both actin bundles and networks, connection to the plasma membrane is accomplished via membrane-microfilament binding proteins which tack the lipid bilayer to the underlying cytoskeleton scaffolding, or by direct binding of actin to an integral membrane protein.

Microtubules are polymers of the protein tubulin which exists in solution as a dimer of two isoforms, α-tubulin and β-tubulin. As shown in Figure 2.5, these tubulin dimers form short protofilaments by arranging themselves longitudinally. These protofilaments quickly associate laterally into curved sheets, eventually wrapping around to form a hollow microtubule consisting of 13 protofilaments. Additional tubulin dimers attach to the ends of the microtubule resulting in elongation. The opposite process results in shrinkage of the microtubule. These tubular structures are approximately 25 nm in diameter and vary in length from a fraction of a micrometer to several hundred micrometers. In contrast to actin filaments, these long, straight structures are solitary in the cytosol, never forming two- or three-dimensional networks. They tend to radiate out from the nucleus of the cell where their negatively charged ends are anchored. The positively charged ends elongate and make contact with the actin network associated with the plasma membrane. This creates lines of communication, transport and control from the center of the cell to the periphery, allowing microtubules to play a significant role in organizing cell movements. It is interesting to note that this differs from the apparently random way in which actin

Free tubulin dimer

α-tubulin
β-tubulin

(+) end

(-) end

(a) Protofilament assembly   (b) Sheet assembly   (c) Microtubule elongation
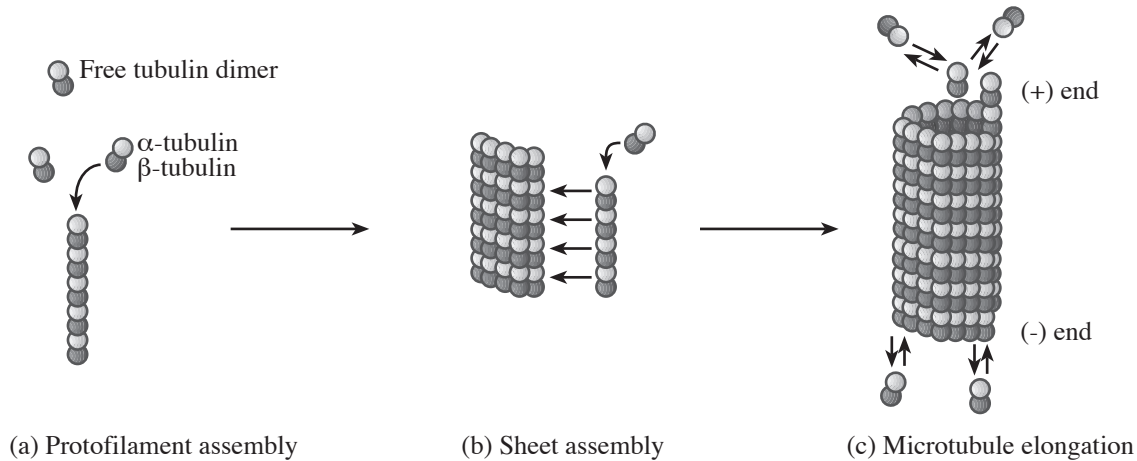
Figure 2.5: Microtubule assembly process. (a) Free tubulin dimers bind together to form short protofilaments. (b) These protofilaments associate laterally into curved sheets which eventually wrap around into a microtubule with 13 protofilaments (c). The microtubule elongates by addition of free tubulin dimers to the tubule. Polymerization at the positively charged end of the microtubule occurs at a rate twice that of the negative end. After [Lodish, et al., 1995].

filaments assemble; actin filaments nucleate from numerous sites throughout the cytosol while almost all microtubule nucleation occurs in a region near the nucleus known as the centrosome.

Microtubules are a large part of the scaffolding which supports and shapes the cell. There are some structures which remain fairly stable while others actively polymerize and depolymerize to perform different functions. During cell mitosis, microtubules actually bind to individual chromosomes and move them to a position midway between the two poles of the cell, where the chromosomes divide. In neuronal cells, the polymerization of microtubules guides the growth of axons and dendrites. The interaction of different microtubule-associated proteins with microtubules allows them to slide against one another (important for changing cellular shape) and move membrane vesicles, polysomes and other components of the cytoskeleton through the cytoplasm (discussed in more detail in Section 2.4).

Intermediate filaments are so named because their size (10 nm diameter) is smaller than the 25 nm microtubules yet larger than the 8 nm microfilaments. They extend through the cytosol, and connect at one end to the cellular membrane by a variety of mechanisms. Their function appears to be purely structural; reinforcing the plasma membrane while the cell changes shape during cell movement. Since these filaments are not involved in cell motility, they are not of great significance to this work and will not be discussed further.

2.3 The Extracellular Matrix and Cellular Adhesion

Surrounding the cellular membrane is a collection of fibrous collagen proteins, hyaluronic acid, proteoglycans (complexes of polysaccharides and proteins), and glycoproteins (proteins linked to chains of carbohydrates). This is collectively known as the extracellular matrix (ECM). Its composition varies depending on the cell type, tissue type, and culture conditions, but the majority of the required components are contained within standard cell culture medium containing serum. It is this matrix that forms the connections between cells *in vivo* and allows cells to attach to surfaces *in vitro*. Since it is responsible for the attachment of cells to a substrate in culture, the extracellular matrix exerts some control over cellular shape (cells are spherical in suspension and flatten out as they attach to a surface). By changing the surface properties of the cell culture substrate (e.g. patterning of self-assembled monolayers (SAMS)), binding of the ECM to the surface, and therefore cell attachment, can be controlled. Thus, it is possible to control the shape of cells (they can be formed into squares for instance), and in fact direct cell life and death [Chen, et al., 1997]. Chen, et al. observed that by simply changing the shape a cell was forced to take when adhering to a surface, cells were switched from growth to *apoptosis* (cell fragmentation). This is clear evidence that there are specific transmembrane signaling mechanisms through which the ECM and other factors (such as mechanical structures) influence cell behavior.

There is a great deal of research aimed at understanding ECM components and their effects on cellular shape and function. As mentioned above, numerous researchers are working on controlling the attachment of ECM components to affect how cells attach to substrates *in vitro*. However, for this work it is only important to remember that the ECM forms a bridge between the cellular membrane and the substrate upon which the cells are cultured. No chemical modifications (e.g. SAMS) or patterning of the substrate were performed in these studies. However, an understanding of the adhesion mechanisms is important for interpretation of impedance data obtained with extracellular electrodes as is described in Chapter 7.

As a cell comes into contact with a solid surface, there are specific sites where adhesion occurs known as *focal contacts* or *adhesion plaques*. The formation of adhesion sites typically depends on two proteins found in serum containing culture media: fibronectin and vitronectin which form part of the ECM. These proteins bind to the culture surface and express specific sequences which are recognized by cell-surface receptors (a family of receptors known as *integrins*).
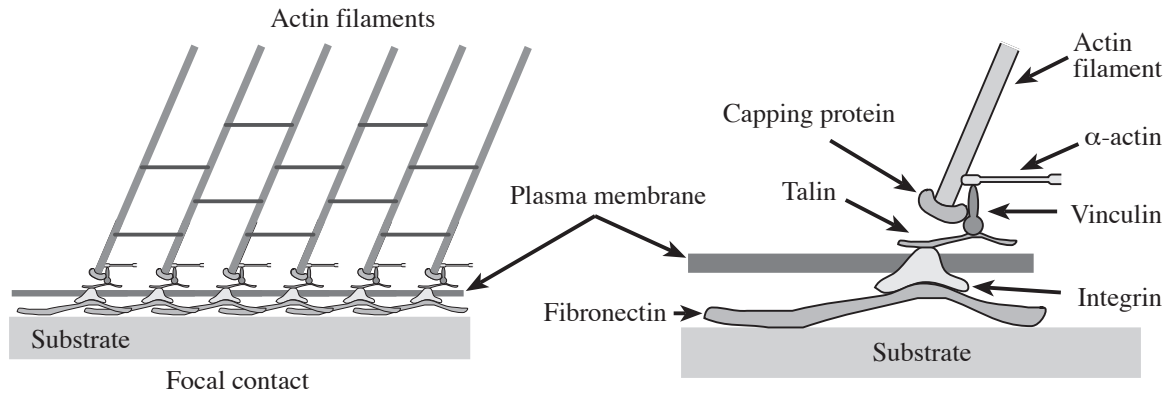
Figure 2.6: A focal contact or adhesion plaque. The actin cytoskeleton is attached to the extracellular matrix (represented here by fibronectin) via a chain of proteins connected to the integral protein integrin. This area of close contact is usually an oval around 1 μm long separated from the substrate by 1 to 15 nm. After [Bray, 1992].

As shown in Figure 2.6, integrins are transmembrane proteins that bind to fibronectin (or vitronectin, or some other component of the ECM). A chain of other proteins (talin, vinculin, α-actin) connects the integrin to an actin filament, thereby effectively coupling the cytoskeleton to the cell culture substrate. These focal contact areas are generally oval patches roughly 1 μm long and separated from the substrate by 1 to 15 nm. With a migrating cell, new focal contacts are made at the leading edge of the cell while focal contacts further back detach. Thus, the cellular membrane rolls over the top of the cell while the base remains fixed in space. Of course, this motion also involves the action of actin filaments and microtubules as is described in Section 2.4.

2.4 Cellular Motility

In Section 2.2.2, the role of actin and tubulin in cell morphology and structure was discussed and the involvement of such structures in cell motility was alluded to. But how does polymerization and depolymerization of protein filaments result in movement of the cell? What is needed is an enzyme capable of converting chemical energy into mechanical force; a *motor protein*. Myosin is thought to be largely responsible for this type of conversion as it relates to movement of the cellular membrane. Myosin hydrolyzes ATP and converts this chemical energy into mechanical energy, allowing movement of the myosin molecule along the actin filament. While there are several different forms of myosin which contribute in different ways to cellular function, this discussion will focus on myosin II (involved in contraction) and myosin I (involved in movement of the plasma

membrane relative to the actin scaffolding). The basic mechanism of action of myosin II may best be understood by examination of Figure 2.7. If the orientation of the actin filament is conducive to binding a myosin molecule, the myosin will slide or walk along the fiber. In the event that the myosin binds to two parallel actin filaments (contained in a bundle for instance), the myosin will attempt to slide along both fibers. However, both ends of the molecule are restricted, so this mechanical force results in the movement of the two actin filaments against each other in opposite directions. This is the basis of cellular contraction and is involved in movement of the actin bundle as the cell migrates.

Myosin I differs from myosin II in that it contains only one head and has a significantly shorter tail region. The head region binds to actin filaments while the tail is able to bind to several different structures. It can crosslink to form a structure similar to myosin II and cause contraction of actin filaments as shown in Figure 2.7. The tail can bind to membrane vesicles and act as a carrier for movement along actin fibers. Additionally, myosin can act as a bridge between the actin filaments and the cellular membrane, or move the membrane relative to the actin network.

Tubulin has its own set of motor proteins that act much in the same way as myosin on actin. Dynein and kinesin are two such proteins that harness the energy of ATP hydrolysis to generate mechanical force. Binding of a single myosin-like head to a tubulin fiber can result in movement of the protein along the microtubule, or in cases where the tail has attached to another structure (organelles, sacs of membrane, membrane vesicles, chromosomes, etc.), move those structures along the microtubule. The motion of kinesin is directed towards the positively charged end of the microtubule (the perimeter of the cell or the end
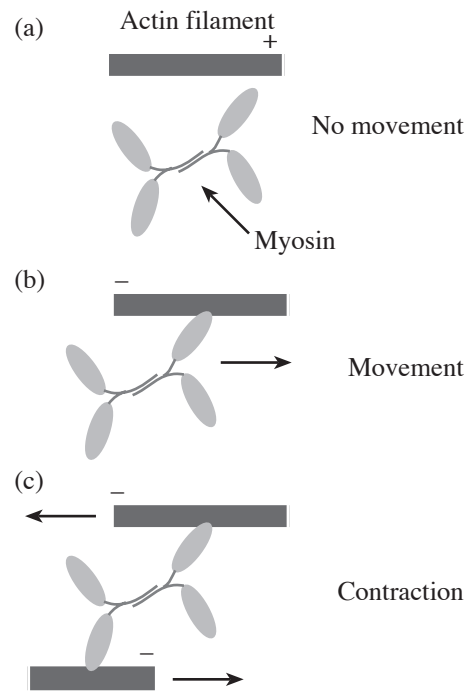
Figure 2.7: Movement of myosin along actin filaments. (a) Binding of myosin heads to the actin filament does not occur if the filament is in the incorrect orientation. (b) If the actin filament is correctly oriented, the myosin slides along the fiber towards the positively charged end. (c) In the instance where binding occurs at both ends of a bipolar aggregate, the two actin filaments will be moved against each other. This is the molecular basis of contraction. After [Bray, 1992].

of an axon) while that of dynein is directed towards the negatively charged end (the center of the cell or the cell body in the case of an axon).
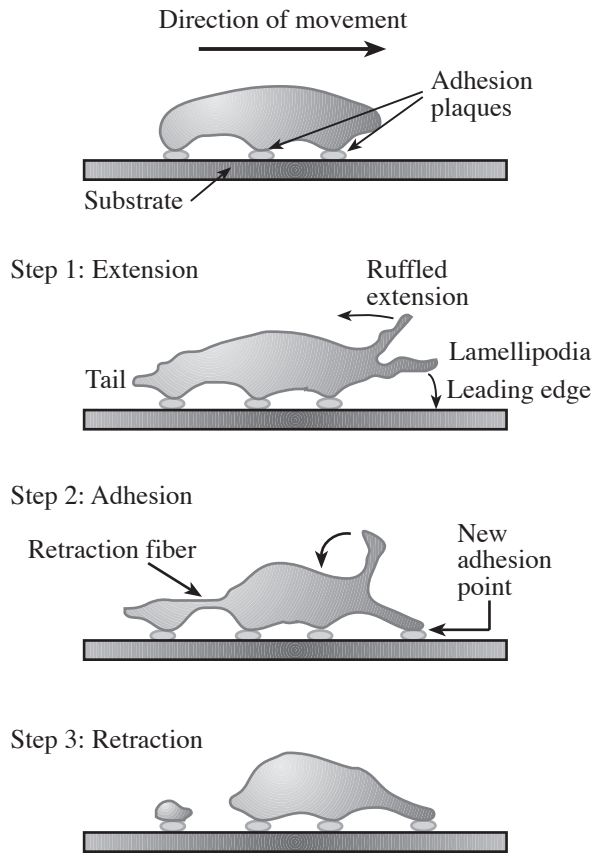
Figure 2.8: The steps in cell motility. During cell movement, lamellipodia extend from the leading edge of the cell. Some attach to the substrate while others move backward over the ventral surface of the cell. As the cell is pulled forward using the new adhesion points as an anchor, the tail section becomes elongated (retraction fiber) and the lamellipodia ruffles along the ventral surface of the cell collapse. Eventually the retraction fiber breaks and the tail retracts into the cell body. Generally a small portion of the membrane is left behind. After [Lodish, et al., 1995].

The tail region of dynein also has the ability to bind directly to microtubules, allowing two microtubules to slide against one another as described above for the interaction of myosin II with two actin filaments. This is responsible for such things as the beating of cilia and flagella, and may contribute to cell movement in concert with the actions of actin filaments.

The combined action of motor proteins, polymerization and depolymerization of actin filaments and microtubules, and the formation of adhesion plaques all result in the motion of cells. As shown in Figure 2.8, cell motility involves an extension of the leading edge of the cell, attachment of this new extension to the substrate, and contraction of the rear portion of the cell using the newly formed adhesion plaques as an anchorage point. This cycle is repeated as necessary for the cell to move in response to chemical, physical, or other environmental stimuli (see [Fuhr, 1996] for a discussion of these different environmental stimuli: mechanical micro-barriers, electrical and optical

fields, and surface coatings). Extension of the leading cell margin requires the assembly of actin filaments, which create the extending microspikes and lamellipodia. This process is

driven by free actin molecules diffusing to the advancing region of the cell where they add to the positive end of the actin filament. Additional membrane proteins and actin crosslinkers also move to this region either via diffusion or perhaps by the action of myosin I. As the cell attaches to the surface, these polymerizing actin filaments are bound to integrin which connects the extracellular matrix to the cell's cytoskeleton. While this anchor is being established the trailing edge of the cell undergoes actin contraction (due to the action of myosin II) which pulls the cell towards the point of anchorage. It simultaneously produces hydrostatic pressure which pushes the cytoplasm towards the front of the cell. During all of this, the plasma membrane is being pulled along actin filaments by the action of myosin I, causing the membrane to effectively roll around the cytoplasm. This process continues with the previous focal points of the leading edge becoming adhesion plaques on the underside of the cell. Eventually, these plaques are released as this portion of the cell becomes the trailing edge. While the details of cellular movement are certainly cell specific, this simplistic model is useful for the purposes of this research. With this understanding of the underlying mechanisms of cellular motility, it is possible to design experiments that take this motion into account and perhaps eliminate the motion effects completely. This is discussed in more detail in Chapter 7.

2.5 The Action Potential

To understand how an action potential is generated in electrically active cells, one must first understand how the plasma membrane of a cell (with its embedded ion channels) develops a potential across it. The static electrical state of a cell can best be described as an equilibrium where the chemical and electrical forces acting on ions across the cell membrane are balanced. Constant ionic currents flow, but the net ionic transfer is zero resulting in a constant transmembrane potential. This will be explored in this section along with the result of perturbing the equilibrium condition to generate an action potential.

2.5.1 The Nernst Equation

If one examines the case of two solutions separated by a semipermeable membrane (as is the case with a cell), each containing a salt solution of different ionic concentration, a flow of ions will result. In this example, the membrane is only permeable to one ion (A^+) in the solution. At the moment the two solutions are brought into contact with the membrane, the transmembrane potential will be zero. However, the A^+ ions will diffuse

down their concentration gradient causing one side to become biased with respect to the other. This diffusion will continue until the electric field across the membrane is large enough to balance the forces driving diffusion of A^+ across the membrane. At this point the system is said to be in equilibrium with respect to A^+.

This equilibrium potential was first calculated over 100 years ago by Nernst [Nernst, 1888]. Beginning with the Boltzmann equation of statistical mechanics, the probability of finding a particle in one of two states (p_1 and p_2) is given as the energy difference between those two states ($u_2 - u_1$):

$$\frac{p_2}{p_1} = e^{\left(-\frac{u_2 - u_1}{kT}\right)}$$

(2.1)

where k is Boltzmann's constant (1.381×10^{-23} V•C•K^{-1}) and T is the absolute temperature in degrees Kelvin. Unfortunately, this equation describes the equilibrium distribution of particles in electric and magnetic fields. However, it is possible to rearrange (2.1) to a chemical form by changing the probabilities (p) to concentrations (c) and changing the particle energies (u) to molar energies (U). By considering one mole of an ion S with a charge z_s, one can write the Nernst equation giving the equilibrium potential E_s as a function of the ionic concentration ratio and the valence:

$$E_s = E_1 - E_2 = \frac{RT}{z_s F} \ln \frac{[S]_2}{[S]_1}$$

(2.2)

where $[S]_1$ and $[S]_2$ represent the concentrations of the ion S on each side of the membrane, R is the gas constant (8.315 J•K^{-1}•mol^{-1}) and F is Faraday's constant (9.648×10^4 C•mol^{-1}). In (2.2), RT/F is equivalent to kT/q. From this equation it can be seen that the equilibrium potential varies linearly with absolute temperature and logarithmically with the ionic concentration ratio. The polarity of the potential is determined by the direction of the concentration gradient in the system.

In biological systems, one is concerned with the equilibrium potentials of biologically relevant ions: K^+, Na^+, Ca^{2+}, and Cl^-. Each of these has its own equilibrium potential calculated based on the assumption that the membrane is permeable only to that ion. Typical physiologic values for these are given in Table 2.1 below where the standard convention of membrane potentials being measured intracellular minus extracellular has been used.

Examining the values in Table 2.1, it can be seen that the limits of the transmembrane potential are set on the positive side by calcium and on the negative by potassium. This

Ion	Extracellular concentration (mM)	Intracellular concentration (mM)	$\dfrac{[\text{Ion}]_o}{[\text{Ion}]_i}$	Equilibrium potential @ 37°C (mV)
Na^+	145	12	12	+67
K^+	4	155	0.026	-98
Ca^{2+}	1.5	10^{-7} M	15,000	+129
Cl^-	123	4.2	29	-90

Table 2.1:   Free ionic concentrations and equilibrium potentials for mammalian skeletal muscle after [Hille, 1992].

holds true for most cell types even though the equilibrium potentials are different. In all cases, both potassium and chloride drive the intracellular potential negative with respect to the extracellular, while sodium and calcium attempt to drive it positive. All of these ionic forces act in concert to define the actual transmembrane resting potential as is discussed in detail in the next section.

2.5.2 Resting Membrane Potential

As described above, the semipermeable membrane allows flow of certain ions between the intracellular and extracellular fluids, which causes a potential to develop across the membrane as defined by the Nernst equation. For all excitable cells, the net result is a negative transmembrane potential (with respect to an extracellular reference) since the membrane has far more open K^+ channels than Na^+, Cl^- or Ca^{2+} channels. In order to calculate a more accurate transmembrane potential, it is necessary to modify the Nernst equation so that the concentrations of the ions are weighted in proportion to the number of open channels through the membrane; in other words, their permeability constants (P_{Na}, P_K and P_{Cl}):

$$E = \frac{RT}{F} \ln \frac{P_K K_o + P_{Na} Na_o + P_{Cl} Cl_i}{P_K K_i + P_{Na} Na_i + P_{Cl} Cl_o} \tag{2.3}$$

In (2.3), the "o" and "i" subscripts indicate "outside" and "inside" the cell respectively. The relative positioning of the "i" and "o" terms for chloride are the inverse of those for potassium and sodium to account for the negative charge of that ion. Calcium is neglected in the calculation since there are few normally open calcium channels; the *resting membrane potential* is determined mainly by K^+, Na^+ and Cl^- (with the major contribution due to K^+). For a more thorough analysis of the resting membrane potential see [Nicholls, et al., 1992; Kandel, et al., 1991; Weiss, 1996].

The equilibrium condition described by (2.3) is not entirely accurate for cellular systems since it neglects contributions by other ionic current paths. Recall that Section 2.2.1 described the role of integral proteins in formation of ion specific channels and active transport pumps. The resting membrane potential is determined not only by the leaky K^+ channels, but also by the sodium-potassium pump which is powered by the hydrolysis of ATP. This pump actively transports three Na^+ ions out of the cell for every two K^+ ions transported into the cell, thereby lowering the transmembrane potential (measured inside minus outside). This is a minor contribution to the overall membrane potential, contributing a maximum of -11 mV [Nicholls, et al., 1992].

Neglecting the voltage- and ligand-gated ionic channel effects, pertubations from the equilibrium situation established across the membrane result in increased (or decreased) ionic flow to counteract the pertubation. Thus the resting membrane potential is maintained at a constant level within narrow limits. But what happens when the membrane potential is driven far beyond its resting state? In electrically active cells such as neurons and muscle cells, this can result in large, ionically driven excursions from the resting transmembrane potential; this is known as an *action potential*.

2.5.3 Gating of Ion Channels: Effect on the Transmembrane Potential

It can be seen from (2.3) that a change in the permeability of any type of ion channel will significantly affect the potential developed across the cell membrane. Recalling the relative intracellular and extracellular concentrations of the ions from Table 2.1, it is evident that opening of K^+ channels will result in the efflux of positively charged potassium from the cell. This causes what is known as *hyperpolarization*; the transmembrane potential becomes more negative. Increasing the permeability of Cl^- ions will have a similar effect with a large influx of negatively charged chloride also hyperpolarizing the cell. Increasing permeability of both Na^+ and Ca^{2+} channels causes an influx of positively charged ions which tends to *depolarize* the cell; the transmembrane potential becomes less negative and may even become positive.

It is such changes in permeability that are responsible for the action potential; an electrical signal responsible for the functioning of the brain, the contraction of muscle, beating of the heart, and much of our sensory perception. As a cell is depolarized, a threshold level is reached for opening of voltage gated channels (often Na^+ at this stage). This change in membrane permeability causes an influx of ions that tend to further depolarize the cell. As different transmembrane voltages are reached, different classes of voltage-dependent ion channels are recruited, resulting in the rapid depolarization,

overshoot (potential becomes positive), and repolarization of the cell membrane. This forms the basis of the action potential. It can be initiated by direct electrical contact with another cell that has "fired" and action potential, or by ligand binding to receptor sites that cause changes in ionic channel permeability.

The permeability changes described above were empirically modeled in 1952 by Hodgkin and Huxley [Hodgkin and Huxley, 1952]. Their kinetic theory successfully predicted the flux of ions across a cellular membrane and the resulting changes in the transmembrane potential. The conductance of individual channels was varied based on time constants (dependent on temperature and transmembrane potential) for activation and deactivation of each channel type. This ionic channel gating was described by a first order reaction

$$I_{ionic} = \bar{I}_K n^4 + \bar{I}_{Na} m^3 h + \bar{I}_{Ca} df + \bar{I}_l \tag{2.4}$$

where I_{ionic} is the total ionic current through the membrane, $\bar{I}_K$, $\bar{I}_{Na}$, $\bar{I}_{Ca}$, and $\bar{I}_l$ are the the maximum currents associated with K^+, Na^+, Ca^{2+} and leakage respectively, and n, m, h, d and f are gating variables dependent on the time constants associated with activation and deactivation of the channel. This model formed the basis of all subsequent work dealing with voltage-gated ionic channels and was used in the action potential modeling of Chapter 6. For a detailed description of this model, the reader is referred to excellent reviews in [Hille, 1992] and [Weiss, 1996].

2.5.4 The Traveling Wave

As described above, Hodgkin and Huxley empirically modeled the ionic currents which flow through the channels of excitable membranes. They combined this model with core conductor theory to predict the propagation of an action potential (a *traveling wave*) down a cylindrical, unmylenated nerve fiber. In this theory, the total transmembrane current is given by:

$$I_{total} = K \frac{d^2 V_m}{dt} = C_m \frac{dV_m}{dt} + I_{ionic} \tag{2.5}$$

$$K = \frac{a}{2Rv^2} \tag{2.6}$$

where V_m is the transmembrane potential, C_m is the membrane capacitance per unit area, I_{ionic} is the current due to flow of ions through ionic channels in the cellular membrane,

and the constant K is dependent on the radius of the fiber (a), the axoplasm resistance (R) (which may be loosely correlated to the seal resistance (R_{seal}) in the cultured cell system) and the conduction velocity (v). This total current passes through the membrane, travels along the fiber and then passes back through the membrane forming local current loops. As will be discussed in Chapter 3, it is this current traveling parallel to the cell membrane which is monitored using extracellular electrodes for the case of traveling waves.

2.5.5 Action Potential in Cardiac Tissue
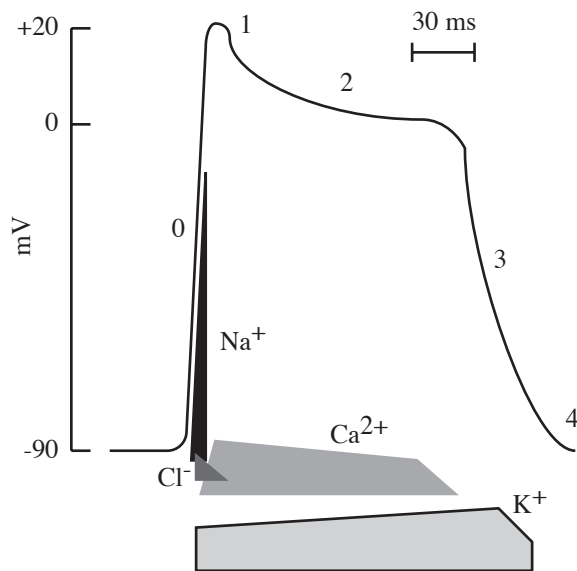
Figure 2.9: Phases of a human cardiac action potential. The relative conductances of each of the four major ionic channels are also shown, where the area of the shaded regions is proportional to the conductance of that channel. In phase 0, a large influx of Na^+ ions causes the rapid depolarization and overshoot of the membrane. As the Na^+ channels close and Cl^- channels open, there is an initial rapid repolarization (phase 1). Phase 2 is known as the plateau and is due to the slower, prolonged opening of Ca^{2+} channels. The final repolarization (phase 3) is due to closure of the Ca^{2+} channels while the K^+ channels remain open (allowing potassium efflux). The resting potential is restored in phase 4. After [Ganong, 1993].

There is a great deal of information regarding how action potentials are generated in nerve tissues and propagated over large distances in the body. However, this discussion will focus on the action potential generated in cardiac tissue since it is the most relevant to this research. As shown in Figure 2.9, the cardiac action potential involves the combined action of at least four major classes of biologically active ions. In the human system, the resting membrane potential is around -90 mV. If the membrane becomes depolarized to approximately -70 to -80 mV, the sodium channels open and allow a large influx of Na^+, causing a rapid depolarization and overshoot (the transmembrane potential becomes positive). After a brief period, these channels close and remain closed until the action potential is over. This is a phenomenon known as inactivation and occurs with almost all gated ion channels. It sets a limit

44

Voltage-gated
Na^+ channel
T - Ca^{2+} channel - "transient" calcium channel opens when cell is more depolarized
L - Ca^{2+} channel - "long-lasting" calcium channel requires less depolarization
K^+ channel
Ligand-gated, G-protein dependent
Acetylcholine-sensitive K^+ channel
Adenosine-sensitive K^+ channel
Ligand-gated, G-protein independent
ATP-sensitive K^+ channel
Stretch-activated channels

Table 2.2:   Types of gating of cardiac ion channels after [Ganong, 1993].

on the duration of different portions of the action potential, as well as the overall rate at which a cell may fire. As the Na^+ influx drives the transmembrane potential more positive, the threshold for opening of Cl^- channels is reached. These channels remain open briefly allowing a small influx of chloride ions which cause a rapid (and small) repolarization. At the same time, calcium and potassium channels are opened and remain open for an extended time. Thus, there is an influx of Ca^{2+} and efflux of K^+ which tend to balance each other resulting in the plateau phase of the AP. The calcium channels close before the potassium channels, resulting in the repolarization of the membrane. Eventually the equilibrium condition (resting membrane potential) is reached.

While the above discussion mentioned only one type of channel for each of the ions, there are actually several types which all contribute to the AP. These are outlined in Table 2.2. As mentioned previously, gating of ion channels can be triggered by attainment of a specific transmembrane potential (threshold) or by binding of a ligand to the channel. This ligand binding is often dependent on G-proteins (nucleotide regulatory proteins) which can couple cell surface receptors to catalytic units. These catalytic units create intracellular second messengers that travel through the cytosol and bind to the channels causing them to open. G-proteins can also couple receptors directly to ion channels to control gating. For the purposes of this work, a more detailed understanding of these ligand binding mechanisms is not necessary. Awareness of their existence and recognition that they can affect channel permeability in the same manner as transmembrane voltages is sufficient.

The next question which comes to mind when discussing cardiac tissue is how does the signal propagate through the heart? Unlike nerve cells where axons and dendrites carry

the action potential from one location to another, cardiac cells grow in close contact to one another and form what are called *gap junctions*. Integral proteins (called *connexons*) form channels through the membrane of the cell. When the connexon in the membrane of one cell lines up with connexon in another cell, a channel is formed between the cells through which substances can pass without entering the extracellular solution. This acts as an electrical connection through which the depolarization in one cell can initiate depolarization in a neighboring cell. If this depolarization is sufficient to trigger opening of the Na^+ channels, then the neighboring cell will fire its own action potential. In this way the action potential is propagated through cardiac tissue. The result is a traveling wave which can be loosely modeled using the core conductor theory presented above.

Contraction of the tissue is initiated by the action potential. The AP triggers the release of internal stores of Ca^{2+} which binds to *troponin C* (troponin C inhibits the interaction between actin and myosin). With the troponin C bound, the actin-myosin interaction is able to occur allowing contraction of actin filaments. This is the basis of contraction in all muscle, including cardiac tissue. Since contraction was not studied in this research, a more detailed explanation is not warranted.

The mechanisms by which an action potential is initiated and propagated in human cardiac tissue has been discussed in detail above. While it is doubtful that the precise shape of the AP and the exact makeup of the ionic channel populations is the same across species, the underlying principles governing their interactions are the same. In Chapter 6, the action potential of avian (embryonic chicken) myocytes cultured *in vitro* will be discussed in detail as it relates to this research.

2.6 Membrane Impedance

For any given homogeneous conducting material, a bulk property called the resistivity (ρ) can be defined having the dimensions of $\Omega \bullet cm$. Given this intrinsic property of the material, the resistance of any arbitrary shape may be determined:

$$R = \frac{\rho L}{A} \tag{2.7}$$

where A is the cross-sectional area in cm^2 and L is the length of the material in cm. Thus, if we consider a single ion channel to be a cylinder of known length and cross-sectional area filled with a solution of known resistivity, it is possible to estimate the resistance. This value needs to be adjusted to include such factors as the availability of ions to actually pass through the channel as well as the ease with which the channel passes ions. For the

purposes of this research, it will be assumed there is an adequate supply of ions available for transport through the membrane and that the membrane itself does not hinder that transport in any way beyond the physical constrictions used to determine the resistance.

The total resistance of the plasma membrane can then be calculated by considering the parallel combination of all the ionic channels permeating the membrane that are open for ion transport. Measurement of the membrane resistance can thus be used as an indicator of how many ionic channels are open at any given time. Indeed, the first suggestion that the fluxes of sodium and potassium ions associated with an action potential had to be attributed to holes or channels through the membrane was deduced by measurements of transmembrane impedance of the squid giant axon [Hodgkin and Huxley, 1952]. Individual ionic channels have a resistance (when open) of 5 to 500 GΩ depending on the channel type and tissue. Depending on the cell type, the location of the patch of membrane, and the transmembrane potential, the overall membrane resistance can range from 1MΩ to 100 GΩ•μm^2. This data was compiled using individual channel resistances and density ranges found in [Hille, 1992] for a variety of tissues and channel types.

The plasma membrane itself is an insulating layer separating two conducting solutions (i.e., a capacitor). The capacitance is determined by the permeability of the material (ε_r), the area (A) and the thickness (d):

$$C = \frac{\varepsilon_r \varepsilon_0 A}{d} \tag{2.8}$$

where ε_0 is the permeability of free space (8.85×10^{-12} C•V^{-1}•m^{-1}). For most biological membranes, the total lipid bilayer thickness (d) is approximately 8 nm resulting in a membrane capacitance of approximately .01 pF/μm^2 [Hille, 1992]. Changes in membrane resistance due to the opening of channels should not significantly alter the capacitance of the measured impedance since the channel density is relatively low. Impedance data on giant squid axon membrane exhibited less than a 2 per cent change in capacity with a 40-fold decrease in membrane resistance [Cole and Curtis, 1939].

Thus, the simplest model of a cellular membrane is a parallel RC circuit where the resistance is variable (being dependent on the state of the ion channels). Classically, the membrane properties of cells were deduced by driving a square pulse across a membrane and measuring the exponential voltage decay over time:

$$V = V_0 e^{\left(-\frac{t}{RC}\right)} \tag{2.9}$$

where V_o is the starting voltage. Thus, by measuring the voltage over time and assuming a capacitance value of 0.01 pF/μm^2, scientists were able to deduce the membrane resistance.

As will be discussed in detail in Chapter 5, there are other ways of measuring the complex impedance characteristics (determination of both resistance and capacitance) of the membrane using sinusoidal excitation across the tissue or cells to be measured. However, when actively driving biological materials it is important to understand their dispersive behavior. A great deal of work has been done in this area by H.P. Schwan who examined the permittivity and conductivity of tissue and cell suspensions. His work showed that there are three distinct regions of dispersion which must be considered when measuring the impedance characteristics of biological materials. At low frequencies (50 to 200 Hz) the counter-ion cloud surrounding the surface of the cellular membrane becomes polarized, resulting in what is called the α-dispersion. From approximately 60 kHz to 5 MHz the cell membrane becomes electrically charged (through intra- and extra-cellular pathways) causing what is known as the β-dispersion. At much higher frequencies (1 GHz), the dispersive behavior of water causes the measured permittivity to change (γ-dispersion) [Schwan, 1988]. In each case, the permittivity of the material changed by up to 2 orders of magnitude while the conductivity remained fairly constant (except during the γ-dispersion where the conductivity increased by 2 orders of magnitude).

For measurement of changes in membrane resistance (due to modulation of ionic channel conduction) of cultured cells, all of these dispersive effects may not be important. Assuming a membrane capacitance of approximately 0.01 pF/μm^2, the capacitive impedance is 16 TΩ•μm^2•Hz. This impedance was compared to the range of possible membrane resistances (1 MΩ to 100 GΩ•μm^2) in Figure 2.10. From this figure it can be seen that the capacitive impedance of the membrane always dominates the overall impedance for frequencies above 10 MHz. Thus, the γ-dispersion need not be considered when measuring conductance changes in cellular membranes. However, depending on the actual membrane resistance of the sample, it is possible that both the α- and β-dispersions need be considered. These effects would be evidenced by a changing capacitive component of the measured cellular impedance as the measurement frequency was varied. As will be described in Chapter 5, the impedance measurement system developed for this work operated between 100 Hz and 100 kHz; the extremes coincide with the end of the α-dispersion and the beginning of the β-dispersion respectively. It was hoped that this configuration would limit the impact of dispersive behavior on the measurements.
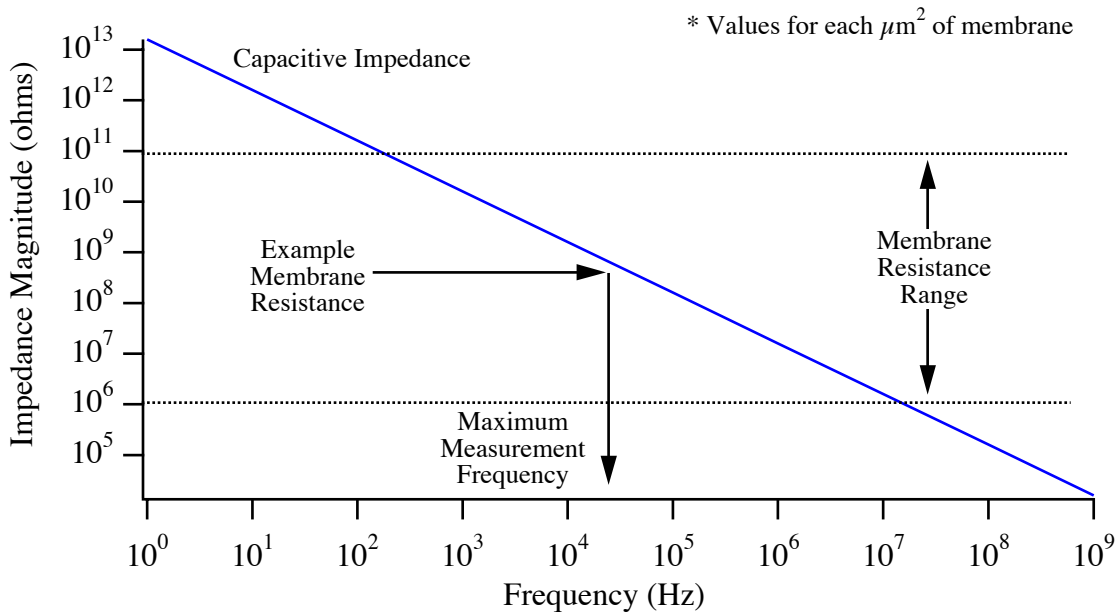
Figure 2.10: Impedance magnitude for each μm² of cell membrane showing the capacitive impedance (assuming 0.01 pF / μm²) and the range of membrane resistances expected. The intersection of the capacitive impedance line with that of the actual membrane resistance provides an estimate of the maximum measurement frequency which should be used (to limit capacitive shunting of the excitation current).

2.7 Summary

The basic theory of cellular function and response has been reviewed. Characteristics of the cellular membrane, ionic channels, the cytoskeleton, and extracellular matrix have all been discussed. The mechanisms of cellular adhesion to cell culture substrates and movement across those substrates was described in detail and will be used in subsequent chapters to design experiments with limited cellular motility. The electrical properties of cells was considered with special attention paid to the generation of a transmembrane potential (both the resting potential and the action potential) as well as impedance characteristics of the plasma membrane. This information will be critical for understanding action potential and impedance experiments performed in Chapter 6 and Chapter 7 respectively.

References

Bray, D., *Cell Movements*, Garland Publishing, Inc., New York (1992).

Chen, C.S., Mrksich, M., Huang, S., Whitesides, G.M. and Ingber, D.E., "Geometric control of cell life and death," *Science*, 276:1425-1428 (1997).

Cole, K.S. and Curtis, H.J., "Electrical impedance of the squid giant axon during activity," *Journal of General Physiology*, 22(5):649-670 (1939).

Fuhr, G., "Examples of three-dimensional micro-structures for handling and investigation of adherently growing cells and submicron particles," *Analytical Methods & Instrumentation, Special Issue μTAS '96*, (1996).

Ganong, W.F., *Review of Medical Physiology*, Prentice Hall, New Jersey (1993).

Hille, B., *Ionic Channels of Excitable Membranes*, Sinauer Associates, Inc., Sunderland, Massachusetts (1992).

Hodgkin, A.L. and Huxley, A.F., "A quantitative description of membrane current and its application to conduction and excitation in nerve," *J. Physiology*, 117:500-544 (1952).

Kandel, E.R., Schwartz, J.H. and Jessell, T.M., *Principles of Neural Science*, Appleton and Lange, Norwak, Connecticut (1991).

Lodish, H., Baltimore, D., Berk, A., Zipursky, S.L., Matsudaira, P. and Darnell, J., *Molecular Cell Biology*, Scientific American Books, New York (1995).

Nernst, W., "Zur kinetik der in lösung befindlichen körper: theorie der diffusion," *Z Phys. Chem.*, 613-637 (1888).

Nicholls, J.G., Martin, A.R. and Wallace, B.G., *From Neuron to Brain*, Sinauer Associates, Inc., Sunderland, Massachusetts (1992).

Schwan, H.P., "Biological effects of non-ionizing radiations: cellular properties and interactions," *Annals of Biomedical Engineering*, 16:245-263 (1988).

Weiss, T.F., *Cellular Biophysics*, MIT Press, Cambridge, Massachusetts (1996).

Chapter 3   MICROELECTRODE THEORY

Inherent non-destructiveness and the avoidance of vexing problems of multiple-electrode placement would both be achieved if an array of closely-spaced, extracellular microelectrodes could be made an integral part of each culture chamber.

C.A. Thomas,, 1972

3.1   Introduction

When a metal microelectrode is immersed in a conducting medium, an electrochemical equilibrium is established. This complex system can be modeled using passive circuit elements as has been described and reviewed in numerous biomedical and electrochemical texts. This chapter begins with a discussion of the physical configuration of the solid/electrolyte interface and a general discussion of the mechanisms leading to the equilibrium condition. The effects of charge transfer and diffusion on the overall electrode impedance is explored as is the electrolyte impedance. The dominant electrode noise mechanisms and options for its reduction are discussed. Parasitics due to the substrate, interconnects, and electrolyte are described with equations for their estimation. The chapter ends with a discussion of the transduction of biological signals for both action potential recording and impedance measurements.

3.2   The Solid - Electrolyte Interface

When a solid is placed into an *electrolyte* (a solution where charge is carried by the movement of ions) an electrified interface immediately develops. While this occurs for any solid (metal, semiconductor, insulator) immersed in an electrolyte [Sui and Cobbold,

1979], this discussion will focus on the mechanisms responsible for its formation in the case of metals since this is the easiest to understand and the most relevant to this research.
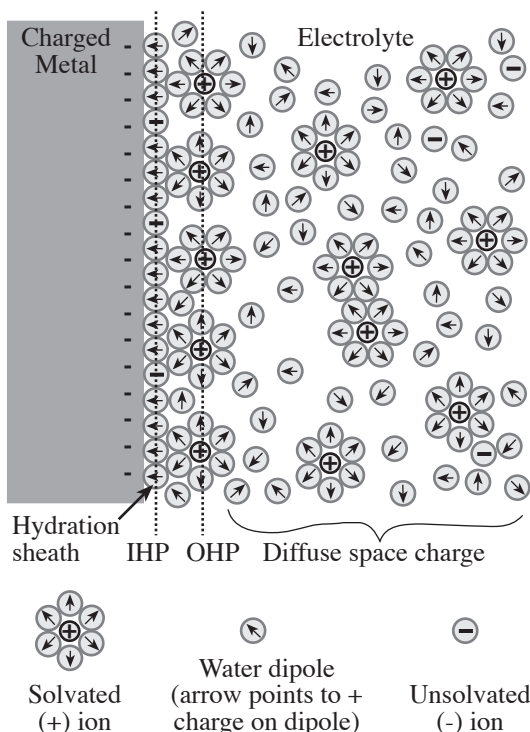
Figure 3.1: A schematic representation of an electrified interface. The hydration sheath, inner and outer Helmholtz planes are shown as is the diffuse space charge layer. Adapted from [Bockris and Reddy, 1970].

At the instant when a metal is placed in an ionically conducting solution, the metal and the solution are electroneutral. Chemical reactions occur immediately whereby electrons are transferred between the metal and the electrolyte ($A^+ + e^- \rightarrow A$). This results in the formation of an electric field between the electrode and the electrolyte that influences further chemical reactions (thus making them *electrochemical*). This induced electric field inhibits the reduction reaction ($A^+ + e^- \rightarrow A$) while accelerating the oxidation reaction ($A \rightarrow A^+ + e^-$). These two competing reactions eventually reach an equilibrium condition whereby the currents due to electron transfer to and from the metal are equal. This equilibrium exchange current density flows across the interface in both directions resulting in a net current of zero.

The electric field generated by these electron transfer reactions also has an impact on the electrolyte. Water dipoles orient themselves in the field in a layer at the metal surface forming what is known as the *hydration sheath*. Just beyond the water dipoles are solvated ions (result of the electron transfer with the metal) that form a layer, the locus of which is known as the *outer Helmholtz plane* (OHP). There is also specific adsorption of ions (cations or anions) at the electrode surface interspersed with the orientated water dipoles. The contact adsorption of these ions tends to be very chemically dependent and partly oblivious to the charge on the metal. It is possible to have anions specifically adsorb to the surface of a negatively charged metal. The locus of centers of these ions is known as the *inner Helmholtz plane* (IHP) (although in some texts it is the locus of the orientated water dipoles which is termed the IHP) and can affect the overall charge density profile of the

interface. The net result of these reactions, adsorptions and orientations is the creation of the *electrical double layer* (or simply *double layer*); an electrified interface describing the interphase region at the boundary of an electrolyte. This is illustrated in Figure 3.1 where the arbitrary case of positive ions at the OHP and electrons at the metal surface has been assumed. The choice of an unsolvated negative ion for specific adsorption was also arbitrary and independent of the other charges in the system. The space charge region shown has a graded profile with the strongest field at the interface, diminishing to zero in the bulk electrolyte as will be discussed in more detail below.

3.2.1 Interfacial Capacitance: Helmholtz, Gouy - Chapman and Stern

As mentioned above, when a metal and electrolyte come into contact, a space charge region is formed in the electrolyte at the interface. However, the exact structure of this region is difficult to determine. Initial theories developed by Helmholtz assumed the charge of solvated ions was confined to a rigid sheet at the OHP, and was equal and opposite to that in the metal [Helmholtz, 1879]. With the orientated water dipole layer acting as a dielectric, the model predicted the interface would behave like a simple capacitor. This capacitance (in the Helmholtz model) is determined by the dielectric permittivity of electrolyte $(\varepsilon_o \varepsilon_r)$, the area of the interface (A), and the distance of the OHP from the metal electrode (d_{OHP}):

$$C_H = \frac{\varepsilon_o \varepsilon_r}{d_{OHP}} \tag{3.1}$$

where C_H is the capacitance per unit area (F/m^2), ε_o is the permittivity of free space $(8.85419 \times 10^{-12}$ F/m) and ε_r is the relative permittivity of the electrolyte. Assumptions of ε_r and d may be used to determine a Helmholtz capacitance per unit area. Kovacs assumed an ε_r of 6 for oriented water dipoles at the interface (can be as high as 78) and an outer Helmholtz plane distance of 5Å (both for physiological saline at 25°C), yielding a worst case Helmholtz capacitance (C_H) of 0.14 pF/μm^2 [Kovacs, 1994]. This rough estimate is often useful as a design guide, although numerous factors can affect both ε_r and d.

The simple model of Helmholtz suffered from an inadequacy; it neglected the dependence of capacity on potential which had been observed experimentally. Since the OHP was determined by how close the solvated ions could get to the electrode, there was no accommodation for movement of those ions. In 1910 to 1913, Gouy and Chapman modified the simple Helmholtz model (a rigid sheet of solvated ions) by considering mobile solvated ions at the electrode surface [Gouy, 1910; Chapman, 1913]. These mobile

ions were influenced by thermal forces in addition to the electrical forces already described. The result was an *ion cloud* near the interface where the combined effects of thermal and electrical forces equilibrated to form a time-averaged ionic distribution. This extended the space charge layer further into the bulk electrolyte while maintaining the same total charge. In their model, the distribution of this space charge was concentrated at the OHP, tending toward zero in the bulk solution (a linear potential drop across the hydration sheath was not assumed). This allowed the capacity to change by movement of ions in response to an applied potential. Detailed mathematical derivations of the models that describe this behavior and take into account the nonlinear distribution of the mobile ions have been reviewed in detail in several texts [Bard and Faulkner, 1980; Bockris and Reddy, 1970] and will not be repeated here. However, it is useful to examine the resulting relationships for the potential distribution and the capacitance. For relatively small applied voltages (<50 mV) the voltage drop through the space charge region can be estimated as an exponential decay:

$$V(x) = V_o e^{\left(-\frac{x}{L_D}\right)}$$

(3.2)

where V_o is the potential at the electrode (x=0), x is the distance from the electrode, and L_D is the *Debye length*. The Debye length characterizes the spatial decay of potential and can be viewed as the characteristic thickness of the diffuse layer:

$$L_D = \sqrt{\frac{\varepsilon_o \varepsilon_r V_t}{2n^0 z^2 q}}$$

(3.3)

where V_t is the thermal voltage (kT/q), n^0 is the bulk number concentration of ions in the electrolyte (ions/liter), z is the valence of the ions, and q is the charge on an electron $(1.60219 \times 10^{-19}$ C). It is interesting to note that for most solutions of physiologic makeup (approximately 300 mM/liter), the width of this diffuse layer is extremely small (< 10 Å) as shown by Table 3.1 below

The differential capacitance per unit area (F/m^2) can be calculated by:

$$C_G = \frac{\varepsilon_o \varepsilon_r}{L_D} \cosh\left(\frac{z V_o}{2 V_t}\right)$$

(3.4)

where the first term $(\varepsilon_o \varepsilon_r / L_D)$ is simply the capacitance per unit area of two plates separated by a distance L_D, and the effects of mobile charges are compensated for by the hyperbolic cosine.

While the Gouy-Chapman model was an improvement over that of Helmholtz, it generally overestimates the interfacial capacitance. The capacity varies more strongly with applied potential than is observed experimentally and it is too dependent on ionic concentration. Stern rectified this inconsistency by combining the Gouy-Chapman model with that of Helmholtz. He combined a layer of bound ions at the OHP with a diffuse ion cloud beyond it [Stern, 1924]. Thus, the total interfacial capacitance was the series combination of both capacitances:

$$\frac{1}{C_I} = \frac{1}{C_H} + \frac{1}{C_G} \qquad (3.5)$$

where C_I is the total interfacial capacitance, C_H is the Helmholtz capacitance and C_G is the Gouy-Chapman capacitance due to the diffuse ion cloud as described by (3.1) and (3.4) respectively. Equation (3.5) results in a linear potential drop between the electrode and the OHP with a near exponential decay from the OHP to the bulk solution as shown in Figure 3.2. As the potential at the electrode is increased, the ions in the diffuse layer are pulled toward the electrode (electrical forces dominate over thermal). This affects the hyperbolic cosine term in (3.4) resulting in an increase in C_G. As C_G is
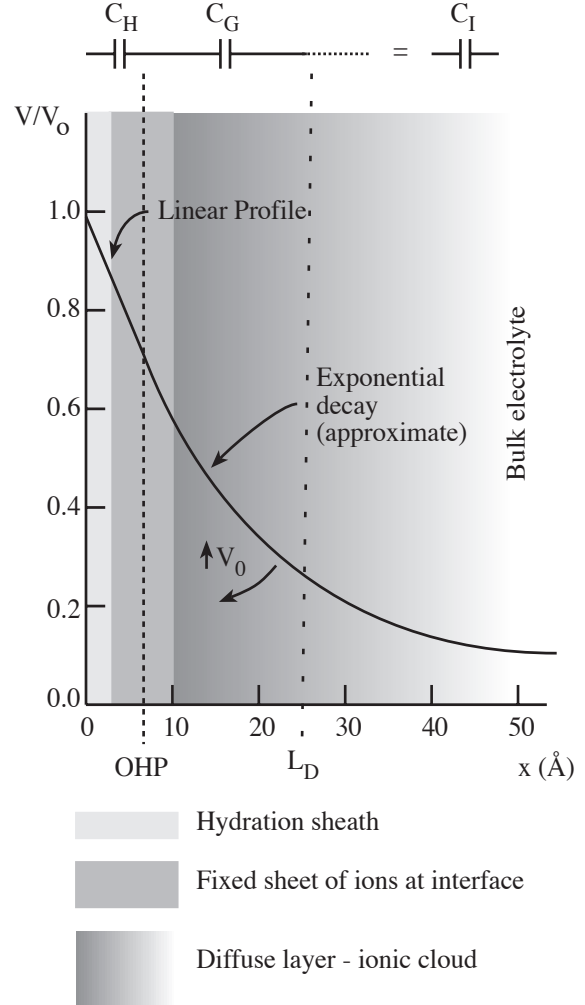
Figure 3.2: Potential profile representation. The total interfacial capacitance is the series combination of the capacity of a fixed sheet of charge at the interface and the capacity of the diffuse ionic cloud. In the region between the electrode and the OHP, a linearly graded potential exists as the voltage is dropped across the oriented water dipoles. Beyond the OHP, the potential decays almost exponentially. This decay is dependent on the voltage at the interface and becomes sharper as the potential (V_0) is increased (as shown by the arrow). The position of L_D will shift to the left as the ionic concentration of the electrolyte is increased. Adapted from [Bard and Faulkner, 1980].

Molar concentration (mMoles / liter)	L_D (Å)
1000	3.0
100	9.6
10	30.4
1	96.2
0.1	304

Table 3.1: Characteristic thickness of the diffuse layer at 25°C after [Bard and Faulkner, 1980].

increased, the series combination of (3.5) becomes dominated by the smaller C_H term and the total interfacial capacitance (C_I) approaches that predicted by (3.1). With very low potential and dilute electrolyte solutions, the total interfacial capacitance may be dominated by C_G.
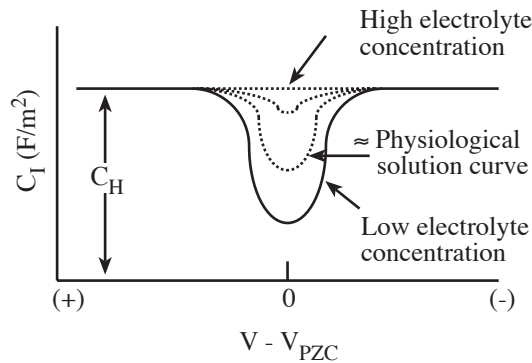
Figure 3.3: Changes in the interface capacitance with electrolyte concentration and potential. As the electrolyte concentration increases, the contribution of C_G to the total interfacial capacitance decreases and C_I approaches the fixed value of C_H. Similarly, when the potential moves away from the potential of zero charge - PZC (potential where the charge on the electrode is zero) C_I increases to C_H according to the hyperbolic cosine relation of (3.4). After [Bard and Faulkner, 1980].

From (3.3) and (3.4) it can be seen that the Gouy-Chapman capacitance is also dependent on the concentration of the electrolyte. As the molar concentration increases, the Debye length (L_D) decreases (as shown in Table 3.1) which causes a corresponding increase in the diffuse layer capacitance (C_G). This effect is shown in Figure 3.3 in combination with the effects of changing potential. For most physiological systems where the electrolyte solution is approximately 300 mOsm/kg, if there is zero bias applied (as is the case for an electrode monitoring extracellular action potentials), C_H and C_G will be on the same order (around 0.14 pF/μm^2) resulting in a net capacitance of approximately 0.07 pF/μm^2 (using the worst case assumptions of kovacs described above). When a bias is applied (as is the case for impedance

measurements), the effective plate width of C_G decreases causing the overall capacitance to be dominated by the Helmholtz capacitance. Thus, the capacitance increases to a maximum dictated by the Helmholtz capacitance (approximately $0.14pF/\mu m^2$).

The above analysis of the interfacial capacitance did not consider the effect of specifically adsorbed ions at the electrode surface. While these ions can have an effect on the overall electrode impedance [DeRosa and Beard, 1977], the resulting models are complex and beyond the scope of this work. The basic models and concepts examined herein are sufficient for development of a fundamental understanding of the electrode-electrolyte interface.

3.2.2 The Overpotential and Charge Transfer Resistance

The capacitance that develops at the electrode / electrolyte interface and how it changes with the concentration of the electrolyte and the applied potential has been discussed above, but this does not describe the entire electrical picture. If a DC potential is applied across the interface, a current may flow under certain conditions. Thus, it is important to consider the addition of a resistive path in parallel to the capacitive in the electrical model of this interface. Unfortunately, as with the capacitive element, this resistor can be non-linear with the applied voltage.

The flow of current through this metal-electrolyte interface requires the net movement of charge in response to an electric field (due to an applied voltage). As was discussed above, at equilibrium there is a constant flow of charge across the interface, but the net flow is zero. Thus, the applied voltage must push the total potential across the interface away from its equilibrium value (V_o). This potential difference ($V - V_o$) responsible for the net flow of charge is termed the *overpotential* η and is thought to be the sum of four different overpotentials:

$$\eta = \eta_t + \eta_d + \eta_r + \eta_c \tag{3.6}$$

where η_t is due to *charge transfer* through the double layer; η_d is due to the *diffusion* of reactants to and from the electrode; η_r is due to *chemical reactions* at the electrode; and η_c is due to exchange of metal atoms with corresponding ions in solution (*crystallization*) [Vetter, 1967]. What this means is that given a potential in excess of the equilibrium condition, part of that potential will drive charge transfer, diffusion, chemical reactions and crystallization. Thus, three parallel currents in series with the diffusion current can be imagined, each driven by a percentage of the total overpotential. For operation of an electrode near its equilibrium condition, the charge transfer overpotential (η_t) tends to

dominate the overall current. As the applied potential is pushed further from equilibrium, diffusion of reactants may become a limiting factor, making the diffusion overpotential (η_d) more significant. For all practical purposes, the overpotentials due to chemical reactions (η_r) and crystallization (η_c) are not of significance in biological applications [Cobbold, 1974].

In Section 3.2 the process by which equilibrium is obtained when a metal is placed in an electrolyte was discussed in detail. The equal but opposite oxidation and reduction currents balanced each other such that a net current of zero resulted. The absolute value of this current (per unit area) is known as the *exchange current density* (J_o). It is dependent on the material properties of the electrode, the electrolyte composition and the resulting oxidation-reduction reactions. The latter is what makes determination of J_o difficult; often the electrochemical reaction that dominates this exchange current is not known. The situation becomes even more difficult in poorly defined electrolytes such as biological media. Thus, J_o is often determined experimentally by measuring the charge transfer resistance around the equilibrium potential of the electrode in the electrolyte of interest. For reference, some published values of J_o are given in Table 3.2 below.

Material / Reaction	J_o (A/cm^2)	Reference
Au in buffered saline	2.00×10^{-9}	Najafi and Wise, 1986
Au, hydrogen reaction	3.98×10^{-6}	Bockris and Reddy, 1970
Pt, hydrogen reaction	7.94×10^{-4}	Weast, 1988
Ir, hydrogen reaction	2.00×10^{-4}	Weast, 1988

Table 3.2: Some published exchange current density values (J_0) for materials and reactions relevant to electrodes after [Kovacs, 1994].

Given that it is possible to measure the exchange current density for the system of interest, that information can be used to determine the current that will flow as a result of an applied potential. If the potential is close to that of the equilibrium situation, then the Butler-Volmer equation can be used to calculate the resulting current J in (A/cm^2):

$$J = J_o \left[e^{\left(\frac{(1-\beta) \cdot z\eta_t}{V_t} \right)} - e^{\left(\frac{-\beta z\eta_t}{V_t} \right)} \right] \qquad (3.7)$$

where J_o is the exchange current density (A/cm^2) as described above, z is the valence of the ion involved in the charge transfer reaction, and β is the *symmetry factor* that reflects the energy barrier differences for the oxidation and reduction reactions. It can be seen that small changes in η_t can produce very large changes in the current density J. Additionally, the exchange current density has a direct impact on the overall current. Thus, the choice of electrode material can significantly impact the amount of current which flows in response to an applied voltage. Since electrochemical reactions (often unwanted) and gas evolution at the interface often occur at higher voltages,

Figure 3.4: Two antiparallel diodes model the charge transfer current of a metal-electrolyte interface.

it is desirable to limit the excursions from equilibrium as much as possible. Thus, for stimulation situations, an electrode material with a high exchange current density (like Pt or Ir) is desirable.

Examination of (3.7) reveals that each exponential term resembles the exponential current which flows through an ideal diode (J_d) in response to an applied forward bias (V_a):

$$J_d = J_{do}\left[e^{\left(\frac{V_a}{V_t}\right)} - 1\right]$$

(3.8)

where J_{do} is the saturation current density [Muller and Kamins, 1986]. If two diodes are assembled in an antiparallel fashion (as shown in Figure 3.4), z = 1 is assumed (since the carriers are electrons and holes), and a diode factor is included to take into account differences between the two diodes, then the addition of the two forward currents would appear as in (3.7). This is a useful, first order model to keep in mind when visualizing the currents that should flow through an electrode in response to an applied potential. A detailed analysis of the rectification properties of electrodes in solution can be found in [Geddes, et al., 1987].

To determine a theoretical value for the resistance that appears in parallel with the interfacial capacitance, it is useful to examine the J-η_t relationship shown in Figure 3.5 (a). While it is not possible to extract a linear resistance value for large

variations in η_t, using a small-signal analysis in the linear regime (Figure 3.5 (b)) it is possible to approximate a *charge transfer resistance* (R_t).

For the conditions given ($\beta = 0.5$, $T = 37°C$, $z = 1$) in Figure 3.5 (b), it can be seen that this approximation for R_t holds for overpotentials less than 50mV peak. This low field estimate is useful for neural recording applications where the applied potential is zero and in impedance spectroscopy applications where the potential can be kept relatively small. The theoretical value for the charge transfer resistance under low field conditions with $\beta = 0.5$ (nonrectifying system) can be calculated by

$$R_t = \frac{V_t}{J_o z} \tag{3.9}$$

in $\Omega \bullet cm^2$ [Kovacs, 1994]. Here the resulting current (J) can be calculated directly from Ohm's law,

$$J = \frac{\eta_t}{R_t} = \frac{J_o z \eta_t}{V_t} \tag{3.10}$$

For instances where higher currents are required (as in stimulation of neural tissue), it is no longer possible to define a pure resistance term. However, by assuming that one
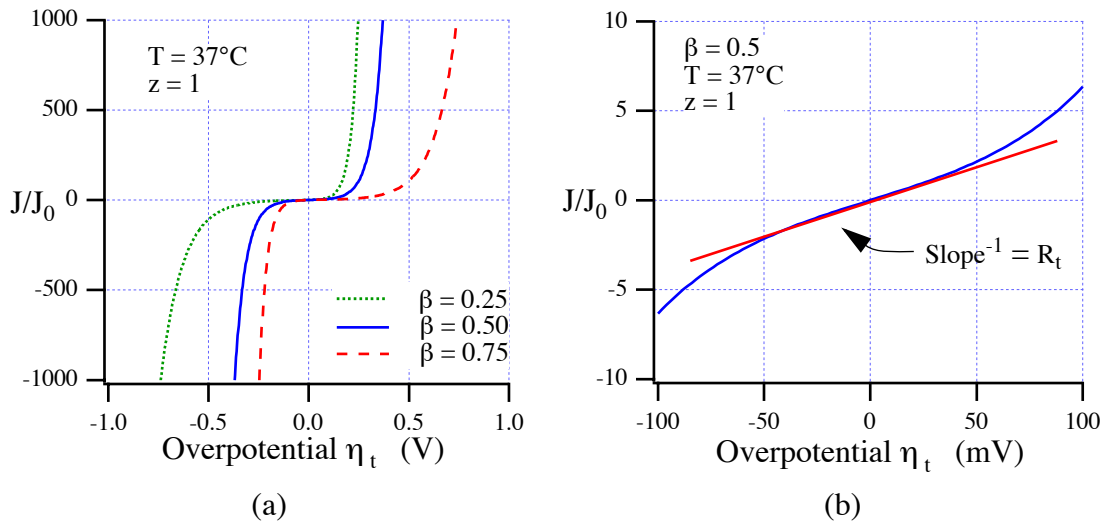
Figure 3.5: Currents calculated using the Butler-Volmer equation. (a) With $\beta = 0.5$, the current voltage relationship is symmetrical around zero. As the symmetry factor is adjusted towards 1 or 0, the J-η_t curve shifts to the right or left (indicating a preference for the oxidation or reduction reactions). (b) Small-signal approximation to (3.7) where the linear region may be used as an estimate for the charge transfer resistance, R_t.

60

exponential term of (3.7) tends toward zero while the other increases in magnitude, the total current may be estimated by

$$J = J_o \exp\left(\frac{z\eta_t}{2V_t}\right)$$

(3.11)

where a nonrectifying system ($\beta = 0.5$) has been assumed. Again, from Figure 3.5 it is evident that the transition from the low field to high field approximations occurs around 50 mV. This limiting value will decrease with increasing valence (z) while increasing with increasing temperature. For real systems of interest, the point of non-linearity can easily be determined by excitation with a pure sinusoid and monitoring the onset of harmonics [Schwan, 1992; Moussavi, 1994].

At this point the model of a metal electrode placed in an electrolyte is a voltage dependent capacitor (C_I) determined from (3.5), in parallel with a charge transfer resistance (R_t) determined from (3.9) for instances where the applied potential is restricted to values less than approximately 50 mV peak. The relative impedances of these two elements determines the basic characteristics of the electrode (neglecting diffusion limits to be discussed in the next section). If the electrode has a very high exchange current density ($J_0 \rightarrow \infty$), the charge transfer resistance tends toward zero. Thus, the slope of the J versus η_t curve is infinite; i.e., even though a significant current density flows across the interface, there is no substantial overpotenital developed. This is termed an *ideally nonpolarizable* interface and describes the optimum material for stimulation of neural tissue.

The opposite situation ($J_0 \rightarrow 0$) results in what is called an *ideally polarizable* interface. It behaves like a capacitor with no faradic (charge transfer) processes occurring. The charge in solution equals the charge on the electrode at all times. However, as noted above, this capacitance is not independent of potential.

Of course no material in practical applications is ideally polarizable or nonpolarizable, but rather somewhere in between. What is of importance is the magnitude of the resulting current relative to the exchange current density. If the resulting current is small with respect to J_o, then the interface should not be perturbed far from equilibrium. Thus nonpolarizable behavior would be observed. However, if the current is large compared to J_0, one can expect the interface to be far removed from equilibrium, resulting in polarizable behavior.

61

3.2.3 Diffusion and the Warburg Impedance

As mentioned above, in most cases the charge transfer overpotential dominates the resistive part of the electrode impedance (neglecting the solution resistance which will be described in Section 3.2.4). But the situation changes when the current density (AC or DC) is so large that reactants are not able to diffuse from the bulk to the interface fast enough. The current becomes diffusion limited resulting in a diffusion overpotential (η_d). This additional impedance must be placed in series with the charge transfer resistance (R_t) since physically diffusion and charge transfer must occur as a serial process; reactants diffuse to the interface where they contribute to oxidation or reduction reactions. While there is a theoretical steady-state diffusion resistance for near DC conditions [Cobbold, 1974] this discussion will focus on the AC case since that is representative of the situations encountered in this work.

If the case of a sinusoidal forcing function acting on the ions at the metal-electrolyte interface is considered, these charged particles will move in response to the applied electric field. This results in a sinusoidally varying spatial concentration of the ions rather than the linearly graded distribution described in Section 3.2.1. However, as with the linear case, the ions will still be concentrated near the OHP. As the frequency of excitation is increased, it becomes more difficult for the ions to follow the field. Thus, the effects of diffuse ion cloud become less significant. At high enough frequencies, the ions are not able to follow the field at all, resulting in this diffusional impedance tending towards zero.

In 1899, Warburg proposed a model for this frequency dependent diffusional impedance

$$|Z_w| = \frac{k}{\sqrt{f}} \tag{3.12}$$

where k is a constant determined by the electrochemistry and mobility of the ions involved in the charge transfer reaction and f is the excitation frequency [Warburg, 1899]. This impedance can be represented by either a series or parallel combination of a resistance and capacitance (both non-linear). When placed in series with the charge transfer resistance it effectively models the behavior of a metal electrode in solution under AC conditions.

The Warburg impedance elements may be theoretically determined [Kovacs, 1994] by the following equations, provided that the diffusion is dominated by a single ion species and the electrode is operated near equilibrium:

$$R_w = \frac{10^3 V_t}{z^2 q n^0 \sqrt{\pi f D}} \tag{3.13}$$

$$C_w = \frac{1}{2\pi R_w} \tag{3.14}$$

$$Z_w = \left[\frac{1}{R_w} + j2\pi C_w\right]^{-1} \tag{3.15}$$

where f is the frequency in Hertz, D is the diffusion coefficient (cm^2 / sec) of the ion in question, R_w is in $\Omega \bullet cm^2$ and C_w is in C / cm^2. Substitution of (3.14) into (3.15) reveals that the Warburg impedance has a constant magnitude of

$$|Z_w| = \sqrt{2} R_w \tag{3.16}$$

with a constant phase of -45°.

The above model works well for systems where the electrode is operated near equilibrium using an AC forcing function. It does not predict the DC behavior well, but this is of limited concern for the applications presented herein. However, when measuring the impedance of physical electrodes it is important to remember that the Warburg elements are not measured alone, but rather in concert with the charge transfer resistance and the interfacial capacitance. If the electrochemical reactions proceed at a slow rate, the resulting R_t will be large and will dominate the resistive part of the measurement and the overall impedance will vary as ω^{-1} (as would be expected for the parallel combination of a resistor and capacitor). However, in instances where the charge transfer reactions proceed rapidly, the diffusion limiting components (Warburg elements) will dominate the resistive path resulting in an overall impedance variation of $\omega^{-1/2}$. It is interesting to note that the presence of proteins will shift behavior from diffusion limited to reaction rate limited, presumably due to inhibition of the oxidation and reduction reactions due to adsorption of proteins to the metal surface [Gesteland, et al., 1959]. If proteins adsorb to the surface, then the effective surface area available for electron exchange is reduced. Thus, for biological applications where proteins are present, a shift in electrode characteristics is expected as the electrode is allowed to sit in the physiologic media (*in vivo* and *in vitro*) and the overall electrode impedance is expected to vary as ω^{-1}.

3.2.4 The Spreading Resistance

The final circuit element which must be included in the basic electrode/electrolyte model is the *spreading resistance*. As the name implies, this resistance models the effects of the spreading of current from the localized electrode to a distant counter electrode in the solution. It can be calculated by integrating the series resistance of shells of solution moving outward from the electrode where the solution resistance (R in Ω) is determined from

$$R = \frac{\rho L}{A} \tag{3.17}$$

where ρ is the resistivity of the electrolyte ($\Omega \bullet cm$), L is the length (cm) and A is the cross-sectional area (cm^2) of the solution through which the current passes. There are numerous approximations for electrodes of different shapes and configurations. Of specific interest for microelectrodes fabricated using planar, integrated circuit fabrication techniques are square and circular electrodes with one side exposed to the electrolyte. For a circular electrode of radius r (cm), the spreading resistance is given by

$$R_s = \frac{\rho}{4r} = \frac{\rho \sqrt{\pi}}{4\sqrt{A}} \tag{3.18}$$

in Ω where A is the area of the circular electrode in cm^2 [Newman, 1966]. For a rectangular electrode of length l and width w (both in cm), Kovacs calculated the spreading resistance [Kovacs, 1994] using the formula

$$R_s = \frac{\rho \ln\left(4\frac{l}{w}\right)}{\pi l} \tag{3.19}$$

From these equations it can be seen that the spreading resistance varies as the square root of the electrode area (for symmetrical shapes) rather than being directly proportional as was the case for the circuit elements discussed so far [Kovacs, 1994].

The full circuit model as developed thus far appears as shown in Figure 3.6. This works well for simple electrode systems in pure electrolytes (those without proteins, etc.). For instances where proteins are present, it is necessary to use empirical methods for determination of the electrode model parameters. The parameters related to electrode area must also be adjusted if the geometrical area of the electrode does not match the physical area as will be discussed further below.
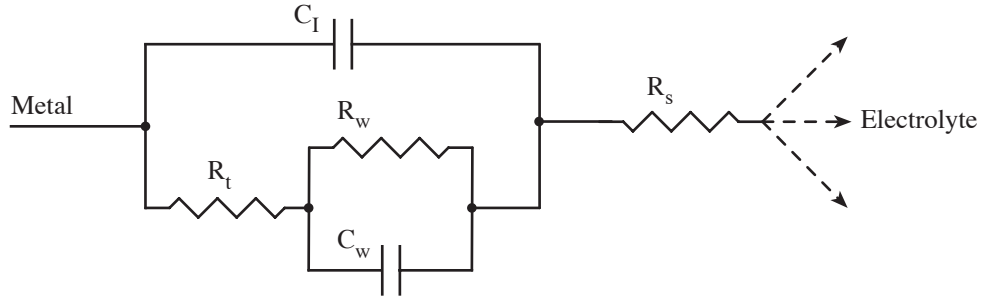
Figure 3.6: Circuit model for the metal-electrolyte interface including the interfacial capacitance (C_I), charge transfer resistance (R_t), diffusion-related Warburg elements (R_w and C_w), and the solution (spreading) resistance (R_s).

3.3 Electrode Noise and Signal Attenuation

As with most circuit elements, there is an intrinsic noise associated with the metal-electrolyte interface. This noise has been empirically shown to be thermal [Gesteland, et al., 1959], following the standard Johnson noise equation for the rms voltage noise of a resistor:

$$V_{rms\ noise} = \sqrt{4kTR_N\Delta f} \tag{3.20}$$

where k is boltzman's constant (1.38×10^{-23}J/K), T is the absolute temperature in kelvin, R_N is the real part of the electrode impedance in ohms, and Δf is the bandwidth of interest. For reference, this theoretical thermal noise voltage is plotted versus R_N in Figure 3.7. It is important to remember that R_N is the *effective* resistance of the electrode and will be attenuated by the electrode capacitance as the frequency is increased.
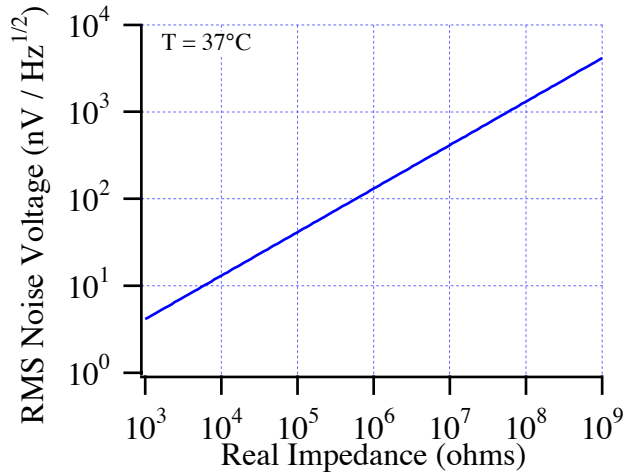
Figure 3.7: Theoretical noise voltage plotted versus the real part of the electrode impedance at 37°C. Noise is quoted as nV per root hertz since it is the bandwidth not the actual frequency that is significant.

For practical applications, the electrode impedance is measured in the bandwidth of interest and the obtained resistance is used in equation (3.20) to estimate the thermal noise. This noise is compared to the anticipated signal levels to determine if electrode impedance reduction is required. For impedance measurements where homodyning techniques are employed, the effective bandwidth of the measurement is significantly reduced making this thermal noise less significant. However, saturation of any amplification prior to the homodyning stage is possible, making this noise an issue for most practical systems.

In addition to noise considerations, the recording techniques and circuit configurations utilized often make reduced electrode impedance desirable. Take for example the common circuit shown in Figure 3.8 to be used for recording action potentials from an electrically active cell positioned over the electrode. Any signal present at the electrode / electrolyte interface will be attenuated by the voltage divider created by the electrode impedance and the input impedance of the amplifier (or other circuitry such as AC coupling and bias resistors to ground, parasitics associated with the microelectrode construction, etc.). Since most of the voltage will drop across the largest impedance, it is desirable to limit that of the electrode as much as possible. For measurement of cellular membrane characteristics, it is desirable for the electrode impedance to be significantly lower than that of the membrane if changes in the membrane impedance are to be observed. For both cases, reduced electrode impedance can be accomplished by either increasing the *geometric* size of the electrode or by increasing the *surface* area through control of electrode roughness. Since electrode size is often limited to the dimensions of the cell for these applications,
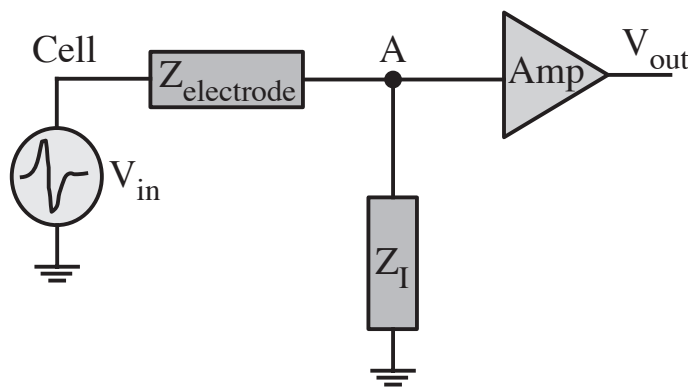
Figure 3.8: Common circuit for recording electrical activity (action potentials) from living cells. The action potential (V_{in}) signal is attenuated by the voltage divider created by the electrode impedance ($Z_{electrode}$) and the amplifier circuit input impedance (Z_I). Thus, reduction of $Z_{electrode}$ results in less signal loss.

increasing surface area without altering the geometric area is desirable. This is the focus of the next section. For a more detailed analysis of electrode noise sources and recording configurations see [Della Santina, 1994].

3.3.1 Platinum Black and the Electrode Impedance

As mentioned above, it is often desirable to decrease the electrode impedance for signal-to-noise (SNR) considerations. For applications where single cell characteristics are to be analyzed, increasing the geometric size of the electrode beyond that of the cell is undesirable. Thus, impedance reduction is generally accomplished by electroplating additional metal onto the surface of the electrode in such a way that a sponge-like or dendritic deposit results. This greatly increases the *surface* area of the electrode and results in electrode impedance reductions as outlined in Table 3.3. Electrodeposition is performed by immersing the electrode in an electroplating solution (generally chloroplatinic acid) and applying a DC potential across the electrode / solution interface. The exchange reactions occurring at the surface will result in the deposition of the metal [Feltham and Spiro, 1971; Harrison and Thompson, 1973] according to:

$$Pt^{IV}Cl_6^{-2} + 2e^{-1} \leftrightarrow Pt^{II}Cl_4^{-2} + 2Cl^{-1} \tag{3.21}$$

$$Pt^{II}Cl_4^{-2} + 2e^{-1} \leftrightarrow Pt + 4Cl^{-1} \tag{3.22}$$

$$Pt^{IV}Cl_6^{-2} + 4e^{-1} \leftrightarrow Pt + 6Cl^{-1} \tag{3.23}$$
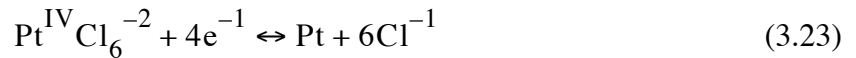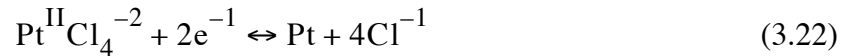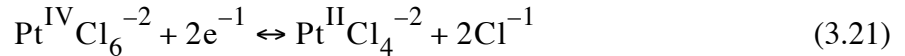
If the potential is sufficiently high, diffusion limited deposition will occur resulting in the metal "reaching out" into the solution. This is responsible for the dendritic or sponge-like nature of the deposit and results in a visually dark film. Hence these deposits are often termed black (e.g., platinum-black). Depositions of this kind can easily reduce the electrode impedance by two orders of magnitude [Robinson, 1968; Schwan, 1968] by effectively increasing the surface area of the electrode. Additionally, they increase the total amount of current that can be passed without pushing the electrode far from equilibrium.

There are other techniques that may be used to reduce the electrode impedance such as micropatterning the surface, etching the surface of the metal to form pits, and chemical modifications (such as activation of iridium to form iridium oxide). These have been reviewed in detail in the literature [Kovacs, 1994] and will not be repeated here. For this work, platinization was utilized for reduction of electrode impedance to acceptable levels.

Electrode model components	Symbol	Impedance scaling with frequency (f), surface area (A_S) and geometric area (A_G)
Interfacial capacitance (C_H and C_G)	C_I	$\left\|Z_{C_I}\right\| = \dfrac{k}{f A_S}$
Charge transfer resistance	R_t	$\left\|Z_{R_t}\right\| = \dfrac{k}{A_S}$
Warburg impedance	$R_w \mathbin{/\!/} C_w$	$\left\|Z_w\right\| = \dfrac{k}{A_S \sqrt{f}}$
Spreading Resistance	$R_s{}^{\dagger}$	$\left\|Z_{R_s}\right\| = \dfrac{k}{\sqrt{A_G}}$

† **Since the conductance of an electrolyte is due to movement of ions with limited mobility (around 6 orders of magnitude lower than an electron), some frequency dependence is expected. As the driving field increases in frequency, the ions have more difficulty following that field. Thus an inductive behavior should be observed at sufficiently high frequencies. The models utilized herein do not take this into phenomenon into account since the driving frequencies for impedance studies were limited to 100 kHz.**

Table 3.3: Scaling properties of microelectrode model parameters with frequency, geometric area and surface area. Adapted from [Kovacs, 1994].

There are different ways in which the effects of an altered electrode surface may be applied to the electrode-electrolyte model developed above. Edell developed a model impedance based on the assumption of cylindrical pores of known diameter and length [Edell, et al., 1986]. This pore impedance was placed in parallel with the interfacial capacitance and the series combination of the warburg elements and the charge transfer resistance. However, it is almost impossible to determine what the pore characteristics are in practice, making it difficult to apply the formulas. Hence, they are not repeated here. The simpler solution is to increase the effective area of the electrodes for all calculations except the spreading resistance (which is determined by the geometrical area of the electrode). This is the method which will be employed herein. Thus, no alterations to the basic circuit model of Figure 3.6 are required. The relative scaling of all model components with area and frequency is given in Table 3.3 below. Both geometric area and surface area relationships are given to allow for inclusion of electrode surface treatments (e.g. platinization) in the relationships. If a smooth noble metal is used as the electrode surface, then the geometric and surface areas may be identical.

3.4 Interconnect and Parasitics

The design and layout of planar microelectrode arrays will be covered in detail in Chapter 4. However, the basic structure will be explored here so that an explanation of the parasitics may be included in the planar microelectrode model.

Microelectrodes created using integrated circuit fabrication technology have the basic structure depicted in Figure 3.9. The substrate is generally either an insulator (glass or plastic) or semiconductor (silicon). In cases where the substrate is conductive, a capacitive parasitic path (C_s) exists between the metal conductors (electrodes, interconnects and bond-pads) and the substrate. This capacitance can result in cross-talk between adjacent elements (through R_{sub}) if the substrate is not grounded or a reduction in signal if

Figure 3.9: Physical structure of a planar microelectrode array and the associated parasitics after [Kovacs, 1994]. The array is immersed in an electrolyte resulting in an electrode impedance, Z_e as discussed in the previous sections. There is a parasitic capacitance between the interconnects and the electrolyte (C_p); between the interconnect, electrode and bond-pad layers and the substrate (C_s) connected by the substrate resistance (R_{sub}) (assuming a conductive or semiconducting substrate); and between adjacent interconnect traces (C_c). Not shown are any additional parasitics due to external packaging, bond-wire inductance, etc.

the substrate is held at ground. These parasitics are controlled by the geometrical area of the metal as well as the dielectric thickness. They may be calculated using the standard parallel plate model for a capacitor, but unfortunately, this underestimates the capacitance due to fringing fields. To account for these effects, a more complicated expression can be used

$$C_s = C_{bondpad} + \frac{1.15\varepsilon_0\varepsilon_r LW}{d} + 2.80\varepsilon_0\varepsilon_r L\left(\frac{t}{d}\right)^{0.222} \tag{3.24}$$

where ε_0 is the permittivity of free space, ε_r is the permittivity of the dielectric layer, L and W are the length and width of the interconnect trace (cm) respectively, t is the trace thickness (cm), and d is the thickness of the dielectric layer (cm) [Sakurai and Tamaru, 1983]. The bond-pad capacitance (not part of the Sakurai and Tamaru equation) can be

calculated using the standard parallel plate capacitor model. This should be included since the bond-pad area is often on the same order as that of the interconnects.

Between adjacent conductors another parasitic capacitance (C_c) results in cross-talk between electrode sites. This effect is minimized by maintaining a reasonable distance between interconnect traces (s in cm) as shown by the formula of Sakurai and Tamaru

$$C_c = 2\varepsilon_0\varepsilon_r L\left(\frac{s}{d}\right)^{-1.34}\left[0.03\left(\frac{W}{d}\right) + 0.83\left(\frac{t}{d}\right) - 0.07\left(\frac{t}{d}\right)^{0.222}\right] \qquad (3.25)$$

where d is the thickness of the passivation layer. In the case of the devices used for this research (to be discussed in Chapter 4), the metal interconnects were approximately 500 nm thick and the passivation layer was silicon nitride ($\varepsilon \approx 7.5$ [Wolf and Tauber, 1986]). Thus, for an interconnect separation (s) of 5 μm, a trace width (W) of 10 μm, and a passivation layer thickness (d) of 4 μm, the capacitance per unit length (C_c/L) would be 133 fF/cm; for most applications this would be negligible. More exact estimation of the parasitic cross-talk may be determined by finite element simulation as described in [Najafi, et al., 1990].

The final capacitive parasitic path depicted in Figure 3.9 is between the interconnect and the electrolyte (C_p). This may be estimated using (3.24) and controlled by the thickness of the passivation layer (which replaces d in (3.24)) and the effective geometrical area of the interconnects. Since the bond-pads are generally covered by epoxy or some other packaging material, they should not be included in this calculation as they were for the substrate capacitance. This parasitic capacitance can result in cross-talk between channels, and in cases where the electrolyte is grounded, signal attenuation. The former is of significant concern for impedance measurements where the capacitor (C_p) is actively driven and in parallel with the electrode impedance.

There are other parasitics associated with the packaging of the device as well as the electronics configuration. These will be briefly discussed in Chapter 4 and Chapter 5 respectively. Generally, interconnect resistance (on the order of 10 to 1000 Ω) and bond-wire inductance may be neglected in the total microelectrode model since their effects are negligible compared to the other components.

Given the parasitics described thus far, modifications may be made to the electrode model (Figure 3.6) as shown in Figure 3.10. While the substrate capacitance (C_s) is shown contributing to cross-talk, it could easily be a source of attenuation if the substrate is grounded. In cases where the substrate is itself an insulator, this term completely drops out of the model. The coupling capacitance (C_c) contributes to cross-talk in all cases, but is
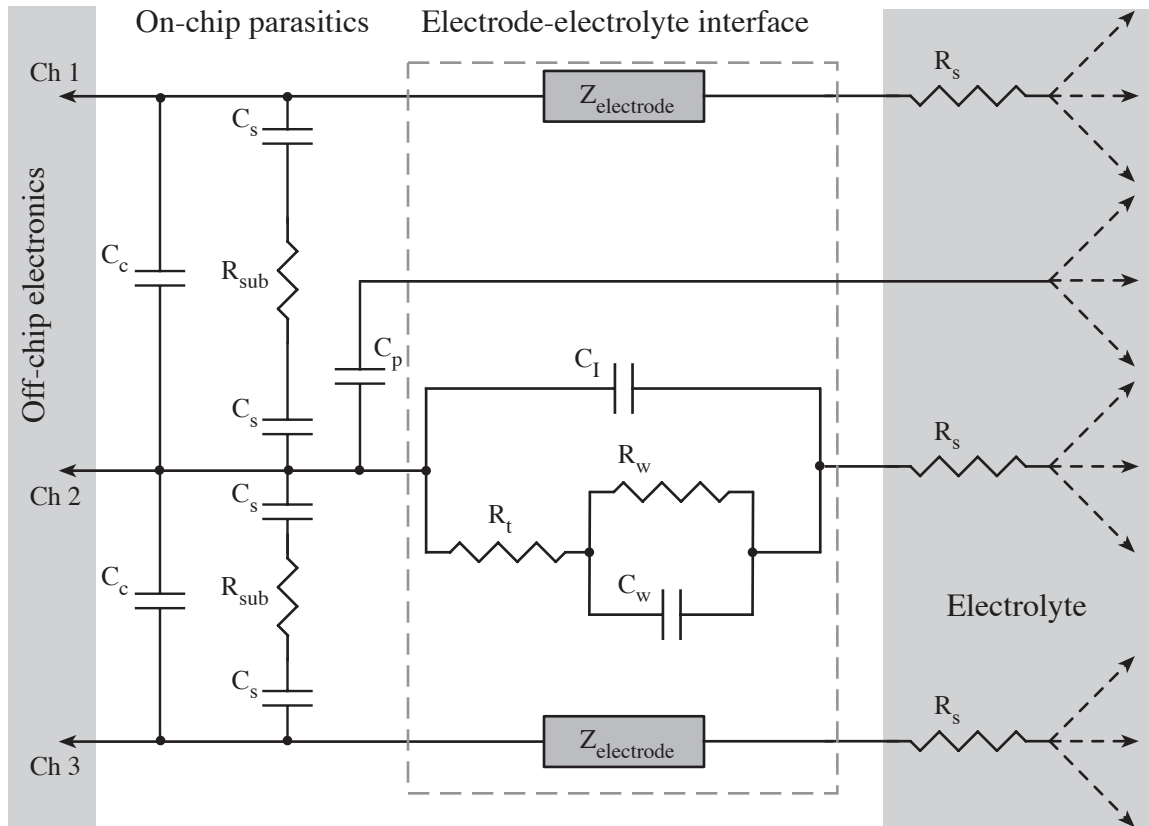
Figure 3.10: Full small-signal microelectrode model including the electrode/electrolyte interface and on chip parasitics for three adjacent channels. The termination of the parasitics depends on the electrical configuration used. A conducting substrate may be grounded making R_{sub} go to ground in the model.

generally negligible for well designed systems. The passivation capacitance (C_p) is correctly shown terminating in the electrolyte which may be ground for some systems. It is important to note that the passivation layer/electrolyte interface also has a double layer and diffusion elements as described for the metal electrode [Sui and Cobbold, 1979]. There would also be a spreading resistance associated with the current path through the electrolyte to a distant electrode. These have a negligible effect on well designed systems (sufficiently small C_p) and have been neglected in the model.

3.5 Transduction of Biological Signals

The properties of electrodes placed in an electrolyte have been discussed in detail above, and appropriate circuit models have been developed for the case of small signals. These models can be used to determine how a biological signal would be converted

(transduced) into an electrical one which can be amplified and processed by external circuitry connected to the electrode. Using a circuit simulator with a voltage or current source modeling an action potential, fairly accurate signal predictions can be made using these detailed models [Grattarola, et al., 1991; Grattarola and Martinoia, 1993; Bove, et al., 1995]. However, there are generalities one can make about the shape of the resulting signal, and there are several different ways of visualizing the actual transduction process as will be discussed below.

3.5.1 The Moving Dipole Model

When an action potential is produced and travels along a cell membrane (or neuronal axon), different regions of the membrane carry different transmembrane potentials. It is this phenomena which allows the AP to propagate. Thus, some sections of the membrane must have a negative transmembrane potential while others exhibit a positive transmembrane potential. This effective charge distribution can be visualized as a moving dipole [Geddes, 1972]. As this dipole moves past the electrode, the charge movement induced across the interfacial capacitance will cause the potential at the amplifier to first fall, then rise and fall again as depicted in Figure 3.11 (for the dipole orientation shown). This is what is observed in an electrocardiogram [Geddes, 1972] and may be the case for extracellular recording from cultured myocytes

Figure 3.11:   A dipole moving past an electrode at point P after [Geddes, 1972]. The dipole charge induces a mirror charge at the electrode. As the dipole moves past the electrode, the polarity of the image charge changes resulting in the characteristic extracellular AP shape shown.

72

[Connolly, et al., 1990] where the action potential propagates in a wave through the sheet of cells.

3.5.2 Traveling Waves and the Seal Resistance

As described in Chapter 2, there are small regions of close adhesion or *adhesion plaques* where the cell membrane is separated from the substrate by 1 to 15 nm. Other regions of the membrane are more loosely coupled and exhibit a cell / substrate separation of up to 100 nm. This region between the cell and the substrate is filled with electrolyte and exhibits a resistance (the *seal resistance*) which can be approximated using (3.17). All basal membrane currents (those flowing through the bottom membrane of the cell) associated with a traveling wave must flow through this seal resistance. The result is a voltage drop between the electrode and the electrolyte bathing the cell which can be monitored using the electrode.

Consider the simplified circuit schematic of the cell / electrode interface shown in Figure 3.12. The transmembrane potential which represents an intracellular recording is shown as V_{in}. The current flowing through the basal membrane is the sum of the ionic and capacitive currents as described in Chapter 2 where a traveling wave is assumed. As this current flows through the seal resistance, a voltage is developed at node A which is proportional to the second derivative of the transmembrane potential (recall equation (2.5)). This voltage is also proportional to the magnitude of R_{seal} as was experimentally verified [Breckenridge, et al., 1995] by correlating the measured seal resistance of *Lymnaea* neurons cultured on a microelectrode array to the recorded extracellular signal strength. A near linear, directly proportional correlation was observed. In the extreme of an infinite seal resistance, the voltage at node A would correspond to the intracellular potential, thereby simulating a whole-cell patch configuration. This trend (presented in Figure 3.13) has been shown
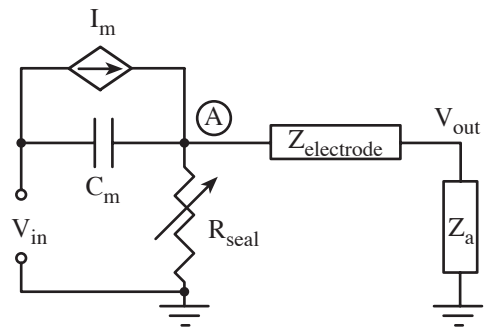
Figure 3.12: Simplified circuit schematic of the cell / electrode junction. V_{in} is the transmembrane voltage, C_m is the basal membrane capacitance, I_m is the basal ionic current, R_{seal} is the seal resistance, $Z_{electrode}$ is the electrode impedance, and Z_a is the input impedance of the amplifier, bias resistors and parasitics to ground.
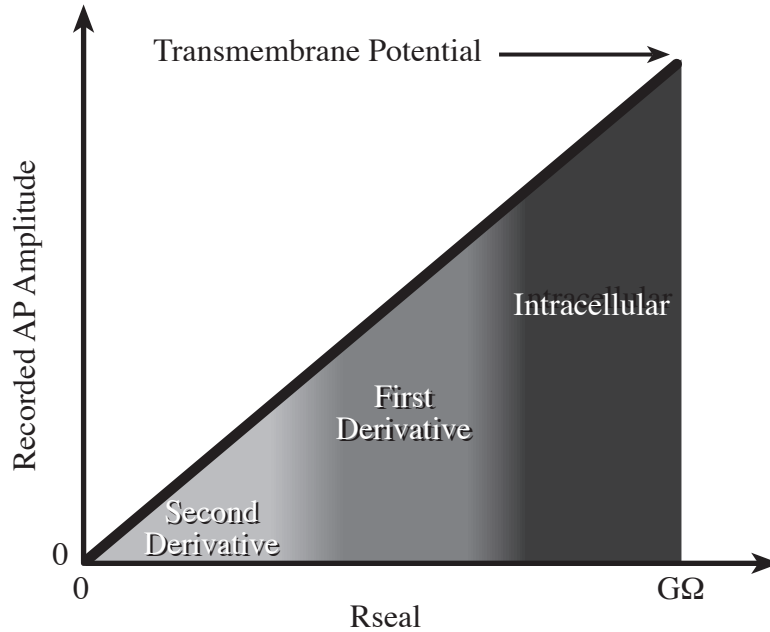
Figure 3.13: Characteristic action potential signal recorded with an extracellular microelectrode as the seal resistance is varied. For low seal resistances, the amplitude is small and a second derivative behavior is observed (assuming no additional derivative due to the electrode itself). As the seal resistance is increased, the amplitude of the recorded AP increases and the order of the derivative decreases. For very high seal resistances a whole-cell patch configuration is approached and the intracellular signal is measured.

experimentally by [Regehr, et al, 1989; and Breckenridge, et al., 1995] and via simulation by [Grattarola and Martinoia, 1993].

3.5.3 Electrode Transduction

The voltage signal at node A is then transduced by the electrode according to the model developed herein. For most practical systems in the bandwidth of interest, the electrode is mostly capacitive. This electrode capacitance creates a pole with the input impedance (Z_a), which results in an additional derivative for frequencies below the pole. Thus, the signal presented to the amplifier (V_{out}) is proportional to the seal resistance and either the second or third derivative of the action potential for the case of a traveling wave. Additionally, the voltage divider created by $Z_{electrode}$ and Z_a can cause signal attenuation if Z_a is not significantly larger than $Z_{electrode}$. Thus, it is important to design the measurement system with low electrode impedance and high Z_a to ensure limited signal attenuation and to prevent the introduction of an additional derivative to the measured signal.

3.5.4 Impedance Signals

The above discussion described how an electrode transduced the biological signal from a cell (or group of cells) firing action potentials. However, this is different than the mechanism by which impedance changes are sensed. For impedance measurements, a constant AC voltage (or current) is applied to the electrode and the resulting current (or voltage) is monitored. Thus, the overall impedance of the electrode / electrolyte combination, parasitic elements, and biological material (cells) are measured. If measurements are made prior to addition of the biological material, then that baseline may be subtracted from the biological measurement to obtain an estimate of the biological impedance (neglecting changes to the electrode due to adsorption of proteins, etc.). Likewise, any changes in the impedance while the cells are positioned over the electrode may be attributed to changes in the cellular impedance. If the frequency of the measurement is changed, the impedance characteristics of the electrode will change as described previously. However, this may be easily factored out of the resulting measurements.

3.5.5 Optimized Electrode Structures

In addition to the noise and signal attenuation issues described in Section 3.3, and the seal resistance correlation described above, the basic structure of the fabricated microelectrode array can also influence the recorded extracellular signal strength. Lind, et al. modeled the extracellular signal strength for a spherical cell surrounded by extracellular fluid, a cell above an extracellular electrode, a cell above an electrode in a groove, and a cell above an electrode in a cubic pit where the groove an pit dimensions were slightly larger than the cell [Lind, et al., 1991]. The resulting extracellular voltages calculated were 142 μV, 168 μV, 391 μV, and 1.2 mV respectively. Thus, a significant improvement was predicted by confining the space around the cell. Such structures (grooves and pits) may be fabricated using integrated circuit fabrication techniques, although the use of organic films such as polyimide is often required to obtain the film thicknesses required (approximately 10 μm). These materials are less robust than the silicon nitride and silicon dioxide films often utilized as passivation layers, making them more difficult clean and use repeatedly. However, for applications requiring measurement of extremely small signals, these structural methods may be required. The electrode design employed must always reflect the application intended.

3.6 Summary

A model of a metal microelectrode immersed in an electrolyte has been described. The effects of electrode material, geometric and physical areas, frequency of observation or excitation, and parasitics due to electrode construction using IC fabrication techniques were explored. Noise and signal attenuation were considered along with techniques for limiting their impact on the recorded signal. Finally, several ways of considering the transduction of the biological signal through the electrode to attached electronics were described for both the recording of action potentials and the measurements of biological impedance. While these simple techniques are only guidelines, they can provide the insight required for interpreting biological signals recorded using microelectrodes.

References

Bard, A.J. and Faulkner, L.R., *Electrochemical methods*, John Wiley & Sons, Inc., New York (1980).

Bockris, J.O'M. and Reddy, A.K.N., *Modern electrochemistry*, Plenum Press, New York (1970).

Bove, M., Grattarola, M., Martinoia, S. and Verreschi, G., "Interfacing cultured neurons to planar substrate microelectrodes: characterization of the neuron-to-microelectrode junction," *Bioelectrochemistry and Bioenergetics*, 38:255-265 (1995).

Breckenridge, L.J., Wilson, R.J.A., Connolly, P., Curtis, A.S.G., Dow, J.A.T., Blackshaw, S.E. and Wilkinson, C.D.W., "Advantages of using microfabricated extracellular electrodes for in vitro neuronal recording," *Journal of Neuroscience Research*, 42:266-276 (1995).

Chapman, D.L., *Phil. Mag.*, 25(6):475 (1913).

Cobbold, R.S.C., *Transducers for biomedical measurements: principles and applications*, Wiley, New York, 412-475 (1974).

Connolly, P., Clark, P., Curtis, A.S.G., Dow, J.A.T. and Wilkinson, C.D.W., "An extracellular microelectrode array for monitoring electrogenic cells in culture," *Biosensors and Bioelectronics*, 5:223-234 (1990).

Della Santina, C.C., "Silicon regeneration-type multi-microelectrodes for electrophysiology in the eighth cranial nerve," Doctoral thesis, University of California at Berkeley, Technical report number ICL94-036 (1994).

DeRosa, J.F. and Beard, R.B., "Linear AC electrode polarization impedance at smooth noble metal interfaces," *IEEE Transactions on Biomedical Engineering*, BME-24(3):260-268 (1977).

Edell, D.J., Clark, L.D. and McNeil, V.M., "Microfabrication technology for development of chronic neural information transducers," *Proc. Int. Electron Devices Mtg.*, Los Angeles, California, Dec. 7-10, pp. 180-183 (1986).

Feltham, A.M. and Spiro, M., "Platinized platinum electrodes," *Chemical Reviews*, 71(2):177-193 (1971).

Geddes, L.A., *Electrodes and the measurement of bioelectric events*, John Wiley & Sons, Inc., London (1972).

Geddes, L.A., Foster, K.S., Reilly, J., Voorhees, W.D., Bourland, J.D., Ragheb, T., and Fearnot, N.E., "The rectification properties of an electrode-electrolyte interface operated at high sinusoidal current density," *IEEE Transactions on Biomedical Engineering*, BME-34(9):669-672 Sept. (1987).

Gesteland, R.C., Howland, B., Lettvin, J.Y. and Pitts, W.H., "Comments on Microelectrodes," *Proceedings of the IRE*, 47:1856-1862 (1959).

Gouy, M., "Sur la constitution de la charge électrique a la surface d'un electrolyte," *J. Phys.*, 9:457-468 (1910).

Grattarola, M., Martinoia, S., Massobrio, G., Cambiaso, A., Rosichini, R. and Tetti, M., "Computer simulations of the responses of passive and active integrated microbiosensors to cell activity," *Sensors and Actuators*, B4:261-265 (1991).

Grattarola, M. and Martinoia, S., "Modeling the neuron-microtransducer junction: from extracellular to patch recording," *IEEE Transactions on Biomedical Engineering*, 40(1):35-41 (1993).

Harrison, J.A. and Thompson, J., "The electrodeposition of precious metals: a review of the fundamental electrochemistry," *Electrochemica acta*, 18:829-834 (1973).

Helmholtz, H.L., "Studien über electrische grenzschichten," *Ann. Phys. Chem.,* 7:377-382 (1879).

Kovacs, G.T.A., "Microelectrode models for neural interfaces," In *Enabling technologies for cultured neural networks* (Stenger,D.A. and McKenna, T.M., eds.), 121-165, Academic Press, New York (1994).

Lind, R., Connolly, P. and Wilkinson, C.D.W., "Finite-element analysis applied to extracellular microelectrode design," *Sensors and Actuators*, B3:23-30 (1991).

Moussavi, M., Schwan, H.P. and Sun, H.H., "Harmonic distortion caused by electrode polarization," *Medical and Biological Computing*, 121-125, March (1994).

Muller, R.S. and Kamins, T.I., *Device electronics for integrated circuits*, John Wiley & Sons, New York (1986).

Najafi, K. and Wise, K.D., "An implantable multielectrode array with on-chip signal processing," *IEEE J. Solid-State Circuits*, 21(6):1035-1044 (1986).

Najafi, K., Ji, J. and Wise, K.D., "Scaling limitations of silicon multichannel recording probes," *IEEE Transactions on Biomedical Engineering*, 37(1):1-11 (1990).

Newman, J., "Resistance for flow of current to a disk," *J. Electrochemical Society*, 113(5):501-502 (1966).

Regehr, W.G., Pine, J. and Rutledge, D.B., "A long term in vitro silicon-based microelectrode-neuron connection," *IEEE Transactions on Biomedical Engineering*, 35:1023-1032 (1988).

Regehr, W.G., Pine, J., Cohen, C.S., Mischke, M.D. and Tank, D.W., "Sealing cultured invertebrate neurons to embedded dish electrodes facilitates ling-term stimulation and recording," *J. Neuroscience Methods*, 30:91-106 (1989).

Robinson, D.A., "The electrical properties of metal microelectrodes," *Proceedings of the IEEE*, 56(6):1065-1071 (1968).

Schwan, H.P., "Electrode polarization impedance and measurements in biological materials," *Annals of the New York Academy of Sciences*, 148(1):191-209, Feb. (1968).

Schwan, H.P., "Linear and nonlinear electrode polarization and biological materials," *Annals of Biomedical Engineering*, 20:269-288 (1992).

Stern, O., "Zur theorie der elektrolytischen doppelschicht," *Z. Elektrochem.*, 30:508-516 (1924).

Sui, W.M. and Cobbold, R.S.C., "Basic properties of the electrolyte-SiO_2-Si system: physical and theoretical aspects," *IEEE Transactions on Electron Devices*, ED-26(11):1805-1815 (1979).

Sukarai, T. and Tamaru, K., "Simple formulas for two- and three-dimensional capacitances," *IEEE Trans. Electron Devices*, ED-30(2):183-185 (1983).

Vetter, K.J., *Electrochemical kinetics: theoretical and experimental aspects*, Academic Press, New York (1967).

Warburg, E., "Ueber das verhalten sogenannter unpolarisirbarer elektroden gegen wechselstrom," *Ann. Phys. Chem.*, 76:493-499 (1899).

Weast, R.C., (Ed), *CRC handbook of chemistry and physics*, CRC Press, Boca Raton, Florida (1988).

Webster, J.G. (Ed.), *Medical Instrumentation*, Second Edition, Houghton Mifflin company, Boston (1992).

Wolf, S. and Tauber, R.N., *Silicon processing for the VLSI era, volume 1: process technology*, Lattice Press, Sunset Beach, California (1986).

Chapter 4   MICROELECTRODE DESIGN, FABRICATION AND TESTING

Don't let cells dry on the chips, or civilization as we know it will come to an end....

David Stenger, 1995

4.1 Introduction

When developing a cell culture vessel with microelectrodes for monitoring the electrical properties of living cells, there are many considerations that must be addressed. All materials utilized must be biocompatible, at least for the relatively short term (weeks) experiments required for this research. The ability to maintain the *physiochemical* environment of the cells must be preserved while providing the flexibility to perform electrical measurements. The desire for spatially localized electrode sites must be balanced against such things as electrode impedance, and the signal-to-noise ratio of the measurement to be performed. The surface upon which the cells are to be cultured (electrodes and insulating layers) must be conducive to cell attachment and growth while simultaneously performing other functions such as signal transduction or electrical and chemical insulation. These issues and others will be discussed in detail in the sections below which will describe the design, fabrication, packaging, and testing of the microelectrode arrays utilized in this research.

4.2 Microelectrode Design

For whole cell based biosensor applications monitoring extracellular action potentials and cellular impedance of anchorage dependent cell types, a cell culture substrate containing microelectrodes upon which the cells can be cultured is required. As described in Chapter 3, the electrode must provide a low impedance electrical connection to the cell. The adhesion of cells to the passivation layer utilized is also of considerable importance since a loosely coupled cell provides a shunt path for current which decreases the signal strength for both impedance and action potential measurements.
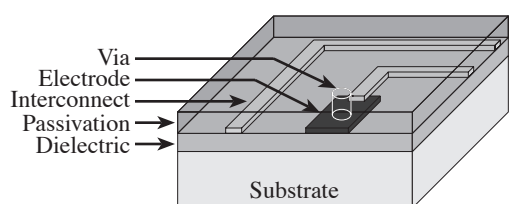
Figure 4.1: Basic electrode structure consists of a substrate, dielectric insulation (if required), microelectrode metal, interconnect metal, passivation to electrically and chemically isolate the metals, and vias etched through the passivation to define the electrode site.

It is desirable to have the substrate material and format conducive to parallel fabrication techniques since this greatly reduces construction time and costs. For this work, silicon and glass substrates were utilized in a standard 100 mm diameter circular format. This allowed for standard microlithographic processes to be utilized. The electrode materials chosen were standard selections for the measurement of biological signals (gold, iridium and platinum) and could be applied and patterned in a parallel fashion. The passivation layer that insulates the electrical interconnects from the electrolyte bathing the cells was silicon nitride, which has been shown to provide excellent biocompatibility and adequate cellular adhesion. These materials constitute the substrate upon which the cells are cultured.

4.2.1 Substrate

Two different materials were utilized as a substrate for the fabrication of planar microelectrode arrays: silicon and glass. Silicon was used for the first generation chips since it was readily available, allowed for possible circuit integration (not done with these devices), and was suited to standard integrated circuit fabrication technologies. Thermal silicon dioxide was used as an insulating dielectric layer to isolate the electrodes and interconnects from the semiconducting substrate. While these chips functioned well for action potential experiments, the parasitic capacitance to the substrate (C_S) was

problematic for biological impedance measurements. Additionally, these devices were light sensitive. As light shone on the silicon, carriers were generated. In the regions where a metal-oxide-semiconductor structure was present, these carriers moved in response to the intrinsic field present in the depletion region at the silicon surface. This change in charge was capacitively mirrored in the metal (electrodes or interconnects) and amplified by the action potential amplifier. Thus, for time varying light conditions, a significant time varying voltage could be observed at the electrode (on the order of tens of mV). This problem could be solved by the addition of a light shield beneath the dielectric layer or by biasing the substrate with respect to the metal traces and interconnects. However, the addition of a light shield would increase the parasitic effects of C_s and biasing could cause electrochemistry at the electrode-electrolyte interface. Thus, alternative substrate materials were explored.

The second generation chips were fabricated on polished 100 mm circular glass substrates. Glass was able to withstand the processing temperatures (for this process $T_{max} = 300°C$) and, if the back side was coated with metal (or any opaque material) it could be used with automated integrated circuit manufacturing equipment. Additionally, if properly packaged, the transparent substrate could allow for optical inspection of the cultured cells using standard inverted microscopy (not done for these devices). The use of glass as the substrate effectively eliminated the substrate parasitics (C_s) and the light sensitivity since the glass was non-conductive. These chips worked well for both action potential recording and measurement of biological impedances.

4.2.2 Electrodes

Electrode fabrication is a two step process as will be discussed in detail in Section 4.3. First the metal is deposited and then a via (or hole) is etched through the passivation layer to define the active electrode area. It is this area which contacts the electrolyte and is used in calculations of the model parameters for the electrode / electrolyte interface and the spreading resistance. As shown in Figure 4.2, the metal area is larger than the via. This is important since when defining subsequent layers using lithographic techniques, alignment to previous layers is necessary. When using materials such as iridium, platinum and gold patterned with lift-off (to be defined later) on a non-standard substrate such as glass, this alignment may be difficult. Thus, errors of up to 1 μm were not uncommon. For these reasons, the electrode pads were designed to be at least 2 μm larger than the largest electrode diameter (defined by the via etch through the passivation layer).
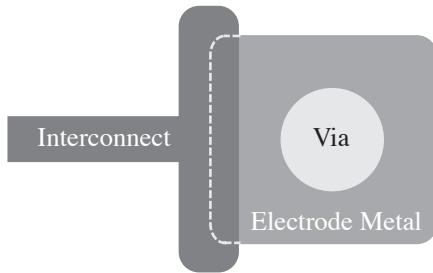
Figure 4.2: Conceptual drawing of a microelectrode. The electrode metal layer is larger than the via (which defines the active electrode area) to allow for misalignment during fabrication. For the same reasons, the interconnect metal overlaps that of the electrode.

The cell types utilized in this research ranged in diameter from 5 to 100 μm. Thus, an electrode of comparable (or smaller) size was desirable. Three masks were utilized for the via etch step (discussed in Section 4.3), each containing different via diameters (thereby defining various sized electrodes). One had electrodes of 10μm diameter, one with 22 μm diameter, and one with six different diameters ranging from 4.4 μm to 24.7 μm (six electrodes each with areas of 480 μm^2, 240 μm^2, 120 μm^2, 60 μm^2, 30 μm^2, and 15 μm^2). The variable size electrode array allowed for better modeling of electrode characteristics as they related to geometric area as well as an investigation of the optimum size electrodes for monitoring action potentials and biological impedance changes. The majority of chips utilized herein were of this type. The basic layout of the 6 × 6 element electrode array is shown in Figure 4.3

A total of 36 electrodes (6 × 6 array) were fabricated to provide a significantly large number of recording sites. While a larger number may be desirable for some applications, the number of interconnects quickly become problematic, and on-chip multiplexing is required. For this research utilizing passive electrodes, it was felt 36 electrodes provided a good balance between the number of recording sites and packaging manageability. With the inclusion of four larger electrodes to be used for grounding the electrolyte, the total number of required interconnects was 40.

The electrode separation was chosen to allow for monitoring of cultured cell network properties if desired while limiting crosstalk due to neighboring cells. Studies have been performed [Breckenridge, et al., 1995] where current (400 nA) was injected in the vicinity of an extracellular electrode and the resulting voltage was monitored. The detected current fell to 50% 30 μm away from the electrode (as compared to the signal observed with current injected directly above the electrode). At 128 μm the response had fallen to 10% of the maximum. Breckenridge, et al. concluded that a 100 μm separation between electrodes was sufficient to limit crosstalk to insignificant levels; a conclusion which was consistent with finite element analysis modeling performed in the same group [Lind, et al., 1991]. While this crosstalk would most likely be less with cells positioned over the electrodes
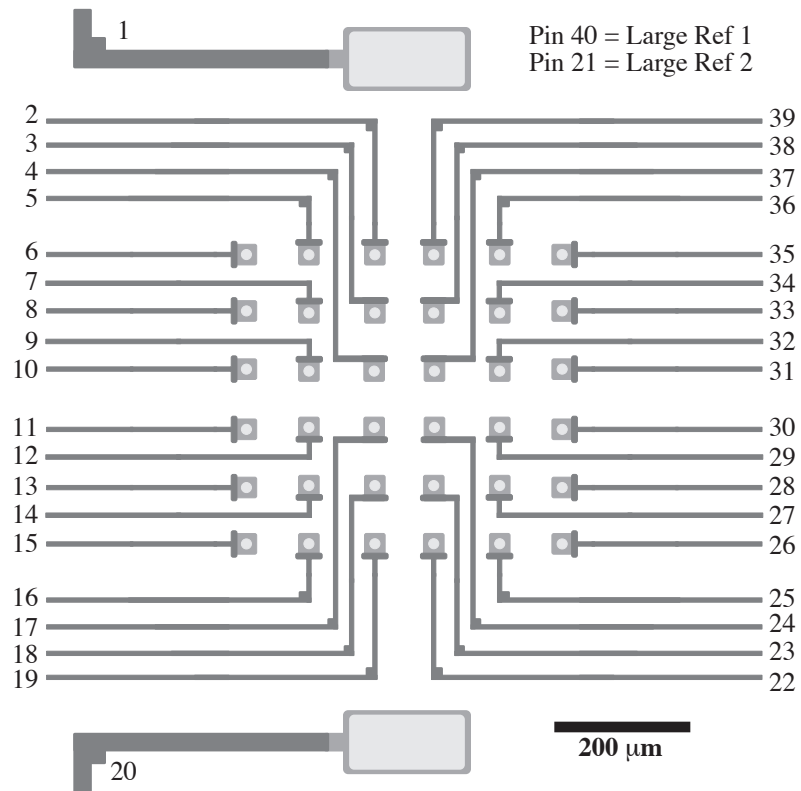
Figure 4.3: Basic layout of the 6×6 element microelectrode array. The active electrodes range in size from 15 to 480 µm^2 and are on a 100 µm pitch. Two small reference electrodes are shown while two large reference electrodes are beyond the field of view. The numbers shown correspond to the package pin to which the electrode is connected

(due to the cellular impedance), this conservative electrode separation was used for this microelectrode array design.

Three different noble metals were used for the electrodes fabricated for this study: gold, platinum, and iridium. All have excellent properties for biological use (biocompatibility, corrosion resistance, etc.) and have been utilized extensively in the literature. Gold is perhaps the easiest to use due to its ductile nature and has been fabricated on both the silicon and glass substrates. Iridium is the most difficult to utilize due to high film stresses in deposited films, however it is also the most physically and chemically robust. In its activated state (Ir oxide), it makes and excellent material for stimulation studies where high current densities must be passed through the electrodes [Tanghe, et al., 1990]. Iridium electrodes were only made on the silicon substrates, making them suboptimal for biological impedance measurements. The platinum electrodes have been fabricated on glass substrates making them suitable for both AP and impedance studies. Platinum has a higher exchange current density than either gold or iridium (in its

unactivated state) as shown in Table 3.2. It also has advantages in instances where the application of platinum black is used for electrode impedance reduction as will be discussed below.

As discussed in Chapter 3, when a metal is placed in an electrolyte, charge transfer reactions occur at the interface until an equilibrium is reached. The equilibrium potential results from a complex combination of electrode material properties, electrolyte concentration, reactions occurring at the interface, etc. Since the electrode properties (exchange current density, etc.) play a role in reaching equilibrium, different materials will reach different equilibrium potentials. If two different metals are placed in the same electrolyte, the different equilibrium potentials may be enough to drive additional (non-equilibrium) reactions. This results in electrochemistry and is the basis upon which a battery supplies power. This is of concern when designing microelectrodes for biological studies. When platinum is electroplated onto the electrode surface, the film may or may not completely cover the underlying electrode. Even in cases where a contiguous platinum black film is applied, over time degradation of the electroplated material occurs due to physical and chemical abrasions. This often results in pinholes though the film down to the underlying electrode material. If this material is something other than platinum, then the possibility for localized electrochemistry at the pinhole sites exists (due to different equilibrium potentials of the two metals). The effect of this possible electrochemistry on cultured cells is unknown. To remove this variable from the experiments conducted with cultured cells as part of this research, only platinized *platinum* electrodes were used (for both AP and impedance measurements).

4.2.3 Interconnects

The choices for interconnect layers are as varied as the metals that can be evaporated or sputtered using standard integrated circuit fabrication techniques. Several may come to mind including aluminum, copper, polysilicon, and the materials used for the electrodes (platinum, gold and iridium). Aluminum is perhaps the easiest to work with and is a standard in integrated circuit fabrication. However, there are problems when aluminum is in contact with gold (one of the electrode materials utilized herein); intermetallics are formed which exhibit poor electrical conductivity, brittleness and a coefficient of thermal expansion significantly different than either Au or Al. One such intermetallic, $AuAl_2$ has a characteristic purple color which gave rise to the name *purple plague* [Selikson, 1965]. Additionally, Au diffuses faster in Al than does Al in Au. Thus, voids are formed over time which can result in an open circuit at the connection [Footner, et al., 1987]. In addition to
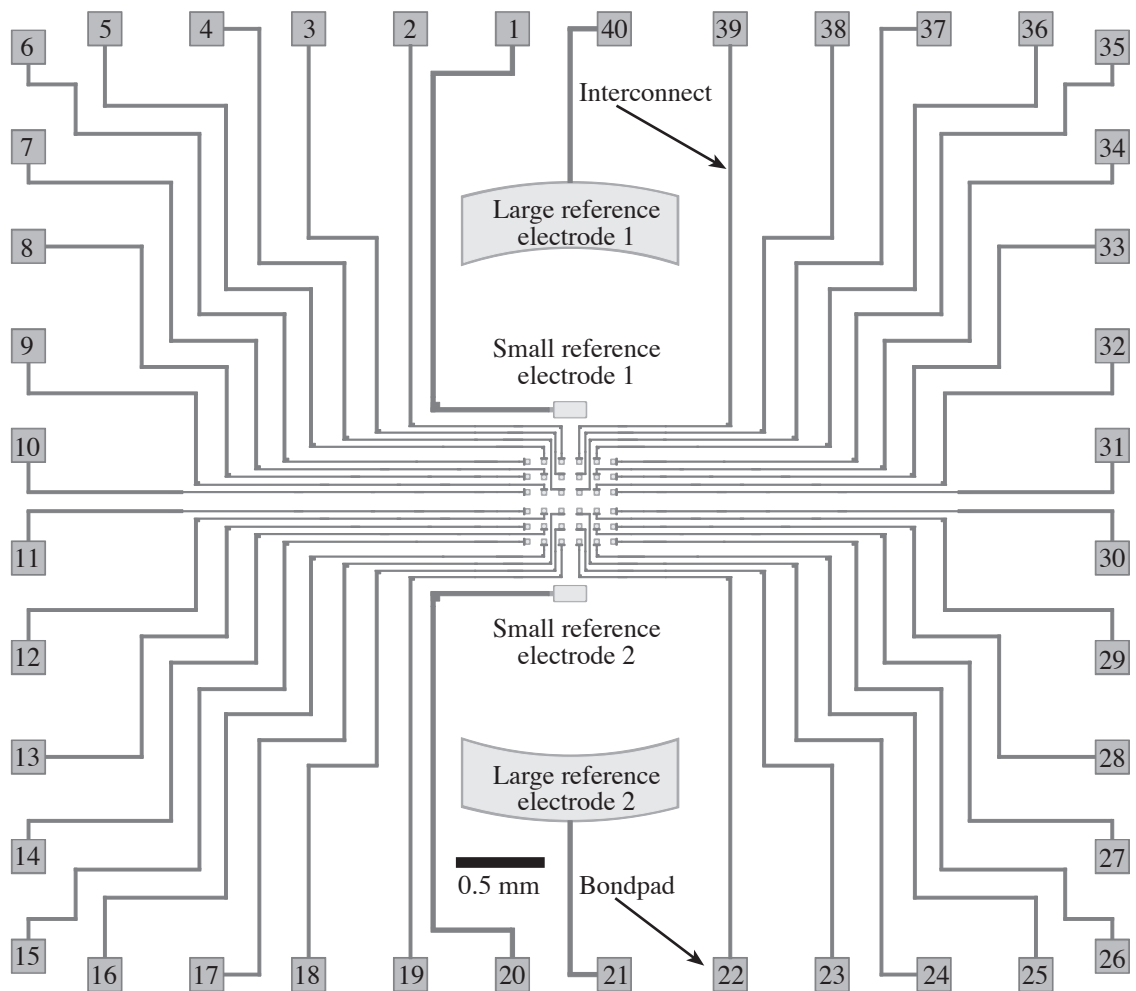
Figure 4.4: Layout of the entire microelectrode array including the reference electrodes, interconnects and bondpads. The bondpads around the outer edge of the die are used for bondwire connections to the 40 pin DIP, with the numbers corresponding to the DIP pin number.

the problems descried above involving the connection to gold films, aluminum also undergoes some morphological changes at the temperature of the passivation layer deposition utilized for these devices (300°C), which could result in spiking and pinhole development through the passivation. For these reasons, Al was not used as the passivation layer. Copper has excellent conductive properties, but is also cytotoxic (it is used as an anti-bacterial cladding in some cell culture incubators for this reason). Thus, if any pinholes are present in the passivation it could affect cell growth. Polysilicon, while easily manufactured, fairly biocompatible and able to withstand the subsequent processing temperatures, exhibits a resistivity at least 3 orders of magnitude higher than that of the metals discussed. Platinum and iridium could both be used for interconnect (low

resistivity, biocompatibility, chemical and thermal robustness), however they make wire bonding between the chip and the package difficult. For these reasons gold was chosen as the interconnect material. It exhibits a low resistivity, chemical and thermal robustness, and it facilitates bondwire connections.

Interconnect spacing was kept to a minimum of 10 μm to both limit the cross talk capacitance, C_c and facilitate fabrication using lift-off structures. As will be discussed in Section 4.3, a lift-off process is used to define all the metal traces. While a line pitch of 3 μm has been successfully achieved in the past using this process [Kewley, et al., 1997], a wider margin results in higher yields. Additionally, tighter packing was not required for the number of electrodes within the array. Where the interconnect metal connected with the electrode metal, an overlap of 12 μm was used to ensure a low impedance contact and that alignment errors (as discussed above and shown in Figure 4.2) did not result in an open circuit at this point.

The chip was designed (9 mm x 9 mm) as shown in Figure 4.4, to fit in a standard 40 pin ceramic dual-in-line package (DIP) with a 1 cm square well. Thus, the maximum interconnect length was approximately 4.5 mm, terminating at one end on the electrode and at the other on a bondpad 200 μm square (made of the interconnect metal). This bondpad contributes significantly to the substrate capacitance (for conducting or semiconducting substrates) and must be included in the calculation of C_s.

4.2.4 Passivation Layer

There are generally two different classes of materials used as passivation layers for planar microelectrode arrays: organic polymers (photoresist and polyimide) and glass like thin films (silicon dioxide and silicon nitride). Both photoresist and polyimide have been used successfully to passivate the interconnect metal and work well. In short-duration studies with cultured cells, both photoresist and polyimide have been shown to be biocompatible and facilitate cellular attachment (see Chapter 1). Both are easily patterned, can be hardened using heat and / or ultraviolet light, and exhibit a lower dielectric constant ($\varepsilon_r = 2.7$ [Kuperstein and Whittington, 1981]) than either SiO_2 or Si_3N_4. Their main disadvantage is durability, since they cannot withstand harsh chemical cleans. In instances where prolonged and repeated use over months is desirable, these organic polymers are a poor choice.

Silicon dioxide, while having a lower dielectric constant ($\varepsilon_r=3.9$) than silicon nitride ($\varepsilon_r=7.5$) does not effectively block ion transport. This is a major cause of metal-oxide-semiconductor (MOS) transistor failure [Muller and Kamins, 1986]. Thus, it

can be a poor choice to passivate active devices placed in an electrolyte. Additionally, movement of ions through the passivation layer may reduce the effective electrical isolation of the layer. The possible use of a bilayer passivation layer structure was explore (using a thick low dielectric oxide covered by a thin ion blocking nitride layer), however, in the case of silicon dioxide deposited on glass substrates using plasma-enhanced chemical vapor deposition (PECVD), there was difficulty experienced when etching through the layer. Thus, oxide could not be used for these devices.

Silicon nitride was therefore the material of choice for passivating the electrodes used for this research. It conformally coats surfaces (as does the PECVD silicon dioxide), is easily patterned, impermeable to ions (in some cases), biocompatible, and attractive for cellular attachment if properly cleaned. First generation chips fabricated on silicon had a PECVD silicon nitride passivation layer of 1 μm thick. This was found to be adequate for AP measurements, but limited the resolution of biological impedance measurements due to current shunting through the passivation parasitic (C_p). Thus, the second generation chips (glass substrates) used 4 μm of silicon nitride, providing a significant reduction in this electrolyte / interconnect capacitance.

4.2.5 Electrode Model Estimations

The model components were estimated using the theoretical and empirical formulas described in Chapter 3. For each component either worst case or average values were computed as outlined in Table 4.1 below. All calculations were for circular, bare platinum electrodes. To include the effects of platinization, the surface area of the electrodes would have to be increased as outlined in Chapter 3.

Model Parameter	Symbol	Defining equation	Dimensions and properties of interest$^\Delta$	Area independent value	Value w/ $A=15\mu m^2$	Value w/ $A=480\mu m^2$
Helmholtz capacitance	C_H	(3.1)	$\varepsilon_r = 78.5^\dagger$ $d_{OHP} = 5$ Å	1.4 pF/μm^2	21 pF	667 pF
Gouy-Chapman capacitance	C_G	(3.4)	$\varepsilon_r = 78.5^\dagger$ $z = 1$ $n^0 = 93\times10^{21}$ ions/l$^\Delta$ $V_0 = 50$ mV‡ $L_D = 7.8$ Å	1.3 pF/μm^2	20 pF	643 pF
Interfacial capacitance	C_I	(3.5)	See above	0.7 pF/μm^2	10 pF	326 pF
Charge transfer resistance	R_t	(3.9)	$z = 1$ $J_0 = 8\times10^{-4\dagger\dagger}$ A/cm^2	3.3 G$\Omega\bullet\mu m^2$	214 MΩ	6.8 MΩ
Warburg Impedance	Z_w	(3.13) (3.16)	$z = 1$ $n^0 = 93\times10^{21}$ ions/l$^\Delta$ $f = 1$ kHz $D = 4\times10^{-5}$ cm^2/sec‡‡	694 k$\Omega\bullet\mu m^2$ $\angle-45°$	46 kΩ $\angle-45°$	1.4 kΩ $\angle-45°$
Spreading Resistance$^\psi$	R_s	(3.18)	$\rho = 72$ $\Omega\bullet cm^\Delta$	319 k$\Omega\bullet\mu m$	82 kΩ	15 kΩ
Passivation capacitance	C_p	(3.24)	$\varepsilon_r = 7.5$ $d = 4$ μm $t = 500$ nm $W = 10$ μm $L = 3$ mm^{œ}	difficult to make area independent from formula	0.92 pF	

$^\Delta$**For all calculations a temperature of 25°C is assumed. The electrolyte is assumed to be 0.9% NaCl (154 mMolar).**
†**Assumed for water at 25°C.**
‡ **This value is assumed. If $V_0 = 0$, then $C_G = 0.89pF/\mu m^2$ and it will dominate the interfacial capacitance. For larger values of V_0, the helmholtz capacitance will dominate C_I.**
†† **Platinum hydrogen reaction from Table 3.2.**
‡‡ **Average diffusion coefficient calculated assuming an ion mobility of 8×10^{-4} cm^2/Vsec and a voltage of 50mV.**
^{œ} **Fairly good estimate of trace length not covered by epoxy during the packaging process.**
$^\varphi$**Assuming a silicon substrate. C_s will be zero for the glass substrate chips.**
$^\kappa$ **Minimum interconnect spacing on the chip. This will therefore be a worst case analysis.**
$^\psi$ **Area independent value for the spreading resistance valid for circular geometry only.**

Table 4.1:   Theoretical electrode model parameters for the fabricated microelectrode arrays used in this research.

Model Parameter	Symbol	Defining equation	Dimensions and properties of interest$^\Delta$	Area independent value	Value w/ A=15μm^2	Value w/ A=480μm^2
Substrate capacitance	C_s	(3.24)	$\varepsilon_r = 3.9$ $d = 1\ \mu$m $t = 500$ nm $W = 10\ \mu$m $L = 4.5$ mm$^\varphi$ bondpad area=40k μm^2	difficult to make area indepen- dent from formula		3.54 pF
Coupling capacitance	C_c	(3.25)	$\varepsilon_r = 7.5$ $d = 4\ \mu$m $s = 10\ \mu$m$^\kappa$ $t = 500$ nm $W = 10\ \mu$m $L = 4.5$ mm	difficult to make area indepen- dent from formula		0.024 pF

$^\Delta$**For all calculations a temperature of 25°C is assumed. The electrolyte is assumed to be 0.9% NaCl (154 mMolar).**

†**Assumed for water at 25°C.**

‡ **This value is assumed. If $V_0 = 0$, then $C_G = 0.89$pF/μm^2 and it will dominate the interfacial capacitance. For larger values of V_0, the helmholtz capacitance will dominate C_I.**

†† **Platinum hydrogen reaction from Table 3.2.**

‡‡ **Average diffusion coefficient calculated assuming an ion mobility of 8x10^{-4} cm^2/Vsec and a voltage of 50mV.**

^{œ} **Fairly good estimate of trace length not covered by epoxy during the packaging process.**

$^{\varphi}$**Assuming a silicon substrate. C_s will be zero for the glass substrate chips.**

$^\kappa$ **Minimum interconnect spacing on the chip. This will therefore be a worst case analysis.**

$^\psi$ **Area independent value for the spreading resistance valid for circular geometry only.**

Table 4.1 (continued): Theoretical electrode model parameters for the fabricated microelectrode arrays used in this research.

4.3 Fabrication Process
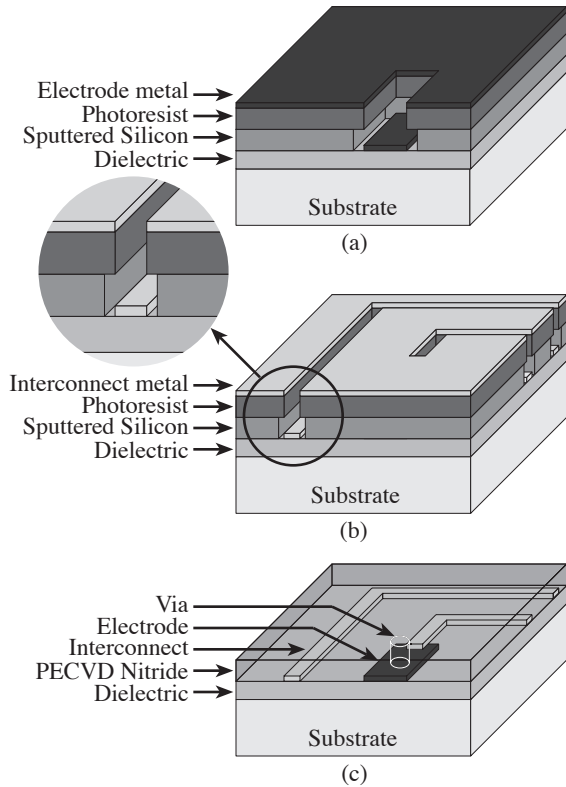
Figure 4.5: Electrode array fabrication procedure (not to scale). (a) Over an insulating SiO$_2$ layer, a bilayer lift-off structure consisting of sputtered silicon and photoresist was used for electrode metal definition. (b) The same lift-off method was used for definition of gold interconnects and bondpads. (c) A PECVD silicon nitride film was deposited and patterned to define the electrode and bondpad regions. Wafer dicing, followed by chip cleaning and packaging, complete the fabrication procedure.

The basic fabrication process is shown in Figure 4.5. It is described for both the silicon and glass substrate cases with differences noted where appropriate. A (100) p-type silicon wafer was thermally oxidized to provide an insulating 500 nm SiO$_2$ layer (this step is deleted for glass substrates). BOROFLOAT™ borosilicate float glass (US Precision Glass, Santa Rosa, California) was used as the substrate for the microelectrodes fabricated on glass. The material was 100 mm in diameter and 800 μm thick with beveled edges and a 60/40 polished surface. A major flat was cut into the wafer (using a silicon wafer as a template) to allow integrated circuit fabrication equipment equipped with automated flat finders to process the glass wafers. Additionally, the backside was coated with 50 nm of evaporated Cr to allow use in the automated wafer handling equipment. From this point, both silicon and glass substrates were processed in the same manner.

Platinum, iridium or gold electrodes were patterned using a bilayer lift-off structure consisting of sputter deposited silicon (500 nm) and Shipley 1813 photoresist (1 μm). The resist was patterned using standard photolithographic techniques and an isotropic silicon plasma etch (CF$_4$ / O$_2$) was used to undercut the sputtered silicon underlayer. A 250 nm layer of platinum, iridium or gold was then sputter deposited using chrome (25 nm) as an adhesion layer, resulting in a Cr / electrode metal bilayer on the exposed SiO$_2$ surfaces and on top of the photoresist. The photoresist was then removed

using a 4:1 mixture of H_2SO_4 (96%) and H_2O_2 (30%), thereby removing the unwanted chrome and electrode metal. The remaining sputtered silicon was then plasma stripped (C_2ClF_5 / SF_6) to leave the desired electrode film on the substrate.

The above lift-off method was repeated for patterning of the gold interconnects and bondpads. Au (500 nm) was evaporated on the structure, again using Cr (25 nm) as an adhesion layer. Acetone was used to dissolve the photoresist and thereby remove the Cr / Au not adhering to the substrate. Once again, the sputtered silicon was plasma stripped to leave the desired gold pattern.

The interconnects and electrodes were passivated with 4 μm of plasma enhanced chemical vapor deposited (PECVD) silicon nitride. This process was done at low temperature (300°C) to both limit gold roughening and to allow for potential circuit integration beneath the electrode array if desired. Dual-frequency rf excitation of the plasma (13.5 MHz and 187 kHz) was utilized to allow low stress films (typically < 50 MPa tensile) to be deposited. Typical deposition parameters were 650 mTorr of pressure, 10 sccm NH_3 and 2000 sccm of 2% SiH_4 in N_2. Following nitride deposition, vias were etched through the film using a plasma etch (C_2ClF_5 / SF_6) to define the electrode geometries and open the bondpads. The wafer was then diced and cleaned.

4.4   Packaging and Handling Protocols

The substrate upon which the cells are cultured must be contained within a package to house the cell culture media and maintain sterility. The historical examples of planar microelectrode arrays for cultured cell studies described in Chapter 1 all utilized some type of glass or plastic ring attached to the substrate to form the cell culture chamber. Electrical connections were made by a pressure connection to large bondpads on the substrate. While this packaging technology does contain the culture media and maintain sterility, the ease with which the chip may be inserted into the measurement electronics is moderate to poor since careful alignment is required and connections are made from the top surface.

An alternative packaging technique employed in this work utilized a standard DIP within which the cell culture substrate was attached. Bondwire connections were made between the chip and the package and encapsulated in a non-toxic epoxy. The actual cell culture housing was made by attaching a standard polystyrene cell culture dish (with a hole drilled in the center) to the packaged substrate using the same non-toxic epoxy. The finished cell culture chamber allowed for culture of cells in a sterile environment. The

cells could be maintained in a standard incubator until needed for experiments, at which point the DIP was connected to the electronics using a zero insertion force (ZIF) socket.

4.4.1 Chip Preparation, Placement and Wire Bonding

Following fabrication of the chips as outlined in Section 4.3, the individual dice were cleaned as follows. Photoresist used as a protective layer for dicing the chips was removed with room temperature acetone (2 minutes) followed by isopropyl alcohol (IPA) at 60°C for 2 minutes. The chips were rinsed well in deionized (DI) water for several minutes and then placed in a 4:1 solution of H_2SO_4 (96%) and H_2O_2 (30%) for 2 minutes. This effectively removed any organic residue from the photoresist. Following this cleaning procedure, the chips were again rinsed for 5 minutes in DI water and then in IPA at 60°C for 2 minutes. The latter facilitated drying of the chips which was important to limit residue due to absorption of debris into any liquid left on the surface. The chips were placed into a 90°C oven for 30 minutes to complete the cleaning procedure.

At this point the chip was bonded into a 40 pin ceramic DIP (KD-78302-C from Kyocera America, Inc., San Jose, CA). A small drop of two-part, 5 minute epoxy (MasterMend®, Locktite Corp., Rocky Hill, CT) was placed in the center of the 0.40 inch package cavity and a chip was manually aligned and pressed into place using a gloved finger. Care was taken to ensure excess epoxy did not spill over onto the bondpads located on the package and the chip. The packaged chip was placed in a 70°C oven for one hour to ensure adequate curing of the epoxy.

Electrical connections between the chip and the package were made at 150°C using a universal wedge bonder with the bonding parameters adjusted to provide classic ball and stitch bonds to the chip and package bondpads respectively. The resulting packaged chip is shown in Figure 4.6. Details on wire bonding locations between the chip and the package may be found in Appendix A.

4.4.2 bondwire Encapsulation and Chamber Attachment

The cell culture chamber consists of a 35 mm diameter polystyrene cell culture dish (with an 8 mm hole drilled in the center of the bottom) attached over the packaged electrode array. Following drilling of the hole, excess plastic was removed manually with a razor and the petri dish was cleaned using 70% ethanol and dried in a 70°C oven for 30 minutes. At this point it was ready for attachment to the packaged electrode array.
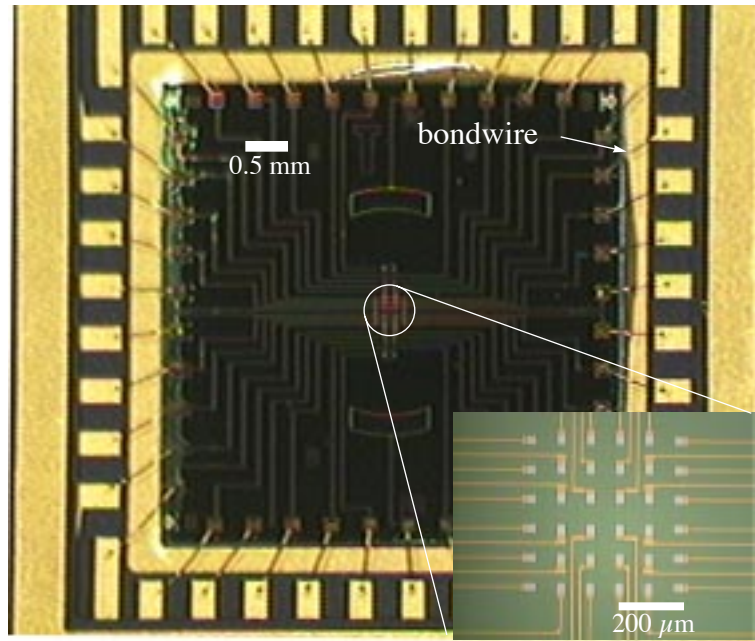
Figure 4.6: Photograph of a packaged microelectrode array without bondwire encapsulation. bondwire connections are easily seen between the chip and the package. The inset shows the 6 × 6 element electrode array.

Two different epoxies have been used for bondwire encapsulation and chamber attachment: Epo-Tek 87-GT (Epoxy Technology, Inc., Billerica, MA) and Master Bond SUPREME 42HT/T (Master Bond Inc., Hackensack, NJ). The Epo-Tek 87-GT is a two component epoxy designed for encapsulation of bondwires for integrated circuit chips. It has a high volume resistivity, relatively low dielectric constant, low viscosity, low elastic modulus (making it a low stress encapsulant), and contains no solvents. The latter is particularly important for this application since it is often difficult to fully remove solvents from an epoxy upon curing. This remaining solvent can leach into the cell culture system and have a detrimental effect on the cells.

Master Bond SUPREME 42HT/T is also a two component epoxy containing no solvents. It was designed for the medical devices industry and withstands radiation, steam, and ethylene oxide (ETO) sterilization procedures. The epoxy also has a high resistivity, low elastic modulus, low dielectric constant, low viscosity, and absorbs little moisture. Additionally, it is more resistant to harsh chemicals (acids, bases, and solvents) than the Epo-Tek 87-GT, and withstands ultrasonic vibrations at 40 kHz. The latter is important for the platinization procedure to be discussed in the next section.
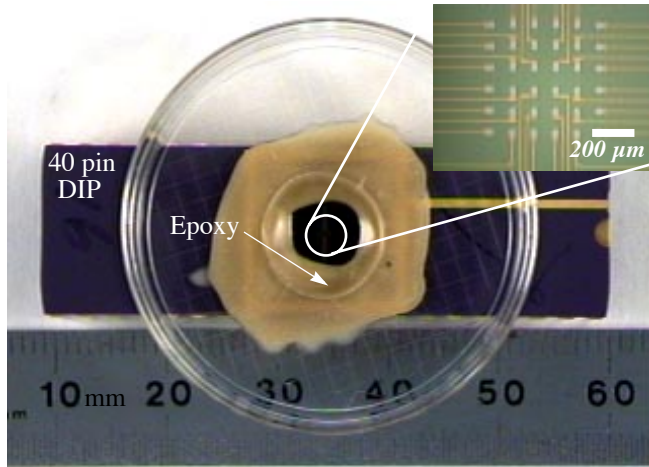
Figure 4.7: Photograph of a microelectrode array packaged in a ceramic 40 pin DIP. bondwires are encapsulated in epoxy and a 35 mm polystyrene cell culture dish (with hole drilled in the center) is attached to the top. Inset shows a close-up of the 6×6 element electrode array.

Both epoxies were manually mixed and applied over the bondwires using a 19 gauge, blunt tipped syringe. Care was taken to limit encroachment of the epoxy onto the microelectrode recording sites and reference electrodes. A thin ring of epoxy was also applied to the bottom of the cell culture dish around the 8 mm hole. The dish was then manually aligned over the array and pressed into place using a twisting motion to ensure uniform spreading of the epoxy for a good seal. The fully assembled chips were then placed in a 70°C oven for 3-8 hours to fully cure the epoxy, resulting in the cell culture chamber shown in Figure 4.7. At this point the chips encapsulated with Master Bond SUPREME 42HT/T were ready for platinization of the electrodes, but the Epo-Tek 87-GT chips required further processing. This epoxy was less viscous than the other and tended to leach small amounts of epoxy out onto the active area of the electrode array. This was removed by exposure to an oxygen plasma (O_2=200 standard cubic cm (sccm), pressure=3 Torr, power = 370 mW/cm^2) for 20 to 40 minutes in a parallel plate plasma etcher. Any oxidized residue was removed by rinsing in deionized (DI) water for several minutes followed by forced air drying of the surface and baking at 70°C for 1 hour. At this point these chips were ready for platinization.

Several other possible encapsulation materials were investigated as well, but they suffered from numerous difficulties. EP30HT and EP42HT/T (Master Bond Inc., Hackensack, NJ) were both two component epoxies tested for use with cultured cells. The EP30HT suffered from significant water absorption, making it a poor choice for bondwire encapsulation. EP42HT/T performed similarly to SUPREME42HT/T, but was slightly less viscous, making application without encroachment on the electrode arrays difficult. The final material tested was polyethylene. This biocompatible thermal plastic is extremely chemically robust, allowing cleaning with harsh oxidizers such as piranha (4:1 mixture of H_2SO_4 and H_2O_2). Additionally, it easily melts over the bondwires and forms a strong

adhesive bond to the silicon nitride of the microelectrode array chip. Rapid thermal cycling from room temperature to liquid nitrogen temperatures resulted in no cracking or breakage of bondwires in the brief tests performed. Thus, this material was a promising candidate for bondwire encapsulation. However, practical use required the simultaneous creation of a cell culture housing (much like the 33 mm polystyrene petri dish) since the temperatures required to melt the polyethylene (125°C) were above the melting temperature of polystyrene. Thus, injection molding of the polyethylene directly over the packaged array was required which was beyond the capabilities of the Stanford laboratory. Therefore, the epoxies described above were used for bondwire encapsulation for the chips used herein.

4.4.3 Platinization Procedure

For the applications described herein, low impedance electrodes were desirable, as described in Chapter 3. The easiest method of obtaining lower electrode impedance regardless of electrode material was by electrodeposition of platinum black. The electroplating solution utilized consisted of 100 ml H_2O, one gram of lead acetate ($PtCl_6H_2$) and 0.01 gram of chloroplatinic acid ($Pb(C_2H_3O_2)_2$) [Gesteland, 1959]. Five
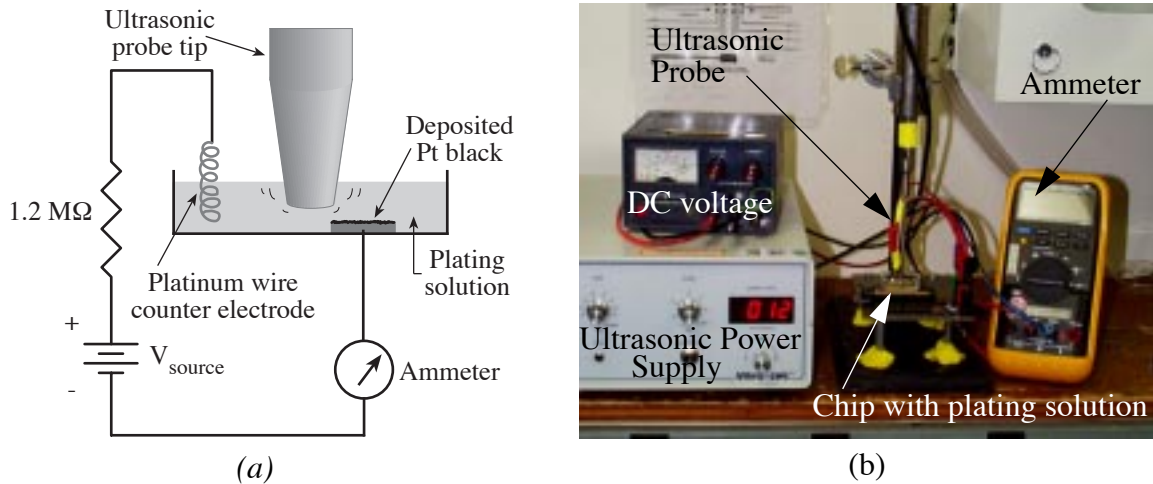
Figure 4.8:   Electroplating setup for deposition of platinum black. (a) Schematic diagram of setup showing DC voltage source, 1.2MΩ current limiting resistor, coiled platinum wire immersed in the solution to act as a counterelectrode, 1/8 inch ultrasonic probe tip (40 kHz), and ammeter for monitoring the electrodeposition current. (b) Actual setup used for Pt black deposition. The packaged electrode array was placed in a 40 pin ZIF socket and electrical connections to the electrodes to be platinized were made via manual jumpers. Multiple electrodes (including reference electrodes) could be platinized simultaneously.

milliliters of this solution was placed in the cell culture chamber (electrode array, 40 pin DIP and 35 mm petri dish), which was connected to manual jumpers through a ZIF socket. The jumpers allowed for any or all of the electrode sites to be placed in the current path used for electrodeposition. As shown in Figure 4.8, a voltage supply (approximately 25 to 30 volts) drove a 1.2 MΩ resistor in series with the electrodes, solution and counter electrode to supply a constant, DC current of 5 nA/μm^2. This was monitored using an ammeter and the voltage was manually adjusted to provide this current density. To ensure uniform electroplating and adhesion of the platinum, ultrasonic agitation was used [Marrese, 1986]. An ultrasonic transducer probe (1/8 inch diameter) operating at 40 kHz was immersed approximately 3 mm into the electroplating solution. It is important to note that the ultrasonic probe power supply was connected to line power through an isolation transformer. This was required since the probe was electrically connected to ground which prevented deposition of platinum black on the electrodes. The ultrasonic power was increased from zero until *cavitation* (formation and collapse of minute bubbles of vapor in liquids) was observed, and then reduced as much as possible while still maintaining cavitation. This resulted in an output power of approximately 13 watts which was sufficient to remove any loosely adhering deposits. Higher power levels often resulted in stress fractures appearing in the silicon nitride passivation layer and were therefore avoided. For all electrodes described herein, electrodeposition was performed by first applying ultrasonic energy to clean the surface for 15 seconds, followed by continued ultrasonic and a constant DC current for 45 seconds. This was found to provide adequate impedance reduction (approximately 1-2 orders of magnitude) without significantly increasing the height of the electrode above the passivation layer.

4.4.4 Cell Culture Chamber Cleaning, Sterilization and Storage

The cell culture chambers were cleaned (both immediately after platinization and following cell culture) by rinsing well with DI water and then placing several ml of 5% detergent in the chamber. The detergent used (Contrad 70, Decon Labs, Inc., PA) was a phosphate free, chlorine free, biodegradable formulation specifically designed for cleaning glassware used in the laboratory. It effectively removed dried proteins and rinsed completely from the chip surface. The 5% solution was recommended by the manufacturer for cleaning tissue culture plates. Significantly higher concentrations of detergent attacked all the epoxies tested. The detergent was allowed to sit for 12 to 24 hours to fully remove any biological materials on the electrode array surface.

Following treatment with detergent, the chips were rinsed for several hours under a continuous flow of DI water to ensure full removal of the detergent (which would be detrimental to cell growth). Impedance characteristics were measured at this point (in 0.9% NaCl solution) and the chips were briefly rinsed again in DI water.

Chips to be stored for extended periods were rinsed well with 70% ethanol, briefly dried with forced air, and then baked dry at 70°C for 1 to 2 hours. They were stored in clean 150 mm petri dishes. The chips were stored dry to limit the possibility of contamination; bacteria, molds and fungus require aqueous (or at least moist) environments to proliferate and survive.

Chips that were to be used for cell culture were sterilized by soaking in 70% ethanol for 10 minutes within a sterile biosafety cabinet. It is important to note that this procedure did not effectively sterilize chips where contamination had already occurred; these chips were discarded since the chamber material (polystyrene) did not withstand autoclaving. Following the ethanol soak, the chips were rinsed 3 times with sterile distilled water and one time with cell culture media using aseptic techniques. The chambers were filled with 2 ml of culture media and transferred to an incubator for at least 30 minutes prior to culturing cells on the surface.

4.5 Testing

Routine testing of the fully fabricated and packaged electrode arrays consisted of electrode impedance measurements both before and after platinization. These values were compared to those theoretically expected from the electrode model parameters outlined in Table 4.1 using increased area estimates for the platinized electrodes in conjunction with the area independent values. The results of these tests will be described in detail.

The long term characteristics of the epoxies used were also tested under cell culture conditions. Chips were allowed to soak in 0.9% NaCl at 37°C for up to 3 months, and the electrode impedance characteristics were periodically monitored. Changes in the epoxy encapsulation properties due to poor adhesion or adsorption of moisture were expected to manifest themselves in changes in the measured electrode impedance characteristics. These results will be outlined below.

4.5.1 Electrode impedance

Electrode impedances were measured using a system to be described in detail in Chapter 5. A sinusoidal voltage of approximately 100 mV pk-pk was applied to one electrode at a time. A coiled Pt wire (approximate surface area = 40×10^6 μm^2) was immersed in the 0.9% NaCl solution and held at virtual ground by a transimpedance stage. The resulting current was monitored to provide the real and imaginary parts of the overall impedance of the system. The impedance of the Pt wire was negligibly small (see Appendix B), making the measured impedance representative of the smaller electrode.

The impedance data shown in Figure 4.9 is for three chips with 6 electrodes of each size. The chips were packaged using SUPREME42HT/T and cleaned following the standard procedure outlined in Section 4.4.4, with the addition of a 15 second ultrasonic clean (as described in Section 4.4.3) in DI water to ensure clean surfaces following epoxy curing. Note the 15 μm^2 electrodes exhibited significant variation in the phase, most likely due to non-linear behavior. This will be explored in more detail below.
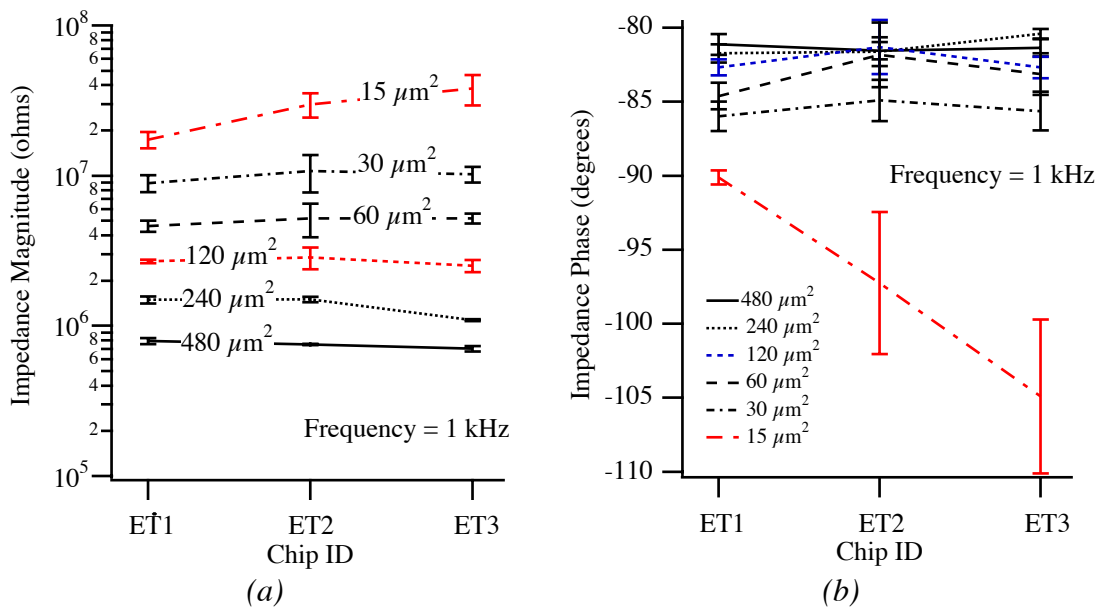
Figure 4.9: Measured electrode impedance magnitude (a) and phase (b) for three chips (ET1, ET2, and ET3) with six electrodes of each size. Bare platinum electrodes of varying sizes were measured with respect to a large Pt counter electrode in 0.9% NaCl. The electrodes were cleaned with ultrasonic prior to impedance measurements. Error bars represent one sigma. All data were taken at 1 kHz. The phase data for the 15 μm^2 electrode indicates non-linear behavior, making its accuracy suspect.

This data was compiled to provide average magnitude and phase data for all 18 electrodes of each size (3 chips, each with 6 electrodes of each size) as shown in Figure 4.10. A comparison of Figure 4.9 and Figure 4.10 shows that the intra chip variations were on the same order as the inter chip impedance variations. Thus, the packaging techniques most likely did not adversely affect the electrode impedances. Note the near linear relationship between electrode area and impedance, and the relatively small change observed in phase. The deviation from linearity (and increased phase) at the smallest electrode size may have been due to electric field concentrations at the edges causing the current density to be in excess of that allowed for linear behavior. Without platinization (which both increases the area and distributes the electric field) the electrode could not support the current density resulting from the 100 mV pk-pk drive signal and maintain linearity. This can be easily seen by looking at the impedance versus frequency as shown in Figure 4.11. Note the phase is larger than -90° at low frequencies (< 1 kHz) for all electrode sizes, with the deviation increasing for decreasing electrode area (as the perimeter to area ratio (equal to 2/r) increased). The exact nature of this phenomena was
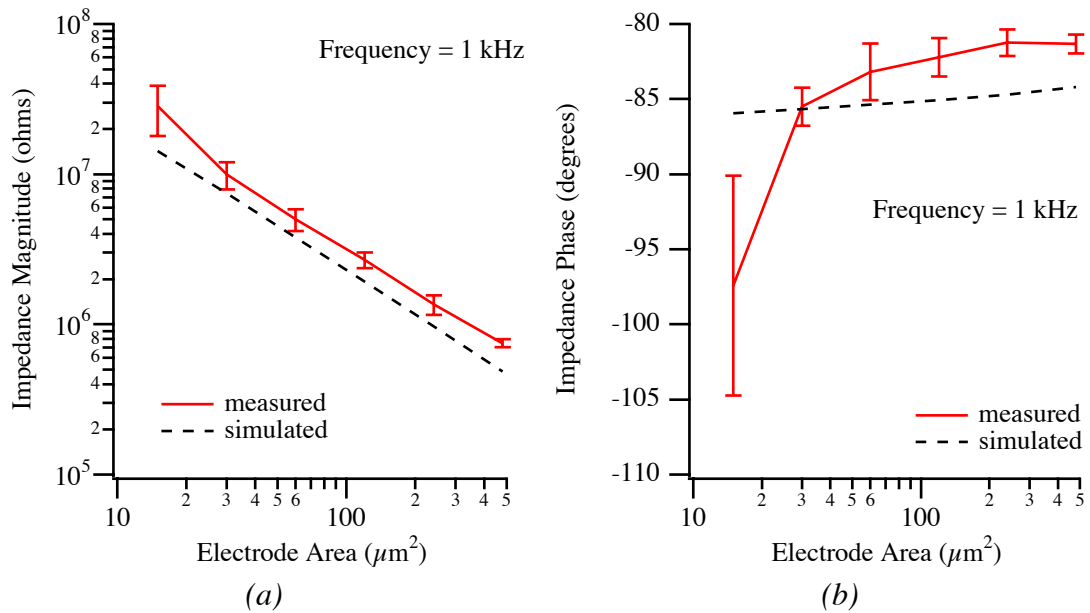
Figure 4.10: *Measured and simulated electrode impedance magnitude (a) and phase (b). Bare platinum electrodes of varying sizes were measured with respect to a large Pt counter electrode in 0.9% NaCl. The data shown are the average of 18 electrodes of each size (6 electrodes from each of 3 chips). Error bars represent one sigma. All data were taken at 1 kHz. This is a compilation of the data presented in Figure 4.9. The non-linearity in magnitude was probably due to excessive current densities in the smallest electrodes. Simulated results utilized the electrode component values outlined in Table 4.1.*

not examined in detail since platinized electrodes were used for all experiments. However, the existence of non-linear electrode behavior was verified as outlined below.

Comparison of the measured electrode impedances to those theoretically determined (Table 4.1) was accomplished by simulating the electrode model using the circuit simulator HSPICE. This was done for the all six electrode sizes, and the resulting impedance magnitude and phase versus electrode area was added to the plot of Figure 4.10 for the case of 1 kHz. Note the close correlation to the measured data. The spectral characteristics were examined in the range of 100 Hz to 100 kHz for both the measured and simulated data as shown in Figure 4.11 and Figure 4.12.

There was close correlation between measured and simulated results for frequencies above 1 kHz. Below this frequency, the simulated data indicates charge transfer process contribute significantly to the total current (since the impedance is becoming less capacitive). Thus, it is at this point that non-linearities due to currents in excess of the exchange current density would be expected. As described previously, this was observed experimentally (Figure 4.11(b)) for the case of unplatinized electrodes.
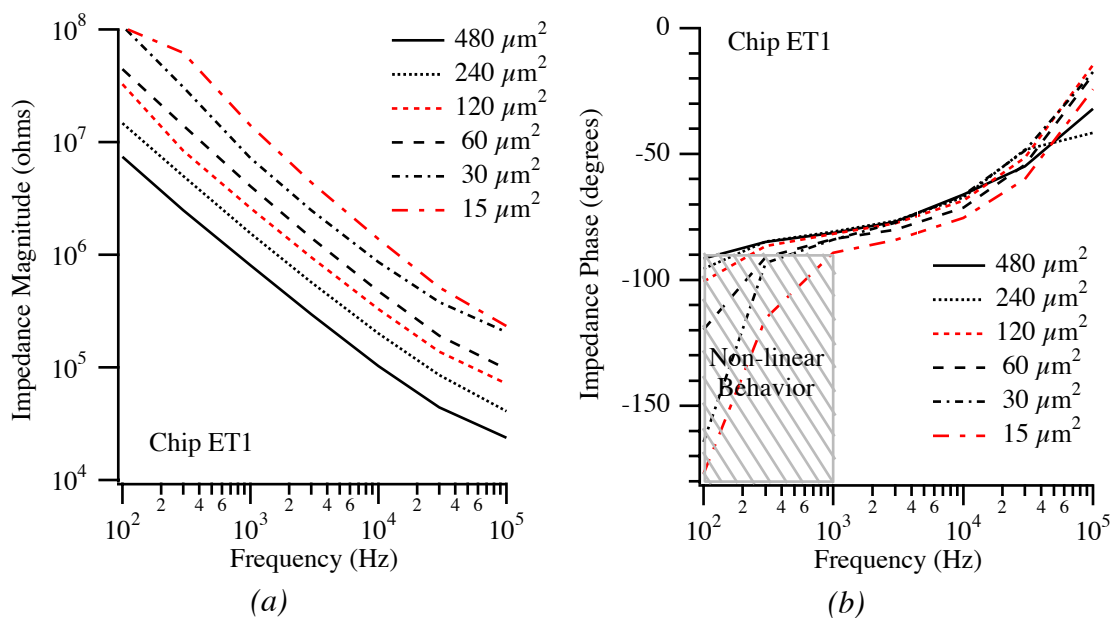
Figure 4.11: Measured impedance magnitude (a) and phase (b) for 6 different bare Pt electrodes on chip ET1. Note that around 1 kHz the phase began to drop off significantly for the smallest electrode. This was the most likely the onset of non-linearity due to excessive current density. The impedance values above 1kHz should be approximately correct for all electrode sizes.

To verify that the large phases (more negative than -90°) shown in Figure 4.11 were indeed due to non-linear behavior of the electrodes, the total harmonic distortion (THD) induced by the electrode was measured for each size electrode over the entire frequency range. The amplified output of the transimpedance stage was buffered and monitored using a FFT spectrum analyzer (SRS model SR760). The THD was recorded and plotted in Figure 4.13 for both platinized and bare Pt electrodes. Note the significant distortion for the smallest size electrodes at low frequency. This corresponds well with the deviations from normal behavior exhibited in Figure 4.11. Only data for 100 Hz was taken for the platinized case since no significant distortion was observed. Higher frequencies exhibited THD on the same order as that shown for 100 Hz.

Overall, excellent agreement was observed between theoretical and actual electrode impedances. Variations in measured impedances were small both on a single chip and chip to chip. Non-linearities were observed at low frequencies, presumably due to excessive current densities flowing through the electrodes, with the onset of non-linearity agreeing with simulated results and measured harmonic distortion.

(a)   *(b)*
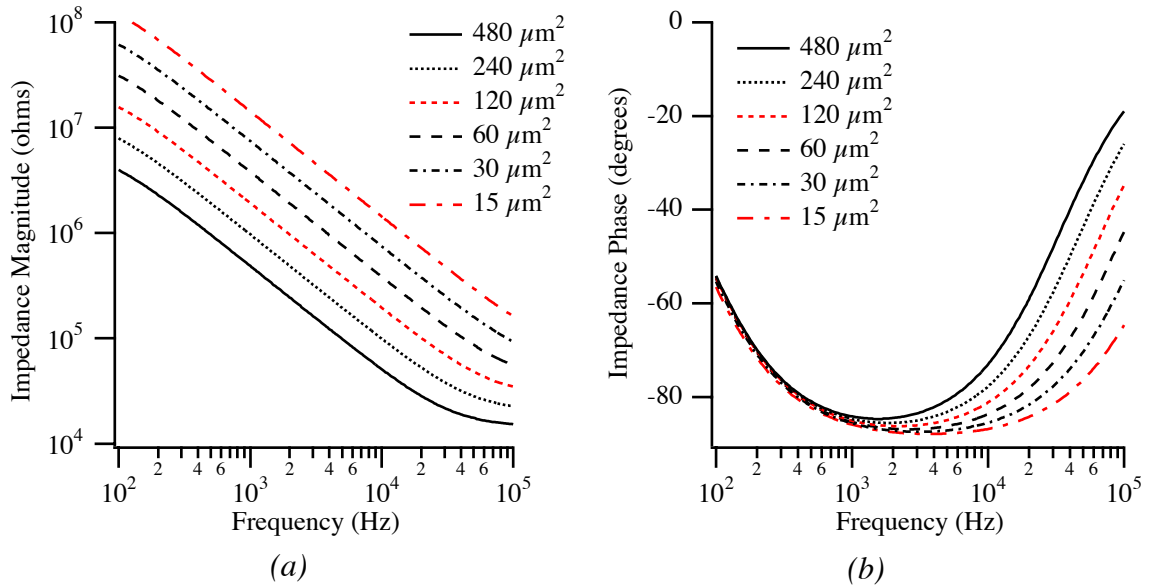
Figure 4.12: Simulated impedance magnitude (a) and phase (b) for 6 different electrode sizes. Note that at around 1 kHz the impedance begins become less capacitive. This indicates that charge transfer is becoming more important in the current flow. Thus, non-linear behavior should be noticed at this point as was observed in Figure 4.11. Note: the decreasing phase at low frequencies is a result of the exchange current density used. For lower exchange current densities, (6-8× lower) the charge transfer resistance becomes larger and the impedance appears capacitive between 100 Hz and 1 kHz (data not shown).
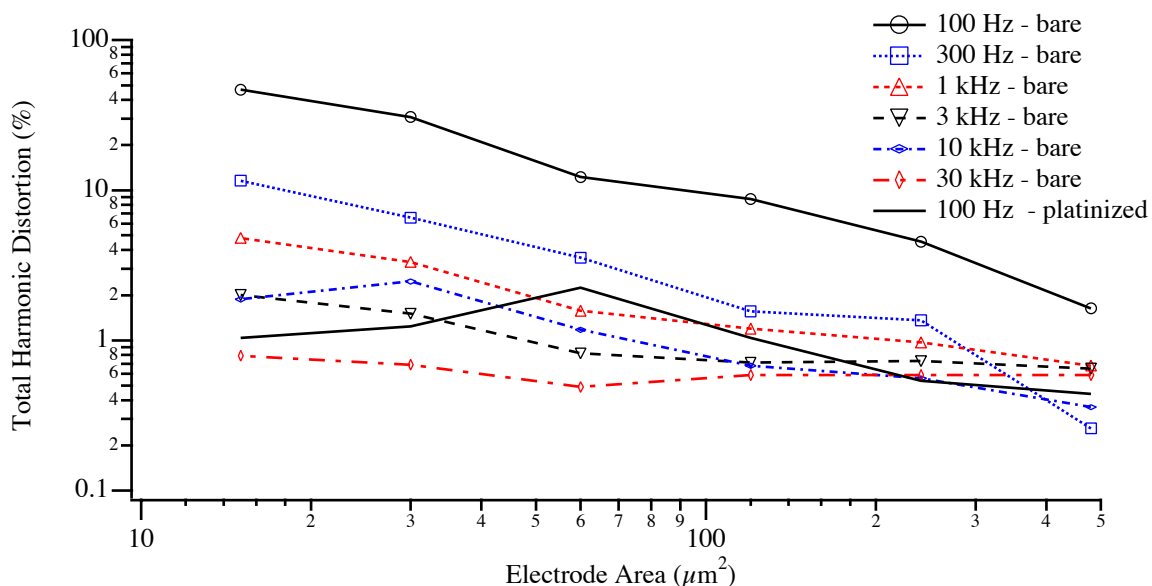
Figure 4.13: Total harmonic distortion (THD) due to normal drive (100 mV pk-pk) of the electrodes. Data has been adjusted to subtract out distortion due to the signal source. Note the significant THD present at low frequencies for the smallest electrode sizes. Platinization of the electrodes significantly reduces this effect.

4.5.2 Platinum Black Deposits

Platinum black deposited as described in Section 4.4.3 on bare Ir electrodes both with and without ultrasonic agitation resulted in deposits as shown in Figure 4.14. Note the significant reduction in dendritic growth as a result of the ultrasonic energy removing those fragile or loosely adhered deposits. The deposition performed without ultrasonic was significantly larger than shown in the SEM immediately following electroplating. However, gentle rinsing with water removed the majority of the platinum black leaving the deposit shown in Figure 4.14(a). While little of the original deposit remained, the dendritic nature of DC electrodeposition without ultrasonic agitation was clearly shown.

Electrodeposition of Pt black with ultrasonic agitation was performed on the chip (ET1) used for the impedance measurements shown in Figure 4.11. The impedance characteristics of the platinized electrodes were measured (Figure 4.15) and compared to the bare chip data. Simulations using an area value ten times that of the electrode (for all electrode elements except the spreading resistance which used the geometric area) yielded impedance plots similar to those shown in Figure 4.15 (simulation data not shown). To highlight the reduced impedance obtained by deposition of platinum black on the electrodes, the ratio of the bare Pt electrode impedance magnitude to that of platinized Pt

102

(a) *(b)*
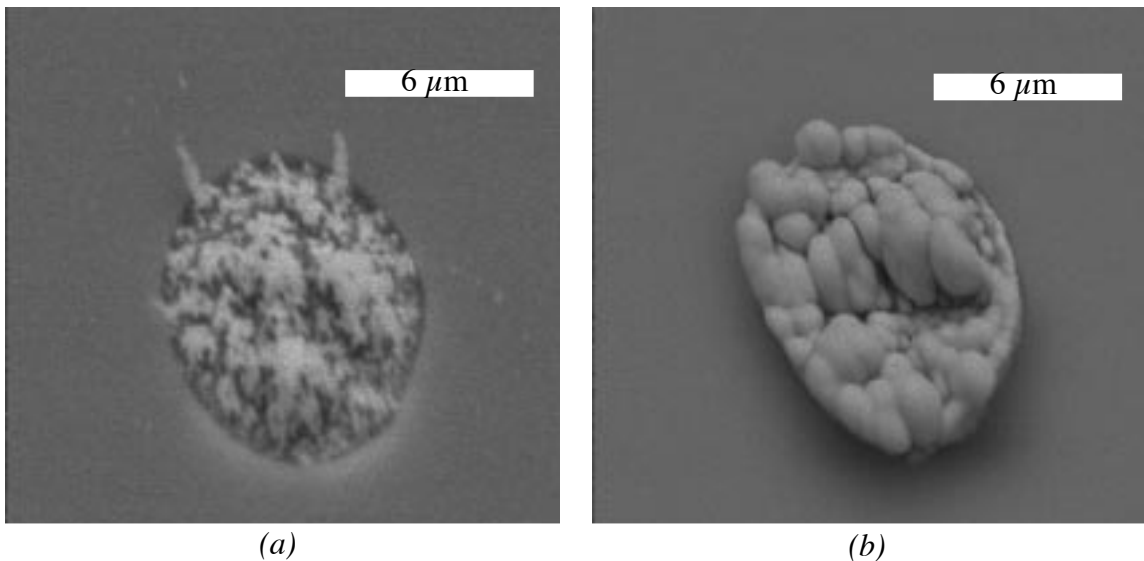
Figure 4.14: Scanning electron micrographs of platinized electrodes without (a) and with (b) ultrasonic agitation. The slight skew evident (electrodes are circular) is due to charging of the polystyrene petri dish altering the image. Both electrodes were 10 µm diameter iridium with 1 µm of silicon nitride passivation. Electrodeposition was performed as outlined in Section 4.4.3. The dendritic growth in (a) was actually 2 to 3 times the size of the electrode immediately after electrodeposition. However, the majority of the deposit was removed during gentle rinsing of the array. This highlights the delicate and fragile nature of electroplated platinum black without ultrasonic agitation. The deposit in (b) was significantly more dense and robust. Note that with 4 µm of silicon nitride the deposit in (b) would not have protruded beyond the passivation.

electrodes was taken and plotted in Figure 4.16. Values below 1 kHz were not plotted due to the non-linear behavior of the bare electrodes in this regime. Note that most electrodes exhibited a factor of 10 reduction in impedance magnitude at 1 kHz. The impedance reduction was not as pronounced at high frequencies where the spreading resistance begins to dominate the measurement. This was expected since the spreading resistance scales with geometric area rather than surface area (which is increased by deposition of platinum black).

The amount of impedance reduction obtained was variable and depended on the time of the deposition, the ultrasonic power achieved, and the physical location of the ultrasonic probe tip. Since both the power and probe location were adjusted manually for each chip, large deviations were likely. In practice, impedance reductions between one and two orders of magnitude were obtained.

It is possible to obtain uniform electrode impedances by electrodeposition of platinum black if the electrode impedance is monitored during deposition. This could be done using
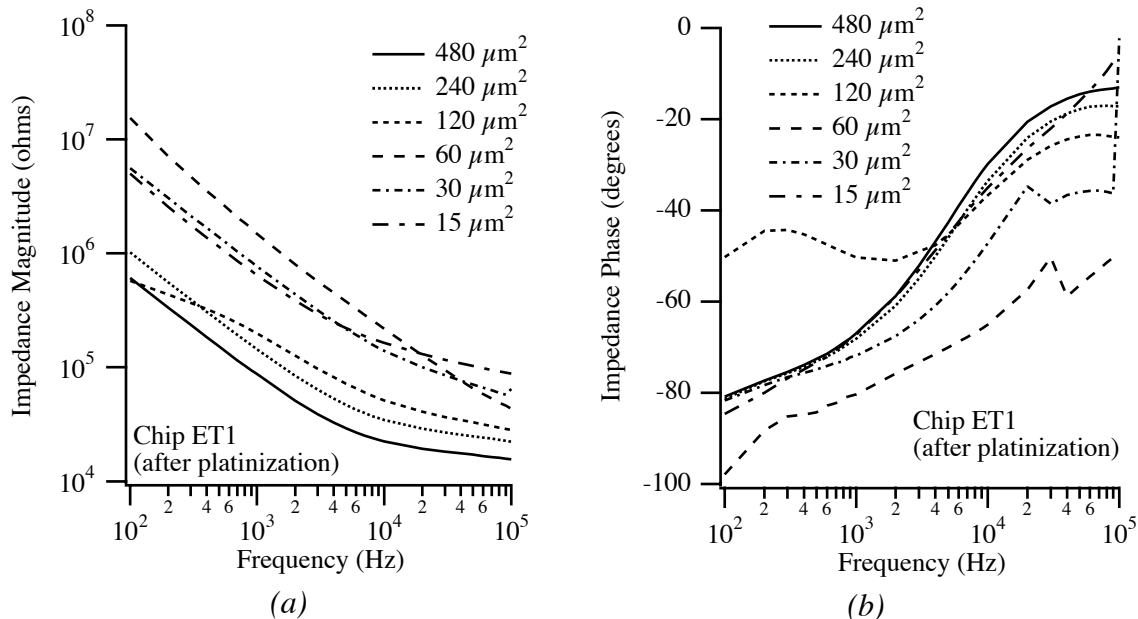
Figure 4.15: Measured impedance magnitude (a) and phase (b) for 6 different electrodes on chip ET1 following deposition of platinum black. A comparison to Figure 4.11 shows the impedance magnitude decreased by approximately one order of magnitude for this chip. The non-linear behavior at low frequencies has also been significantly diminished.
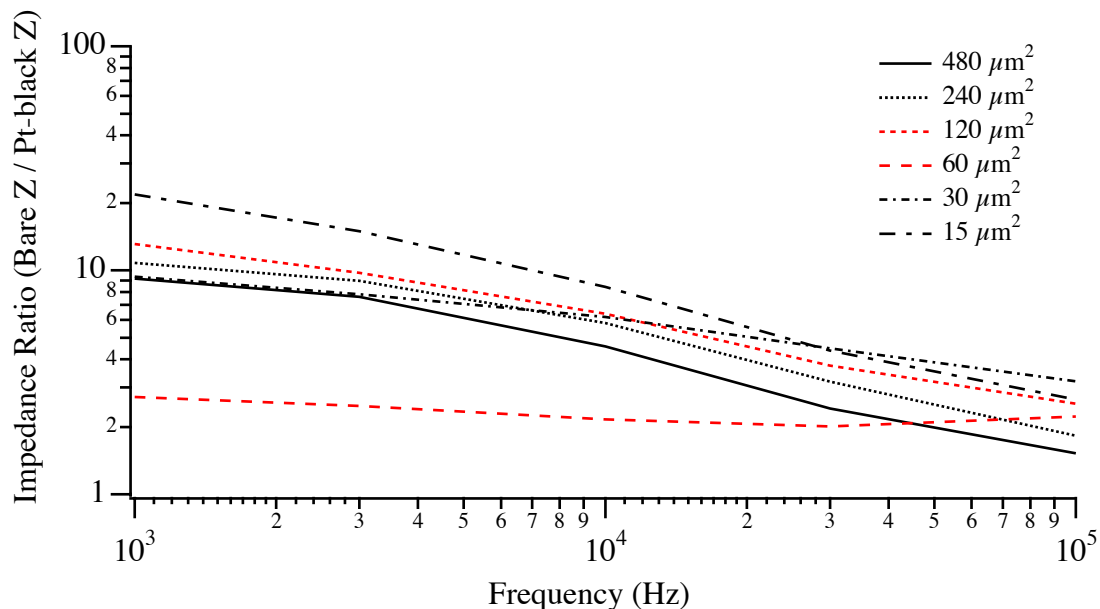
Figure 4.16: Ratio of the bare Pt electrode impedance magnitude to that of the platinized Pt electrodes for chip ET1 (extracted from the data of Figure 4.11 and Figure 4.15). Data below 1 kHz not shown since bare electrodes exhibited non-linear behavior in this regime.

a closed-loop system such that deposition occurred until a standard impedance was obtained at a given frequency. Such a system has been described by [Robinson, 1968], where a small AC signal was superimposed on the DC electroplating voltage, and an AC coupled amplifier was used to monitor the impedance. While this system was manually controlled, an automated configuration for platinization of an array of electrodes could be easily implemented.

4.5.3 Electrode Noise

As described in Chapter 3, electrode noise has been empirically shown to be thermal in nature and exhibit a white spectral characteristic. The magnitude of the noise is proportional to the square root of the real portion of the electrode impedance. Electrode noise was measured using the test configuration shown in Figure 4.17. The microelectrode array was immersed in solution and a single electrode was connected to the input of a non-inverting amplifier stage. The output of this low input leakage (< 25 fA) amplifier was fed directly into a FFT spectrum analyzer which measured the rms noise voltage per root frequency. Measurements were performed by first grounding the input to the amplifier and

Figure 4.17: Electrode noise measurement setup.

measuring the inherent electronic noise. The power of this noise voltage was then subtracted from all subsequent measurements on microelectrodes. Measurements were recorded at 1 kHz (linewidth = 15.63 Hz, acquisition time = 64 msec, averaged 500 times) for several electrodes on two different chips, one bare Pt and the other platinized. The input referred results were plotted against the real part of the electrode impedance (measured immediately following noise measurements) in Figure 4.18 along with the theoretical Johnson noise at 25°C. Note the excellent agreement between the measured results and the calculated thermal noise as predicted in Chapter 3.

The noise generated by a metal microelectrode in a conductive solution appears to be thermal in nature for both platinized and bare Pt electrodes. All noise measurements were below $100 \mathrm{nV_{rms}} / \sqrt{\mathrm{Hz}}$ (at 1 kHz) which would translate into $10 \ \mu \mathrm{V_{rms}}$ across a 10 kHz bandwidth. This is reasonable for measurement of action potentials. For the case of

Figure 4.18: Measured microelectrode noise versus the measured real impedance for several platinized and bare Pt electrodes at 1 kHz. Note the excellent agreement to the theoretical Johnson noise calculated for resistance values at 25°C.

impedance, since heterodyning techniques were utilized this type of thermal noise would generally not be a problem.

4.5.4 Epoxy Encapsulation Testing

Testing the effectiveness of epoxy in electrically insulating the bondwires and bondpads was difficult. As shown in Figure 4.19, there are three different parasitic paths which can result from immersion of the array in a conductive solution, only two of which are dependent on the epoxy. Z_{leak1} represents a parasitic impedance due to the absorption of moisture and ions by the epoxy. Initially, the epoxy represents a very small capacitance between the bondwires and bondpads and the electrolyte. As electrolyte is absorbed in the epoxy, the capacitance increases (due to the decreasing effective dielectric spacing) and is placed in series with the resistance of the saturated epoxy. In the extreme, this parasitic would become purely resistive as the absorbed solution contacted the bondwires or bondpads. A similar situation exists for the seal between the epoxy and the passivation layer (represented by Z_{leak2}). As electrolyte invades this space, the same capacitive / resistive behavior described for Z_{leak1} should be observed. The final region of concern is the passivation itself. While silicon nitride is often assumed to be an excellent ion barrier, different deposition processes and conditions can result in widely variant film characteristics. If the passivation layer is permeable to ions, then precisely the same

situation described for Z_{leak1} would be expected for regions of the passivation exposed to the electrolyte, with contact being made to the interconnect metals rather than the bondwires and bondpads.

The combined effects of Z_{leak1}, Z_{leak2}, and Z_{leak3} on the overall impedance can be deduced by measuring the electrode impedance immediately following packaging (before these parasitic paths become an issue) and then subsequently monitoring the impedance over time as the packaged array is allowed to sit in solution. This was done for two chips (platinum electrodes fabricated on glass substrates with 4 μm of silicon nitride passivation), one using Epo-Tek 87GT encapsulation and the other using SUPREME 42HT/T. Electrode impedances were measured in 0.9% NaCl and monitored over a period of three months where the chips were stored in an incubator at 37°C. The resulting spectral impedance plots are shown in Figure 4.20 and Figure 4.21 for Epo-Tek 87GT (bare Pt electrodes) and SUPREME

Figure 4.19: Diagram of packaged microelectrode array (not to scale). The epoxy encapsulation covers the bondpads and bondwires and must adhere to the passivation layer well. Saline absorption into the epoxy is represented by the parasitic path Z_{leak1}, electrolyte leakage between the passivation and epoxy is represented by Z_{leak2}, and ion transport through the passivation layer is represented by Z_{leak3}.

42HT/T (platinized Pt electrodes) epoxy encapsulations respectively. Both are for a single 480 μm^2 Pt electrode over a period of 93 days. All other electrodes on each chip exhibited similar characteristics (not shown).

For the chip with bare Pt electrodes (Figure 4.20), the impedance magnitude increased over time by the same factor for all frequencies. This was indicative of decreasing effective electrode area. While the mechanism has not been validated, it is postulated that absorption of species to the electrode surface (perhaps organics from the epoxy encapsulation) effectively decreased the electrode area and was responsible for this increase in impedance magnitude.

Examination of the magnitude and phase data revealed impedance characteristics at day 0 similar to a capacitor and resistor in series as would be expected if the interfacial capacitance (C_I) dominated the electrode impedance at the frequencies measured. The

Figure 4.20: Measured impedance magnitude (a) and phase (b) for packaged electrodes soaked in 0.9% NaCl solution for several months. Data from one 480 μm² electrode is shown and was characteristic of all electrodes measured. Electrodes were bare platinum on glass substrates with 4 μm of silicon nitride passivation. Epo-Tek 87GT epoxy was used for encapsulation.

series resistance would be the spreading resistance of the electrolyte. As the chip was allowed to soak in solution, this characteristic slowly changed. At day 93, the low frequency magnitude and phase were both smaller than day 0, indicating the presence of a parasitic resistive path. The high frequency magnitude and phase characteristics were representative of a parasitic capacitive element dominating the impedance, coupled with a smaller spreading resistance (due to the effective larger area of the parasitic element contact with the solution).

Similar results were observed for the platinized Pt electrodes of Figure 4.21. An increase in impedance magnitude was observed for low frequencies where the impedance was not limited by the spreading resistance. Since the starting impedances were significantly lower (one order of magnitude) than for the bare Pt electrodes, no effect from a parasitic resistive element was observed at low frequencies over the duration of the soak. At higher frequencies however, two things became apparent; the spreading resistance was significantly reduced (evidenced by the reduced magnitude at high frequencies at day 93 as compared to day 0), and a parasitic capacitance was increasing the phase.
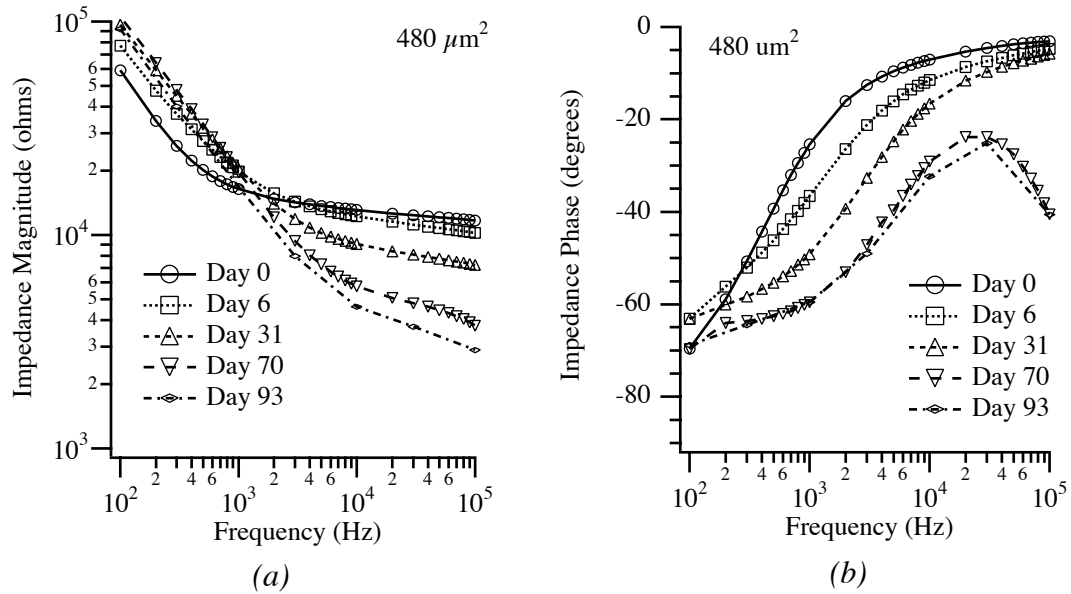
Figure 4.21: Measured impedance magnitude (a) and phase (b) for packaged electrodes soaked in 0.9% NaCl solution for several months. Data from one 480 μm² electrode is shown and was characteristic of all electrodes measured. Electrodes were platinized platinum on glass substrates with 4 μm of silicon nitride passivation. SUPREME 42HT/T epoxy was used for encapsulation.

The long term soak tests depicted in Figure 4.20 and Figure 4.21 indicated the creation of capacitive and resistive parasitic paths was probable. However, it was impossible to determine if this was a result of moisture absorption in the epoxy, a poor seal of the epoxy to the passivation layer, or failure of the passivation layer to block ion transport since these three parasitic paths were in parallel. To discriminate between these failure modes, it would be necessary to perform three experiments. First the ion blockage characteristics of the passivation layer would have to be verified using standard leakage current techniques. Next, the electrode array would have to be completely covered with a thin layer of epoxy and soaked in solution over time. Changes in impedance would indicate problems with water and ion absorption in the epoxy. Following identification of a passivation layer which blocked ion transport and an epoxy which did not suffer from significant water and ion absorption, leakage between the epoxy and the passivation layer could be tested for using the packaged chips and tests outlined above.

While the data obtained as part of this study did not indicate the failure mechanism, separate data obtained at the completion of these experiments indicated the silicon nitride passivation layer used (StrataGlass, Mountain View, CA) was permeable to ions [Flannery,

1998]. Tests were performed by depositing 0.3 μm of silicon nitride over a patterned Al electrode. This test structure was placed in a 23% KOH solution and linear sweep voltammetry was used to determine current to voltage relationship. After just 24 hours, the film exhibited significant leakage current which was attributed to pinholes in the film. Thus, it is probable that at least part (if not all) of the parasitic effects observed in the soak test measurements performed herein were due to failure of the nitride layer to block ion transport. While this silicon nitride did not effectively block ion transport, other films deposited by PECVD have been shown to perform well in ionic solutions and would be an excellent alternative to the films utilized herein [kovacs, 1998].

4.5.5 Impedance Drift

As mentioned in Section 4.4.4 the chips were generally stored dry to prevent the possibility of contamination. When the electrodes were once again immersed in solution and the electrode impedance was immediately measured, impedance drift was often observed. This can be seen from the long term impedance measurements of Figure 4.22. This newly packaged, platinized electrode array (platinized electrodes were used for this
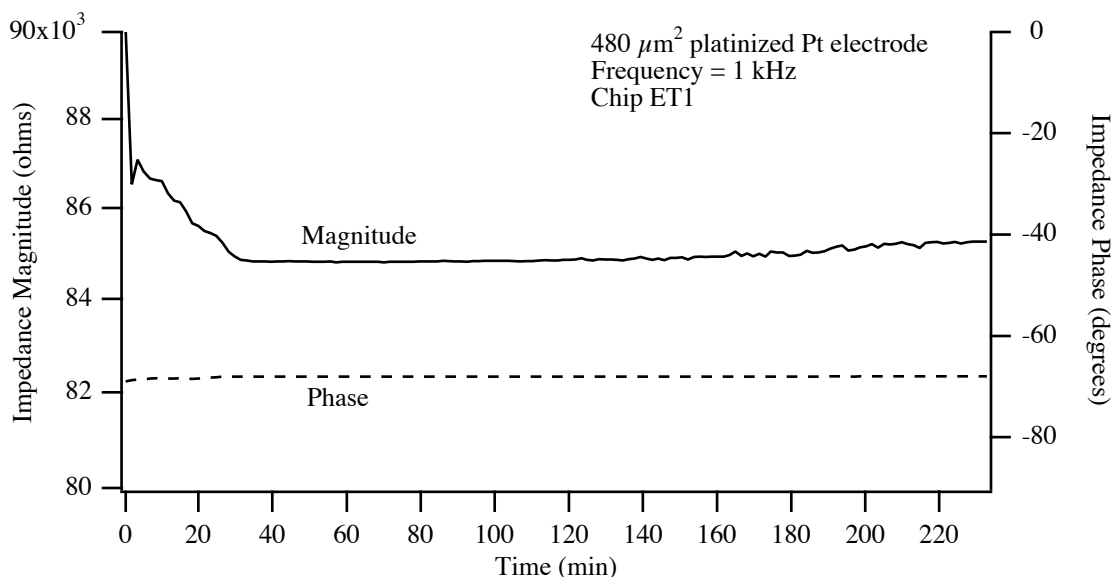
Figure 4.22: Impedance magnitude and phase drift for a platinized Pt electrode over time. The chip was stored dry, placed in the measurement system, 0.9% NaCl was added and measurements were immediately begun. Data shown for a chip which had not been used previously for cell culture. The total decrease in impedance was approximately 5% over a 30 minute time period. Similar changes were observed for all platinized Pt electrodes in the array (data not shown).

experiment since no bare Pt electrodes were utilized for cultured cell studies) had been stored dry, was covered with 0.9% NaCl, and impedance measurements were immediately begun and continued for 4 hours. The result was a rapidly decreasing impedance magnitude (approximately 5% reduction) over a time period of approximately 30 minutes. This effect could have been caused by the transport of ions into the passivation layer as described in Section 4.5.4. Since the chip had not been in contact with saline for a significant period of time prior to these tests, the distance the ions moved into the passivation should have been small. Thus, saturation of the effect should have occurred quickly.

It is also possible this effect was caused by trapped gases in the porous platinum black deposit being slowly dissolved in solution. The trapped gas near the surface of the Pt black enters the solution according to a first order reaction, resulting in the initial rapid decay in impedance observed. However, as the reaction proceeds and the solution level travels further into the pores of the Pt black, the process becomes diffusion limited and the rate slows down. Since the impedance is (to first order) inversely proportional to electrode area, and the effective electrode area is increasing as more solution contacts the edges of
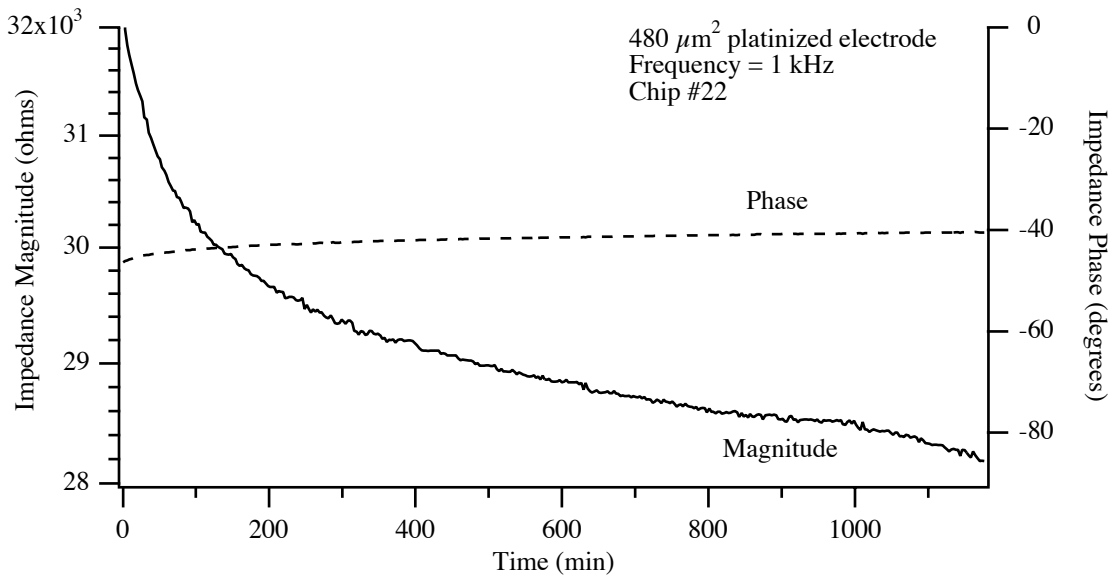
Figure 4.23: Impedance magnitude and phase drift for a platinized Pt electrode over time. The chip was stored dry, placed in the measurement system, 0.9% NaCl was added and measurements were immediately begun. Data shown for a chip which had been used repeatedly for cell culture experiments over several months. Total drift was approximately 13% over 28 hours. Similar changes observed for all electrodes in the array (data not shown).

the Pt black pores, it is possible the changes in measured impedance with time track this rate of dissolution of the trapped gasses.

Chips that had been used repeatedly for cell culture exhibited a more significant impedance drift as shown in Figure 4.23. An impedance magnitude decrease of approximately 13% was observed over a 28 hour time period. Note the length of time required for saturation of the effect was significantly longer than for new chips (Figure 4.22). It is possible this effect was due to ion transport through the passivation layer or into the epoxy. However, a detailed analysis of this phenomenon is beyond the scope of this work.

From the above data it can be seen that it is important the electrodes be *hydrated* prior to impedance measurements if the absolute impedance value is to be used in calculations.

(a)   *(b)*
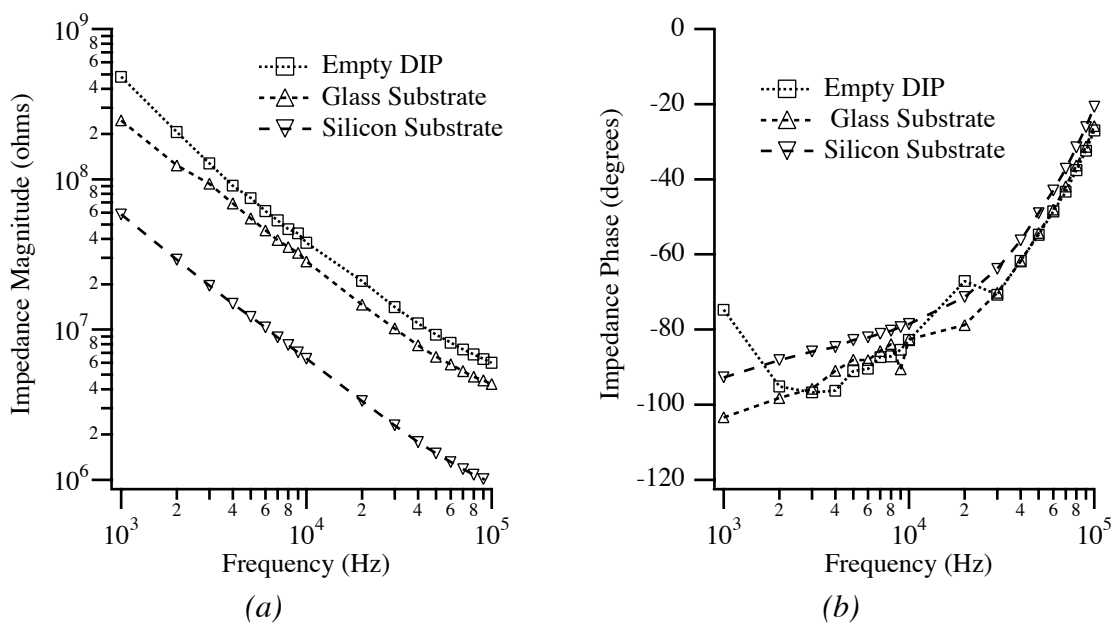
Figure 4.24: Measured impedance magnitude (a) and phase (b) to determine parasitics associated with the packaging techniques used. Data shown for an empty DIP package and microelectrode arrays on glass and silicon substrates packaged as described in Section 4.4.2. Note that for the glass substrate, almost all parasitic paths are due to the DIP package itself. For all cases the parasitic impedance was representative of a capacitance and resistance in series. The resistance is assumed to be surface conduction for all cases except the silicon substrate chip where conduction through the semiconducting substrate was most likely responsible. For the silicon substrate case, the measured capacitance agrees well with the estimate of substrate capacitance in Table 4.1.

For all measurements performed herein, this was done for a minimum of 2 hours which eliminated the drift observed for relatively new electrode arrays.

4.5.6 Parasitics

To determine the total parasitics resulting from the electrode design and packaging techniques (neglecting parasitics to the electrolyte), electrode impedances were measured on a packaged microelectrode array without any electrolyte. The result is as shown in Figure 4.24 for electrodes on silicon and glass substrates as well as an empty DIP package (no chip). For all cases the measured impedances were representative of a capacitance and resistance in series as would be expected. Note that for microelectrode arrays fabricated on glass substrates, impedance measurements on biological material should be possible up to 200 MΩ at 1 kHz (neglecting parasitics to the electrolyte). From Table 4.1, the anticipated worst case parasitic to the electrolyte at 1 kHz was 173 MΩ neglecting any ion transport through the passivation layer. Thus, it is reasonable to assume impedances on the order of 100 to 200 MΩ at 1 kHz could be monitored with the current chip design and packaging techniques. Instrumentation limits on the measured impedance are explored in Chapter 5

4.6   Summary

Microelectrode arrays were designed and fabricated for use in cultured cell action potential and impedance measurements. The combination of glass substrates and platinized electrodes allowed for relatively low impedance, low parasitic electrode elements of varying size (15 to 480 μm^2). The materials used, and novel packaging techniques employed have proven to be non-toxic and conducive to cellular attachment and growth, while allowing uncomplicated insertion into electronic measurement equipment. Long term tests of the materials used indicated the development of a parasitic current path most likely due to transport of ions through the silicon nitride passivation layer used for these chips (other silicon nitride layers have been shown to effectively block ion transport). Electrode impedances correlated well with theoretical values, although platinization was required to prevent nonlinear effects at low frequencies for the smallest electrode sizes. Total packaging and chip parasitics were definitely low enough for action potential measurements and should be adequate for measurement of ionic channel membrane conductance changes if a high seal resistance is obtained. This will be explored in more detail in Chapter 5.

References

Breckenridge, L.J., Wilson, R.J.A., Connolly, P., Curtis, A.S.G., Dow, J.A.T., Blackshaw, S.E. and Wilkinson, C.D.W., "Advantages of using microfabricated extracellular electrodes for in vitro neuronal recording," *Journal of Neuroscience Research*, 42:266-276 (1995).

Flannery, A., *Personal communication*, April (1998).

Footner, P.K., Richards, B.P. and Yates, R.B., "Purple plague: eliminated or just forgotten?," *Quality and Reliability Engineering International*, 3(3):177-184 (1987).

Gesteland, R.C., Howland, B., Lettvin, J.Y. and Pitts, W.H., "Comments on Microelectrodes," *Proceedings of the IRE*, 47:1856-1862 (1959).

Kewley, D.T., Hills, M.D., Borkholder, D.A., Opris, I.E., Maluf, N.I., Storment, C.W., Bower, J.M. and Kovacs, G.T.A., "Plasma-etched neural probes," *Sensors and Actuators* A58:27-35 (1997).

Kovacs, G.T.A., *Personal communication*, June (1998).

Kuperstein, M. and Whittington, D.A., "A practical 24 channel microelectrode for neural recording *in vitro*," *IEEE Transactions on Biomedical Engineering*, BME-28(3):288-293 (1981).

Lind, R., Connolly, P. and Wilkinson, C.D.W., "Finite-element analysis applied to extracellular microelectrode design," *Sensors and Actuators*, B3:23-30 (1991).

Marrese, C.A., "Preparation of strongly adherent platinum black coatings," *Analytical Chemistry*, 59(1):217-218 *(1986)*.

Muller, R.S. and Kamins, T.I., *Device electronics for integrated circuits*, John Wiley & Sons, New York (1986).

Robinson, D.A., "The electrical properties of metal microelectrodes," *Proceedings of the IEEE*, 56(6):1065-1071, June (1968).

Selikson, B., "The role of compound formation on semiconductor device reliability," *Physics of Failure in Electronics*, 3:365-377 (1965).

Tanghe, S.J., Najafi, K. and Wise, K.D., "A planar IrO multichannel stimulating electrode for use in neural prostheses," *Sensors and Actuators*, B1:464-467 (1990).

Chapter 5 INSTRUMENTATION FOR MONITORING CELLS CULTURED ON MICROELECTRODE ARRAYS

This circuit is so simple... how could it possibly not work?

Gregory Kovacs, 1997

5.1 Introduction

The study of cultured cell systems as described in Chapter 1 requires that the biological signals be transduced to a form that can be manipulated externally. For the systems described herein, this is accomplished using metal microelectrodes as outlined in Chapter 3. The transduced biological signal must then be amplified, filtered, and processed to obtain the desired signal information. For action potential measurements, this entails the use of low noise amplification and filtering, generally followed by some form of computer based post processing of the waveforms. Impedance measurements require additional instrumentation including low noise voltage or current sources, transimpedance and / or voltage amplification, and subsequent signal processing to obtain the real and imaginary parts of the impedance from the measured signal. This chapter begins with a discussion of the noise sources relevant to both measurement systems and then describes the actual systems utilized for this work. The chapter ends with a discussion of the thermal regulation and fluidic systems required for experimentation on living cells.

5.2   Noise Sources

In all measurement systems and all signal sources, there is noise. For measurement of biological signals from cells cultured on a microelectrode array, this often takes the form of electrode noise, biological noise, electronic noise, and interference from external sources. Electrode noise is generally thermal in nature as was discussed in Chapter 3. This noise may be minimized by reducing the real portion of the electrode impedance through such methods as deposition of platinum black. Interference from external electromagnetic sources such as 60 Hz line power, circuitry, etc. can generally be reduced to manageable levels by careful shielding of the cell culture chamber and unbuffered biological signals. For frequencies beyond the band of interest, electronic filtering attenuates these interference signals. Different electronic configurations (such as differential measurements) may also be used to limit the effects of common mode interference noise on the measured signals.

5.2.1   Electronic Noise

Noise due to electronics is of greatest concern at the point where the transduced electronic signal is buffered or initially amplified. Thus, care must be taken to ensure that the input referred noise of all front end amplifiers is sufficiently low to allow measurement of the desired signals with an acceptable signal to noise ratio (SNR). Since most extracellular action potentials are in the range of 50 μV to 1 mV pk-pk, the amplifier noise should be limited to around 10 to 25 μV pk-pk (or higher) depending on the application and how much averaging is acceptable. An excellent review of low noise electronic design may be found in [Motchenbacher and Fitchen, 1973] and configurations for biological recording in [Metting va Rijn, et al., 1990, 1991]. For measurement of biological impedance, the limits on allowable noise in the source voltage (current) and current (voltage) sense amplifier depends greatly on the electronic techniques used for measurement of the signal. The different measurement options are discussed in Section 5.4.

5.2.2   Biological Noise

Biological noise is intrinsic to the living system being monitored and generally has spectral energy in the same frequency bands as the desired signal, making it difficult to filter out. For action potential measurements, this noise is often the result of other electrically active cells in the vicinity of the electrode. These signals are superimposed on

the APs of the cell(s) being monitored and contribute to the overall noise of the system. This is of greatest concern for noise generating cells located closer than 100 μm to the electrode (and cell(s)) being monitored [Breckenridge, et al., 1995]. However, without surface treatments to inhibit cellular attachment in the regions surrounding an electrode, this noise will always be present. If the signals are uncorrelated, averaging can be used to isolate the signal of interest from the surrounding biological noise. This technique can increase the signal to noise ratio by up to the square root of the number of samples taken [Cobbold, 1974] and will help with not only biological noise, but the other types mentioned above as well.

For the case of impedance measurements, biological noise is more difficult to define. Much depends on the type of response which is being monitored. If impedance characteristics of the cellular membrane are being monitored, then cell motility and changes in cell / substrate coupling will contribute to the noise of the measurement. Unfortunately there are no electronic or averaging methods to reduce this type of noise. This will be discussed in detail in Chapter 7.

5.3   Action Potential Measurement System

An integrated amplifier / filter array was developed at the Stanford Transducers Laboratory (Stanford University, Stanford, CA) by Dr. Ion Opris (currently at Opris Consulting, Cupertino, CA) for use in action potential measurements. While it has been described in detail elsewhere [Borkholder, et al., 1996; Kewley, et al., 1997], the basic design and characteristics are outlined here. Additionally, the incorporation of this amplifier into an action potential monitoring system is described along with the commercially available electronics and data acquisition software utilized with it. The characteristics of the fully configured system are also presented.

5.3.1 Integrated 18 Channel Amplifier Design and Characteristics

An 18-channel amplifier / filter array (Figure 5.1) was implemented on a 2.2 mm square chip in the MOSIS (ISI, Marina del Rey, CA) 2 μm low-noise analog CMOS process. A differential pair configuration was used with each channel amplified with respect to a reference input. The pass-band gain was provided in three stages with the output buffer B designed to drive a 10 nF load, thereby facilitating direct ribbon cable connection to data acquisition equipment. The output was fed back into A_3 to set the DC output level to an on-chip reference value. The low-pass cutoff was fixed at 30 kHz by the
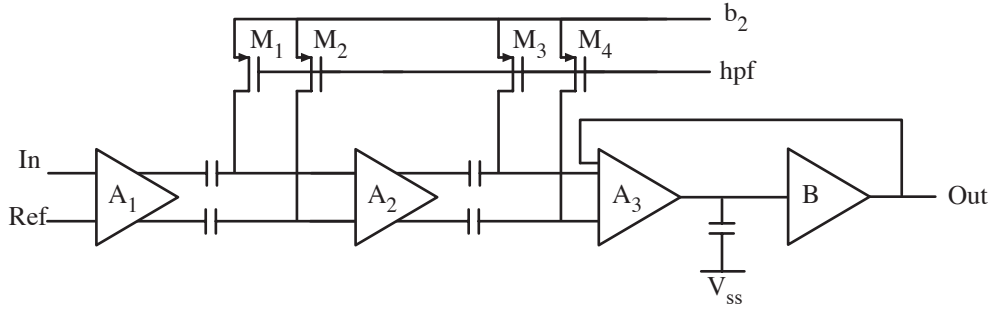
Figure 5.1: Simplified schematic of one channel of the integrated amplifier array showing the filtering elements. M_1 through M_4 and the coupling capacitors between amplifier stages set the second order high-pass filter characteristics.

shunt capacitor between A_3 and B. The coupling capacitors in combination with M_1 to M_4 (which were biased in the subthreshold regime) created the 2-pole high-pass filter (HPF). By controlling the voltage drive on these subthreshold transistors (via an external pin connected to hpf), the high pass cutoff was varied between 3 Hz and 10 kHz. Chip performance is summarized in Table 5.1 below.

Gain (midband)	45dB
Noise (input referred)	9μVrms (10Hz -30kHz)
Output Swing	400mV pk-pk @ 1kHz (with 0.34% THD)$^\Psi$
Power Supplies	±2.5V
Power Dissipation	10mW for 18 channels and bias circuits
Fixed LPF	30 kHz
Tunable HPF	3 Hz to 10 kHz
$^\Psi$ **Output swing corresponding to a 2.2 mV pk-pk AP at the amplifier input (usual for recordings from cultured chick myocardial cells).**	

Table 5.1: Integrated 18 channel amplifier / filter array specifications.

5.3.2 Incorporation of the Amplifier into an AP Monitoring System

The amplifiers described above were incorporated into a front end AP measurement system as shown in Figure 5.2. Electrical connection to the electrode array was accomplished using a zero insertion force (ZIF) socket. The electrodes were AC coupled to the amplifiers using a 1 μF capacitor in each signal path with a 1 MΩ resistor tied to ground to set the DC potential. This combination provided a single pole, high pass filter at

0.2 Hz. While a larger resistance value could have been used to limit signal attenuation (due to the voltage divider effect of the electrode impedance and the resistor to ground), it could have resulted in slightly higher noise and would have increased sensitivity to external noise sources. Additionally, the resistor networks used as part of the design (to
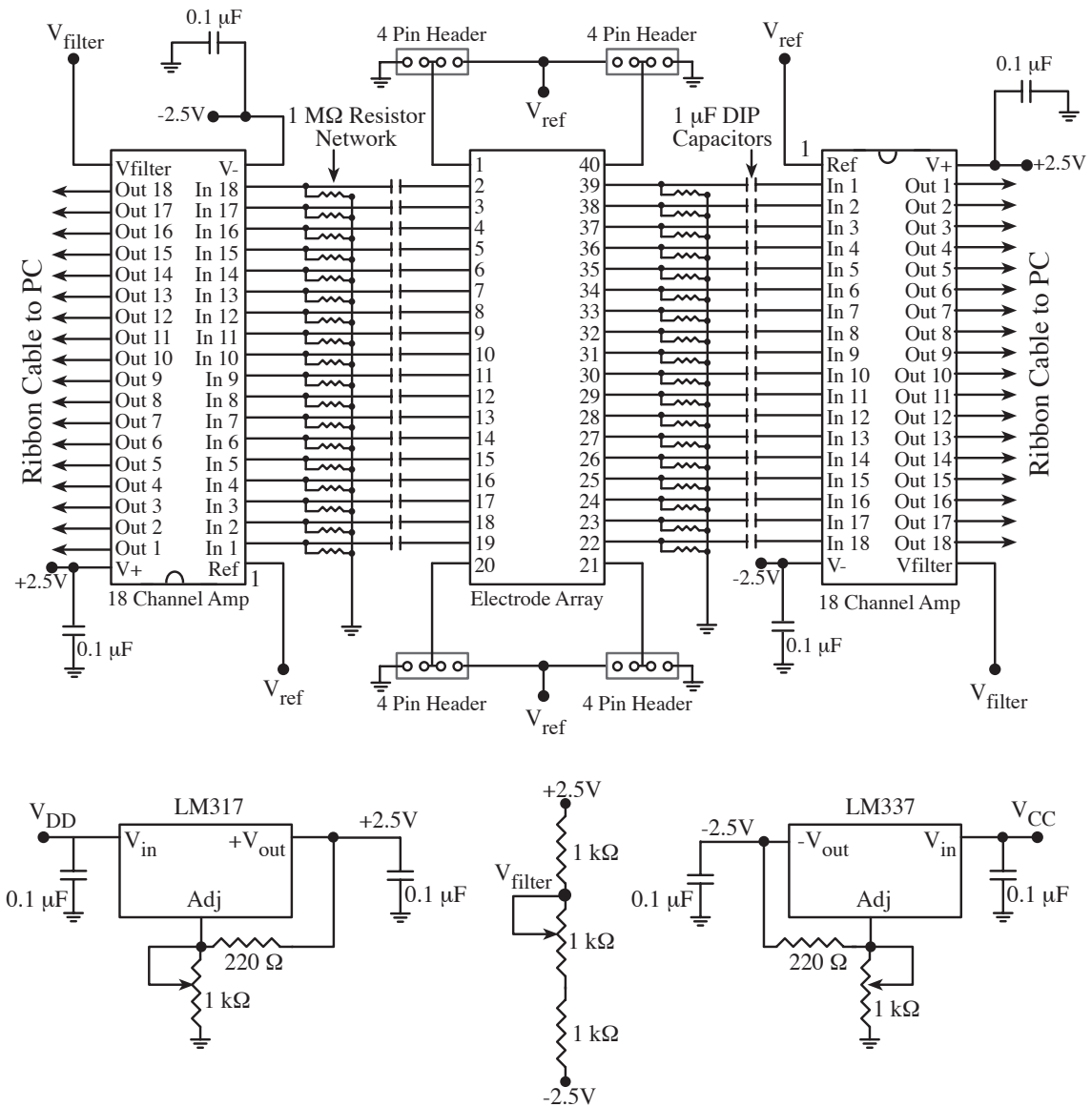
Figure 5.2: Action potential measurement system schematic. The electrode array was AC coupled to the integrated 18 channel amplifiers through 1 µF capacitors. The outputs of the amplifiers were connected to the PC with ribbon cable. Two 9 volt batteries were down-regulated to ± 2.5 volts to power the amplifiers. A voltage divider was used to set the tunable HPF voltage (V_{filter}). Jumpers were used to connect the reference electrodes on the electrode array to either ground or the amplifier reference. Generally, the reference node of the amplifiers was connected to ground.

reduce component size and facilitate PCB fabrication) were not available in sizes larger than 1 MΩ. Ideally, given typical platinized electrode impedances of tens of kΩ in the frequency band of interest (100 Hz to 3 kHz), the bias resistor would have been around 5 to 10 MΩ to limit attenuation to less than 1%.

The amplifiers were operated with ± 2.5 volt supplies derived from two 9 volt batteries and adjustable voltage regulators. The reference pin on the amplifier was generally tied to ground and a reference electrode placed in the solution (either a reference on the electrode array or a coiled Pt wire immersed in the solution). This single ended measurement configuration in combination with the AC coupling was required to minimize unbalancing of the differential input pair of the amplifier. The cutoff frequency of the tunable HPF was
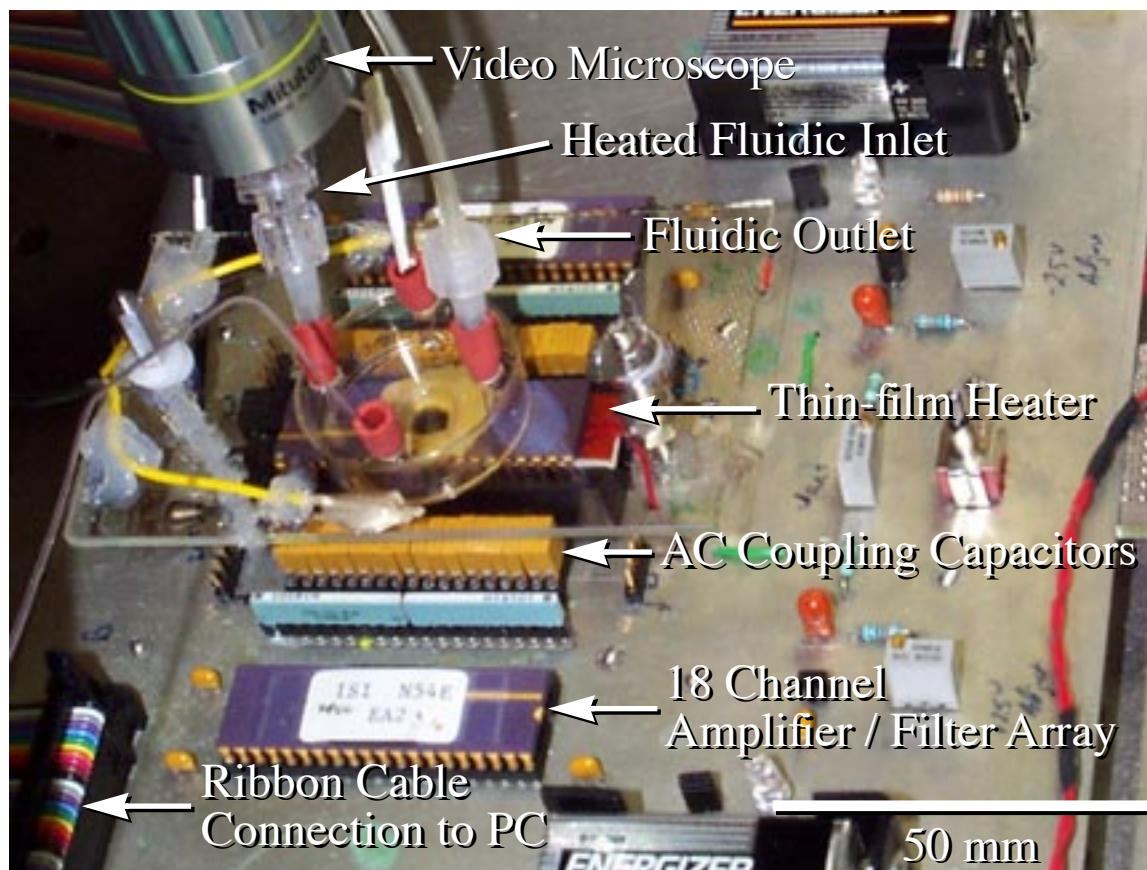
Figure 5.3: Measurement setup used for AP monitoring. The electrode array was connected to the electronics via a ZIF socket. The amplified action potentials (through the AC coupled custom 18 channel amplifier / filter arrays) were measured by direct connection to a PC via ribbon cables. The amplification system was powered by two 9 volt batteries. Thermal regulation was achieved with a thin film heater under the chip, a resistively heated, ITO coated glass plate above it, and a heated continuous flow perfusion system.

controlled with a 1 kΩ potentiometer setting the voltage of V_{filter}. Generally this was operated around ground to set the filter at 3 Hz. Thus, for all measurements the amplifier was used with its full bandwidth of 30 kHz. While additional low pass filtering to the bandwidth of interest (3 kHz) would have reduced the total in-band noise, the additional complexity of 36 channels of filtering was deemed too great for this prototype system.

Each of the four reference electrodes on the microelectrode array (see Figure 4.4) were connected to a four pin header strip allowing connection to either ground or the reference pin of the amplifiers. The output of the amplifiers directly drove ribbon cable connections to the PC. The fully functional system is shown in Figure 5.3 where the electrode array, amplifiers, AC coupling capacitors and ribbon cable connections are clearly visible. The heating and fluidic components labeled are discussed in more detail in Section 5.5.

5.3.3 Data Acquisition

Action potentials from cells cultured on the electrode array were amplified by the integrated amplifier / filter arrays described above. The amplified AP signals were routed via ribbon cable to a PC-based data acquisition system capable of simultaneously monitoring up to 32 channels and storing the digital, 12-bit data to disk (Experimenter's Workbench 32 by DataWave Technologies, Colorado). The maximum sampling rate of the system was 312 kHz for all 32 channels. To limit the amount of post processing of the data required, and allow for direct measurement of the peak amplitude of the action potential, the number of channels was limited to eight to allow for 39 kHz sampling rate per channel. While this was significantly above the theoretically required Nyquist sampling rate of 6 kHz (2 times the action potential signal bandwidth), it allowed for direct reproduction of the acquired waveform without the need for upsampling and interpolation. It is important to note that the sampling rate of 39 kHz did not prevent aliasing of noise outside of the bandwidth of the action potential. Recall that the amplifier bandwidth was 30 kHz since no external filtering was done. Thus, it is expected that some noise aliasing did occur resulting in a decreased SNR.

For each experiment all 36 electrodes were initially monitored and the best eight signals chosen for recording. A threshold trigger was set which allowed a 10 msec time segment around the AP to be captured and stored to disk. The 12-bit ADC of the system was set so that the least significant bit (LSB) was 600 μV. Given the midband gain of the amplifiers of 45 dB, this correlated to an input referred amplitude of approximately 3 μV, which was significantly lower than the noise of the system. Since limited averaging was

done for these studies, SNRs much larger than one were required and quantization noise was not expected to be an issue.

5.3.4 System Performance

The system was initially tested with an electrode array in 0.9% NaCl without cells cultured on its surface. Using platinized electrodes and grounding the solution with an immersed coiled Pt wire connected to ground, the total noise at the amplifier outputs was measured. This noise was approximately 80 μV pk-pk (input referred) as measured with a digital oscilloscope operating in envelope mode. Assuming a Gaussian distribution for the noise, this represents approximately 13 μVrms of equivalent noise at the amplifier input. The additional 4 μVrms of noise (over the amplifier itself) was due to the 1 MΩ bias resistor to ground, electromagnetic interference, and the real part of the electrode impedance as described in Chapter 3.

The system was used to monitor spontaneous electrical activity from cultured embryonic chick myocardial cells as described in detail in Chapter 6. While all of the data presented shows excellent SNR, action potentials as small as 80 μV pk-pk have been successfully recorded (with SNR $\approx$ 1:1). System stability was evaluated by monitoring
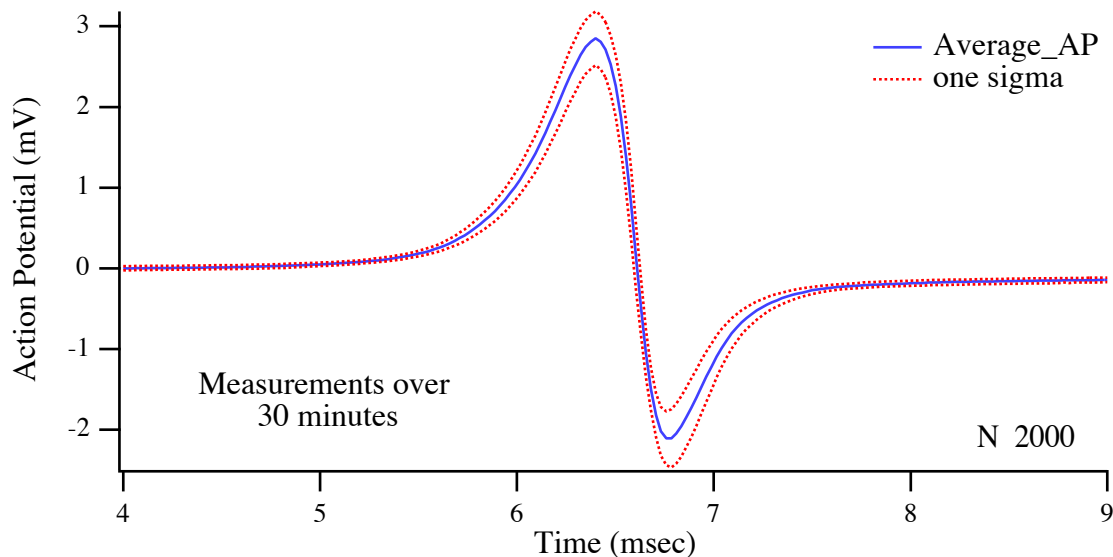
Figure 5.4: AP stability in the recording system. Measurements were taken on a single channel over a 30 minute time period. Data was stored digitally on the PC using the system previously described. The average and standard deviations of the AP are shown for approximately 2000 action potentials.

action potentials over extended periods. Figure 5.4 shows a recorded action potential averaged over 30 minutes (approximately 2000 APs) and the resulting standard deviations of the waveform. The relatively stable signal achieved indicated all system components (including thermal and fluidic to be discussed later) were functioning well and would be sufficient for monitoring changes in AP shape due to pharmacological manipulation. The stability presented in Figure 5.4 was characteristic of that achieved for all experiments presented in Chapter 6.

5.4 Impedance Spectroscopy Measurement System

An impedance spectroscopy system has been developed for measurement of biological impedances associated with cells cultured on microelectrodes. Traditional impedance measurement approaches and justification for the approach chosen are described. Each component of the impedance system is outlined with detailed circuit schematics provided where appropriate. System calibration procedures and the mathematics required for extracting the unknown complex impedance are described in detail. The overall system performance is then explored with measurement range and accuracy compared to those required for determination of cellular membrane impedances.

5.4.1 Design considerations

Historically there are several methods for measuring the impedance of biological material. Aside from the methods described in Chapter 1 for cultured cells, numerous techniques have been used for measurement of more macroscopic biological tissues [Cole and Curtis, 1939; Hodgkin and Huxley, 1952; Dijkstra, et al., 1993]. Perhaps the most common technique is that of a balanced bridge circuit as shown in Figure 5.5. If the resistances R_1 and R_2 are equal, then the output voltage (V_{out}) will equal zero only when the parallel combination of R_v and C_v is equivalent to the unknown impedance (Z_u). For instances where changes in the measured impedance are to be monitored, it is possible to balance the bridge as described. Any changes in Z_u will then be registered as deviations of V_{out} from zero. The inclusion of a phase detector at the output (referenced to the input (V_{osc})) allows for discrimination between resistance and reactance changes. This system works well for manual monitoring of impedances where it is possible to use decade boxes for the variable capacitance and resistance, and has been successfully utilized for measurement of the impedance characteristics of suspensions of cells and colloidal particles in electrolyte solutions [Schwan, 1957; Schwan, et al., 1962]. However, for

automated systems where real time balancing may be required, precision variable resistors and capacitors controlled by voltage or logic are difficult to obtain. This problem is compounded when large impedances or a broad range of impedances are to be measured as is the case for monitoring single cell impedance characteristics.
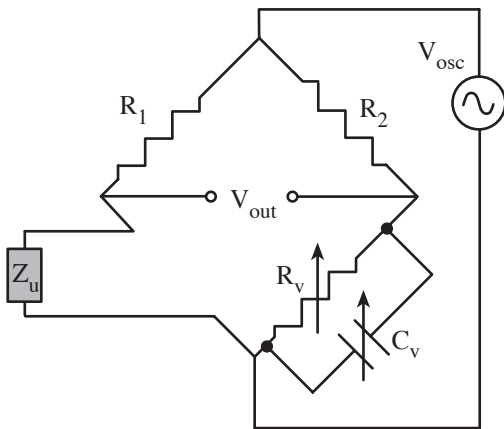
Figure 5.5: Balanced bridge circuit. If the resistances R_1 and R_2 are set equal to each other, then the value of the unknown impedance Z_u will equal the parallel combination o f R_v and C_v when the output voltage (V_{out}) is zero. This will be valid only for the frequency of excitation.

As outlined in Chapter 1, Giaever and Keese used a constant current source arrangement with a voltage and phase sensitive detector to monitor the impedance characteristics of populations of cells plated on a planar electrode [Giaever and Keese, 1986]. This arrangement assumed that a 1 MΩ resistor placed in series with the unknown impedance would dominate the overall impedance resulting in a constant current. This worked extremely well for this system since relatively low impedances (electrode and cellular) were measured. For cases where a broad range of impedances are to be measured, this technique requires the use of a variable (or switchable, discrete) current limiting resistance so that the constant current model remains valid. If the unknown impedance is dynamically changing, this may become difficult to control.

It is also possible to drive the unknown impedance with a known voltage and monitor the resulting voltage or current as shown in Figure 5.6, where the gain of each stage is indicated. The transimpedance configuration monitors the current while the voltage divider topology measures the voltage. In both cases, it is desirable to limit the value of R_s in order to lessen the effects of parasitic capacitive paths in parallel with the resistance. Thus, significant gain following these stages is required when large impedances are measured. The effectiveness of these methods in monitoring changes in an unknown impedance ($Z_{unknown}$) can be deduced by taking the derivative of the gain with respect to $Z_{unknown}$

$$\frac{d}{dZ_{unknown}} Av_{voltagedivider} = \frac{-R_s}{(R_s + Z_{unknown})^2} \tag{5.1}$$

$$\frac{d}{dZ_{unknown}} Av_{transimpedance} = \frac{-R_s}{Z_{unknown}^2} \tag{5.2}$$

From these equations it is can be seen that the transimpedance method is more sensitive to changes in $Z_{unknown}$ than the voltage divider method for instances where $Z_{unknown}$ and R_s are comparable. However, for the case of $Z_{unknown} \gg R_s$, the two topologies provide the same sensitivity to changes in $Z_{unknown}$. For measurement of a broad range of impedances, the transimpedance topology is superior.

Historically there has been limited work examining the impedance characteristics of single cells cultured on planar electrodes [Connelly, et al., 1989; Lind, et al., 1991; Breckenridge, et al., 1995], and these studies have focused on monitoring the adhesion and motility characteristics of the cells over a limited impedance range. The goal of this work was to observe cellular membrane characteristics and modulation of ionic channel conductances through pharmacological manipulation in addition to the motility and adhesion characteristics observed by others. Thus the system was designed to operate over a large impedance and frequency range. It was hoped the broad range capabilities of the system would allow for this observation under different circumstances and with a variety
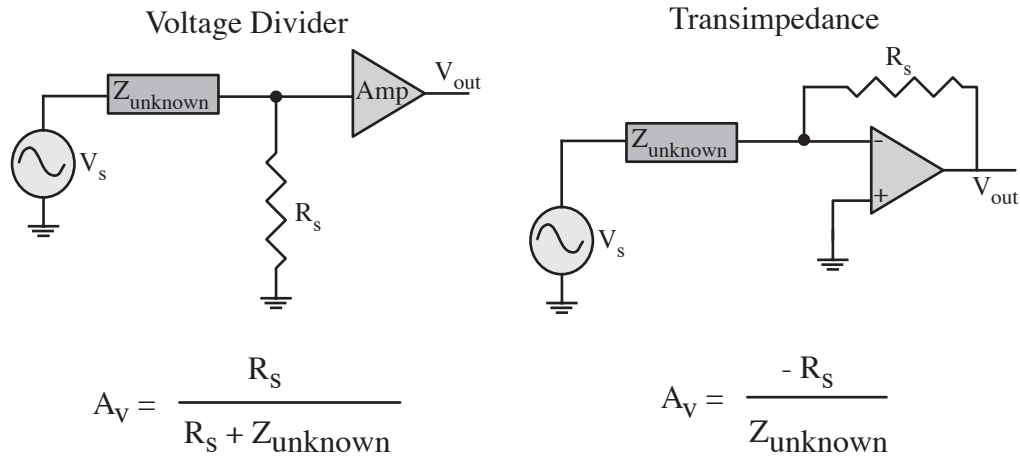
Figure 5.6: Two different topologies for monitoring changes in an unknown impedance when driven with a voltage source. A voltage divider technique results in the signal gain shown (assuming an amplifier gain of 1), while the transimpedance technique results in a different gain equation. In both cases the source voltage and the resistance R_s is known.

of different cell types. To measure a broad range of impedances over decades of frequency, a constant voltage source was used with a transresistance current sense circuit and variable amplification at the output.

Given that relatively large impedances could be measured and the voltage source amplitude was limited to less than 100 mV pk-pk (due to linearity concerns) as outlined in Chapter 3, the anticipated current to be monitored (via the transimpedance stage) would be small. With the source voltage limited to 50 mV peak, a impedance of 100 MΩ would result in 500 pA peak current. Reliably measuring this current given the inherent electrode and amplifier noise would have been extremely difficult without the use of lock-in amplifier techniques. Thus, the system included homodyning elements to confine the analysis to the signal frequency of interest.

As described in Chapter 2, there are three distinct regions of dispersion which must be considered when measuring the impedance characteristics of biological materials; the α-, β- and γ-dispersions [Schwan, 1988]. This system was designed to operate between 100 Hz and 100 kHz, the extremes coinciding with the end of the α-dispersion and the beginning of the β-dispersion respectively. It was hoped this configuration would limit the effect of this dispersive behavior on the measurements.

5.4.2 System Structure

The basic system structure is depicted in Figure 5.7. A PC driven quadrature synthesizer provided a sine and cosine output of known frequency and amplitude. This signal was attenuated to a maximum of 50 mV peak and then routed to a single microelectrode via an analog multiplexer. A coiled platinum wire immersed in solution was held at virtual ground and acted as the counterelectrode for collection of the resulting current. This current was converted to a voltage by the resistance R_S and then amplified. This amplified signal was analog multiplied by the original sine and cosine waveforms and low pass filtered to provide real and imaginary vectors. Using these vectors, the original source amplitude and the value of R_S, the real and imaginary components of the measured impedance could be determined.

5.4.3 Signal Source and Attenuation

The quadrature synthesizer and the attenuator used in the system were developed by Prof. Gregory Kovacs (Stanford University). A STEL-1172B (Stanford Telecom, Sunnyvale, CA) quadrature synthesizer chip was the core of the signal source. This 50

126
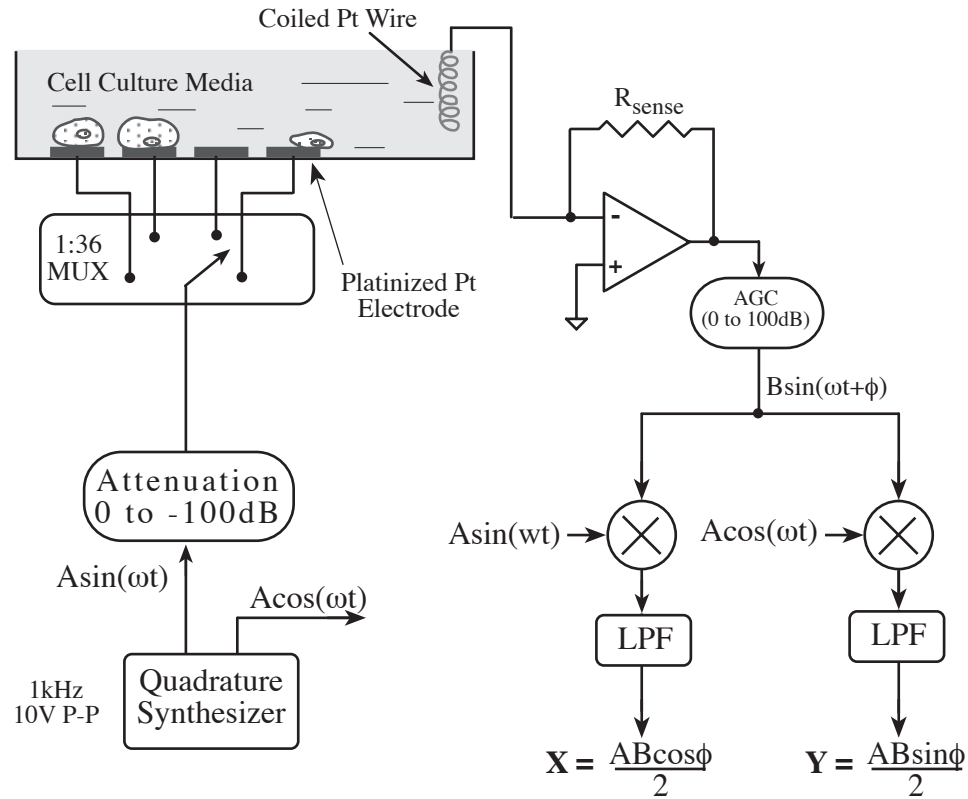
Figure 5.7: PC controlled impedance measurement system. An AC voltage drove one microelectrode at a time, and the resulting current was converted to a voltage, amplified, and homodyned to yield the real and imaginary components of the measured impedance.

MHz, 32-bit numerically controlled oscillator provided sine and cosine outputs of 8-bit amplitude and 10-bit phase resolution. When coupled with two digital-to-analog converters (DAC) and low pass filtering, quadrature, analog outputs of controlled frequency were possible. This synthesizer was built on a PCL-750 prototype development card (American Adventech Corp., Sunnyvale, CA) which contained the necessary logic for interfacing to an IBM PC including: the memory address decoder, I/O address decoder, data line buffer and address line buffer, eight I/O write control signals and eight I/O read control signals. The quadrature synthesizer was built on the breadboard area and the entire board was inserted into a standard 62-pin ISA slot in the PC. The basic circuit schematic of the synthesizer is shown in Figure 5.8.

The sine wave output from this quadrature synthesizer was attenuated to the desired level using the circuit presented in Figure 5.9. A chain of buffers was connected so that the output of the first was attenuated by a factor of 10 and then routed to the input of the next
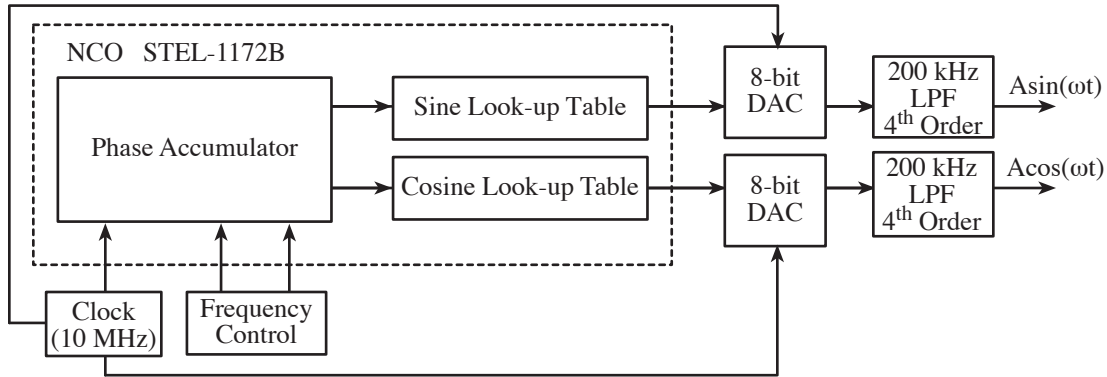
Figure 5.8: Quadrature synthesizer block diagram. A frequency number provided to the numerically controlled oscillator (NCO) was digitally integrated in the accumulator to provide instantaneous digital phase information. This digital phase word was converted to a digital amplitude word by the look-up table. The sine and cosine signals were provided by converting the 8-bit digital amplitude words to analog signals with the digital-to-analog converters and then low pass filtering at 200 kHz to remove aliased frequency components. The output frequency was limited to approximately 40% of the clock frequency.

buffer. This was repeated 5 times allowing attenuation of the original signal by up to 10^5. The desired output was chosen using relays and connected to the multiplexers controlling electrode selection.

The performance of the signal source was evaluated using a SRS760 FFT spectrum analyzer (Stanford Research Systems, Inc., Sunnyvale, CA) across the 100 Hz to 100 kHz band of interest. The total harmonic distortion (THD) was measured at discrete frequencies as outlined in Table 5.2.

Frequency (Hz)	THD (%)
100	3.26
300	1.44
1k	0.08
3k	0.09
10k	0.32
30k	0.41

Table 5.2: Measured total harmonic distortion of the signal source.
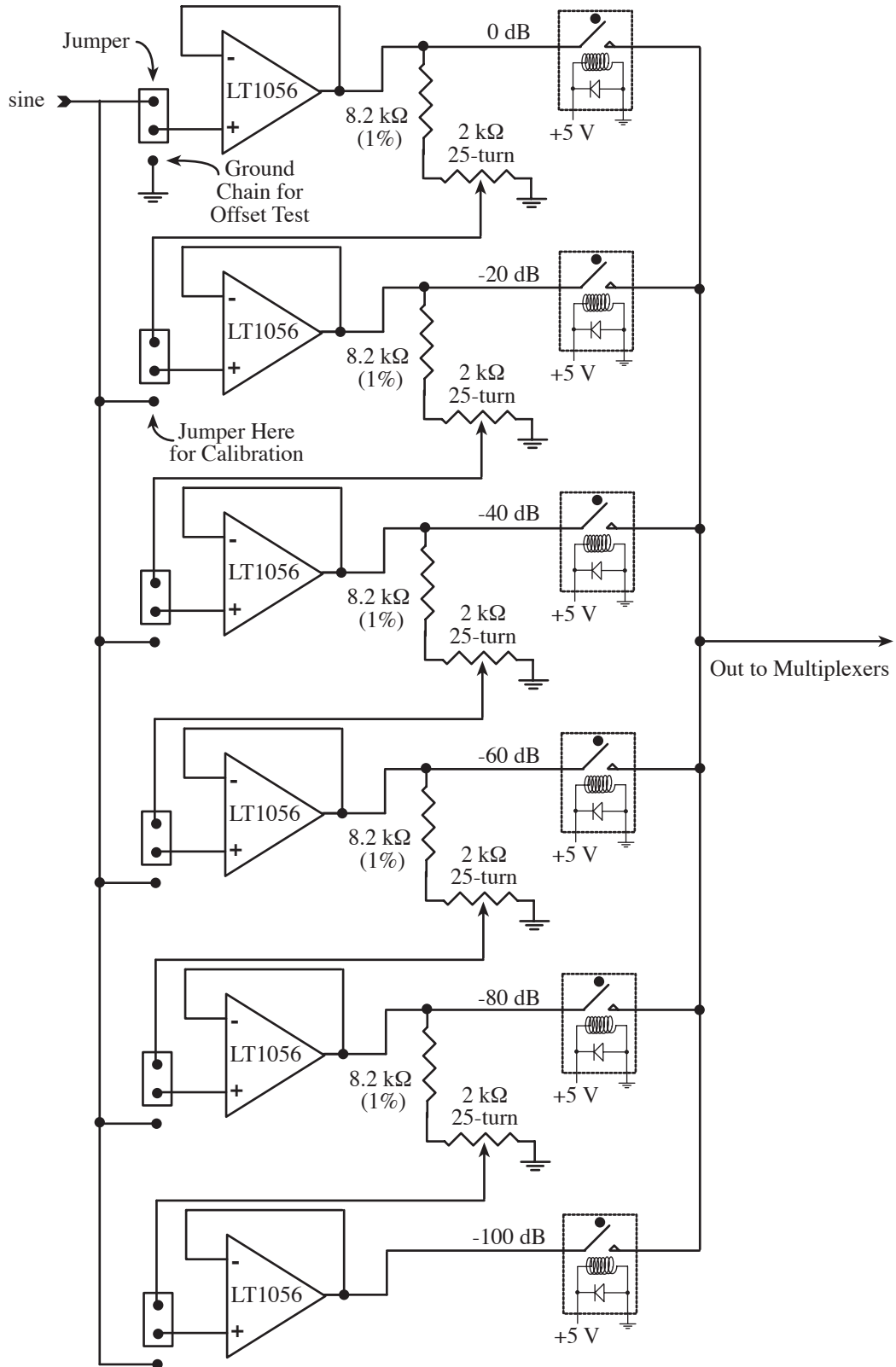
Figure 5.9: Attenuator circuit schematic. The chain of buffers and voltage dividers provided relay addressable attenuation of 0 to 100 dB.

129

The high percentage distortion at 100 Hz and 300 Hz was due entirely to spikes at higher frequencies (25 kHz, 50 kHz and 75 kHz for the 100 Hz signal and 75 kHz and for the 300 Hz signal). These were presumably due to quantization error at the DAC output. The STEL-1172B utilized an 8-bit look up table which effectively quantized the sine wave into 256 equal parts. For the 100 Hz signal, this corresponded to a 25.6 kHz stepping frequency. This quantization noise and its harmonics (50, 75, 100, 125, 150, and 175 kHz) were below the 200 kHz LPF following the DAC output and were therefore not attenuated. It is important to note that the total harmonic distortion was probably higher than indicated by the spectrum analyzer which had a limited measurement range of 100 kHz. The 300 Hz signal resulted in a stepping frequency of 76.8 kHz which corresponded well with that observed by the spectrum analyzer. This was also unaffected by the 200 kHz LPF. The 1 kHz signal quantization error frequency (256 kHz) was above the LPF and did not contribute to the THD measurement. The characteristics of this signal source at lower frequencies could be greatly improved by a tunable LPF at the DAC output to remove this undesirable noise.

At higher frequencies (10 kHz and 30 kHz) the THD increased slightly. This was most likely due to the output frequency being greater than the clock frequency (f_c) divided by 1024. As the output frequency was increased with respect to the clock, the sine function appeared more discontinuous since there were fewer samples in each cycle (recall that an 8-bit look up table with 1024 samples was used in the STEL-1172B). Since the clock frequency was 10 MHz for the system, this limiting output frequency was 10 MHz divided by 1024 or 9.77 kHz. This corresponded well with the onset of increased THD in Table 5.2.

5.4.4 Interface to the Electrode Array

The electrode array was interfaced to the impedance system through a ZIF socket as for the AP system. As shown in Figure 5.10, the sine wave output of the quadrature synthesizer was connected to a single microelectrode in the array via three analog multiplexers (MUXs) (addressing controlled by the PC interface card described below). The coiled platinum wire immersed in the solution was then connected to the output header and subsequently the input of the transimpedance stage. Each of the four reference electrodes on the chip was connected to one pin of the 12-pin header to allow their use as the counter electrode if desired. A known value resistor ($R_{cal} = 10.00$ k$\Omega \pm 0.1\%$) was also available for connection between the reference electrodes and the output for calibration

Figure (schematic of electrode array interface board):

12 Pin Header
Out — To Transimpedance Stage
Cal
A sin(ωt)
R_{cal}

Left MUX — ADG406 16:1 MUX:
+12 V — VDD; NC; NC; E9 — S16; E10 — S15; E11 — S14; S13; E12 — S12; E13 — S11; E14 — S10; E15 — S9; GND; NC; A3 — A3
D; VSS — -12 V; S8; S7; S6; S5; S4; S3; S2; S1; EN ← A; A0 ← A0; A1 ← A1; A2 ← A2
A sin(ωt)

Electrode Array (pins 1–40)

Right MUX — ADG406 16:1 MUX:
+12 V — VDD; NC; NC; S16; S15; S14; S13; S12; S11; S10; S9; GND; NC; A3 — A3
D ← A sin(ωt); VSS — -12 V; S8 — E31; S7 — E30; S6 — E29; S5 — E28; S4 — E27; S3 — E26; S2 — E25; S1 — E24; EN ← B; A0 ← A0; A1 ← A1; A2 ← A2

Bottom MUX — ADG408 8:1 MUX:
A0 → A0; C → EN; -12 V — VSS; S1; P16 — S2; P18 — S3; P23 — S4; D
A1 ← A1; A2 ← A2; GND; VDD — +12 V; S5 — P17; S6 — P19; S7; S8 — P22

Power Supplies = ± 12 V
Address Lines: A0 - A3
Control Lines: A, B, C
Electrode connections labeled E1, E2, etc.

Figure 5.10: Schematic of the electrode array interface board. The attenuated sine wave from the quadrature synthesizer was connected to all three MUXs. The PC controlled which chip was enabled and the address lines chose which electrode was to be driven. The counterelectrode (Pt wire in the solution) was connected to a output pin of the 12 pin header allowing the resulting current to be routed to the transimpedance stage.

purposes as will be described in detail in Section 5.4.8. The analog multiplexers used had an on resistance of only 80 Ω and a channel to channel capacitance of 50 pF. The resulting cross-talk was not an issue in this design since this capacitance represented an impedance much larger than that of the platinized electrodes at all frequencies of interest.

5.4.5 Transimpedance and Gain Stages

The current resulting from the sinusoidal voltage driving the electrode was collected by the coiled Pt wire immersed in the solution. This wire was held at virtual ground by a transimpedance stage as shown in Figure 5.11. The transimpedance amplifier converted the current to a voltage through the resistance R_s which was then amplified by a series of gain = 10 stages. To achieve a broad impedance range detection capability (10 kΩ to 1 GΩ) the total gain of the system was adjustable (automatic gain control (AGC)) by altering the signal path using relays as shown. The output of any one amplifier could be
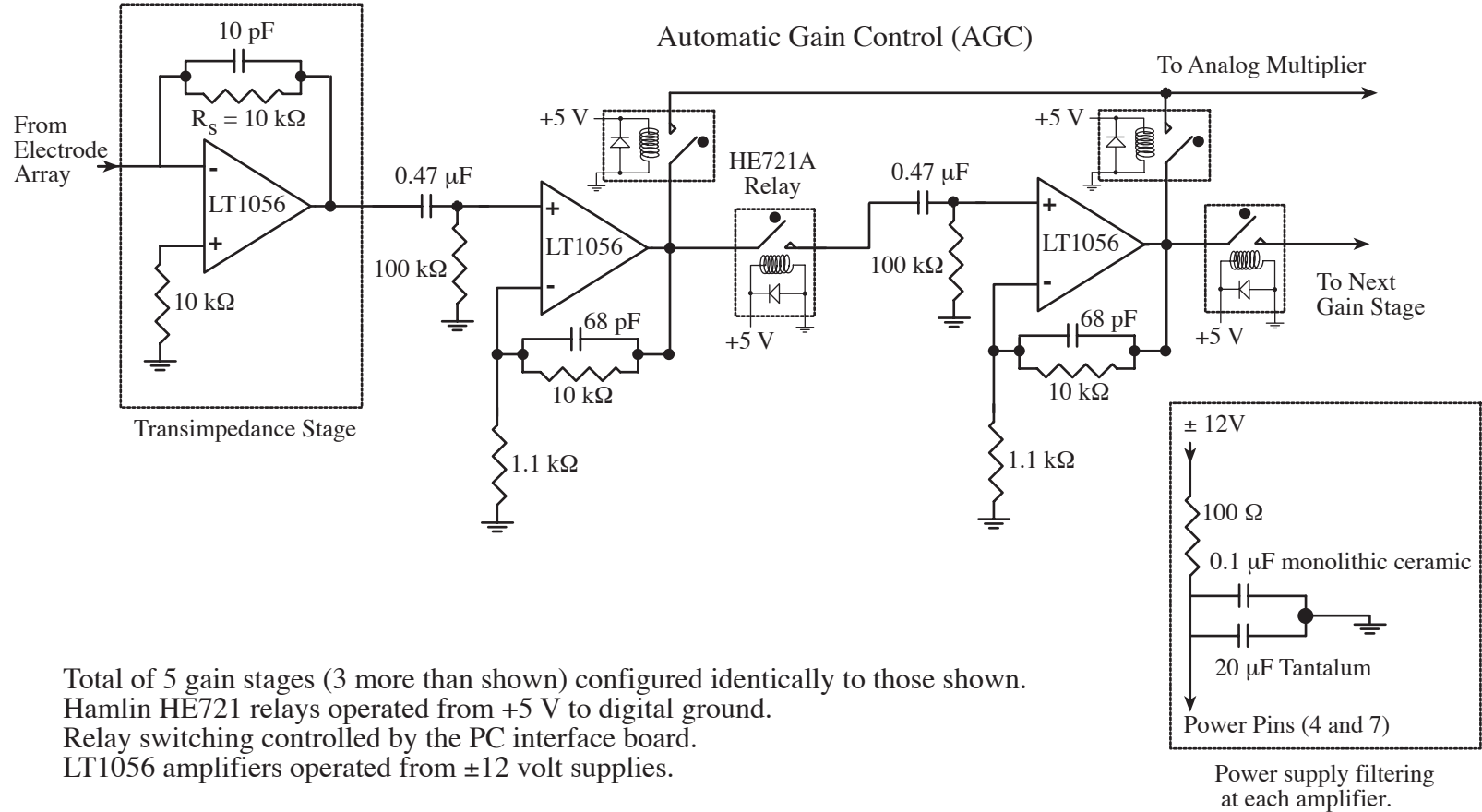
Figure 5.11: *Schematic of the transimpedance amplifier and voltage gain stages. The current signal from the counterelectrode is converted to a voltage by the transimpedance stage and subsequently amplified by the variable gain stage. Different voltage gains are achieved by routing the signal to different numbers of $A_v = 10$ amplifiers.*

ported to the homodyning stage or to the next gain stage. Each gain stage was AC coupled to limit the effects of small DC biasing errors and prevent saturation of the amplifiers.

The output of the transimpedance stage was inversely proportional to the unknown impedance

$$V_{transimpedance} = -V_s\left(\frac{R_s}{Z_{unknown}}\right) = -A'\sin(\omega t + \phi_{unknown})\left[\frac{|R_s|}{|Z_{unknown}|}\right] \quad (5.3)$$

where $Z_{unknown}$ was a combination of the microelectrode impedance, cellular membrane impedance, seal resistance, solution resistance and the counter electrode impedance, and $A'\sin(\omega t)$ was the attenuated source signal presented to the electrode. This signal was then amplified by the chain of gain stages yielding

$$V_{AGC} = B\sin(\omega t + \phi_{unknown} + \phi_{gainstages}) \quad (5.4)$$

where

$$B = A_{V_{gainstages}}A'\left[\frac{|R_s|}{|Z_{unknown}|}\right] \quad (5.5)$$

During actual measurements, the gain was set to the highest level and then reduced until the output was below 7 volts peak (limited to prevent saturation of the analog multiplier). This was determined using a voltage comparator on the PC interface board (to be described later). The bandwidth of each section was limited by the 68 pF capacitor and 10 kΩ feedback resistor which created a pole at 230 kHz. While this was well above the 100 kHz bandwidth of interest, the cascade of amplifiers suffered from a reduced bandwidth according to

$$\omega_{BW} = \omega_{stage} \cdot \sqrt{2^{\frac{1}{n}} - 1} \quad (5.6)$$

where ω_{BW} is the system bandwidth (-3 dB point), ω_{stage} is the bandwidth of a single stage and n is the total number of cascaded stages [Lee, T.H., 1998]. The effective bandwidth of the cascade of amplifiers is given in Table 5.3 below. Note the reduced effective bandwidth as the total gain is increased. While this would be suboptimal for a system assuming a flat response across the bandwidth of interest, the calibration method employed herein (described in Section 5.4.8) takes this into account.

133

Number Gain Stages (n)	Effective Bandwidth
1	230 kHz
2	148 kHz
3	117 kHz
4	100 kHz
5	89 kHz

Table 5.3: Effective bandwidth of a cascade of n identical gain stages, each with a bandwidth of 230 kHz.

5.4.6 Homodyning Stage

The amplified output of the transimpedance stage ($B\sin(\omega t+\phi)$) was multiplied by the original sine and cosine signals (5 volts peak) of the quadrature synthesizer using an AD633 analog multiplier (Analog Devices, Norwood, MA) as shown in Figure 5.12. For multiplication by $A\sin(\omega t)$, the result was

$$W_{sine} = \frac{A\sin(\omega t)B\sin(\omega t + \phi)}{10} = \frac{AB}{20}(\cos(\phi) - \cos(2\omega t + \phi)) \qquad (5.7)$$

and multiplication by $A\cos(\omega t)$, resulted in

$$W_{cosine} = \frac{A\cos(\omega t)B\sin(\omega t + \phi)}{10} = \frac{AB}{20}(\sin(\phi) - \sin(2\omega t + \phi)) \qquad (5.8)$$

where the factor of 10 scaling was due to a buried Zener reference in the AD633. These output signals were low pass filtered using a fourth order butterworth filter designed using the FilterPro™ filter design program (Burr-Brown, Corp., Tucson, AZ). This filter design was chosen since it provided the flattest pass-band with moderately fast initial fall off and acceptable overshoot ($\approx 11\%$). With the filter pole set at 10 Hz, the $\sin(2\omega t + \phi)$ and $\cos(2\omega t + \phi)$ signals from the 100 Hz excitation (the lowest frequency used for measurement) were attenuated by approximately 104 dB.

To ensure proper settling of this filter for a 12 bit data acquisition, the system was allowed to stabilize for 250 msec before acquiring the data. A theoretical settling time of 132 msec was required to settle to 1 LSB of the 12 bit analog-to-digital converter (0.024% of the signal calculated assuming an exponential roll-off according to $e^{-2\pi f t_{settle}}$ where f was the fourth order pole of the filter (10 Hz) and t_{settle} was the settling time) [Franklin, et al., 1994].

The output of the LPF was amplified by a factor C yielding outputs for the sine and cosine multiplications of
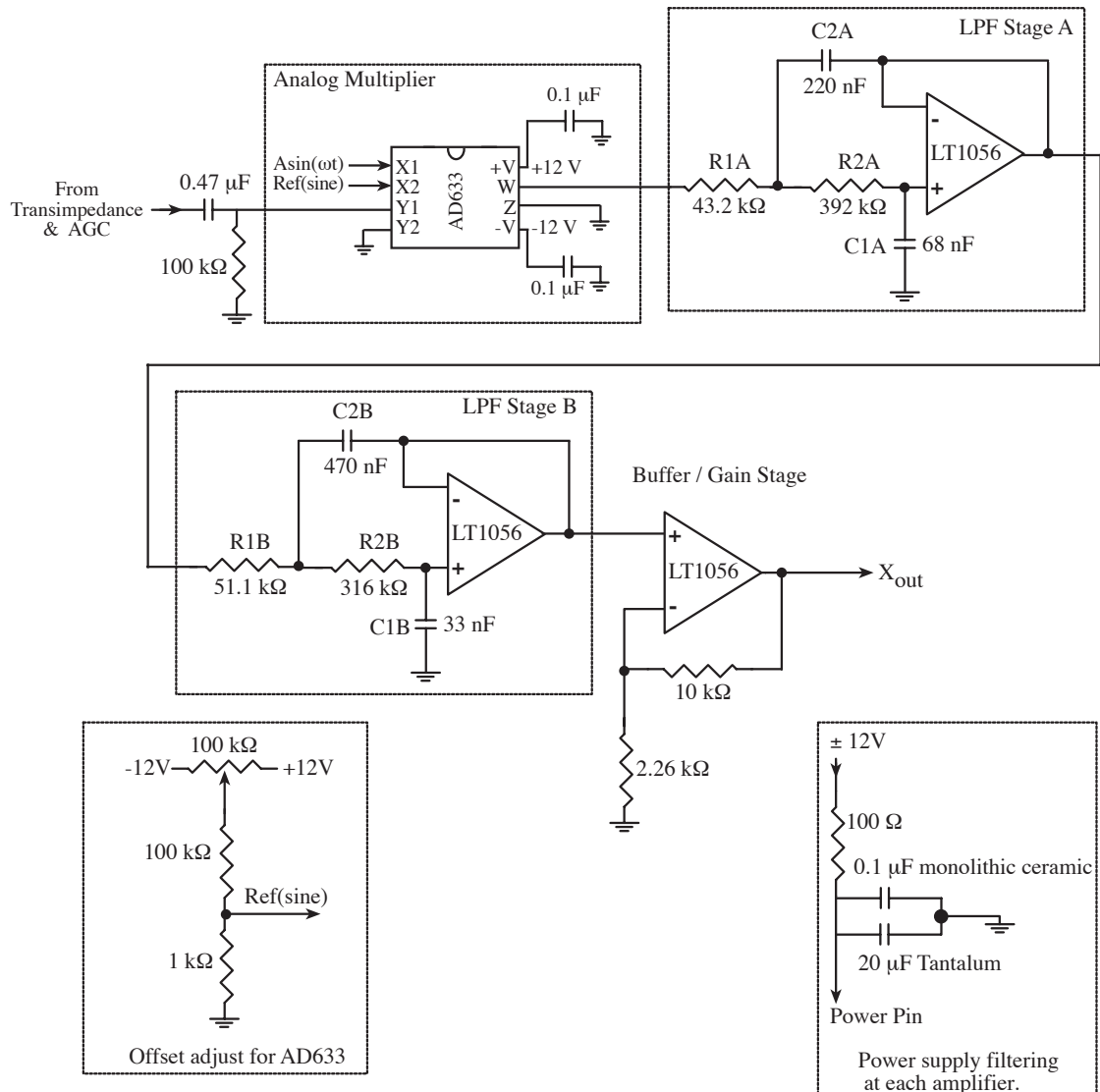
Figure 5.12: Schematic of the analog multiplier and low pass filter stages. The amplified signal from the transimpedance stage was multiplied by the original sine wave signal with an analog multiplier (AD633). A fourth order butterworth filter was then used to low pass filter the resulting signal at 10 Hz. A gain stage amplified the signal to the full dynamic range of the ADC. An identical circuit was used for multiplying by the cosine output of the quadrature synthesizer. Offsets of the analog multipliers were compensated for using the adjustment circuit shown (one for the cosine multiplication and one for the sine).

$$X_{out} = C\frac{AB}{20}\cos(\phi) \tag{5.9}$$

$$Y_{out} = C\frac{AB}{20}\sin(\phi) \tag{5.10}$$

These DC signals were routed directly to two input channels of a 12 bit ADC and used to calculate the unknown impedance. The gain of the final stage ($C \approx 5.5$) was chosen to utilize the full range of the $\pm$ 10V ADC given a maximum possible signal of

$$V_{max} = C\frac{AB}{20} = (5.5)\frac{(5)(7)}{20} = 9.6\text{volts} \tag{5.11}$$

where A was the peak voltage of the synthesizer (limited to 5 V pk for a 50 mV pk signal at the electrode array), B was the amplified signal from the transimpedance stage (limited to 7 volts peak due to the AD633 input restrictions), and a phase (ϕ) of zero or π was assumed.

5.4.7 PC Interface

Control of the analog multiplexers, AGC and measurement of the DC output of the system was accomplished using a custom interface board connected via ribbon cable to a 12-bit data acquisition card (ADA2110 by Real Time devices, State College, PA). The board consisted of two EEPROMs, two latches, and three buffers for control of the AGC relays; a latch and buffer for control of the analog MUXs (electrode selection); and a comparator and flip flop for thresholding the output of the AGC. The configuration was as shown in Figure 5.13.

All of the electronics described in Section 5.4 were implemented using printed circuit boards (PCBs) and assembled as shown in Figure 5.14. This was the configuration used for system evaluation (described below) and all experiments on electrodes and living cells (described in Chapter 7). The fluidic components labeled in the photograph will be described in Section 5.5.

5.4.8 System Calibration and Signal Interpretation

System calibration consisted of two components. First, the transfer function of each gain stage in the series following the transimpedance stage was measured using a SRS780 network analyzer (Stanford Research Systems, Inc., Sunnyvale, CA) over the frequency range of interest (100 Hz to 100 kHz). This gain magnitude and phase information (A_{v1},
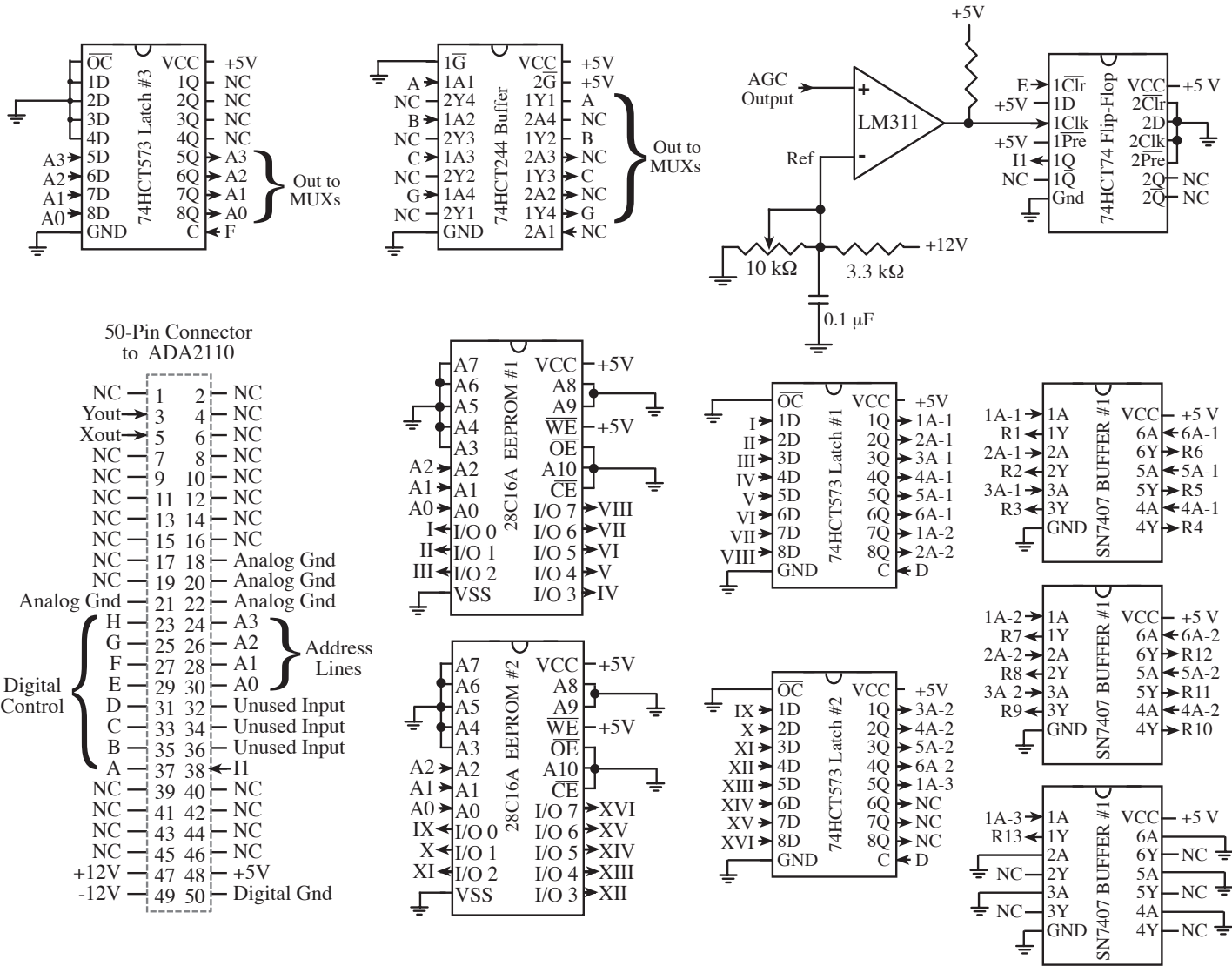
Figure 5.13: Schematic of the PC interface circuitry. The data acquisition board (ADA2110) provided digital lines used for addressing and enabling chips as well as analog and digital input lines used for monitoring the output of the homodyning stage and the voltage comparator (LM311) respectively. Address lines controlled electrode selection as well as the relays for the AGC (via the EEPROMs). The digital signals R1 to R13 controlled the relays of the AGC.
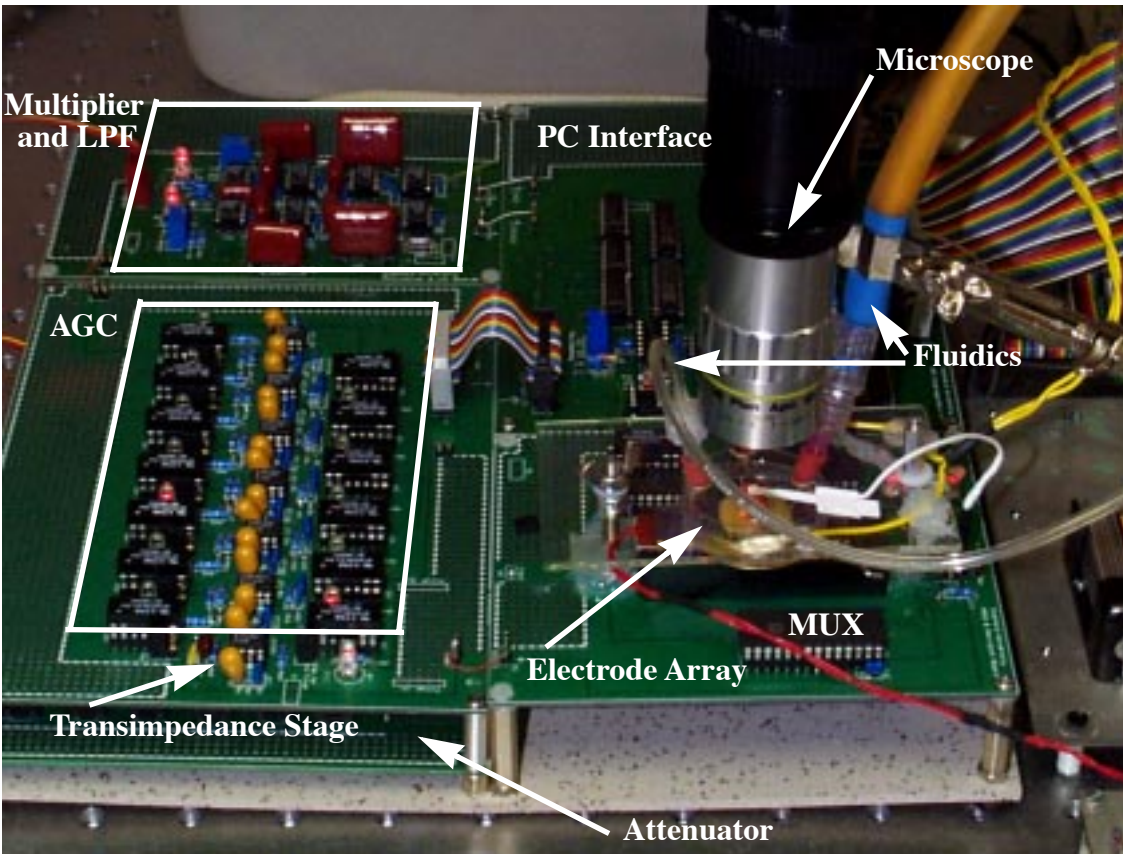
Figure 5.14: Photograph of the impedance system showing the PC interface, multiplexers for electrode selection, electrode array, transimpedance stage, AGC, analog multipliers and LPFs, and the attenuator board. Connection to the PC via a ribbon cable is shown. A video microscope allows for optical observation during experimentation. Fluidic interconnections to be described in Section 5.5 are also visible in the photograph.

ϕ_1, A_{v2}, ϕ_2, etc.) was stored in ASCII format and referenced when taking measurements as described below.

Calibration of the system was accomplished by running measurements with a calibration resistor (R_{cal} = 10.00 kΩ) in place of the unknown impedance at all frequencies of interest. Two gain stages (A_{v1} and A_{v2}) were used for the measurement to maximize the output voltage obtained. The attenuated source amplitude used for this calibration was also be used for actual measurements (making its value fall out of the final equations). The resulting DC outputs from the homodyning stage (X_{cal} and Y_{cal}) were used to calculate a *calibration* magnitude (|Cal|) and phase (ϕ_{cal}) at each frequency using

$$|Cal| = \sqrt{X_{cal}^2 + Y_{cal}^2} \qquad (5.12)$$

$$\phi_{cal} = atan\left(\frac{Y_{cal}}{X_{cal}}\right) \qquad (5.13)$$

During actual measurements, a *measurement* magnitude ($|meas|$) and phase (ϕ_{meas}) were calculated using the DC outputs (X_{meas} and Y_{meas}) and equivalent formulas to (5.12) and (5.13). By taking the ratio of the measured and calibrated magnitudes (using equations (5.4), (5.5), (5.9) and (5.10)) and rearranging, the unknown impedance could be determined:

$$|Z_{unknown}| = (R_{cal}) \cdot (A_{v_{gainstages}}) \cdot \left(\frac{|Cal|}{|meas|}\right) \qquad (5.14)$$

$$\phi_{unknown} = \phi_{gainstages} + \phi_{cal} - \phi_{meas} \qquad (5.15)$$

where $Av_{gainstages}$ and $\phi_{gainstages}$ were determined for each frequency from the stored transfer function data compiled as shown in Table 5.4. Note that for two gain stages (the number used in calibration) no changes to the measured impedance magnitude and phase were necessary. In all cases, adjustments to the calculated phases were made to account for phase sign errors associated with ambiguity in the tangent function.

Number Gain Stages -->	0	1	2	3	4	5
$Av_{gainstages}$	$(A_{v1} \cdot A_{v2})^{-1}$	$(A_{v2})^{-1}$	1	A_{v3}	$A_{v3} \cdot A_{v4}$	$A_{v3} \cdot A_{v4} \cdot A_{v5}$
$\phi_{gainstages}$	$-(\phi_1 + \phi_2)$	$-\phi_2$	0	ϕ_3	$\phi_3 + \phi_4$	$\phi_3 + \phi_4 + \phi_5$

Table 5.4: Transfer function data stored and used to extract the actual unknown impedance from the measurement. The gain terms represent $Av_{gainstages}$ in (5.14) while the phase terms represent $\phi_{gainstages}$ in (5.15). The term used was dependent on the total number of gain stages used in the actual measurement.

The above two-part calibration method involving measurement and storage of the gain stage characteristics was necessary for this system due to the large dynamic range of the instrument. The use of different known value resistors to calibrate the full range of gain stages was explored, but difficulties were encountered with both noise and resistor value accuracy (for high impedance resistors). These problems made this method of self-calibration less accurate than the one described above.

5.4.9 Software User Interface

Custom software written in the Pascal based language Delphi was developed to operate the impedance system described above and provide a user friendly interface. Prototyping software was developed by Scott Petersen (U.C. Davis) and the current windows based program was developed by Derek DeBusschere (Stanford University). It allowed the user to choose source amplitude and frequencies, the number of sweeps to run, time delay between successive sweeps and the electrode sites to monitor as shown in Figure 5.15. The source amplitude was required to match that used in the calibration sequence to limit measurement errors as described in Section 5.4.8. Calibration files were created as shown in Figure 5.16 where the desired source amplitude and frequencies were
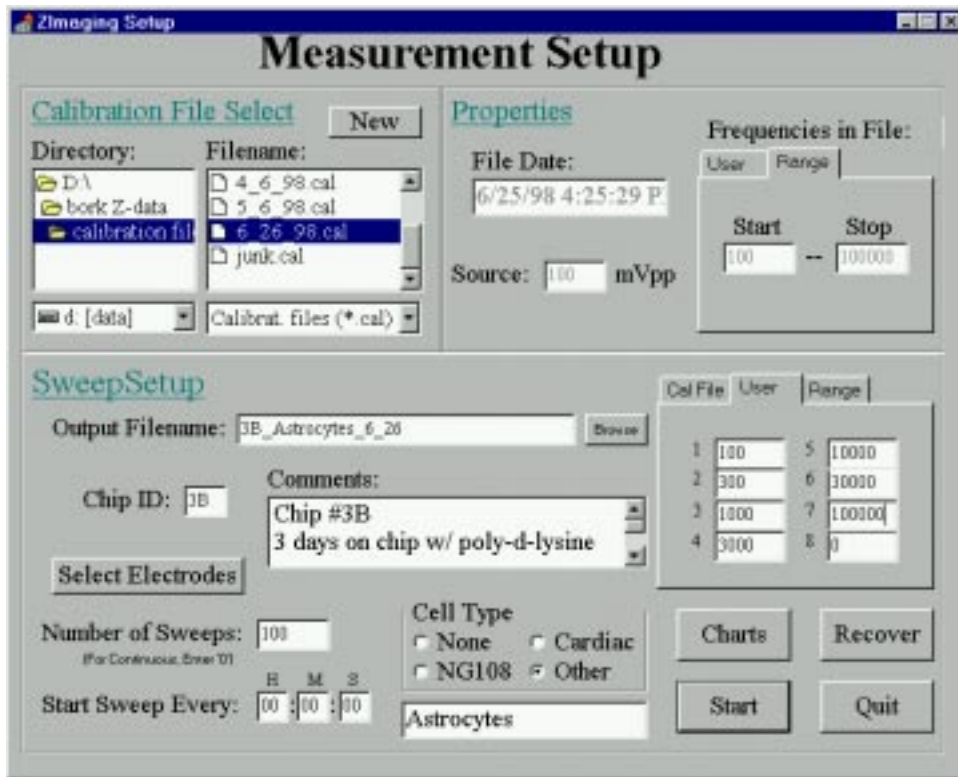
Figure 5.15: Main impedance measurement system software screen. The user chooses a calibration file (or creates a new one) and the source amplitude and allowable frequencies are displayed. Measurement frequencies can be all those used in calibration, up to eight discrete frequencies or a range of frequencies. Electrode selection, number of sweeps, time between sweeps and output filename can also be chosen.

140
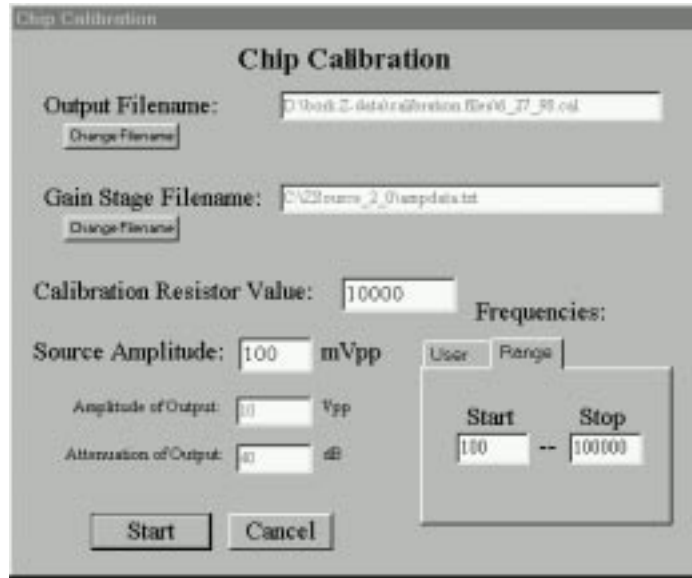
Figure 5.16: Calibration screen showing filename, hardware (gain stage) characteristics file, calibration resistor value, source amplitude, and desired frequencies.

entered. Frequency ranges provided measurements at integer multiples of the frequency (e.g. 100 Hz to 5000 Hz would be measured at 100, 200, 300, 400, 500, 600, 700, 800, 900, 1000, 2000, 3000, 4000, and 5000 Hz). This calibration file could be used for measurements at any or all of these frequencies.

During measurements, a representative picture of the electrode array was displayed (see Figure 5.17) with the real and imaginary (or magnitude and phase) components of the impedance updated in real time next to each electrode. Text could be added to the comment window at any time. An integrated charting program allowed real-time presentation of impedance (real, imaginary, magnitude, phase) versus the sweep number, time or frequency for any or all of the electrodes being monitored as shown in Figure 5.18.

Data was stored in ASCII format, organized either by frequency or sweep number for all electrodes. This allowed for external evaluation of the data as will be presented in Chapter 7. Raw binary files were also stored so that the impedance software charting program could be used to examine old data without using external software packages.
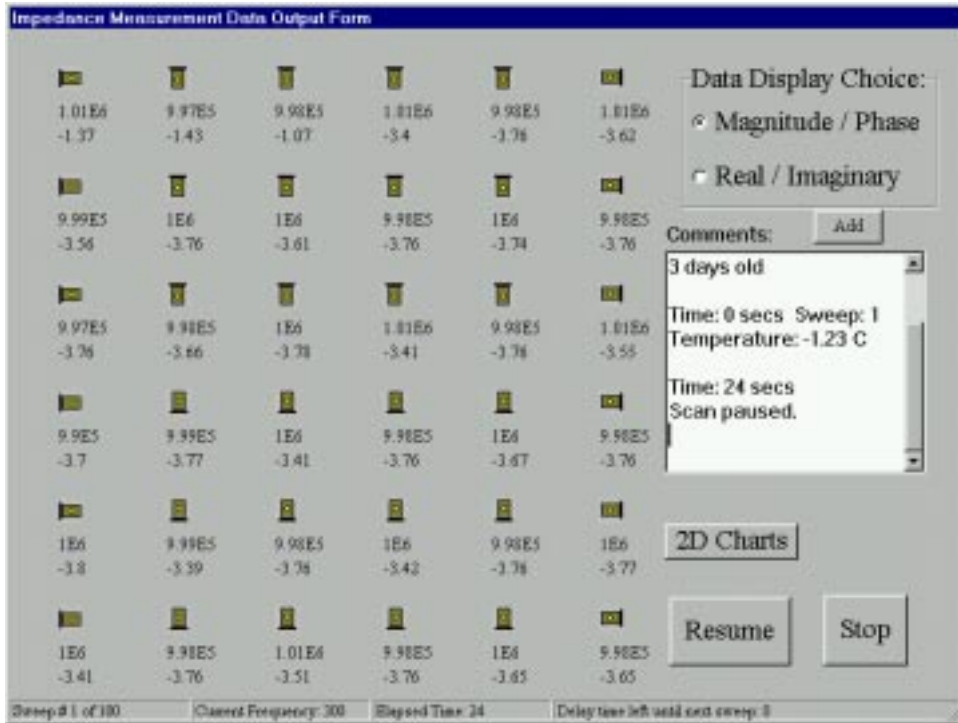
Figure 5.17: Display screen during measurements showing a schematic of the electrode array and the corresponding impedance. Comments could be added at any time.

5.4.10 System Performance

With all portions of the electronics (signal source, MUXs, transimpedance stage, AGC, analog multipliers, LPF, and PC interface) working as anticipated, the capabilities of the system were evaluated using precision resistors as shown in Figure 5.19. The error values shown were calculated from discrete measurements of known value resistors at the locations of the arrows. The shading represents the gradual deterioration of measurement accuracy. From this data it can be seen that the system as developed should accurately measure impedances of several hundred MΩ with less than 10% error, and impedances of tens of MΩ with less than 5% error.

The measured impedance for a dry packaged electrode array (glass substrate) was also plotted versus frequency (Figure 5.19). This impedance was equivalent to a 530 fF capacitance and represented the upper bound of measurable impedance using this system. For impedances above this line, the parasitics would begin to dominate the measurement.

142
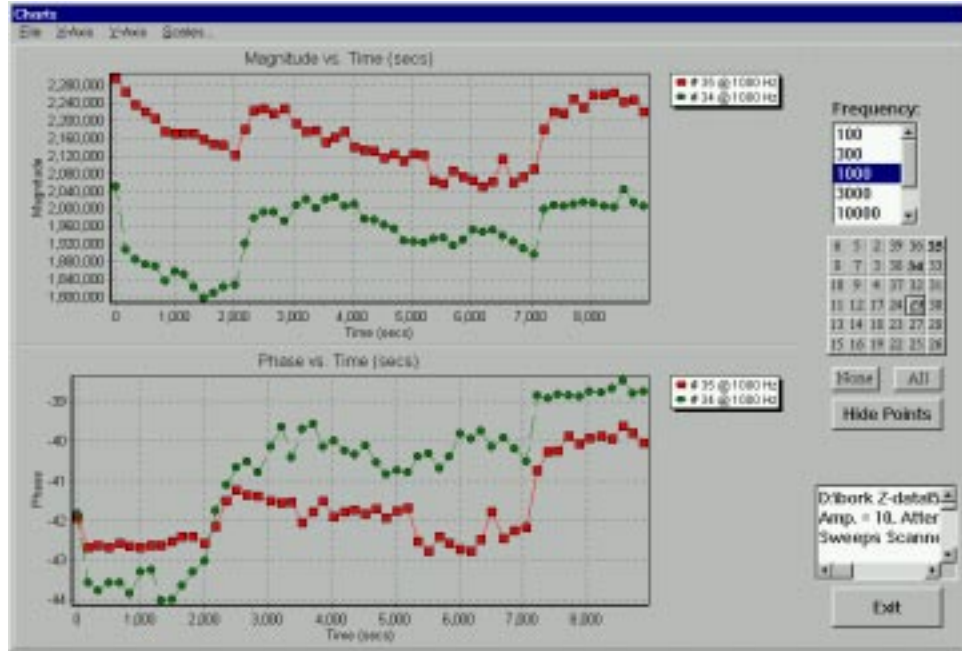
(a)
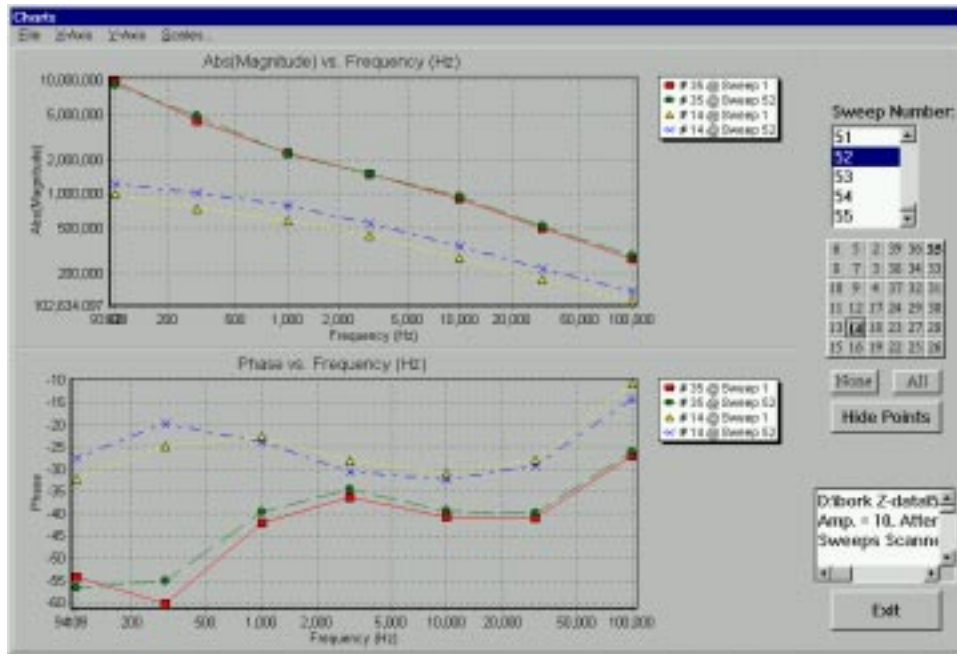
(b)

Figure 5.18: Integrated real-time impedance charting program. (a) Impedance magnitude and phase (or real and imaginary) plots vs. time (or sweep number). Any combination of frequencies and electrodes could be monitored at any time. (b) Impedance vs. frequency for any sweep and electrode combination. This program could also be used to plot data from previous experiments.

143
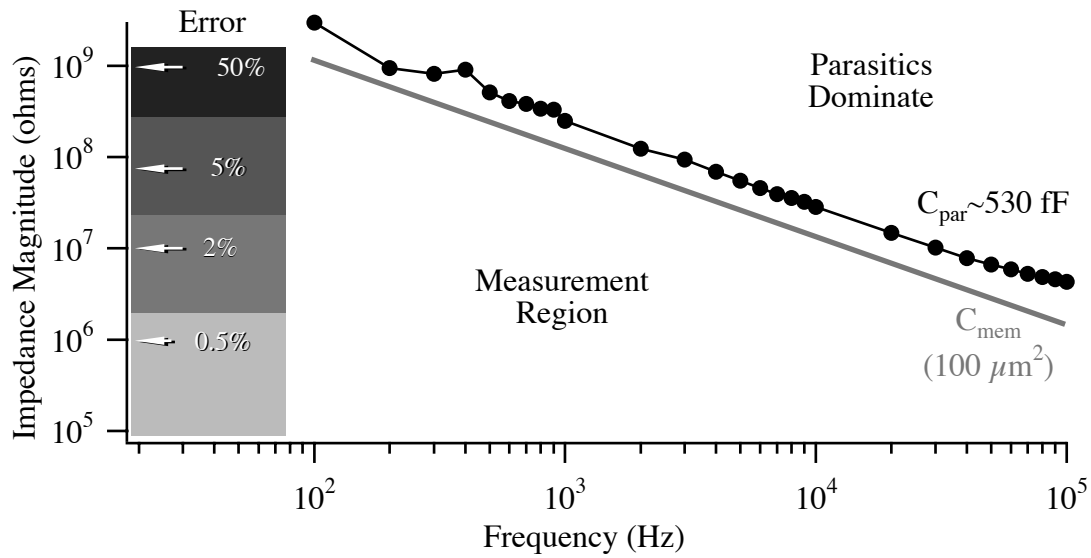
Figure 5.19: Plot of impedance system measured performance. Impedance data with a packaged electrode array (glass substrate) without saline is represented by the dark line with dots. This is equivalent to a 530 fF parasitic capacitance and represents the upper bound for measurable impedances using this system. For reference, the capacitive impedance of a 100 μm^2 portion of cellular membrane is also shown. The error values given are for discrete measurements of known value resistors.

As a reference, the equivalent capacitive impedance of a 100 μm^2 section of cellular membrane (assuming 0.01 pF/μm^2 [Hille, 1992]) was also shown. Note that the system should be capable of resolving this impedance.

5.5 Fluidic and Thermal Regulation Systems

A continuous flow fluid system was developed to allow for perfusion of different media over the cultured cells while maintaining consistent mechanical and thermal characteristics within the cell culture dish. In this way, any changes in cellular behavior could be attributed to a biological response to the toxin or pharmaceutical being tested rather than a change in the environment of the cells. As shown in Figure 5.20, the fluidic system consisted of four reservoirs of recording medium (physiologically balanced salt solutions) positioned approximately one meter above the electrode array. Filtered air was continuously bubbled through these solutions to ensure full oxygenation of the fluids.
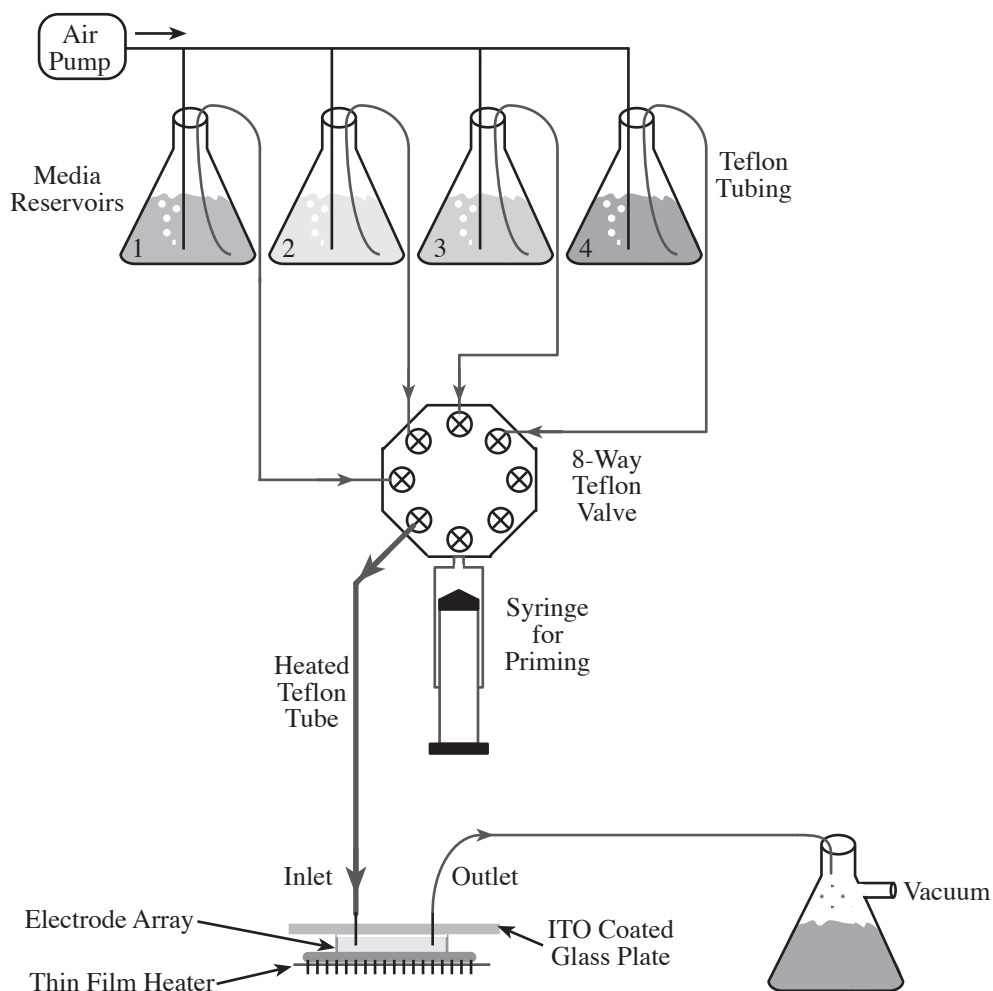
Figure 5.20: Block diagram of the fluidic and thermal systems. The fluid flow from the reservoir to the electrode array was siphon driven. An 8-way valve allowed connection of the medium reservoir(s) to either a syringe (for priming of the system) or to the electrode array. The tubing from the valve to the electrode array heated the fluid to 37°C prior to entering the dish. This combined with a thin film heater below the electrode array package and a resistively heated ITO glass plate positioned over the cell culture chamber maintained the cells at approximately 37°C. A line connected to house vacuum removed excess media from the electrode array.

Teflon tubing (0.422" I.D., 0.66" O.D.) was used to connect the reservoirs to an 8-way teflon valve, allowing any or all to be connected to either a syringe (for priming the system) or a single output to the cell culture chamber. The tubing between the valve and the electrode array was teflon (0.32" I.D., 0.66" O.D.) wrapped with approximately 20 feet of 3 mil, teflon coated platinum wire for resistive heating of the medium prior to entering the chamber. Rubber tubing and silicone sealant insulated this heated tubing. The output

line was coupled to a house vacuum supply to actively draw off the waste medium. Both inlet and outlet connections to the electrode array were made using needles coupled to the tubing using luer-lock connectors. The inlet flow rate was set to approximately 1.5 ml/min by the height of the medium reservoirs and the fluidic resistance of the tubing (determined by tubing length and diameter).

The packaged electrode array was placed in the recording system over a thin film heater (Minco Products Inc., Minneapolis, MN) which was maintained at 37°C as described below. A glass plate coated with a transparent, conductive oxide (indium tin oxide or ITO) was used to cover the cell culture chamber. Electrical current flowing through the ITO resistively heated the glass to prevent condensation and permit optical observation during experiments. Four hole in this plate allowed insertion of a temperature probe, the coiled Pt wire counterelectrode, and the needles for medium input and output.

Thermal regulation of the cell culture chamber at 37°C was accomplished by both the heated fluid flow, and direct heating of the electrode array package as described above.
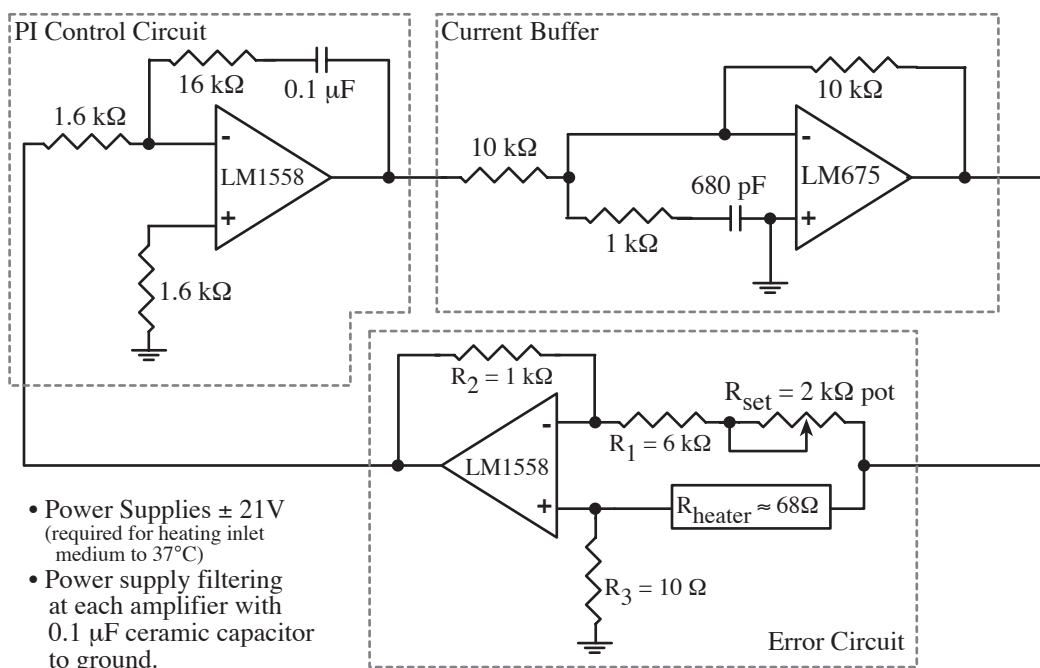
Figure 5.21: *Temperature control circuit. A unity gain current buffer drove the heater element causing the resistance to increase in response to rising temperature. The 2 kΩ potentiometer was used to define the temperature set point. When the ratio of R_{heater} to R_3 was the same as the ratio of ($R_1 + R_{set}$) to R_2, the error signal driving the PI control circuit was zero. This was used to drive the thin film heater situated below the electrode array package as well as the fluidic heating tube.*

The resistive heaters were controlled by identical, custom proportional-integral (PI) controllers which used the thermal coefficient of resistance (TCR) of the metals for closed loop control. The thermal regulation system (Figure 5.21) consisted of a PI control circuit, a current buffer, and an error circuit. The PI control circuit had a pole at DC and a single zero at 100 Hz, with a fixed gain of 20 dB above that frequency. The combination of the current buffer and error circuit had a fixed gain of -40 dB across a 10 kHz bandwidth, making the composite, closed-loop system stable (-20 dB gain above 100 Hz). While the control loop was slow (approximately 1 to 10 Hz), it was significantly faster than the measured thermal time constant of the cell culture system ($\tau > 3$ sec).

The heating element (either the Pt wire wrapped around the inlet tubing or the thin film heater) was part of the error circuit as shown in Figure 5.21. Electrical current supplied to the resistive heater caused a temperature dependent change in the resistance of the metal which was sensed by the error circuit. An error signal was generated if $\frac{R_{heater}}{R_3} \neq \frac{(R_1 + R_{set})}{R_2}$. This error signal was processed by the PI control circuit which drove the unity gain current buffer. The potentiometer (R_{set}) was used to set the desired temperature.

Using a controller circuit for each heating element (one for the thin film heater below the electrode array package and one for the platinum wire wound around the fluidic heating tube) allowed temperature regulation at the chip surface of ± 0.3°C around the set point of 37°C. This was verified by placing a thermistor probe at the surface of the electrode array and monitoring the temperature variations over a one hour time period. The fluidic and thermal regulation systems were used for both the action potential and impedance based measurement systems.

5.6 Summary

Two systems for monitoring cells cultured on planar microelectrode arrays were developed; one was based on action potential measurements while the other was impedance based. The action potential system consisted of two integrated 18 channel amplifier / filter arrays that were AC coupled to the electrode sites. These amplifiers directly drove a ribbon cable connection to the PC where action potential data was digitally collected and stored. This system was shown to provide a stable means of monitoring the extracellular action potential of cultured embryonic chick myocardial cells.

The impedance system consisted of circuitry that connected a sinusoidal signal of known amplitude and frequency to one electrode in the array at a time. The resulting current was collected using a coiled platinum wire immersed in the recording media by a

transimpedance amplifier that converted the current to a voltage. This voltage was then amplified by a controllable gain stage, multiplied in quadrature, and low pass filtered to provide the real and imaginary components of the unknown impedance. The electrodes were designed so that this impedance would be dominated by the cells cultured over the electrode. The system as designed was capable of measuring cellular membrane properties given a sufficiently high seal resistance.

A fluidic and thermal regulation system was developed for use with both the impedance and action potential measurement systems. Fluid flow was siphon driven with the flow rate controlled by the fluidic resistance of the system. A total of four reservoirs were used to allow several different pharmaceuticals or toxins to be tested in a single experiment. The fluid was heated to 37°C prior to entering the electrode array dish. This heated fluid along with a thin film heater directly beneath the electrode array package allowed thermal regulation of ± 0.3°C at the desired temperature of 37°C.

While these systems were based around an electrode array packaged in a standard 40 pin DIP, the general approach could be easily integrated into future systems with different packaging configurations. The design considerations explored for both impedance and action potential measurements are relevant regardless of the form factor utilized for the cell culture chamber. The unifying theme is transduction of biological signals using microelectrodes and the collection of that information.

References

Borkholder, D.A., Opris, I.E., Maluf, N.I. and Kovacs, G.T.A., "Planar Electrode Array Systems for Neural Recording and Impedance Measurements," *Conference Proceedings of the 1996 IEEE Engineering in Medicine and Biology*, Amsterdam, The Netherlands, 10/31-11/3 (1996).

Breckenridge, L.J., Wilson, R.J.A., Connolly, P., Curtis, A.S.G., Dow, J.A.T., Blackshaw, S.E. and Wilkinson, C.D.W., "Advantages of using microfabricated extracellular electrodes for in vitro neuronal recording," *Journal of Neuroscience Research*, 42:266-276 (1995).

Cobbold, R.S.C., *Transducers for biomedical measurements*, John Wiley and Sons, New York (1974).

Cole, K.S. and Curtis, H.J., "Electrical impedance of the squid giant axon during activity," *Journal of General Physiology*, 22(5):649-670 (1939).

Connolly, P., Clark, P., Dow, J.A.T., Curtis, A.S.G., Lind, R. and Wilkinson, C.D.W., "Extracellular electrodes for monitoring cell cultures," Institute of Physics Short Meeting Series No. 21 (IOP Publishing, UK), (1989).

Dijkstra, A.M., Brown, B.H., Leathard, A.D., Harris, N.D., Barber, D.C. and Edbrooke, D.L., "Clinical applications of electrical impedance tomography," *Journal of Medical Engineering and Technology*, 17(3):89-98 (1993).

Franklin, G.F, Powell, J.D. and Emami-Naeini, A., *Feedback control of dynamic systems*, Addison -Wesley Publishing Company, New York, NY (1994).

Giaever, I. and Keese, C.R., "Use of electric fields to monitor the dynamical aspect of cell behavior in tissue culture," *IEEE Transactions on Biomedical Engineering*, BME-33(2):242-247 (1986).

Hille, B., *Ionic Channels of Excitable Membranes*, Sinauer Associates, Inc., Sunderland, Massachusetts (1992).

Hodgkin, A.L. and Huxley, A.F., "A quantitative description of membrane current and its application to conduction and excitation in nerve," *J. Physiol.*, 117:500-544 (1952).

Kewley, D.T., Hills, M.D., Borkholder, D.A., Opris, I.E., Maluf, N.I., Storment, C.W., Bower, J.M. and Kovacs, G.T.A., "Plasma-Etched Neural Probes," S*ensors and Actuators*, A58:27-35 (1997).

Lee, T.H., *The design of CMOS radio-frequency integrated circuits*, Cambridge University Press, New York, NY (1998).

Lind, R., Connolly, P., Wilkinson, C.D.W., Breckenridge, L.J. and Dow, J.A.T., "Single cell mobility and adhesion monitoring using extracellular electrodes," *Biosensors and Bioelectronics*, 6:359-367 (1991).

Metting van Rijn, A.C., Peper, A. and Grimbergen, C.A., "High-quality recording of bioelectric events: Part 1 - interference reduction, theory and practice," *Medical and Biological Engineering and Computing*, 28:389-397 (1990).

Metting van Rijn, A.C., Peper, A. and Grimbergen, C.A., "High-quality recording of bioelectric events: Part 2 - Low-noise, low-power multichannel amplifier design," *Medical and Biological Engineering and Computing*, 29:433-440 (1991).

Motchenbacher, C.D. and Fitchen, F.C., *Low-noise electronic design*, John Wiley and Sons, New York, NY (1993).

Schwan, H.P., "Electrical properties of tissue and cell suspensions" in *Advances in Biological and Medical Physics*, Edited by Lawrence, J.H. and Tobias, C.A., Academic Press, New York, 5:147-209 (1957).

Schwan, H.P., Schwartza, G., Maczuk, J. and Pauly, H., "On the low-frequency dielectric dispersion of colloidal particles in electrolyte solution," *Journal of Physical Chemistry*, 66:1217-2754 (1962).

Schwan, H.P., "Biological effects of non-ionizing radiations: cellular properties and interactions," *Annals of Biomedical Engineering*, 16:245-263 (1988).

Chapter 6   SENSORS BASED ON CHANGES IN ACTION POTENTIAL MORPHOLOGY

Choose which way you would like to be wrong...

Joseph Pancrazio, 1998

6.1 Introduction

The use of extracellular microelectrodes for monitoring the electrical activity of cultured cells was described in detail in Chapter 1. Historically these studies have been limited to examination of conduction velocity [Israel, et al., 1990; Maeda, et al., 1995] and spike train characteristics [Drodge, et al., 1986; Gross, et al., 1992] as the culture conditions or media composition was changed, or as pharmaceuticals or toxins were applied to the cell culture. There has been no reported work examining changes in action potential (AP) morphology. By monitoring the *shape* of the action potential in addition to the amplitude and spontaneous firing rate, it may be possible to extract significantly more information about the cellular response to a pharmaceutical or toxin than was previously possible.

The use of extracellular electrodes to monitor changes in the action potential of spontaneously beating chick myocardial cells is explored in detail in this chapter. The discussion begins with a brief description of the myocardial cells and protocols for their culture. The characteristics of the extracellular action potential is then described, focusing on the nature of the recorded signal and how it relates to the transmembrane potential and ionic flux through the cellular membrane. The use of power spectral density analysis is

then discussed as a means of examining how the shape of the action potential changes with addition of channel-specific agents. Experimental results and simulations are presented for three pharmaceuticals tested on the embryonic chick myocardial cells. The possible use of the PSD technique for deducing the action of an unknown agent is then discussed.

6.2 Cell Information and Protocols

Embryonic chick myocardial cells were cultured on planar microelectrode arrays and used in studies of action potential spectral power changes due to the action of pharmaceuticals and toxins. The basic characteristics of this cell type are presented along with protocols for their culture.

6.2.1 Embryonic Chick Myocardial Cells

When embryonic chick myocardial cells are cultured *in vitro*, they attach to the surface and slowly move together to form a confluent sheet of cells. These cells are connected electrically by gap junctions as described in Chapter 2 and form a *syncytium* (a sheet of physically and electrically interconnected cells). The spontaneous, rhythmic electrical activity of such cellular populations is thought to be due to reduced K^+ efflux causing a slow depolarization of a single cell. As the threshold transmembrane voltage is reached, an action potential is initiated. Following repolarization of the cell, the process repeats, resulting in rhythmic firing of action potentials. These action potentials travel through the syncytium causing depolarization of neighboring cells and a resulting contraction which may be visually observed.

It is important to recall that there are numerous cell types within the heart (pacemaker cells, atrial cells, ventricular cells, etc.), each of which has a different resting membrane potential and different populations of ionic channels. The result is a unique action potential shape associated with the various cell types. For a culture of cells extracted from living organisms, the makeup of the cellular population is not known precisely, making exact prediction of the electrical characteristics difficult. However, it is still possible to extract useful information from the measurement of these cardiac action potentials.

As mentioned in Chapter 2, for atrial and ventricular cells (which make up the majority of the cardiac tissue) there is a rapid depolarization of the cell membrane most likely due to fast acting Na^+ channels, and a plateau phase due to influx of Ca^{2+}. Thus, the pharmacological studies explored in this research focused on these channels.

6.2.2 Cell Culture Protocol

Methods for the culture of embryonic chick myocardial cells are described in detail in Appendix C and generally follow the procedures developed by [De Hann, 1967; Polinger, 1970; and Barry, et al., 1975]. Briefly, fertilized chicken eggs were incubated at 100 °F for 11 days. The developing embryos were removed from each egg and placed in a large petri dish where the head was immediately severed from the body. Following removal of all 36 embryos from the eggs, the hearts were carefully removed from the body and placed in an isotonic salt solution where the arteries could be removed and blood released from the heart chambers. The cardiac tissue was then transferred to another petri dish containing isotonic salt solution where it was diced into fragments small enough to be pulled into a 10 ml pipette and transferred to a trypsinization flask.

The tissue fragments were dissociated into individual cells by repeated *trypsinization* (use of an enzyme treatment to attack proteins holding the cells together). Any large tissue fragments remaining following this procedure were removed by flowing the cell suspension through a cell strainer. The resulting cells (a combination of unwanted fibroblasts and the desired myocytes) were separated from the solution by centrifugation and resuspended in cell culture media. Separation of these cell types was accomplished by a differential adhesion technique [Polinger, 1970] where the cells were incubated in a cell culture dish for 45 minutes. The fibroblasts quickly adhered to the substrate during this time period while the myocytes did not. Removal of the culture media followed by gentle rinsing of the surface was sufficient to collect most of the myocytes while leaving the fibroblasts behind. Following centrifugation and resuspension in culture media, the cells were *plated* onto the chip surface at a density of approximately 1,000 cells / mm^2. This *plating* procedure consisted of injecting the cell suspension over the electrode array and allowing the cells settle out of solution and adhere to the substrate. Spontaneous activity was generally observed (via observation of mechanical motion) one or two days later.

6.3 Extracellular Action Potential Monitoring

Following culture of embryonic chick myocardial cells on microelectrode arrays as described above, APs were measured from the spontaneously beating, two-dimensional sheet of cells two to four days after plating. An optical image of cells cultured on the microelectrode array and typical action potential recordings are shown in Figure 6.1. Note the time delay between AP peaks, corresponding to the finite propagation velocity (approximately 0.95 m/s in this case) of the action potential wavefront through the tissue.
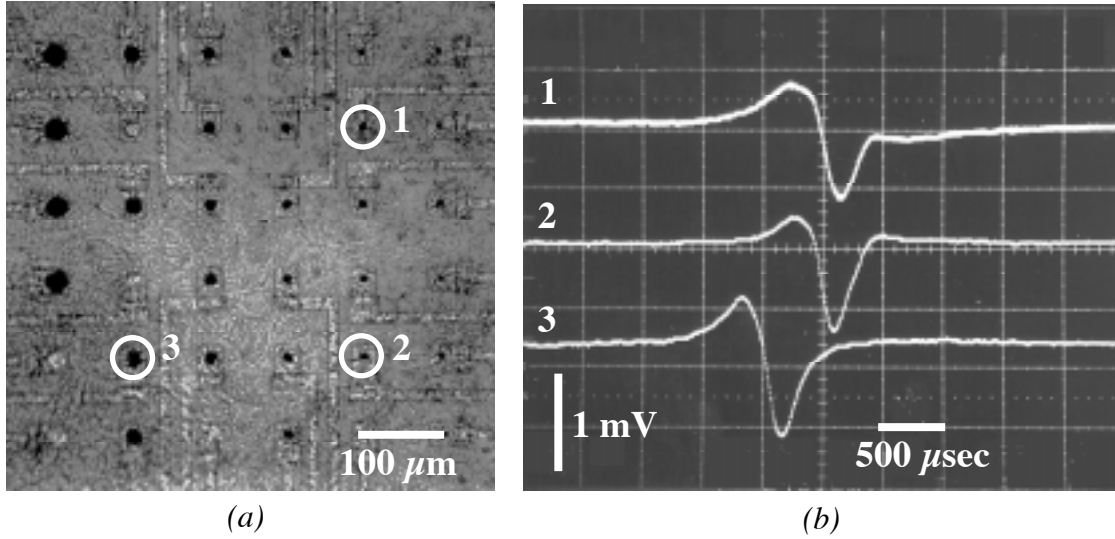
Figure 6.1: (a) Optical view of embryonic chick myocardial cells cultured on the microelectrode array. Spontaneous APs recorded extracellularly from the circled microelectrodes are shown in (b). The time delay observed between action potentials is due to the finite propagation velocity of the traveling action potential through the two dimensional sheet of cells.

This propagation velocity corresponds well with published human atrial and ventricular conduction rates of 1 m/s [Ganong, 1993].

6.3.1 Recorded Action Potential Shape

As described in Chapter 3, the extracellular voltage monitored from cells cultured over a microelectrode array is due to the flow of current by (or through) the electrode. Recall that for a wave traveling down a cylindrical axon (from core conductor theory), the total transmembrane current is given by:

$$I_{total} = K\frac{d^2V_m}{dt} = C_m\frac{dV_m}{dt} + I_{ionic} \tag{6.1}$$

$$K = \frac{a}{2Rv^2} \tag{6.2}$$

where V_m is the transmembrane potential, C_m is the membrane capacitance per unit area, and I_{ionic} is the current due to flow of ions through ionic channels in the cellular membrane. The constant K is dependent on the radius of the fiber (a), the axoplasm resistance (R) (which may be loosely correlated to the seal resistance (R_{seal})), and the

conduction velocity (v). For the case of cultured cardiac cells, the system is not a cylindrical conductor and this equation will not hold exactly. The relationships involved with the determination of the constant K are different, making extrapolation of the seal resistance and conduction velocity impossible from the measured action potential data using (6.1) and (6.2). Development of suitable equations for the case of a sheet of cells cultured over an electrode array was beyond the scope of this work. However, the general assumptions of local current loops (flow through the membrane, along the exterior of the cell, back through membrane and along the interior of the cell) still hold for the case of traveling waves. Since traveling wave behavior was observed, (6.1) can act as a general guideline for the anticipated relationship between the total membrane current and the transmembrane potential.

Assuming that (6.1) will generally hold for the case of a traveling wave in a sheet of cardiac tissue, it is expected that the total current will be proportional to the second derivative of the transmembrane potential. The current will flow through the seal resistance, generating a potential at the electrode equal to the product of I_{total} and R_{seal}. This voltage is transduced by the electrode to provide either a replica of the second derivative of the transmembrane voltage or a third derivative of membrane potential as described in Chapter 3. For the electrodes utilized herein, the impedance was almost purely capacitive in the frequency range of interest. However, combined with the $1 M\Omega$ resistance to ground at the amplifier input, the pole was at a low enough frequency so that the AP was not differentiated. Thus, second derivative behavior was observed.

To explore the effects of amplifier loading on the recorded action potential shape, the AC coupling resistors to ground (at the amplifier input) were varied. As outlined in Chapter 3, both the seal resistance of the cell to the electrode and the parasitic current paths between the electrode and the amplifier can significantly alter the shape of the recorded action potential. It is theoretically possible for the extracellular AP to change from a close approximation to the intracellular AP to the third temporal derivative. Since alteration of the seal resistance was not practical in a controlled manner, the parasitics between the electrode and the amplifier input were varied by alteration of the resistance to ground. As the resistance was increased from $1 M\Omega$ to $10 M\Omega$, the signals became slightly larger since the total signal attenuation changed from 5% to approximately 1% (electrode impedance was approximately $50 k\Omega$ at 1 kHz). The shape of the AP did not change. As the resistance to ground was lowered to $100 k\Omega$, significantly more signal attenuation was observed. Further reduction to $10 k\Omega$ was expected push the pole (formed by the capacitive electrode and the resistance to ground) out to several thousand hertz. Since all

of the recorded AP power was below approximately 3000 Hz, this higher pole location should have resulted in an additional derivative due to electrode transduction. However the signal at this point was too small to be measured, and third derivative behavior was not observed.

6.3.2 Action Potential Power Spectral Density

As described in Chapter 2, the gating of ion channels may be described by a first order reaction [Hodgkin and Huxley, 1952] according to

$$I_{ionic} = \bar{I}_K n^4 + \bar{I}_{Na} m^3 h + \bar{I}_{Ca} df + \bar{I}_l \tag{6.3}$$

where I_{ionic} is the total ionic current through the membrane, $\bar{I}_K$, $\bar{I}_{Na}$, $\bar{I}_{Ca}$, and $\bar{I}_l$ are the maximum currents associated with K^+, Na^+, Ca^{2+} and leakage respectively, and n, m, h, d and f are gating variables. Each of these channel types has a characteristic activation and inactivation time constant that is dependent on both temperature and the transmembrane voltage. These unique time constants result in unique spectral characteristics for the opening and closing of channels in a steady state condition. By examination of the spectral noise present in ionic currents (steady state), it is possible to deduce the ionic channel type contributing to the noise [Stevens, 1972; Neumcke, 1982; Hille, 1992] under voltage clamp conditions.

For the case of an action potential where the transmembrane voltage is dynamically changing, the situation is more complex. In this case the gating variables for each channel type are changing (due to their voltage dependence) making clear spectral characteristics due to specific channels difficult to predict based on classic Hodgkin and Huxley theory. However, this does not preclude the existence of unique power contributions due to specific classes of ion channels. By computing the power spectral density (PSD) of measured action potentials both before and after blockage (or enhanced opening) of a specific class of ion channel via pharmacological manipulation, a spectral signature may become apparent. If different signatures are observed for different classes of ion channels (Na^+, K^+, Ca^{2+}, etc.) then it may be possible to use PSD analysis to generally classify the action of an unknown pharmaceutical or toxic agent. Preliminary studies have been done to examine this theory using extracellular recordings from embryonic chick myocardial cells. The basic procedure was to take the ratio of the AP PSD after addition of a channel-specific agent to the PSD prior to this. In this way, a *modulation function* was developed in the hope that unique signatures across frequency could be observed for agents acting on different classes of ion channels.

For these experiments the power spectral density was calculated by first applying a Hanning window to a single AP and then taking the fast fourier transform (FFT). Multiplication of the resulting complex waveform by its complex conjugate and dividing by the frequency range of the FFT provided an estimate of the power spectral density for the AP waveform. Averages of 20 APs both before and after addition of the channel-specific agent were used to calculate the PSD ratio described above. The frequencies corresponding to each PSD bin were calculated based on the sampling rate (in this case 40 kHz) and the total number of samples taken (in this case ≈ 400).

6.4 Action Potential Simulation using HSPICE

Simulation of spontaneous action potentials was carried out with the circuit simulator HSPICE using Hodgkin-Huxley type models developed for bullfrog atrial cells [Rasmusson, 1990] as described in detail in Appendix D. While differences between the chick and bullfrog were likely, the availability of suitable models was extremely limited. Additionally, the precise composition of the chick cardiac cell population in culture was not known (some combination of atrial, ventricular, and sinoatrial node cell types), making exact modeling difficult. In this system, the cell membrane was modeled as a capacitance in parallel with a number of conductive ionic channels. The model was modified to include two cells connected by a resistive gap junction to simulate the normal electrical connections between cardiac cells. One cell was stimulated using a current pulse, initiating an AP which in turn elicited an AP in the second cell. Simulated results were obtained from this second action potential and compared to those obtained experimentally.

The simulation parameters were slightly modified to provide an intracellular signal similar in shape and duration to those published for embryonic chick myocardial cells *in vitro* [Connolly, 1990]. The second time derivative was then taken to estimate the recorded extracellular signal. The resulting waveforms are shown in Figure 6.2. Note the shape and duration of the second derivative signal are similar to the actual action potentials recorded in Figure 6.1.

As can be seen from the waveforms of Figure 6.2, the second derivative signal is dominated by the rising edge of the AP. While there are components of this signal due to the plateau phase and repolarization of the AP, the rate of change is low enough that the second derivative signal is lost in the noise. Thus, all extracellularly recorded signals were dominated by the rising edge of the action potential. Focusing in on this region, as shown
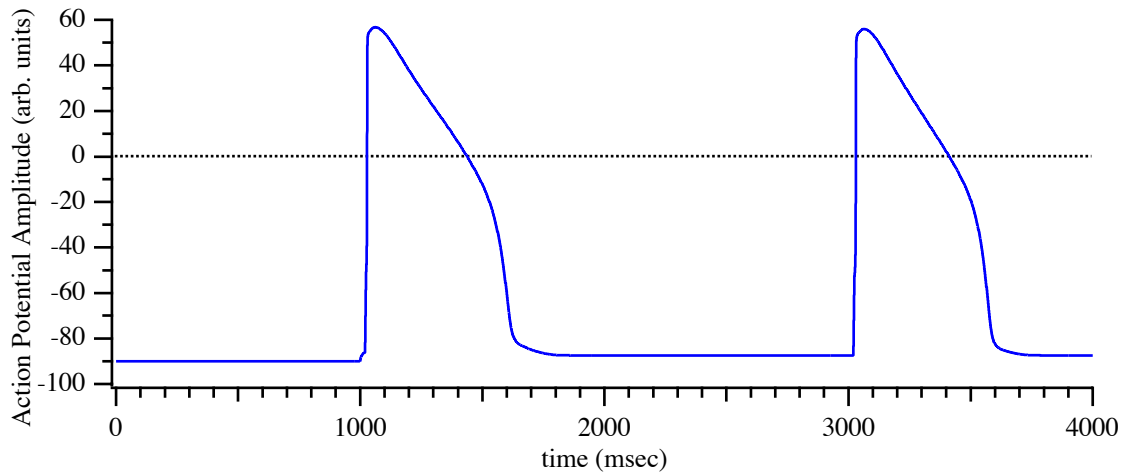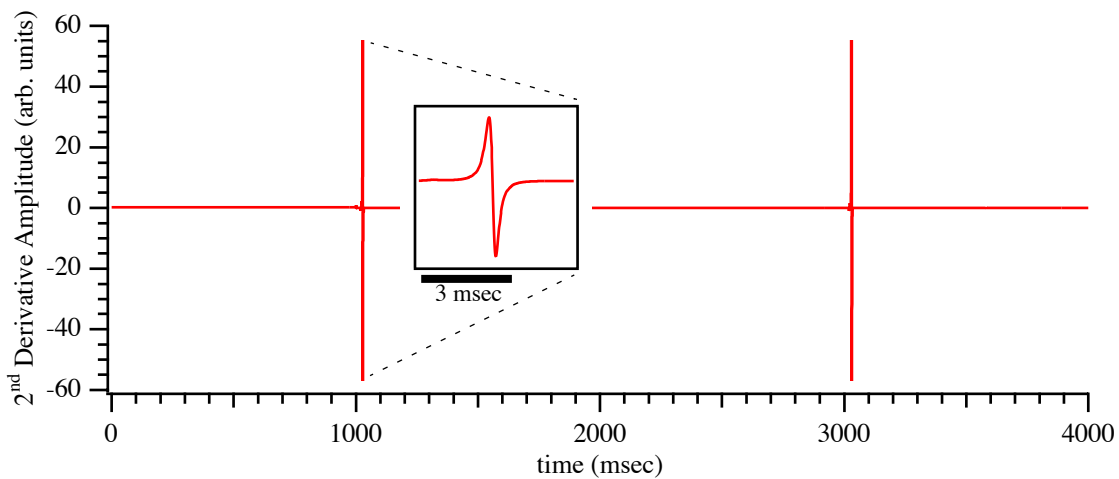
Figure 6.2: Plots of simulated action potentials. Intracellular signals (a) were calculated using HSPICE and Hodgkin-Huxley type equations for the cellular membrane. The second time derivative (b) of this intracellular signal was computed to estimate the expected extracellular signal to be recorded by a microelectrode. An expanded view of the 3 msec wide second derivative signal is shown in the inset of (b).

in Figure 6.3, it is interesting to examine the ionic fluxes responsible for the changes in transmembrane potential. Na^+ influx is orders of magnitude larger than either K^+ or Ca^{2+} during the entire portion of the second derivative signal that is generally observed. Thus, it is expected that any pharmaceuticals or toxins affecting Na^+ conductance or gating properties will have a profound impact on the recorded AP. Changes in Ca^{2+} or K^+ conductance should be secondary effects as those channels affect future gating dynamics of the Na^+ current. However, compounds affecting these other channels should
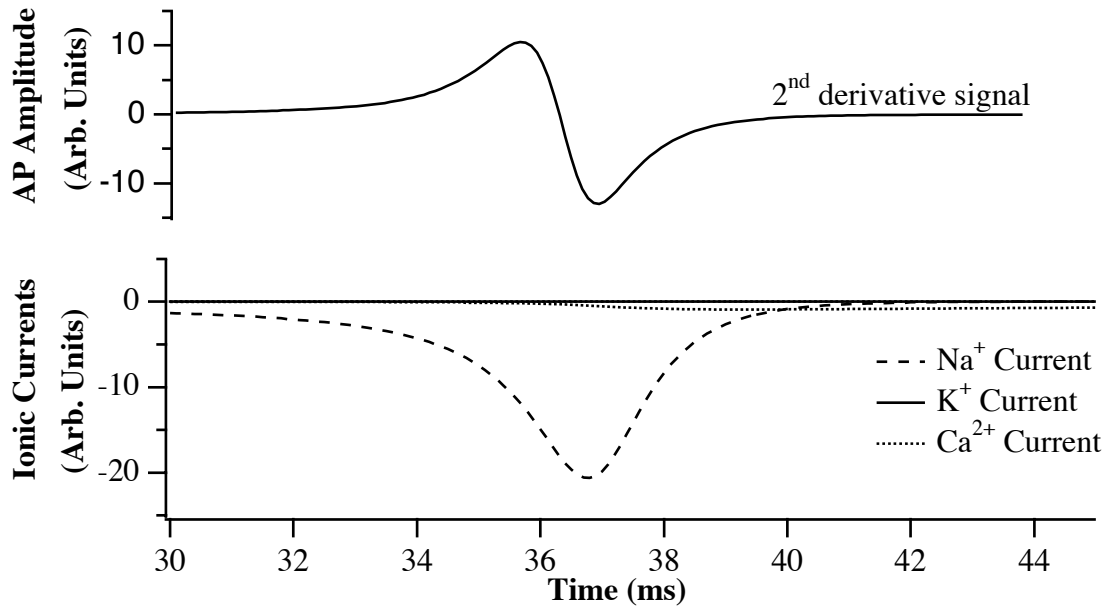
Figure 6.3: Simulated extracellular AP (second derivative) and ionic currents flowing through the cell membrane. Note that the current during the recorded AP is dominated by Na^+ influx (by several orders of magnitude). Thus, response to Na^+ channel modulation is expected to be greater than to Ca^{2+} and K^+ channel modulation.

significantly impact the spontaneous beat rate of the cell culture. Thus, this parameter was also monitored during pharmacological experiments with the chick myocardial cells.

To simulate the effects of different pharmaceuticals and toxins, a conductance multiplier was added to the model for each of the channels of interest (Na^+ and Ca^{2+}). This allowed the action of a channel blocker or agonist to be simulated. For all cases, the amount of attenuation or enhancement was adjusted until the simulated second derivative response matched measured responses as closely as possible. The PSD of the second derivative signal was then taken for both the baseline and altered conductance cases, and a PSD ratio was determined (as outlined above) for comparison to measured responses.

6.5 Action Potential Response to Channel-Specific Agents

The effects of pharmaceuticals or toxins on the action potential of spontaneously excitable cultured cells measured using extracellular microelectrodes has received little attention in the literature. While Gross, et al. have examined the effects of numerous

pharmacological and toxic agents on spike trains of networks of neurons cultured on microelectrode arrays [Gross, et al., 1995], the actual shape of the AP has not been monitored and studied. The work presented herein was focused on two objectives: (1) determining if changes in AP *shape* due to the effects of pharmaceuticals and toxins could be observed with extracellular microelectrodes, and (2) exploring possible techniques for deducing the action of an unknown agent on the cell of interest.

For the study presented herein, the effects of several different channel-specific antagonists and agonists were examined [Borkholder, et al., 1998]. For each case, a microelectrode chip containing cultured chick myocytes was placed in the recording system as described in Chapter 5. A continuous flow of recording media ($\approx$ 1.5 ml / min.) was started and action potential measurements were begun. The APs were allowed to stabilize (fluctuations occur due to changing from culture media to recording media) and baseline measurements were taken. The flow of recording media was then switched to recording media containing the channel-specific agent and the resulting changes in AP shape, amplitude and spontaneous beat rate were recorded. Since the electrode array package contained 3 to 4 ml of media during the experiment, total solution exchange generally required several minutes of media flow. Thus, the cellular response to pharmaceuticals and toxins was not as rapid as would be expected biologically. In all cases the observed time delays were due entirely to the limiting media exchange time.

Concentrations of the channel-specific agents used for these studies were determined empirically. Initial concentrations were estimated based on discussions with several neuroscientists [Perl, 1997; Pancrazio, 1997], and adjusted to provide a repeatable cellular response which did not immediately cease spontaneous activity. Due to the configuration of the perfusion system, media exchange was slow resulting in a slowly varying (increasing with addition and decreasing with rinse) toxin or pharmaceutical concentration in the cell culture chamber. Thus, the concentrations quoted for all experiments do not necessarily represent the concentration presented to the cellular population.

6.5.1 Sodium Channel Blocker: Tetrodotoxin

Tetrodotoxin (TTX) is a naturally occurring toxin found in the gonads and other visceral tissues of some fish of the order Tetraodontiformes (such as the Japanese *fugu*, or puffer fish) and the skin of some newts of the family Salamandridae. This toxin specifically blocks the outer mouth of Na^+ channels in the membrane of excitable cells, thereby preventing flow of this ion through the pore during channel activation [Hille, 1992]. Thus, it is expected that TTX will decrease the rate of depolarization and therefore

160

reduce the magnitude of the measured second derivative extracellular signal. The anticipated effect on spontaneous beat rate is not as clearly defined however, since both K^+ and Ca^{2+} flux determine the time until repolarization of the cell. However, it is possible that a smaller and slower Na^+ flux may result in fewer Ca^{2+} channels being activated. In this instance a faster repolarization time and therefore a higher spontaneous beat rate could be expected.

(a)

(b)
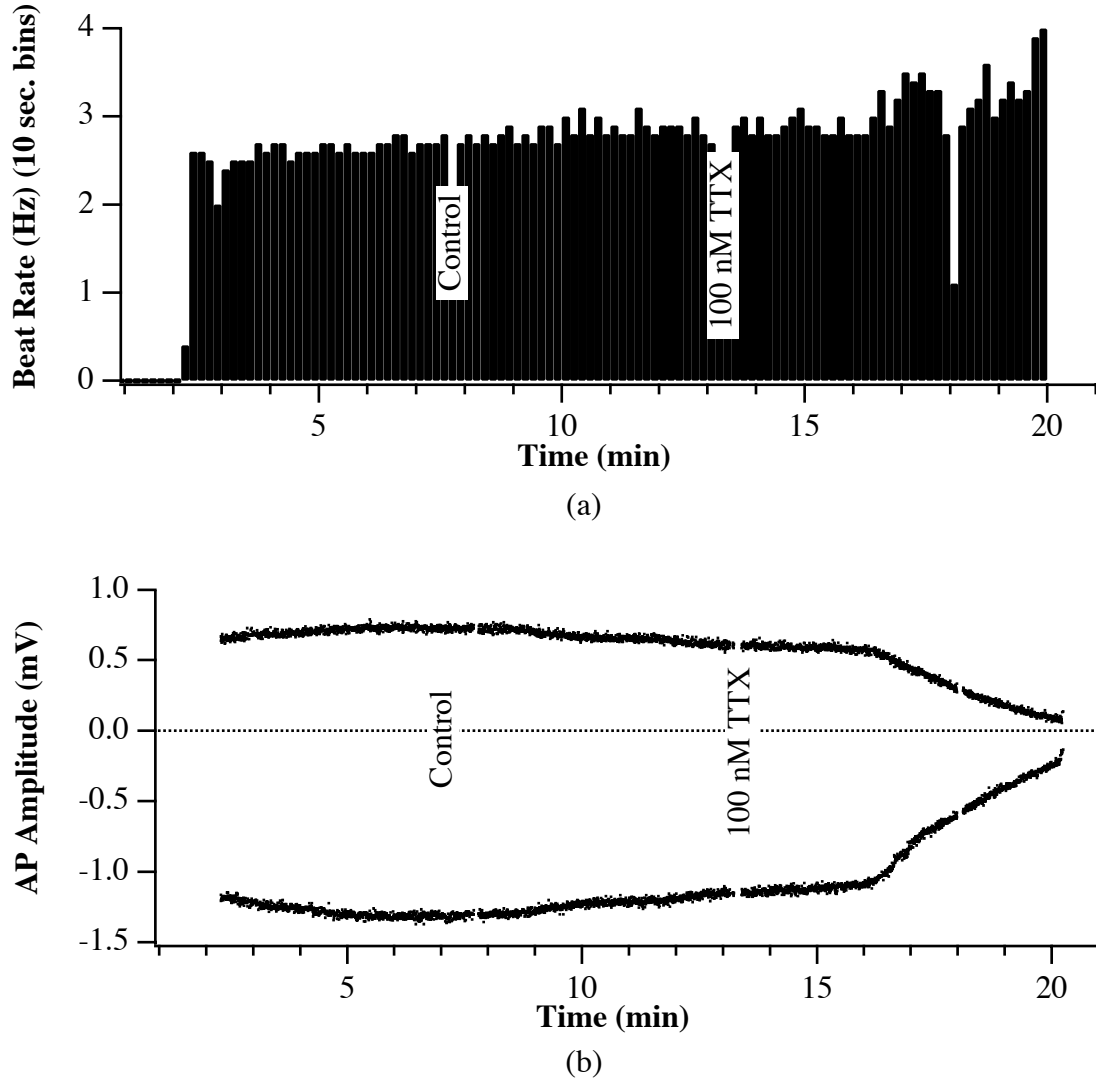
Figure 6.4: Measured spontaneous beat rate and action potential amplitude for cultured embryonic chick myocardial cells in response to 100 nM tetrodotoxin. (a) Representative histogram plot of the change in beat rate as the fast sodium channel blocker TTX was added. A slight rise in rate was observed before the spontaneous AP stopped. (b) Representative AP amplitude plot showing the maximum and minimum peaks (enveloped) of the AP. Note the decrease in amplitude with addition of 100 nM TTX as would be expected.

Numerous experiments were performed monitoring the recorded action potential amplitude and beat rate of spontaneously beating embryonic chick myocardial cells as TTX was perfused over the cells. Representative results are shown in Figure 6.4 for a 100 nM solution (for reference, the average human male would have to consume 1000 liters of this solution to ingest a lethal dose). Addition of TTX caused the beat rate to become sporadic (and in most cases slightly higher) and the recorded AP amplitude to decrease until electrical activity ceased altogether. These results were consistent with those expected for this Na$^+$ channel blocker. While other data were not shown, results from numerous experiments were similar in both magnitude and timing of the response.

Changes in the shape of the AP and, in particular, the power spectral density were also monitored and compared to simulated responses. As can be seen from Figure 6.5, 100 nM tetrodotoxin significantly changed the shape of the recorded action potential. This response was simulated by reducing the total sodium channel conductance by 25% (determined empirically), yielding a qualitatively similar change in AP shape. The time delay observed in the simulated case was due to the slower depolarization of the
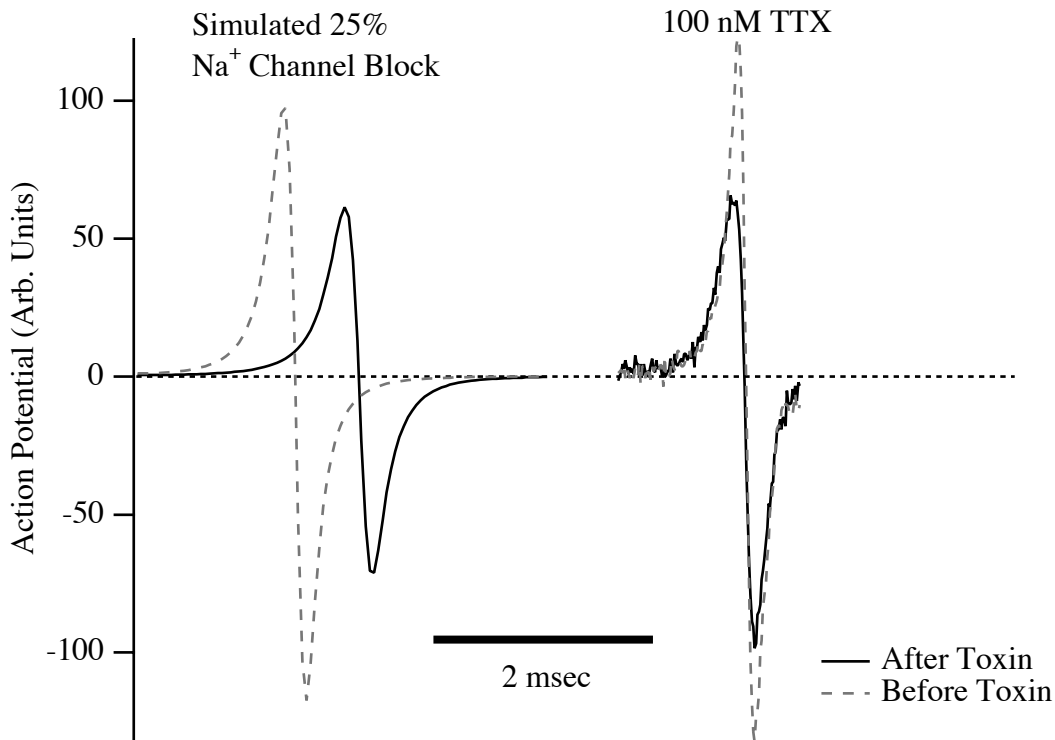
Figure 6.5:   Measured and simulated AP response to tetrodotoxin. Note the qualitatively similar changes in AP shape with addition of 100 nM of tetrodotoxin and the simulated 25% block of sodium channel conductance.

membrane with a reduced Na$^+$ conductance. For the actual measurement this same delay was probably present, but not observed due to data acquisition triggering at a set voltage threshold.

The power spectral density was also calculated for both the simulated and actual responses as shown in Figure 6.6. The data represents three experiments (with 100 nM TTX) from two different cell populations. For the purposes of this study, all cells taken from a single batch of embryos were considered to be from the same cell population. Thus, for this experiment, two chips from one batch of embryos and one chip from a second batch of embryos were used. For each case, the average PSD ratio for eight different electrodes was calculated with error bars of one sigma shown. Note the qualitatively similar responses across the frequency spectrum for all three experiments and the simulation. As expected, changes in the AP and its power spectrum due to modulation of Na$^+$ channel conductance were both consistent and well predicted by the model.
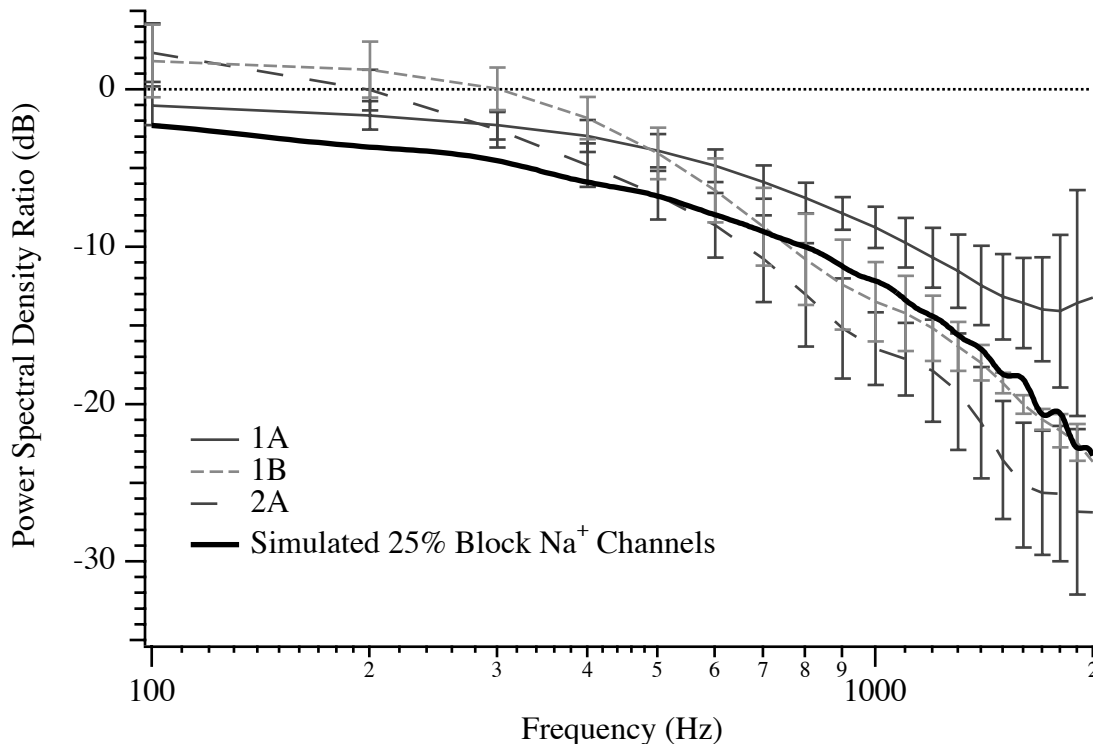
Figure 6.6: *Power spectral density ratio (PSD after pharmaceutical divided by PSD before pharmaceutical) for actual and simulated responses to 100 nM tetrodotoxin. Actual data from three experiments with two different cell populations (1 and 2). Average response from eight electrode sites shown for each experiment with error bars of one sigma.*

6.5.2 Calcium Channel Agonists: Epinephrine and Verapamil

Epinephrine is a naturally occurring hormone released by the adrenal gland which acts on both α- and β–adrenergic receptors. These receptors activate a G-protein cascade (process by which the receptor-coupled GTP-binding regulatory protein (G-protein) binds
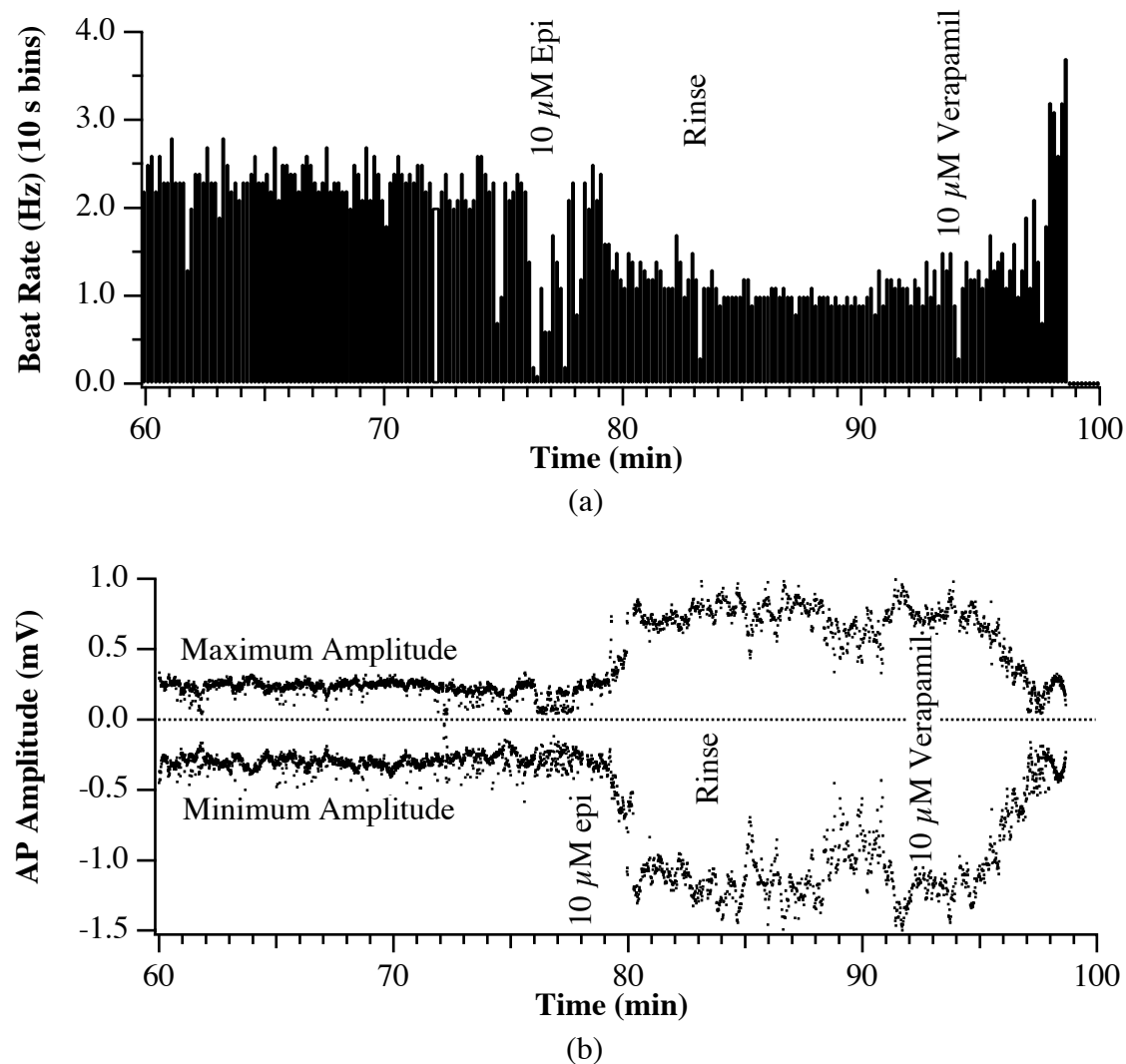
Figure 6.7: Measured spontaneous beat rate and action potential amplitude for cultured embryonic chick myocardial cells in response to 10 μM epinephrine and 10 μM verapamil. (a) Representative histogram plot of the change in beat rate as agents specific to Ca^{2+} channels were added. Epinephrine caused a marked decrease in beat rate while verapamil caused a significant increase until the point where the APs were terminated. (b) Representative AP amplitude plot showing the maximum and minimum peaks (envelope) of the AP with addition of Ca^{2+} channel affecting agents. Epinephrine caused a significant increase in overall amplitude while verapamil caused a marked decrease, eventually stopping the AP.

guanine nucleotides and activates intracellular messenger systems) which enhances Ca^{2+} channel function, thereby causing a larger percentage of the channels to be open and remain open longer. This causes an increase in both action potential size and duration [Nicholls, et al., 1992] which should result in a larger recorded AP and a slower beat rate (due to the longer refractory period) for autonomously firing cells.

Verapamil blocks L-type Ca^{2+} channels (large conductance, long lasting current) and is used extensively as an antiarrhythmic, coronary vasodilator and cardiac depressant clinically. It not only reduces the magnitude of the Ca^{2+} current through the slow calcium channel, but also decreases the rate of recovery of the channel [Hardman, et al., 1996]. Thus, in contrast to epinephrine, verapamil should decrease the amplitude of the recorded AP (in as much as it contributes to the recorded signal) and reduce the duration of the plateau phase, resulting in a faster spontaneous beat rate.
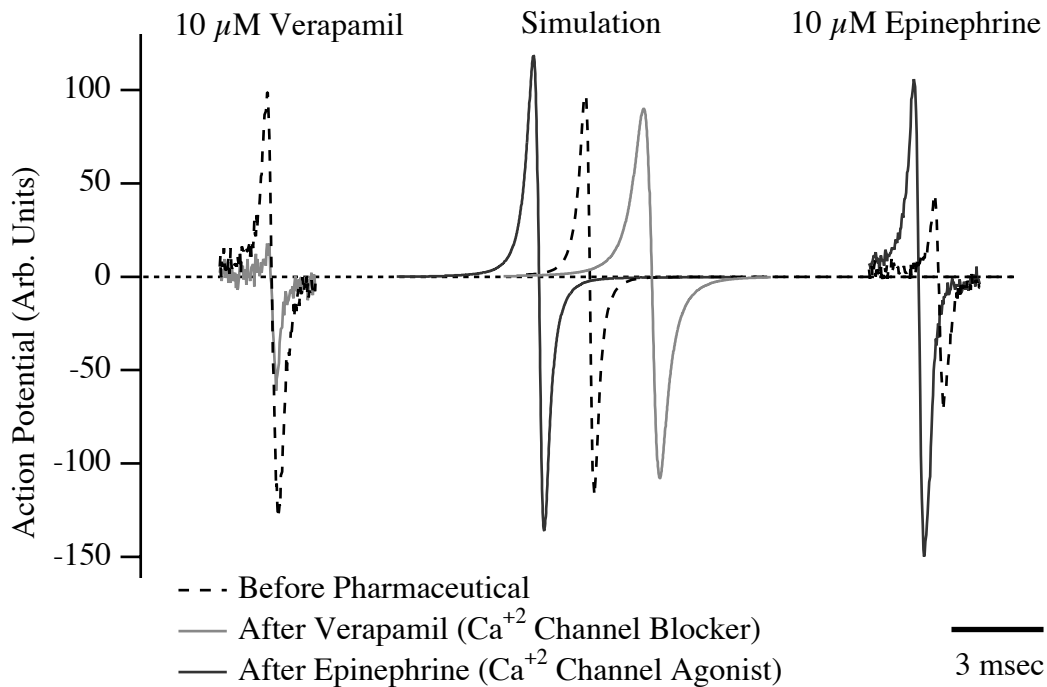
Figure 6.8: *Measured and simulated AP response to 10 µM epinephrine and 10 µM verapamil. Verapamil simulation done with a 50% block of both Ca^{2+} and K^+ channels, while epinephrine was simulated by increasing channel conductance by 10 times. In both cases further variation of channel conductance prevented the AP from firing. Note that while changes in AP shape were readily observed during experimentation, the simulated responses showed little change.*

Numerous experiments were performed examining changes in the spontaneous beat rate and AP amplitude with additions of both epinephrine and verapamil. As can be seen from Figure 6.7, modulation of the Ca^{2+} channel conductance had a significant impact on both the spontaneous beat rate and the recorded AP amplitude. The addition of 10 μM epinephrine consistently reduced the beat rate (due to an extended plateau phase of the AP) and increased the amplitude of the recorded AP. Rinsing this pharmaceutical away resulted in little change over ten minutes. Perfusion with 10 μM verapamil had the opposite effect of the Ca^{2+} agonist epinephrine, causing a rapid increase in beat rate and decrease in AP amplitude. The sudden drop to zero beats per second was due to cessation of spontaneous electrical activity. Note that concentrations 100 times larger than required for tetrodotoxin (Na^+ channel blocker) were necessary to obtain significant changes in the AP. This was to be expected since the rising edge of the action potential (which dominated the recorded second derivative signal) was influenced primarily by Na^+ influx.
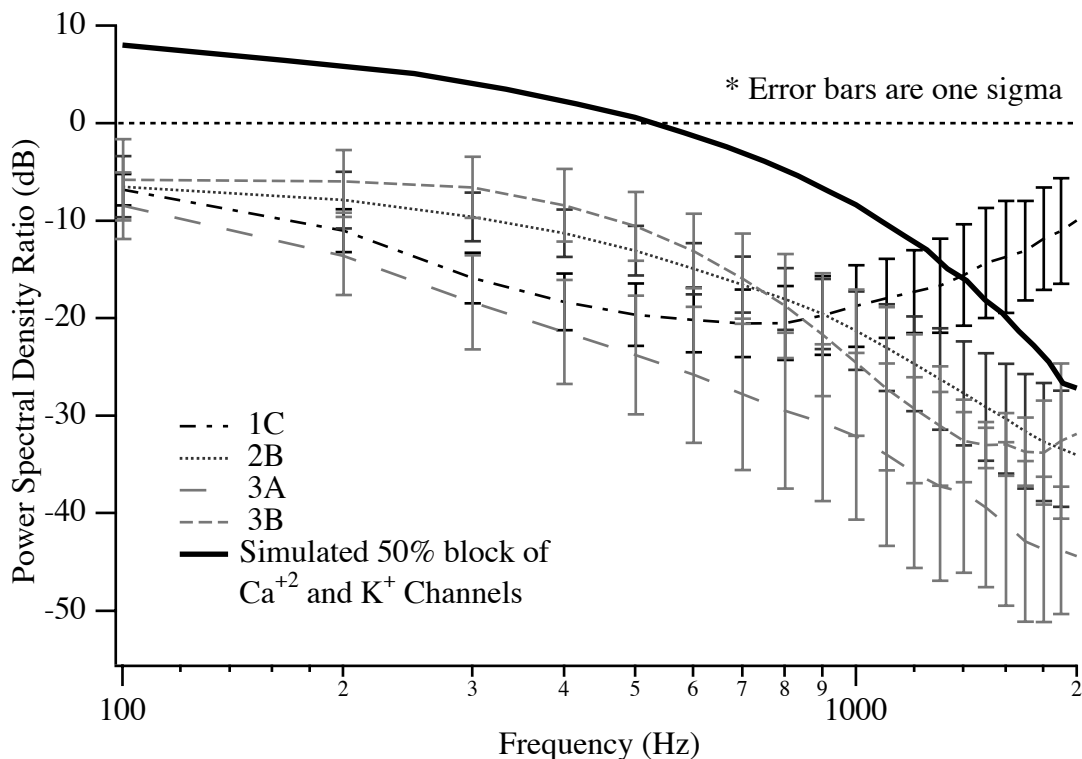
Figure 6.9: Power spectral density ratio (PSD after pharmaceutical divided by PSD before pharmaceutical) for actual and simulated responses to 10 μM verapamil. Actual data from four experiments with three different cell populations (1, 2 and 3). Average response from eight electrode sites shown for each experiment with error bars of one sigma.

166

Changes in the AP shape were also examined as for the case of TTX. As can be seen from Figure 6.8, there was significant modification of the recorded AP shape due to addition of both epinephrine and verapamil. However, modulation of Ca^{2+} channel conductance during simulations resulted in little change in the second derivative signal. For the case of epinephrine simulation, the conductance was increased by 10 times with only the slight change in AP shape shown. Further enhancement of the Ca^{2+} conductance resulted in loss of excitability of the simulated cell. Verapamil simulations involved attenuation of both Ca^{2+} and K^+ conductance since at microMolar concentrations the pharmaceutical has been shown to block potassium channels [Pancrazio, et al., 1991]. Even with a 50% reduction in the conductance of these channels, there was little change in the second derivative signal. While these simulation results were disappointing, they were not totally unexpected. The atrial cell model used did not include any leakage current paths generally thought to be responsible for normal pacing of cardiac tissue. Thus, initiation of an action potential in the model required stimulation. The gating of Na^+
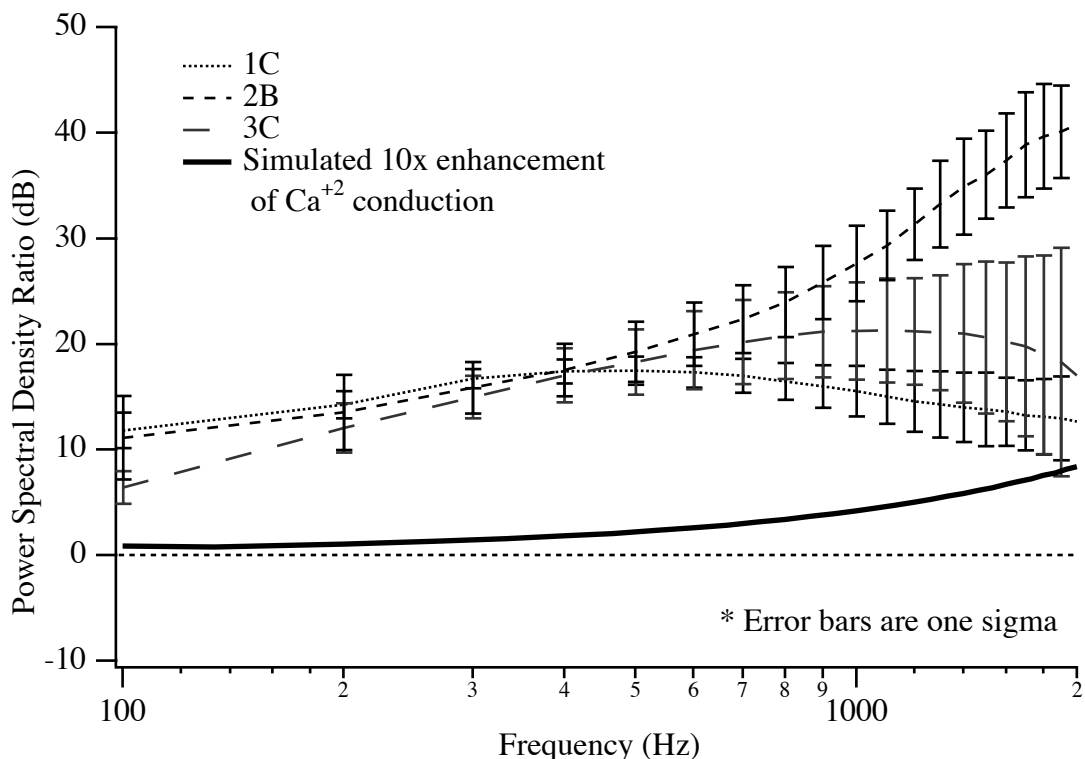

Figure 6.10: *Power spectral density ratio (PSD after pharmaceutical divided by PSD before pharmaceutical) for actual and simulated responses to 10 μM epinephrine. Actual data from three experiments with three different cell populations (1, 2 and 3). Average response from eight electrode sites shown for each experiment with error bars of one sigma.*

channels (responsible for the rising edge of the AP which dominated the second derivative signal) was therefore dictated by the stimulation pulse and not the normal pathways that can be impacted by changes in Ca^{2+} channel conductance. Therefore the simulated responses did not mimic the measured changes in AP shape.

The power spectral density changes for both verapamil and epinephrine were examined and compared to simulated responses as shown in Figure 6.9 and Figure 6.10 respectively. As expected, in both cases the simulated PSD ratio did not match the experimental results at all. The actual data for verapamil was from 4 different experiments with three populations of cells. Note the significant differences in the PSD ratio shape, as well as the scatter present at higher frequencies. Similar shape differences and scatter were observed for the three experiments (three cell populations) using epinephrine. In both cases however, there was relatively little scatter in the low frequency PSD ratio. Since these low frequency responses were different than those observed for TTX, it may be possible to distinguish between channel classes using this low frequency region.

6.5.3 Discussion

The variability in PSD ratio results for modulation of Ca^{2+} channel conductance across populations of cells does not preclude the possible existence of unique modulation function *signatures* within a single cell population. The PSD ratio curves presented in Figure 6.11 are from a single cell population, with the epinephrine and verapamil responses taken from the same chip during the same experiment. Note the unique modulation function shape for each pharmaceutical tested and the mirrored responses between epinephrine and verapamil as expected. Using this as an example, it may be possible (given consistent cell populations) to distinguish between pharmaceuticals and toxins acting on different classes of ion channels based on their power spectral density ratios across frequencies. With the culture protocol utilized for these experiments however, the characteristics of the cell population were extremely variable. Since the entire heart was dissociated and used for culture, each chip represented an unknown and variable combination of atrial and ventricular cells which could respond differently to the pharmaceuticals tested. If consistent cell populations could be used for the experiments, then it is possible that unique modulation functions based on PSD analysis could be determined for action on different ion channels. These modulation functions could then be used to identify the general class of action of an unknown pharmaceutical or toxic agent. Even without consistent cell populations, it is possible that the low frequency PSD ratio could be used for agent identification, since those responses were consistent across cell
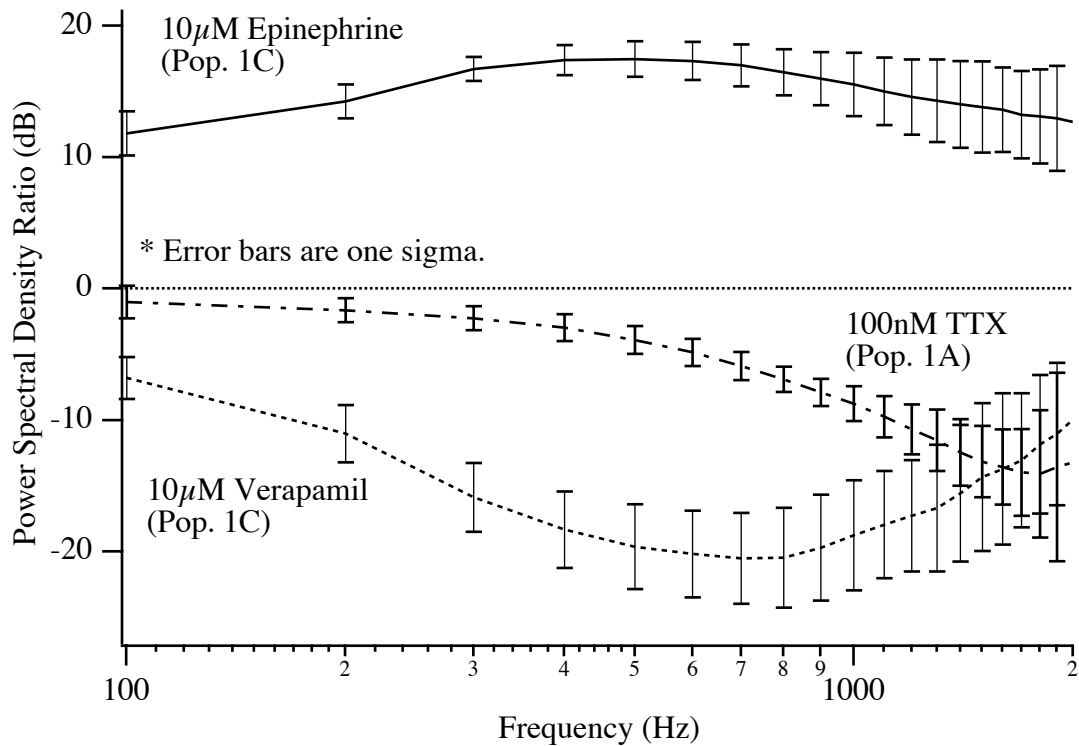
Figure 6.11: Power spectral density ratio (PSD after pharmaceutical divided by PSD before pharmaceutical) for three experiments using one cell population. Responses for 10 μM epinephrine and 10 μM verapamil were taken from the same chip. Note the mirrored responses in the PSD between this agonist and antagonist. The response to 100 nM tetrodotoxin was qualitatively different across the frequencies examined.

populations, and different for each of the channel-specific agents tested. Action potential amplitude and spontaneous beat rate could also provide clues important to agent identification. The combination of such measurement and analysis techniques could significantly expand the practical use of cell based sensors for toxin detection and drug discovery.

6.6 Conclusions

As demonstrated by ourselves and others in the past [Thomas, et al., 1972; Israel, et al., 1990; Connolly, et al., 1990; and Mohr, et al., 1995], action potentials from spontaneously beating chick myocardial cells cultured on microelectrode arrays can easily be measured. However, for the first time, changes in the extracellular AP shape in response to the action of pharmaceuticals and toxins have been studied. Easily measurable

quantities such as the beat rate and AP amplitude have been monitored and found to correlate well with biologically anticipated responses. The use of power spectral density analysis as a tool for classifying the action of a biologically active agent was investigated. The ratio of the PSD after addition of a channel-specific agent to the PSD prior to addition was taken and compared for agents acting on different channels. The results for the Na^+ channel blocker tetrodotoxin were consistent across cell populations and correlated well with simulated responses. The results for the Ca^{2+} channel agonist epinephrine and blocker verapamil were far more variable across cell populations and did not correlate well with the simulated responses (as expected). However, when examining a single cell population, unique modulation functions (PSD ratios) were observed for each of the pharmaceuticals and toxins investigated. Thus, this technique may work well for deducing the action of an unknown agent if consistent cell populations can be used.

References

Barry, W.H., Pitzen, R., Protas, K. and Harrison, D.C., "Inotropic effects of different calcium ion concentrations on the embryonic chick ventricle," *Circulation Research*, 36:727-734 (1975).

Borkholder, D.A., DeBusschere, B.D. and Kovacs, G.T.A., "An approach to the classification of unknown biological agents with cell based sensors," *Solid-State Sensor and Actuator Workshop*, Hilton Head Island, South Carolina, pp. 178-182, June 8-11 (1998).

Connolly, P., Clark, P., Curtis, A.S.G., Dow, J.A.T. and Wilkinson, C.D.W., "An extracellular microelectrode array for monitoring electrogenic cells in culture," *Biosensors and Bioelectronics*, 5:223-234 (1990).

De Hann, R.L., "Regulation of spontaneous activity and growth of embryonic chick heart cells in tissue culture," *Developmental Biology*, 16:216-249 (1967).

Drodge, M.H., Gross, G.W., Hightower, M.H. and Czisny, L.E., "Multielectrode analysis of coordinated, multisite, rhythmic bursting in cultured CNS monolayer networks," *J. Neuroscience Methods*, 6(6):1583-1592 (1986).

Ganong, W.F., *Review of Medical Physiology*, Prentice Hall, New Jersey (1993).

Gross, G.W., Rhoades, B. and Jordan, R., "Neuronal networks for biochemical sensing," *Sensors and Actuators*, B6:1-8 (1992).

Gross, G.W., Rhoades, B.K., Azzazy, H.M.E. and Wu, M.C., "The use of neuronal networks on multielectrode arrays as biosensors," *Biosensors & Bioelectronics*, 10:553-567 (1995).

Hardman, J.G. and Limbird, L.E. (Eds), *Goodman & Gilman's The pharmacological basis of therapeutics*, Ninth edition, McGraw-Hill, New York (1996).

Hille, B., *Ionic Channels of Excitable Membranes*, Sinauer Associates, Inc., Sunderland, Massachusetts (1992).

Hodgkin, A.L. and Huxley, A.F., "A quantitative description of membrane current and its application to conduction and excitation in nerve," *Journal Physiology*, 117:500-544 (1952).

Israel, D.A., Edell, D.J. and Mark, R.G., "Time delays in propagation of cardiac action potential," *American Journal of Physiology: Heart and Circulatory Physiology*, 27(6):H1906-H1917 (1990).

Maeda, E., Robinson, H.P.C. and Kawana, A., "The mechanisms of generation and propagation of synchronized bursting in developing networks of cortical neurons," *J. Neuroscience*, 15(10):6834-6845 (1995).

Mohr, A. Finger, W., Föhr, K.J., Nisch, W. and Göpel, W., "Performance of a thin film microelectrode array for monitoring electrogenic cells in vitro, "*The 8th International Conference on Solid-State Sensors and Actuators*, Stockholm, Sweden, June 25-29, 2:479-482 (1995).

Neumcke, B., "Fluctuation of Na and K currents in excitable membranes," *International Review of Neurobiology*, 23:35-67 (1982).

Nicholls, J.G., Martin, A.R. and Wallace, B.G., *From Neuron to Brain*, Third Edition, Sinnauer Associates, Inc., Sunderland, MA (1992).

Pancrazio, J.J., Viglione, M.P., Kleiman, R.J. and Kim, Y.I., "Verapamil-induced blockade of voltage-activated K^+ current in small-cell lung cancer cells," *Journal of Pharmacology and Experimental Therapeutics*, 257(1): 184-191 (1991).

Pancrazio, J.J., *Personal Communication*, Jan.-Dec. (1997).

Perl, E.R., *Personal Communication*, Jan.-Dec. (1997).

Polinger, I.S., "Separation of Cell Types in Embryonic Heart Cell Cultures," *Experimental Cell Research*, 63:78-82 (1970).

Rasmusson, R.L., Clark, J.W., Giles, W.R., Robinson, K., Clark, R.B., Shibata, E.F. and Campbell, D.L., "A mathematical model of electrophysiological activity in a bullfrog atrial cell," *American Journal of Physiology*, 259(2):H370-H389 (1990).

Stevens, C.F., "Inferences about membrane properties from electrical noise measurements," *Biophysical Journal*, 12:1028-1047 (1972).

Thomas, C.A. Jr., Springer, P.A., Loeb, G.E., Berwald-Netter, Y. and Okun, L.M., "A miniature microelectrode array to monitor the bioelectric activity of cultured cells," *Experimental Cell Re*search, 74:61-66 (1972).

Chapter 7   IMPEDANCE BASED SENSORS

The presence of alternating current electrode polarization can be a major nuisance in biological impedance work.

                                                          H.P. Schwan, 1968

7.1 Introduction

The use of planar electrodes to monitor proliferation, motility and adhesion of populations of cells has been described in the literature as outlined in Chapter 1. While some of the reported work examined individual cells using small microelectrodes, no effort had been made to monitor changes in the cellular membrane properties. This work was focused on first optimizing the electrodes for measuring changes in the cell membrane, and attempting to monitor changes in cell membrane conductance by application of channel-specific agents.

This chapter begins with a description of the cell types used for the experiments and the protocols for their culture. Modeling of the cell / electrode interface is then discussed and work to determine an optimum electrode size is presented. Actual experimental results using NG108 cells and two channel-specific agents are described along with observed motility effects. The use of astrocytes as a low motility alternative to NG108 cells is then explored.

7.2 Cell Information and Protocols

Two different cell lines were used for exploring the use of impedance techniques for the study of cellular membrane properties; a neuroblastoma × glioma hybrid (NG108-15) and embryonic mouse astrocytes. Basic cellular information and brief protocols for their culture are described below. Detailed culture procedures and media formulations can be found in Appendix C.

7.2.1 NG108-15 Cells

NG108-15 (neuroblastoma × glioma hybrid) cells have been utilized extensively for many types of morphological and biochemical studies. They express at least four major families of voltage-sensitive channels (including Na^+, Ca^{2+} and K^+) that respond to a variety of ion channel blockers including tetrodotoxin (for blockage of voltage-sensitive Na^+ conductance) [Kowtha, et al., 1993], and verapamil (for blockage of L-type Ca^{2+} channels) [Wang, et al., 1993]. When cultured in serum-containing medium, the cells proliferate well and exhibit significant motility. Cells moving across the cell culture substrate can be easily observed with time lapse microscopy. These cells are electrically active and can be induced to produce action potentials via injection of current. However, spontaneous firing (as is the case for cardiac cells) does not occur. If the cells are cultured in serum-free medium, the electrophysiological and morphological properties are changed. Proliferation ceases and the cells begin to produce neurites and other extensions which are capable of forming synapses to other tissues and cells. These cells exhibit features characteristic of neurons and are more likely to fire action potentials than their counterparts cultured in serum-containing medium. This electrical activity can even be spontaneous under some circumstances. However, as with most neurons, the extracellular signal strength is low, as is the percentage of cells which are actively firing action potentials [Kowtha, et al., 1993]. For these reasons, NG108-15 cells were not used in the action potential studies. Instead, they were used for studies of cellular impedance; examining both motility issues as well as channel conductance changes.

NG108 cells were cultured in standard polystyrene flasks in a 10% CO_2 incubator at 37°C. When the cells reach confluency, trypsin was used to lift the cells from the substrate. Following centrifugation and resuspension in culture medium, the cells were replated into new flasks and the process was repeated. For culture on electrode arrays, the cell suspension was applied directly over the array and the entire chip was placed in the incubator.

7.2.2 Embryonic Mouse Astrocytes

Astrocytes are glial cells found in the central nervous system of all vertebrates. These neuroglial cells serve as supporting elements in the brain, help to isolate neurons from each other, and are thought to provide nutritional support to neurons. Additionally, they buffer the K^+ concentration in the extracellular space by absorbing excess potassium when neuronal activity is high (this is necessary to prevent the depolarization of neighboring neurons due to accumulation of extracellular K^+). The ability to do this is a direct result of their high permeability to K^+ which is thought to be almost entirely responsible for their membrane potential. In fact, the resting membrane potential has been shown to follow the Nernst equation for K^+ quite well [Nicholls, et al., 1992].

Much like cardiac cells, astrocytes develop cytoplasmic bridges (gap junctions) between cells to form a syncytium. This allows the transfer of ions (such as excess K^+) as well as metabolites, nutrients, neurotransmitters, etc., between cells. They generally exhibit a variety of both voltage- and ligand-gated ion channels in the membrane including at least two types of K^+ channels (one voltage-gated), Cl^- channels, and Ca^{2+} channels. Additionally, they have receptors for such molecules as glutamate, GABA, ACh, and numerous peptides. However, they are not thought to contribute to electrical activity in the brain [Kandel, et al., 1991].

For this research, astrocytes were obtained from a primary culture of embryonic mouse cortical tissue. The tissue was disaggregated into single cells and cultured in plastic culture flasks resulting in a mix of glial and neural cell types. After several passages (removal of cells from the substrate, centrifugation, resuspension of cells in culture media, and plating into new flasks) a near homogeneous population of astrocytes was obtained.

Unlike the morphology observed *in vivo* (astrocytes are generally smaller than neurons (<10 μm) and star shaped), astrocytes *in vitro* become more circular and larger, approaching 100 μm in diameter. Thus, they make an excellent choice for impedance studies where a large cellular size compared to the extracellular electrode diameter is desirable. Additionally, published data utilizing calcium imaging responses to such things as glutamate [Van Den Pol, et al., 1995] may be used as a reference for understanding the acquired impedance data.

7.3   Modeling the Electrode / Cell Interface

As described in Chapter 1, there has been a significant effort in the literature describing the impedance characteristics of populations of cells cultured over large area electrodes and single cells cultured over small microelectrodes. These impedance measurements have provided information about proliferation, motility and cellular adhesion for both electrically active and non-electrically active cell types. However, no effort has been published with the objective of directly measuring cell membrane *properties* using extracellular microelectrodes.

In the hope of monitoring changes in cellular membrane capacitance and conductance, the cell / electrode interface was modeled. These models were used in the design of the impedance system as well as the electrode array.

7.3.1   First Order Model of Cell Positioned Over an Electrode

A schematic view of a cell positioned over a microelectrode is shown in Figure 7.1. The total measured impedance consists of the electrode impedance (Z_e), the resistance between the electrode and the bulk electrolyte due to the thin layer of medium between the cell and the passivation layer (R_{seal}), the membrane capacitance and ion channel resistance over the electrode (C_{m1} and R_{ch1}), the membrane capacitance and ion channel resistance of the top and sides of the cell (C_{m2} and R_{ch2}), the solution resistance (R_{soln}) and the counterelectrode impedance (Z_{co}). Note that in reality R_{seal} is distributed with the capacitance and conductance of the membrane in the region over the passivation layer. For this measurement, the counterelectrode impedance, solution resistance and electrode impedance should all be negligible (assuming platinized electrodes) so that the impedance measurement is dominated by the seal resistance and the cell membrane properties. It is clear that R_{seal} must be on the same order (or larger than) the membrane impedance if changes in membrane properties are to be observed.

Rearranging the schematic and explicitly showing the distributed network consisting of the seal resistance and the capacitance and conductance of the membrane in that region results in the schematic of Figure 7.2, where membrane conductances represent the channel resistance described earlier. The electrode was driven with a voltage source V_s and the counterelectrode (impedance neglected) was held at a virtual ground by the transimpedance amplifier of the impedance measurement system. The model components

176
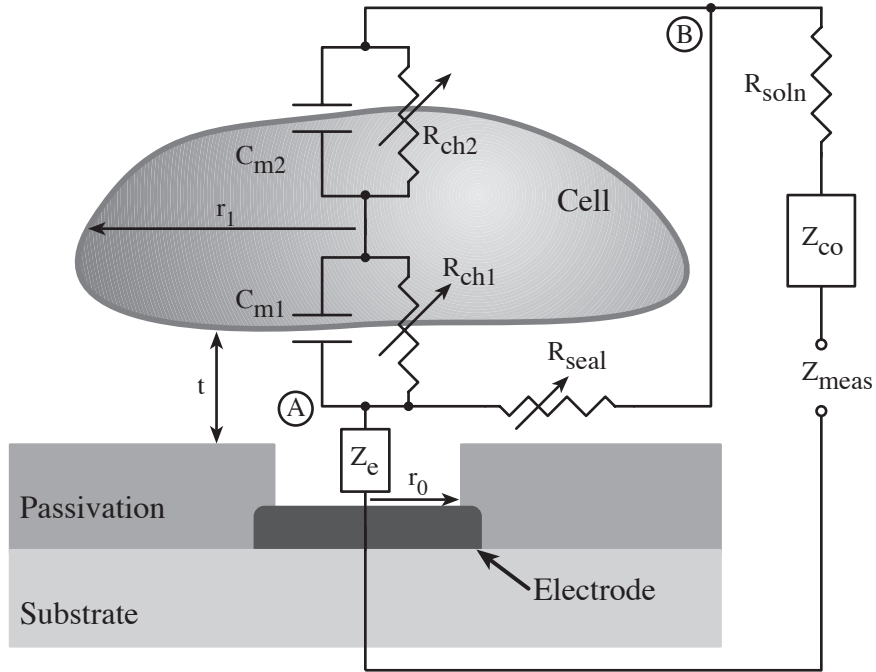
Figure 7.1: Schematic of a cell positioned over an electrode (not to scale). The measured impedance consists of the electrode impedance (Z_e), the resistance between the electrode and the bulk electrolyte due to the thin layer of medium between the cell and the passivation layer (R_{seal}), the membrane capacitance and ion channel resistance over the electrode (C_{m1} and R_{ch1}), the membrane capacitance and ion channel resistance of the top and sides of the cell (C_{m2} and R_{ch2}), the solution resistance (R_{soln}) and the counter electrode impedance (Z_{co}). Note that in reality R_{seal} is distributed with the capacitance and conductance of the membrane in the region over the passivation layer (not shown). Nodes A and B coincide with those labeled in Figure 7.2.

were estimated by assuming a circular cell of radius r_1 centered over a microelectrode of radius r_0. The total seal resistance was estimated by assuming a uniform cell to substrate separation (t) and using the standard formula

$$R = \frac{\rho \cdot L}{A} \tag{7.1}$$

where ρ is the resistivity of the medium, L is the length over which the current flows (radially outward from the electrode), and A is the cross sectional area the current flows through (equal to the perimeter of the circular ring of current times the cell to substrate separation (t)). Note that while changes in the effective resistivity of the solution were possible with small t, these effects were assumed to be negligible and the bulk resistivity of the medium was used. The seal resistance was calculated by integration of (7.1) over the distance between the outer edge of the electrode and the outer edge of the cell, where the

length L was equal to the incremental change in radius (dr), and the area A was equal to the perimeter times the cell to substrate separation ($2\pi rt$)

$$R_{seal} = \int_{r_0}^{r_1} \frac{\rho}{2\pi rt}\,dr = \left(\frac{\rho}{2\pi t}\right)\ln\left(\frac{r_1}{r_0}\right) \tag{7.2}$$

The capacitance and resistance values could be calculated from:

$$C_{m1} = \pi r_0^2 C_A \tag{7.3}$$

$$G_{m1} = \pi r_0^2 G_A \tag{7.4}$$

$$C_{m2} = \pi r_1^2 C_A \tag{7.5}$$

$$G_{m2} = \pi r_1^2 G_A \tag{7.6}$$

$$C_s = C_{m2} - C_{m1} = \pi(r_1^2 - r_0^2)C_A \tag{7.7}$$

$$G_s = G_{m2} - G_{m1} = \pi(r_1^2 - r_0^2)G_A \tag{7.8}$$

where C_A and G_A are the capacitance and conductance of the cellular membrane per unit area and C_s and G_s are the capacitance and conductance of the membrane in the region above the passivation layer (distributed with R_{seal}).
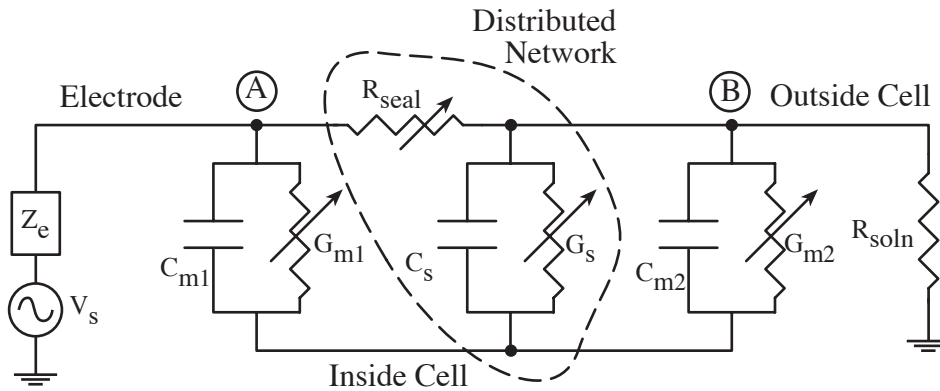
Figure 7.2: *Model of the electrode / cell interface and the relevant impedances. The seal resistance (R_{seal}) is distributed with the capacitance and conductance of the cellular membrane in the region where the cell overlaps the passivation layer. The impedance of the counterelectrode is not shown and is assumed to be negligible.*

Since the seal resistance was distributed with the capacitance and conductance of the membrane in the region above the passivation layer (C_s and G_s), exact calculation of the resulting impedances was difficult. A closed form solution was attempted, but found to be extremely difficult given the circular geometry and decreasing current density as the current travels from the edge of the electrode to the outer edge of the cell. Therefore, this section was divided into weighted discrete sections to approximate the distributed case. Initially the seal resistance was broken into two pieces by calculating an intermediate radius (r_i) given by

$$r_i = r_0 + \frac{r_0 + r_1}{2} = \frac{r_0 + r_1}{2} \tag{7.9}$$

This intermediate radius and (7.2) were used to calculate two weighted seal resistances R_{seal1} and R_{seal2}

$$R_{seal1} = \left(\frac{\rho}{2\pi t}\right) \ln\left(\frac{r_i}{r_0}\right) = \left(\frac{\rho}{2\pi t}\right) \ln\left(\frac{r_0 + r_1}{2r_0}\right) \tag{7.10}$$

$$R_{seal2} = \left(\frac{\rho}{2\pi t}\right) \ln\left(\frac{r_1}{r_i}\right) = \left(\frac{\rho}{2\pi t}\right) \ln\left(\frac{2r_1}{r_0 + r_1}\right) \tag{7.11}$$

which were placed in the circuit model as shown in Figure 7.3. Simulations of the total impedance were performed using SPICE for different electrode radii (r_0) and compared to the model in Figure 7.2 (with the distributed section lumped as shown). Significant differences were observed as expected. The distributed section was then divided into three weighted parts using two intermediate radii (r_{i1} and r_{i2})
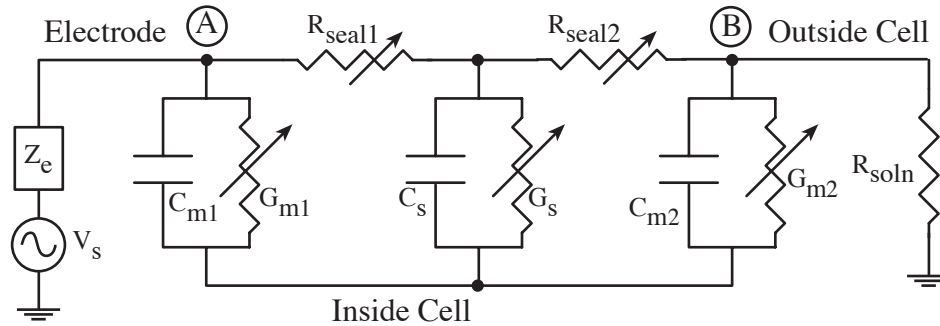
Figure 7.3: *Model of the cell / electrode interface with the seal resistance broken into two weighted pieces R_{seal1} and R_{seal2}.*
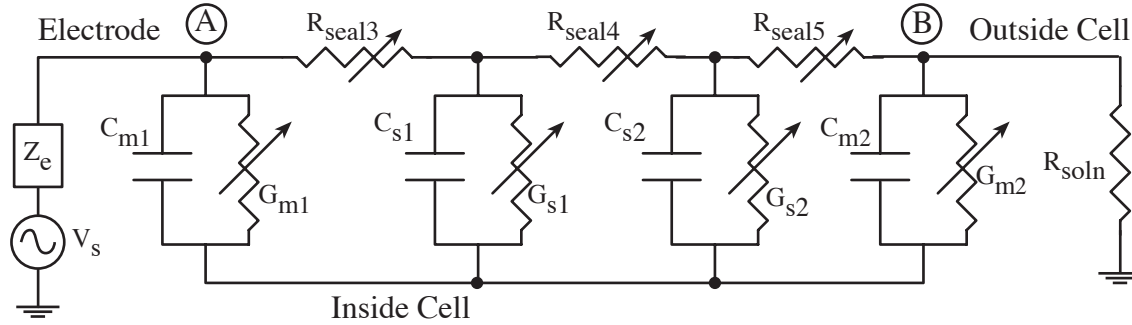
Figure 7.4: Model of the cell electrode interface with the seal resistance broken into three weighted pieces (R_{seal3}, R_{seal4}, R_{seal5}) and the membrane capacitance and conductance in the region above the passivation layer broken into two weighted pieces (C_{s1}, G_{s1} and C_{s2}, G_{s2}).

$$r_{i1} = r_0 + \frac{r_1 - r_0}{3} = \frac{r_1 + 2r_0}{3} \tag{7.12}$$

$$r_{i2} = r_0 + 2\left(\frac{r_1 - r_0}{3}\right) = \frac{2r_1 + r_0}{3} \tag{7.13}$$

These two intermediate radii were used to calculate three weighted seal resistances (R_{seal3}, R_{seal4} and R_{seal5}) while the original intermediate radius (r_i) was used to calculate two weighted capacitance and conductance sections (C_{s1}, G_{s1} and C_{s2}, G_{s2})

$$R_{seal3} = \left(\frac{\rho}{2\pi t}\right) \ln\left(\frac{r_{i1}}{r_0}\right) = \left(\frac{\rho}{2\pi t}\right) \ln\left(\frac{r_1 + 2r_0}{3r_0}\right) \tag{7.14}$$

$$R_{seal4} = \left(\frac{\rho}{2\pi t}\right) \ln\left(\frac{r_{i2}}{r_{i1}}\right) = \left(\frac{\rho}{2\pi t}\right) \ln\left(\frac{2r_1 + r_0}{r_1 + 2r_0}\right) \tag{7.15}$$

$$R_{seal5} = \left(\frac{\rho}{2\pi t}\right) \ln\left(\frac{r_1}{r_{i2}}\right) = \left(\frac{\rho}{2\pi t}\right) \ln\left(\frac{3r_1}{2r_1 + r_0}\right) \tag{7.16}$$

$$C_{s1} = \pi C_A (r_i^2 - r_0^2) = \pi C_A\left[\left(\frac{r_1 - r_0}{2}\right)^2 - r_0^2\right] \tag{7.17}$$

$$G_{s1} = \pi G_A (r_i^2 - r_0^2) = \pi G_A\left[\left(\frac{r_1 - r_0}{2}\right)^2 - r_0^2\right] \tag{7.18}$$

$$C_{s2} = \pi C_A (r_1{}^2 - r_i{}^2) = \pi C_A \left[r_1{}^2 - \left(\frac{r_1 - r_0}{2} \right)^2 \right] \qquad (7.19)$$

$$G_{s2} = \pi G_A (r_1{}^2 - r_i{}^2) = \pi G_A \left[r_1{}^2 - \left(\frac{r_1 - r_0}{2} \right)^2 \right] \qquad (7.20)$$

This distributed section was configured as shown in Figure 7.4 and simulated using HSPICE. The resulting calculated impedances were within 15% of those for the case where the distributed section was broken into two pieces (see Figure 7.5). Additional divisions were expected to slowly improve the accuracy of the model (as compared to a truly distributed network). Given the other assumptions made in the model (uniform cell / substrate separation, resistivity of medium between the cell and passivation layer equivalent to the bulk resistivity, circular cell geometry, cell perfectly centered over the microelectrode, etc.), it was likely that improved accuracy due to a highly distributed model would have been in the noise. Thus, the model of Figure 7.4 was used for all simulations and electrode optimization.

7.3.2 Theoretical Optimum Electrode Size for Observing Changes in Membrane Impedance

In order to observe changes in the cellular membrane impedance due to modulation of ionic channel conductance, it is necessary for the seal resistance to be sufficiently high (tens to hundreds of MΩs). However, as this seal resistance increases, the effective area of the membrane through which the current can flow on the bottom side of the cell is reduced. In the extreme of infinite seal resistance, the area is limited to that of the electrode itself. A limited membrane area results in higher impedances and therefore more noise in the measurements. It is therefore expected that there may be an optimum electrode size for monitoring changes in membrane properties for a cell of a known diameter.

SPICE simulations of the circuit shown in Figure 7.4 were performed for a cell 20 μm in diameter with the electrode diameter (r_0) and the cell to substrate separation (t) both being varied. The other factors assumed in the simulations were the solution resistivity ($\rho = 0.72$ Ω•m), the membrane capacitance per unit area ($C_A = 0.01$ F/m^2), and the membrane conductance per unit area ($G_A = 833$ ℧/m^2). The capacitance value used was normal for cellular membranes while the conductance value was the median of the ranges (median single channel conductance combined with the median channel density for Ca^{2+}, Na$^+$ and K$^+$ channels in parallel) found in [Hille, 1992].
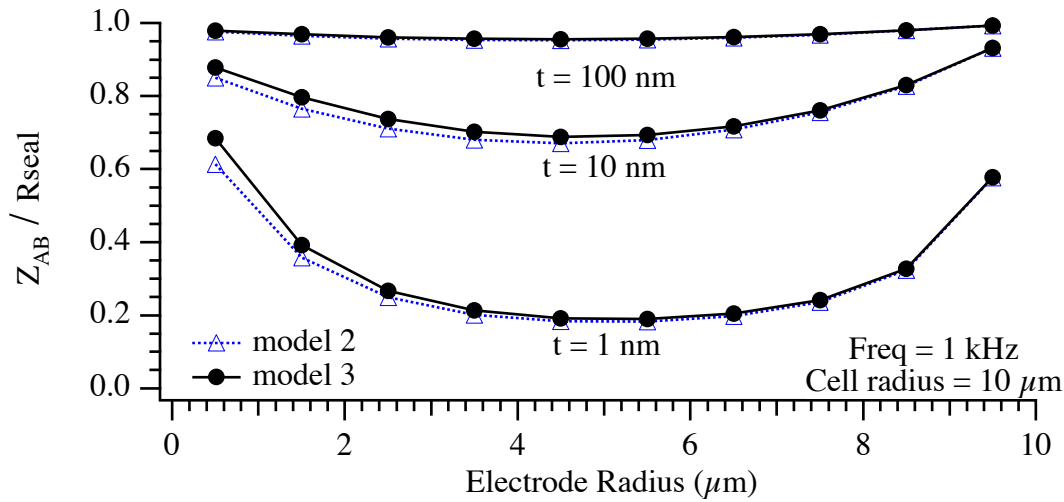
Figure 7.5: SPICE simulations of the circuits of Figure 7.3 (model 2) and Figure 7.4 (model 3) showing the change in the optimization factor (Z_{AB}/R_{seal}) with changing electrode radius (r_0) and cell to substrate separation (t). Note the minimum (indicating optimum electrode size) at $r_0 = 5$ μm, independent of the cell / substrate separation. Also note the close correlation of the two models.

For measurement of membrane properties, it was desirable to have the impedance from A to B in Figure 7.4 small compared to the total seal resistance (R_{seal3} + R_{seal4} + R_{seal5}). In this way, the current would be forced to travel through the cell membrane. Thus, an optimization factor was calculated by dividing the impedance from A to B (Z_{AB}) by the total seal resistance in the simulations. The minimum of this optimization factor indicated the optimum electrode size for monitoring changes in membrane impedance. The results of the simulations are shown in Figure 7.5. As the cell to substrate separation was decreased, the seal resistance increased and the optimization factor decreased as expected. For tight sealing of the cell to the substrate (t = 1 nm [Bray, 1992]), an optimum at $r_0 = 5$ μm was clearly shown. This correlated to the electrode radius being half that of the cell. As the frequency was increased, the flat bottom portion of each of the curves was wider and had a lower value as would be expected, since the capacitance of the membrane shunts the current at higher frequencies while the seal resistance remains constant. For observation of changes in membrane conductance however, it is desirable to work at lower frequencies where the membrane capacitance presents a higher impedance.

7.3.3 Impedance Measurement Interpretation

The above analysis was used to determine the optimum electrode size for monitoring changes in the membrane properties of a cell of known diameter. The models presented could be used to determine the membrane capacitance and conductance and the seal resistance for a given impedance measurement if information about the cell size, coupling, position over the electrode, and ionic channel densities and states were known. However, this analysis did not indicate how to interpret changes in the measured impedance and
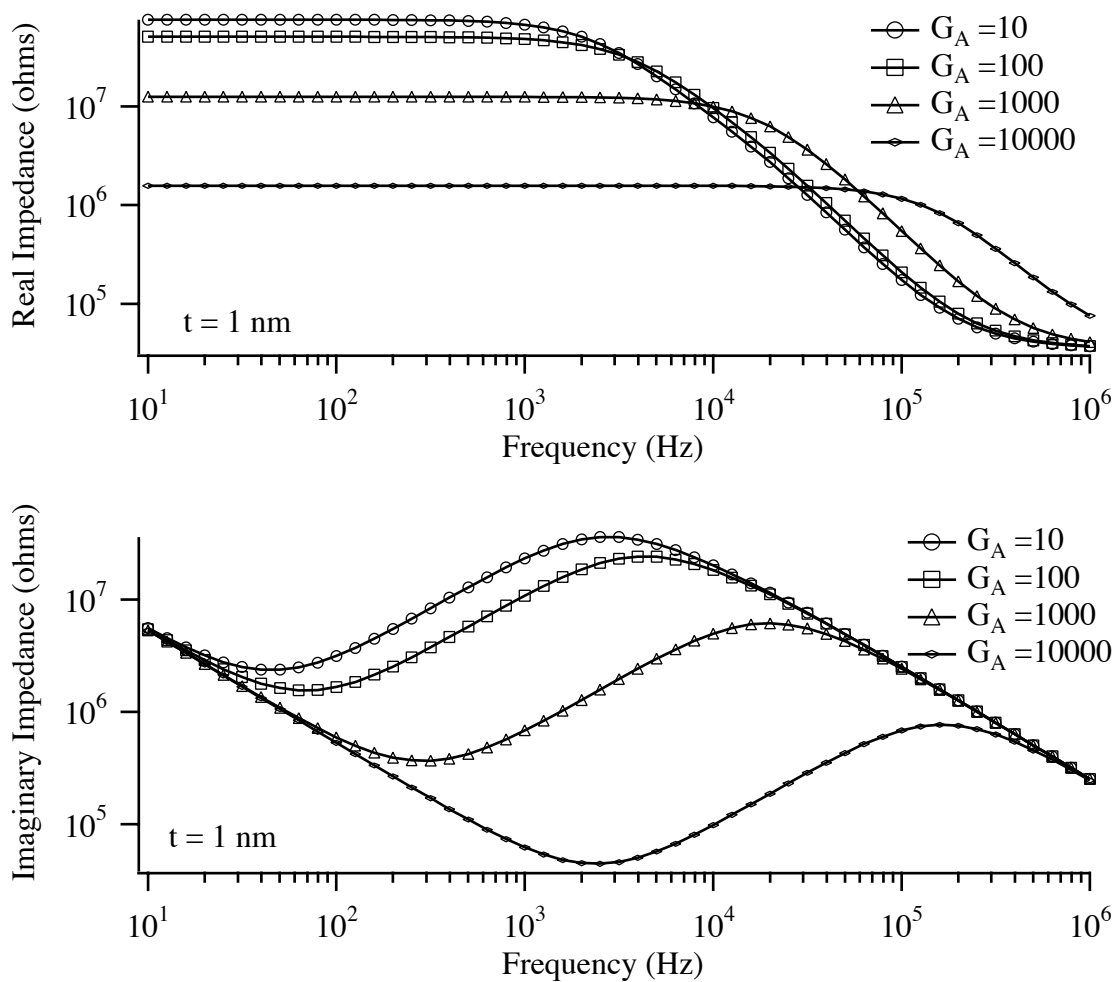
Figure 7.6: Simulated impedance measurements of a 20 μm diameter cell positioned over a 10 μm diameter electrode. A cell to substrate separation of 1 nm was assumed which corresponds to a seal resistance of 80 MΩ. The membrane channel conductance was changed from 10 to 10,000 ℧/m² while the membrane capacitance was fixed at 0.01F/m².

distinguish between modulation of channel conductance and changes in the seal resistance.

As mentioned above, in order for channel modulation effects to be easily observed, it is necessary that the seal resistance be on the same order as the membrane impedance or greater. In the case of low seal resistance, channel conductance modulations will result in significantly smaller changes in the measured impedance. For either case, the seal resistance is essentially in parallel with the ionic channel conductance. While there may be subtle differences in the frequency response due to the distributed capacitance terms,
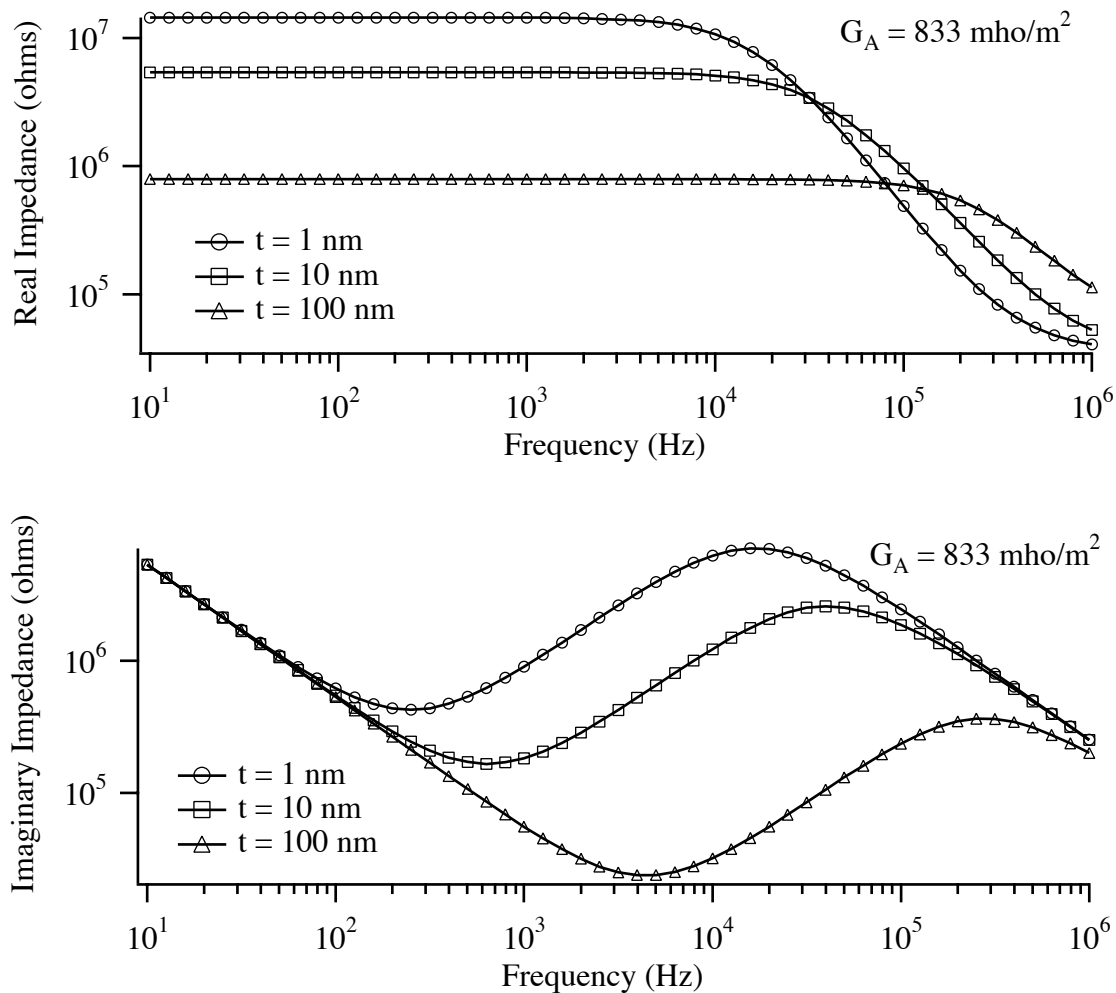
Figure 7.7: Simulated impedance measurements of a 20 μm diameter cell positioned over a 10 μm diameter electrode. A membrane conductance of 833 ℧/m² and capacitance of 0.01F/m² were assumed while the cell to substrate separation was changed from 1 to 100 nm (R_{seal} varied from 80 MΩ to 800 kΩ).

184

changes in channel conductance and modulation of the seal resistance will result in essentially the same change in the measured impedance. This can easily be seen from the SPICE simulations of Figure 7.6 and Figure 7.7 where the channel conductance and seal resistance were changed while keeping all other parameters constant. The electrode was assumed to exhibit capacitive behavior in the frequency range of interest and was given a value of 3 nF (based on average values of measured electrodes). The solution resistance (R_{soln}) was estimated using (3.18) for a circular electrode. The real and imaginary impedances shown in Figure 7.6 and Figure 7.7 are therefore representative of real impedance measurements of the cell / electrode system.

From the simulated results of Figure 7.6 and Figure 7.7 it can be seen that below 100 Hz changes in R_{seal} or the membrane conductance result in changes in the real portion of the measured impedances only. From 100 Hz to 10 kHz there are changes in both the real and imaginary components of the measured impedance, while above 10 kHz the impedance changes are predominantly imaginary. Unfortunately there is little difference between changes in the cell to substrate coupling (R_{seal}) and modulation of the membrane channel conductance. Thus, while a high seal resistance is preferable for monitoring changes in cell membrane conductance, a constant R_{seal} is a requirement. Without a constant R_{seal}, any measured changes in impedance cannot be attributed to ionic channel conductance modulation with any degree of certainty.

7.4 NG108 Impedance Measurements

The impedance of NG108 cells cultured on the planar microelectrode arrays was monitored using the system described in Chapter 5. Cells were plated on the arrays in either serum free of serum containing media (see Appendix C) and allowed to grow for several days prior to running experiments. Impedance measurements were correlated with optical images of cells positioned over the electrodes, channel-specific agents were perfused over the cells to look for modulation of ionic channel conductance, and cellular motility was monitored. For testing of channel-specific agents, the chip was placed in the measurement system and a continuous flow ($\approx$ 1.5 ml/min) of recording media was started. The impedance measurements were allowed to stabilize and the flow was switched to another reservoir of identical recording media to ensure there was no effect from switching flows. With stable impedances, the flow was switched again to a reservoir containing recording media with a channel-specific agent, and changes in the cell / electrode impedance were monitored. Precisely the same experiment was performed

again using an electrode array without cells to ensure the electrode impedance was not directly affected by the pharmaceutical or toxin tested. Concentrations of the channel-specific agents used for these studies were determined empirically. Initial concentrations were estimated based on discussions with several neuroscientists [Perl, 1997; Pancrazio, 1997], and adjusted to provide a measurable cellular response.

7.4.1 Cell Location Monitored Via Impedance

Optical images of cells cultured on the microelectrode arrays provided information regarding cell location. Impedance measurements were shown to provide similar information without the need for a microscope. Figure 7.8 shows both an optical image of cells cultured on the array and a 2-D impedance map of the array. The impedance values shown were calculated to highlight regions where cells were located over electrodes, irrespective of the size of the electrode. The real portion of the bare electrode (no cells) impedance was subtracted from the real portion of the impedance of the electrode with cells and then multiplied by the area of the electrode. This multiplication was done to compensate for the anticipated smaller seal resistance with larger electrodes (given cells of the same size across the array). Close correlation between the 2D impedance map and the optical image was observed. It is important to note that for instances where the location of

(a)   *(b)*
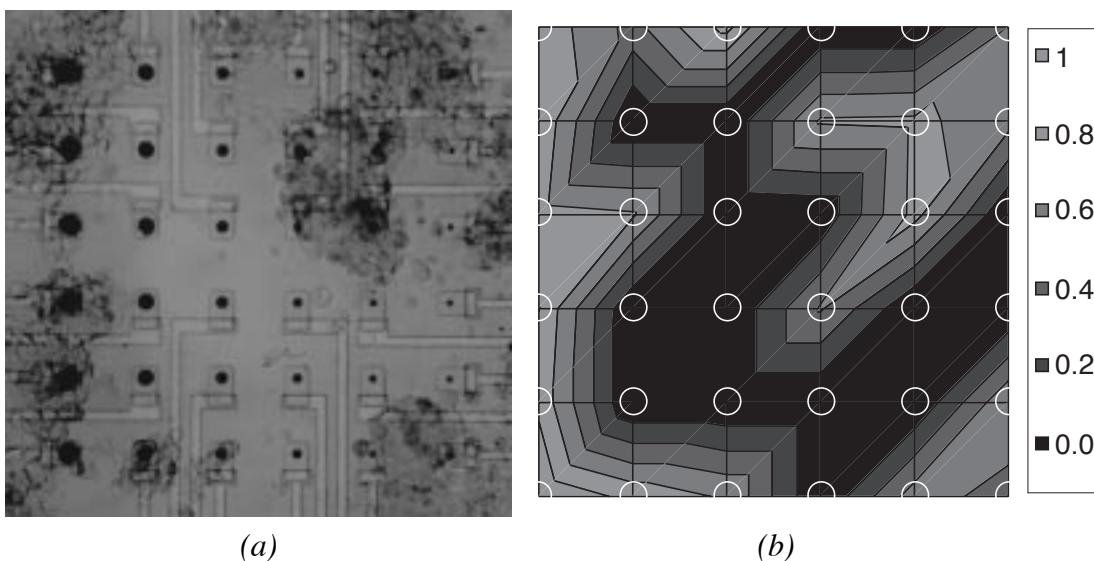
Figure 7.8: NG108 cells cultured in serum containing medium. (a) Optical photograph of cells growing on the microelectrode array. Note the 6 different electrode sizes. (b) 2-D impedance map of the real impedance difference (with cells minus bare electrode) multiplied by the electrode area and normalized to the maximum value. Measurements taken at 10 kHz. Real portion of the impedance was 100 to 700 kΩ for all electrodes.

cells tightly coupled to the electrodes (high R$_{seal}$) is desired, the area multiplication would not be performed.

Constant area electrodes (silicon substrate) were also used for electronically locating cells as shown in Figure 7.9. The 2-D impedance map was calculated by simply dividing the impedance value with cells by that of the bare electrodes (before plating cells). This type of normalization procedure was possible since all electrodes were of the same area and approximately the same starting impedance (in contrast to the variable size electrode array where electrode impedances varied significantly). Note the close correlation between cells positioned over electrodes and higher impedance values.

The results presented in Figure 7.8 and Figure 7.9 were representative of the correlations normally observed between optical images and impedance measurements. Thus, this technique could be used to electronically determine the electrode sites that have cells positioned over them. This could be important when used in conjunction with other measurement techniques such as action potential measurements from neurons, where a tightly coupled cell provides significantly larger signals than one loosely bound to the electrode. Impedance measurements could provide a means of locating candidate cells.

(a)   *(b)*
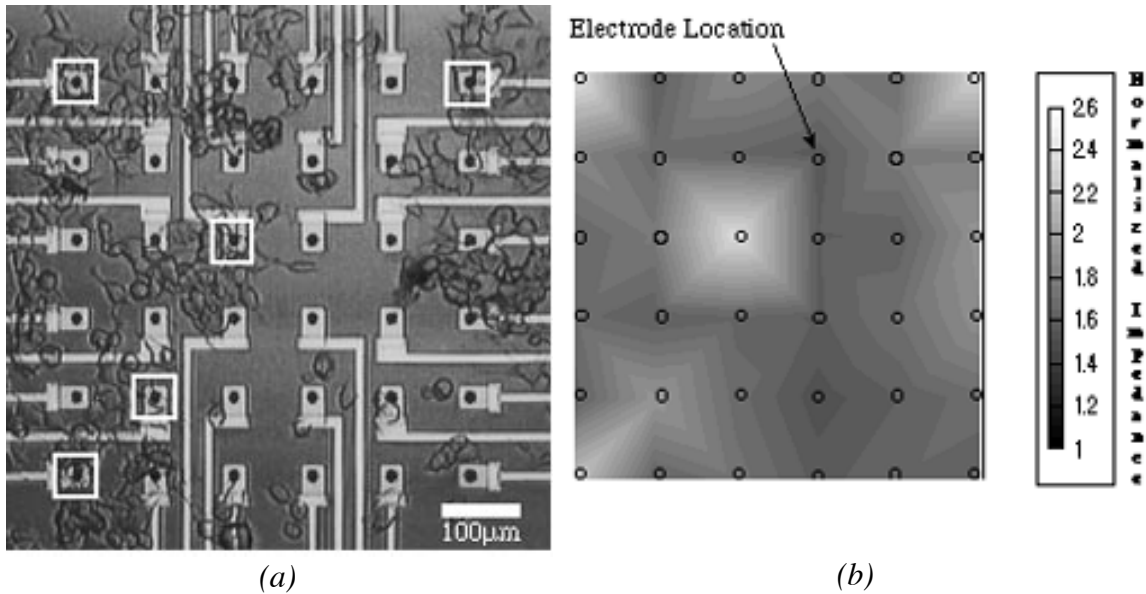
Figure 7.9: NG108 cells cultured in serum containing medium. (a) Optical photograph of cells growing on the microelectrode array (10 µm diameter electrodes). Boxes indicate electrodes with apparent tight cell / electrode coupling as seen by the impedance map in (b). (b) 2-D impedance map of the real impedance with cells divided by that of the bare electrodes. Measurements taken at 1 kHz. Real portion of the impedance was 100 to 500 kΩ for all electrodes.

Additionally, for sensor applications where limiting the volume of data collected may be of importance, this technique could be used to decide which electrodes should be monitored.

7.4.2 Toxin Effects on Impedance

Several different channel-specific agents were tested with cultured NG108 cells in an effort to observe modulation of ionic channel conductance. Two resulted in changes in the measured bare electrode impedance (barium and cadmium ions) and were therefore not used in cell experiments. Others such as tetrodotoxin and verapamil did not have any effect on the electrode impedance and could be used to look for ionic channel conductance modulation.

As outlined in Chapter 6, tetrodotoxin is a direct, specific blocker of Na^+ channels. This toxin has been shown to affect NG108 Na^+ channel conductance [Kowtha, et al., 1993]. Impedance changes resulting from perfusion with TTX were consistent with blockage of ionic channels as shown in Figure 7.10 (recall the simulated impedance changes of Figure 7.6). Both the real and imaginary components of the measured
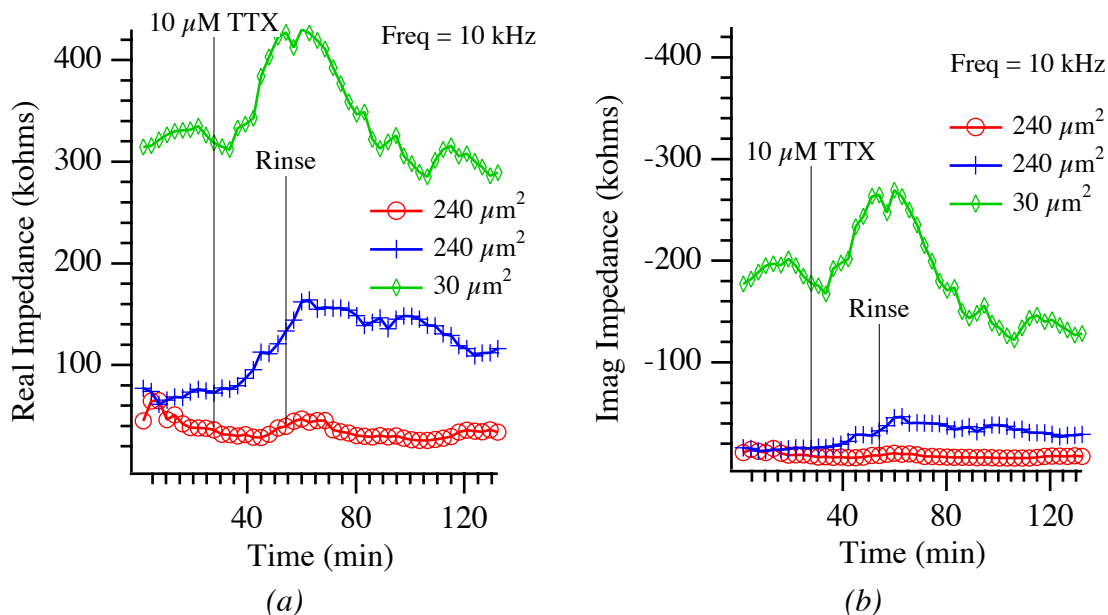
Figure 7.10: *Real (a) and imaginary (b) impedance of NG108 cells cultured on the microelectrode array for one day in serum-containing medium. Note the increase in both the real and imaginary impedance on two of the three electrode sites shown with perfusion of 10 µM tetrodotoxin. All three electrodes had cells visible over the electrode sites with optical inspection.*

impedance increased with addition of the channel blocker and decreased upon rinsing (for the sites where there was a response). However, the impedance magnitudes were low compared to the anticipated range of ionic channel resistances. Thus, it was likely the seal impedance was poor for these samples (which were characteristic of all experiments using NG108 cells). While definite responses were observed on some cell bearing electrode sites in numerous (> 10) experiments with the addition of TTX, these responses were sporadic and did not correlate with tight cellular coupling to the electrode (calculated by subtracting the bare electrode impedance from the measured impedance with cells) as would be expected. For these reasons, it was unclear if the observed responses were due to the action of tetrodotoxin on the Na^+ channels, or if it was a random process that coincidentally correlated to the addition of this toxin.

Verapamil (a Ca^{2+} blocker) was also used to look for ionic channel conductance changes using the same techniques as outlined for TTX. Perfusion with 10 μM verapamil had no effect while 100 μM verapamil showed significant increases in both the real and imaginary components of the impedance as shown in Figure 7.11. As with the TTX results, the magnitude of the impedances was low, suggesting a low seal resistance.
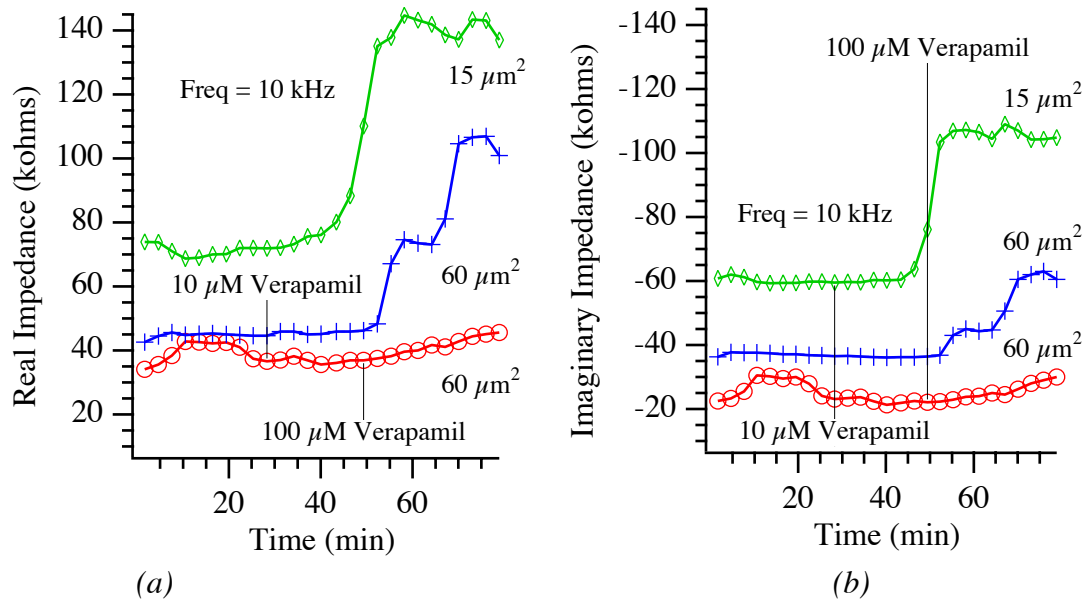
Figure 7.11: *Real (a) and imaginary (b) impedance of NG108 cells cultured on the microelectrode array for three days in serum containing media. Note the increase in both the real and imaginary impedance on two of the three electrode sites shown with perfusion of 100 μM verapamil. There was no observed response with 10 μM verapamil. All three electrodes had cells visible over the electrode sites with optical inspection.*

Responses to verapamil were observed on numerous occasions, but no correlation to cell / electrode coupling could be made. As with TTX, the observed responses could have been due to a random process that correlated to the addition of this pharmaceutical.

Changes in impedance versus frequency with the addition of 100 μM verapamil were examined as shown in Figure 7.11. For this experiment, verapamil was introduced into the dish at time = 45 minutes and the impedances at time = 20 minutes and time = 60 minutes were compared. Note the real portion of the impedance changed at all frequencies while the imaginary component changes were only at the mid to high frequencies (frequency range 100 Hz to 100 kHz). The differences between these plots and the modeled response to changes in channel conductance and seal resistance (Figure 7.6 and Figure 7.7 respectively) were most likely due to a larger capacitance than modeled being in parallel with the seal resistance and ionic channel conductance. Thus, the real portion of the impedance was decreasing with frequency rather than being constant as shown in Figure 7.6 and Figure 7.7.

All of the measured responses for TTX and verapamil over numerous experiments were ultimately inconclusive due to the sporadic nature of the response, and the lack of correlation to high seal resistances. Additionally, the NG108 cells generally suffered from
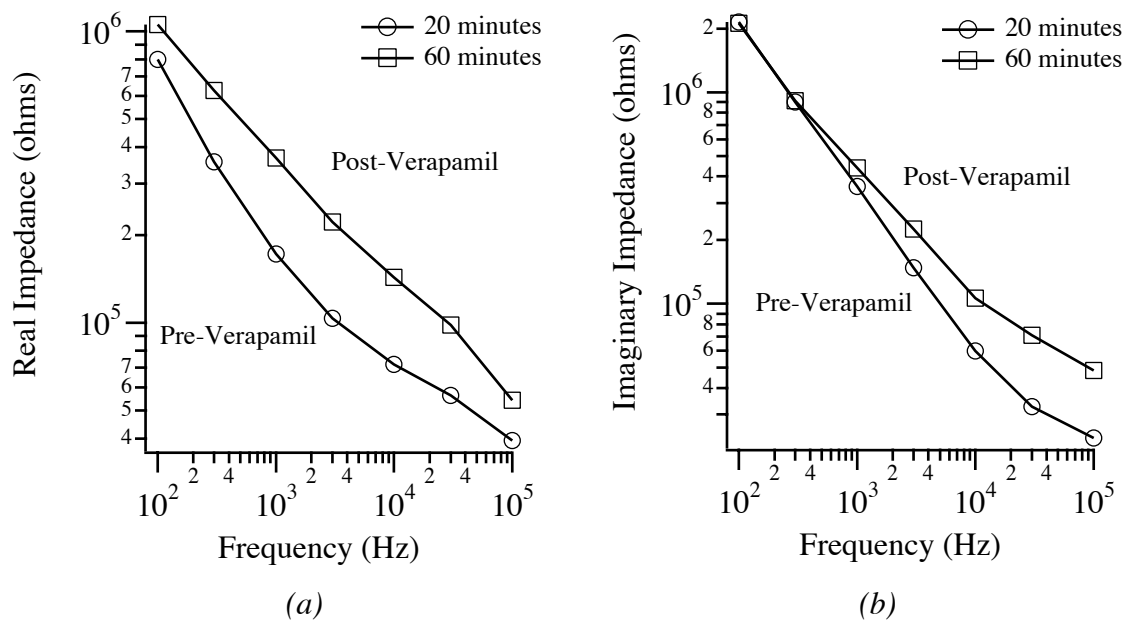
Figure 7.12: Real and imaginary impedance versus frequency for the 15 μm^2 electrode and cell used for Figure 7.11. 100 μM verapamil was perfused over the cells at time ≈ 45 minutes.

low seal resistances (as evidenced by the total measured impedance range limited to several hundred kΩ at 10 kHz). These issues made correlation of the response to channel-specific agents to the modeling for optimum electrode size impossible. Over 50 experiments were performed using NG108 cells cultured on the variable size electrode arrays. In each case, any measurable response to a channel-specific agent was correlated to the measured seal resistance and the electrode size. Unfortunately, no pattern or trend emerged from the data. The discovery of NG108 motility provided another possible explanation for the observed data. It is possible all responses were due to the chance movement of cells at the time of addition of the channel-specific agents as will be described below. This would explain the lack of correlation to the seal resistance and the optimum electrode size model.

7.4.3 Motility Effects on Impedance

Data has been presented showing changes in impedance consistent with the reduction of ion channel conductance. However, similar responses were sometimes observed if the impedance was monitored over time without changing the composition of the recording media (i.e., no channel-specific agents were added). Using time lapse photography it was possible to correlate these changes with movement of cells over the electrodes as shown in Figure 7.13. During the time of the experiment, a cell migrated over electrode #22 as shown in the photographs while electrode #19 remained free of cells. Examination of the impedance plots revealed this movement was correlated with an increase in the real impedance and a corresponding decrease in the imaginary impedance. Note the similarity between these plots and those of Figure 7.10 and Figure 7.11. The response versus frequency was similar to Figure 7.12 as well (data not shown). Thus, it is possible that the effects observed with the channel-specific agents were due entirely to cell motility rather than ionic channel conductance modulation. The inhibition of this motion was therefore required if channel conductance modulation was to be confirmed.

There are numerous pharmaceuticals and toxins which inhibit the polymerization and depolymerization of actin and tubulin. Since these protein structures are involved in cell movement (as described in Chapter 2), inhibition of their normal action should result in cessation of cell movement. If movement can be stopped, then the channel-specific agent experiments could be run again to verify the signals were due to modulation of ionic channel conductance. Four different compounds were tested: taxol, which inhibits tubulin disassembly processes; vinblastine, which inhibits tubulin polymerization and causes tubulin to form crystal-like aggregates; phalloidin, which inhibits actin filament
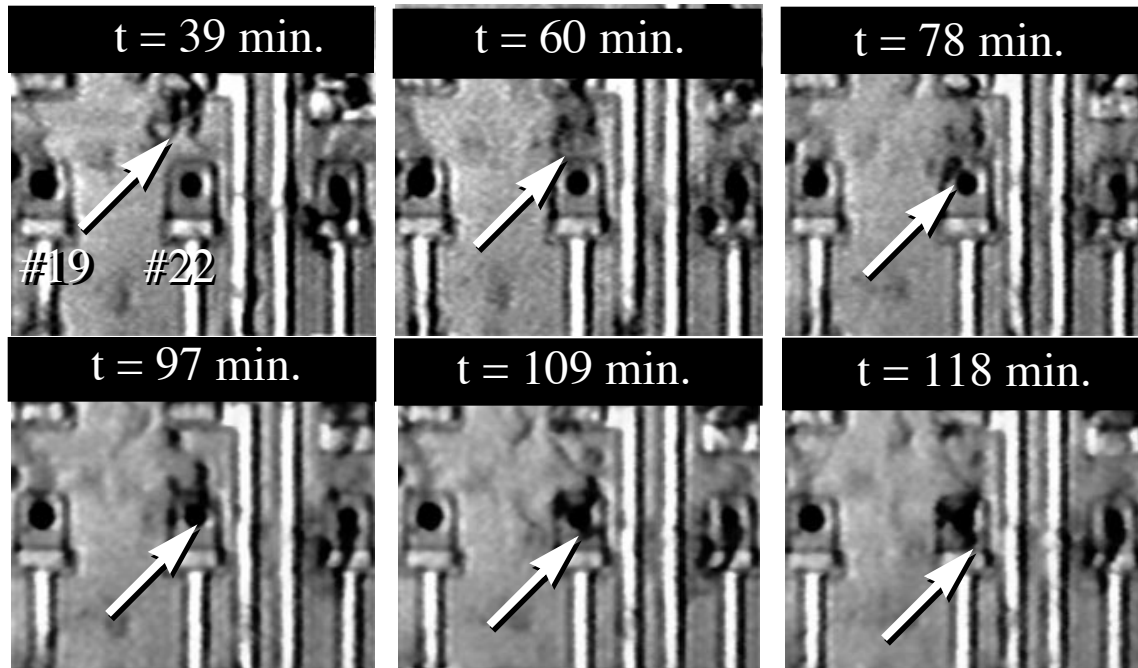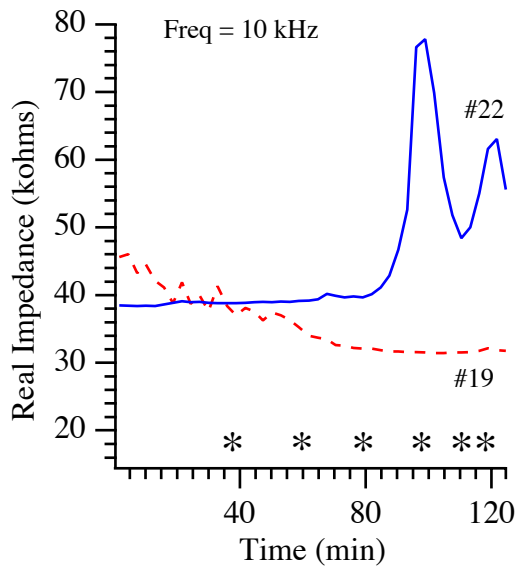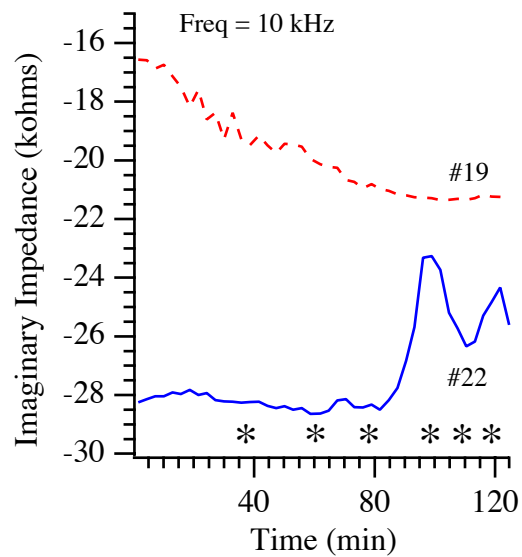
Figure 7.13: NG108 motility with cell cultured for one day in serum containing media. (a) Time lapse photography showing the movement of a cell over electrode #22. The arrow points to the leading edge of the cell in each frame. The times correspond to the time in the impedance plots of (b) and (c). (b) Real impedance over time at 10 kHz. (c) Imaginary impedance over time at 10 kHz. For both cases the asterisks mark the points where the photographs were taken. Image quality is poor, but was the best that could be obtained using a video microscope during the experiment.

depolymerization; and cytochalasin-D, which inhibits actin filament polymerization. Taxol (500 nM), vinblastine (5 μM), and phalloidin (6 μM) had little to no effect on the movement of NG108 cells, even when used together. Changes in impedance of up to 10 × were observed over time with all of these compounds in the recording media. Cytochalasin-D (10 μM) was successful in inhibiting movement of the NG108 cells, however this compound (when used at high enough concentrations to inhibit movement) caused the cells to detach from the surface, resulting in a reduction of the measured impedance. Thus, while this toxin did inhibit movement, it significantly reduced the seal resistance making sensing of changes in channel conductance difficult if not impossible.

With changes in cellular membrane conductance and the seal resistance indistinguishable, and efforts to inhibit motility unsuccessful, a cell type with inherently lower motility was examined.

7.5   Astrocyte Impedance Measurements

As described above, astrocytes have numerous qualities that make them likely candidates for measurement of changes in ionic channel conductance. When cultured *in vitro* they are up to 100 μm in diameter and can form close contacts to the substrate. Both of these characteristics are favorable for the development of high seal resistances. When cultured at the appropriate densities, astrocytes form monolayers in culture with tight junctions between cells. These tight junctions help inhibit cell movement, thereby making astrocytes intrinsically a low motility cell type *in vitro*.

The impedance of embryonic mouse astrocytes cultured on the planar microelectrode arrays was monitored using the same techniques described for the NG108 cells. Cells were plated on the arrays in standard culture media (see Appendix C) and allowed to grow for several days to weeks prior to running experiments. In this instance the experiments were structured around calcium imaging studies performed in [Van Den Pol, et al., 1995] where responses to glutamate and glutamate receptor blockers were monitored. Depending on the cell type, number of days *in vitro* and the culture conditions, different glutamate receptors (*metabotrophic* and *ionotrophic*) are present. Metabotrophic receptor activation results in release of Ca^{2+} from intracellular stores and should not be observed with the impedance measurements performed herein. Ionotrophic receptors however, are linked to Ca^{2+} channel gating, and when activated cause these channels to open. Thus, any glutamate induced *ionotrophic* receptor activation should result in a reduction in the measured impedance. For the majority of astrocytes monitored in Van Den Pol, et al.'s

193

experiments, no metabotrophic receptor responses were observed. However, ionotrophic responses to glutamate were observed and correlated to opening of Ca^{2+} channels in the cellular membrane. This response to addition of glutamate was maintained for over ten minutes in their experiments at which point the glutamate was removed and the Ca^{2+} levels returned to normal. The response resembled a square wave. Addition of a ionotrophic receptor blocker resulted in no response when glutamate was added.

This experiment was repeated using impedance measurements in the hope of observing opening of Ca^{2+} channels in response to glutamate. As a control, the ionotrophic glutamate receptor antagonist cyano-2,3-dihydroxy-7-nitroquinoxaline (CNQX) was used in combination with glutamate. The expected result was a decrease in measured impedance with addition of glutamate, and no response from CNQX or CNQX plus glutamate. Responses from cultured astrocytes are shown in Figure 7.14.

As can be seen from the responses of Figure 7.14, the addition of glutamate caused an increase in the real impedance and a decrease in the imaginary impedance. This was the opposite of the anticipated result. The ionotrophic glutamate receptor antagonist CNQX
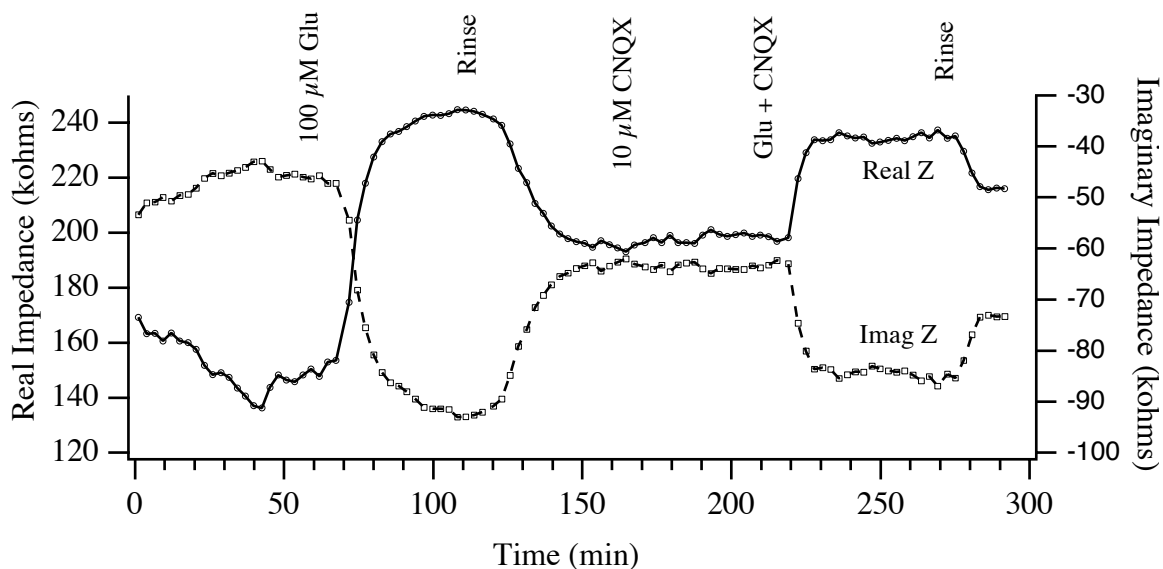
Figure 7.14: Impedance measurements on cultured astrocytes at 45 days in vitro. Addition of 100 µM glutamate resulted in increased real impedance and decreased imaginary impedance. Removal of the glutamate by rinsing resulted in a partial recovery. The glutamate receptor blocker CNQX had no effect while 10 µM CNQX plus 100 µM glutamate elicited the same response as glutamate alone. This effect was also reversible. Measurements taken at 3 kHz on a 480 µm² electrode. This data was characteristic of that observed on most electrodes in the array, and with numerous experiments.
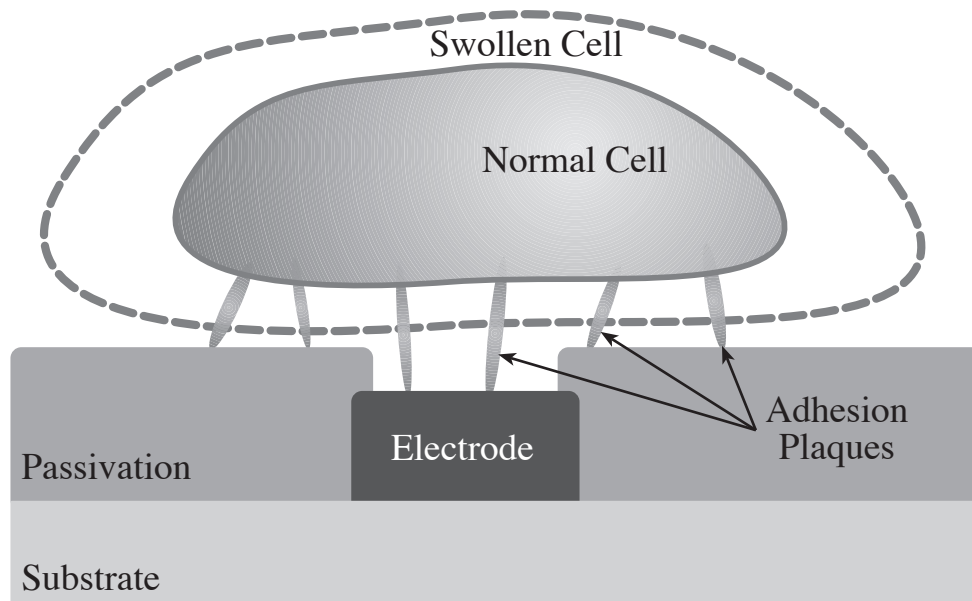
Figure 7.15: Cartoon depicting a possible effect of cell swelling. If the adhesion plaques (focal contacts) holding the cell in place are of low density, then it is possible a large percentage of the cell area has a cell / substrate separation larger than the minimum possible (due to molecular forces, etc.). In this case, swelling of the cell could reduce the cell / substrate separation in all regions that are not focal contacts. This would result in an increased seal resistance and the impedance results observed.

had no effect on the measured impedance alone, but CNQX with glutamate elicited a similar response to glutamate alone. These responses were repeatable and definitely not due to intrinsic cell motility (long term measurements of the impedance with astrocytes resulted in no significant impedance fluctuations). Since CNQX did not inhibit the response, it is doubtful that the changing impedance was due to glutamate binding to the ionotrophic receptor site. However, the responses were consistent with a decreasing cell to substrate separation (increasing R_{seal}). Additionally, the greatest responses were observed for the largest electrode sizes where a lower seal resistance was expected. This was consistent with changes in the seal resistance being responsible for the observed impedance changes.

A decreased cell to substrate separation could be consistent with cell swelling if the cell has close adhesions in a few areas and is more loosely coupled elsewhere. This possibility is depicted in the diagram of Figure 7.15 where the cell to substrate spacing has been exaggerated. Note that the cell is "tethered" to the substrate by the adhesion plaques, and the majority of the cell membrane is further removed from the substrate. As the cell
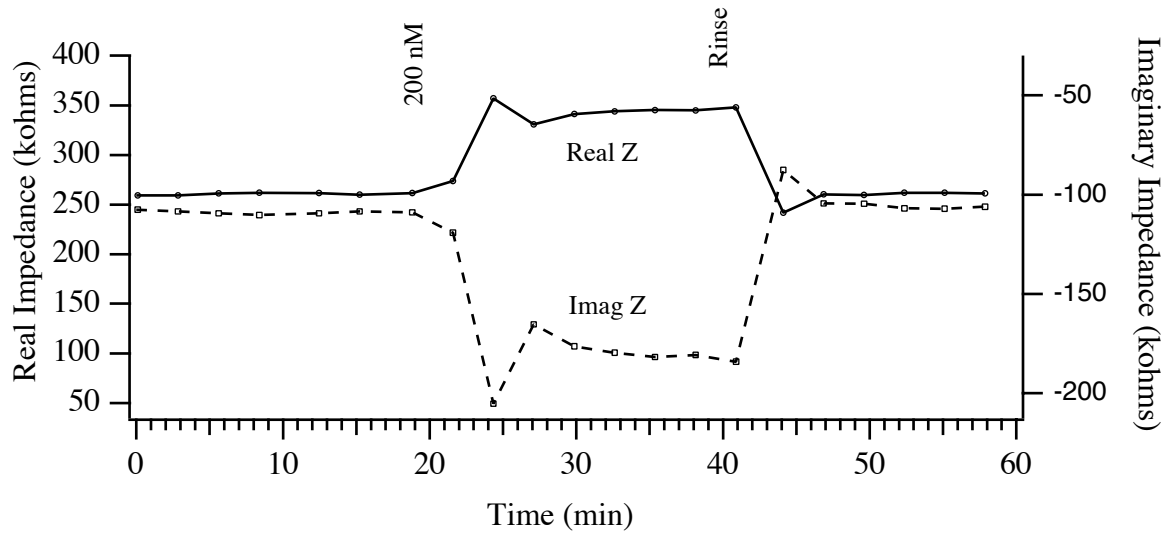
Figure 7.16: Astrocyte response to a hypoosmotic solution. The recording media was changed from the normal 300 mOsm/kg to 200 mOsm/kg. This change in osmotic strength theoretically resulted in 37 psi across the cell membrane, and subsequent cell swelling. The result was an increase in the real impedance and a decrease in the imaginary impedance. These responses were consistent with those observed with addition of glutamate. Measurements taken using a 3 kHz. excitation frequency on a 480 μm^2 electrode. This data was characteristic of that observed on most electrodes in the array, and with numerous experiments.

swells, it is possible the distance between the cell and the substrate would be decreased. This would result in an increase in the real impedance and a corresponding decrease in the effective area contributing to the capacitance on the bottom side of the cell (due to the distributed nature of the cell membrane with the seal resistance). Thus, the results of Figure 7.14 are potentially consistent with cellular swelling. Additionally, glutamate induced swelling of astrocytes has been reported in the literature [Bender, et al., 1995]. In this study 1mM glutamate resulted in a 2 × change in cell volume. The observed swelling was not related to K^+ activation, glutamate uptake within the cell, or ionotrophic glutamate agonists, but rather activation of metabotrophic glutamate receptors. These results are consistent with the experimental results in Figure 7.14 where the ionotrophic glutamate antagonist CNQX did not inhibit the glutamate response.

To experimentally test if the observed response was consistent with astrocyte swelling, the osmolality of the solution was decreased from the standard 300 mOsm/kg to 200 mOsm/kg. This change in osmotic strength presented a pressure of 37 psi (255 kPa or 2.5 atm) across the cell membrane and should have resulted in water flow into the cell,

increasing cellular volume. The results of this experiment are shown in Figure 7.16. As the osmotic strength of the solution was decreased, the real impedance increased while the imaginary impedance decreased. Switching back to a 300 mOsm/kg solution (rinse) resulted in the impedances returning to normal. This response was consistent with the glutamate results presented in Figure 7.14. While this did not conclusively prove the observed response was glutamate induced swelling, it does indicate that the response was consistent with swelling of the astrocytes.

Since the response to glutamate was not consistent with opening of Ca^{2+} channels, it was not possible to correlate the data to the optimum electrode size model developed in Section 7.3.2. Additional work is required improve the seal resistance of the astrocytes to the cell culture substrate so that issues such as swelling do not significantly impact the recorded impedance. If this can be done, then experimentation with channel-specific agents should yield data which can be used to correlate the recorded signal strength with the measured seal resistance. This data could also be used to verify the optimum electrode size modeling if the variable size electrode arrays are used as the substrate for cell culture.

The frequency characteristics of the astrocyte response to glutamate was briefly examined and found to be consistent with a changing seal resistance. Once consistently high seal resistances are obtained with the astrocytes and data on the response to channel-specific agents are collected, it should be possible to use the full capabilities of the developed impedance system to explore the optimum frequency for detection of changes in membrane conductance. Better correlation to the modeling of Section 7.3.3 should also be possible. Unfortunately, the biological studies required for improved seal resistance were beyond the scope of this work, making these correlations impossible at this time.

7.6   Conclusions

The cell / electrode interface was modeled, and an optimum electrode diameter was estimated to be half that of the cell to be measured. Modeling indicated that discriminating between changes in the seal resistance and ionic channel conductance modulation would be difficult if not impossible. Thus, it was important that the cells not move during experimentation if the action of channel-specific agents was to be monitored.

The system developed for monitoring impedances of cells cultured on extracellular microelectrodes was evaluated using two different cell types: NG108 cells and embryonic mouse astrocytes. Correlation of cell location determined optically and cellular coupling

determined via impedance measurements was accomplished. This technique could be of use for any sensor technology where maximized signal strength and reduced quantity of data are important. In particular, for action potential studies the technique would be useful for locating cells tightly coupled to the electrodes (which has been shown to correlate to larger recorded signals).

Attempts to monitor changes in cellular membrane properties using the microelectrodes were less successful. While changes in measured impedances with addition of channel-specific agents were observed with NG108 cells, the signals were indistinguishable from cell movement artifacts. Attempts to pharmacologically inhibit cellular motility were either unsuccessful or resulted in lifting of the cells from the substrate (significantly reducing the total seal resistance). Thus, the experiments with NG108 cells were inconclusive.

The use of astrocytes cultured on the microelectrode arrays eliminated the motility problems encountered with NG108 cells since this cell type formed a monolayer with tight junctions. Experiments to monitor glutamate induced opening of Ca^{2+} channels resulted in changes in measured impedance opposite to those expected. The results were found to be consistent with glutamate induced swelling of the astrocytes however. Thus, while intrinsic motility was not an issue when using astrocytes, swelling may make conclusive observation of ionic channel conductance modulation difficult. It is possible that surface treatments prior to plating the cells could improve the number and density of adhesion plaques thereby limiting the impact of swelling while simultaneously improving the seal resistance. However, experimentation with different surface modifications was beyond the scope of this work.

While six different electrode sizes were available on the electrode array for comparison of the observed responses to the theoretical models (and optimum electrode size), these correlations could not be made with the given data. The response of NG108 cells to channel-specific agents occurred for only a few cells within each experiment and were not correlated to higher seal resistances. It is likely all responses were actually due to cell motility which coincidentally coincided with the addition of the toxin or pharmaceutical being tested. The observed responses of astrocytes to glutamate was thought to be due to changes in R_{seal} rather than ionic channel conductances. Therefore no correlation was possible to the modeled optimum electrode size using this cell type either.

The system developed for measuring the impedance characteristics of cells cultured on a microelectrode array functioned well and within specifications. It allowed impedance data to be obtained across a broad frequency range simultaneously for an array of 36

electrodes over time. When combined with the continuous flow perfusion system, stable experimental conditions could be maintained. The main limitations for the experiments performed herein were poor seal resistances, motility, and cellular swelling. The use of cells which inherently exhibit low motility (e.g. astrocytes) eliminates one of these issues. However, the data collected herein suggests that efforts to improve the cell to substrate coupling are of critical importance if changes in the cellular membrane are to be observed. This should be the focus of any further efforts to measure cellular membrane properties using extracellular microelectrodes.

References

Bender, A.S., Schousboe, A. and Norenberg, M.D., "Pharmacological Characterization of Glutamate-Induced Astrocyte Swelling," *Society for Neuroscience Abstracts*, 21(2):1081 (1995).

Bray, D., *Cell Movements*, Garland Publishing, Inc., New York (1992).

Hille, B., *Ionic Channels of Excitable Membranes*, Sinauer Associates, Inc., Sunderland, Massachusetts (1992).

Kandel, E.R., Schwartz, J.H. and Jessell, T.M., *Principles of neural science, Third Edition*, Appleton and Lange, Norwak, Connecticut (1991).

Kowtha, V.C., Quong, J.N., Bryant, H.J. and Stenger, D.A., "Comparative electrophysiological properties of NG108-15 cells in serum-containing and serum-free media," *Neuroscience Letters*, 164:129-133 (1993).

Nicholls, J.G., Martin, A.R. and Wallace, B.G., *From neuron to brain*, Sinauer Associates, Inc., Sunderland, Massachusetts (1992).

Pancrazio, J.J., *Personal Communication*, Jan.-Dec. (1997).

Perl, E.R., *Personal Communication*, Jan.-Dec. (1997).

Van Den Pol, A.N., Obrietan, K., Cao, V. and Trombley, P.Q., "Embryonic hypothalamic expression of functional glutamate receptors," *Neuroscience*, 67(2):419-439 (1995).

Wang, J.F., Shun, X.J., Yang, H.F., Ren, M.F. and Han, J.S., "Suppression by [D-Pen2, D-Pen5] enkephalin on cyclic AMP dependent protein kinase-induced, but not protein kinase C-induced increment of intracellular free calcium in NG108-15 cells," *Life Sciences*, 52(19):1519-1525 (1993).

Chapter 8   CONCLUSIONS AND FUTURE WORK

What doesn't kill us makes us stronger.

Nietzsche

The use of living cells as sensor elements provides the opportunity for high sensitivity to a broad range of biologically active substances that affect cellular function. These biologically relevant signals can be directly measured using microelectrodes, which provide a stable, non-invasive interface for monitoring populations of cells. The potential uses for such cell-based sensors include environmental monitoring (chemical / biological warfare agents, groundwater contamination, etc.), pharmaceutical screening, drug discovery, and basic neuroscience.

This work was focused on the development of cellular measurement systems based on extracellular action potential monitoring and impedance measurements. Electrode arrays utilizing new packaging techniques were developed to act as the substrate for the culture of anchorage dependent cell types. The action potential system was used to observe changes in the action potential *shape* due to pharmacological manipulation, and determine if the AP characteristics could be used to extract important information about the cellular response. The impedance system was developed to measure cellular membrane properties (capacitance and conductance) and monitor changes due to the action of channel-specific agents.

The fabricated microelectrode arrays were a combination of glass substrates and platinized electrodes which provided the low impedance, low parasitic elements essential for high SNR action potential and impedance measurements. The materials used for electrode fabrication and packaging have proven to be non-toxic and conducive to cellular

attachment and growth. Incorporation of a cell culture chamber with a standard dual in-line package allowed the cells to be easily transferred from an incubator to the measurement systems. The arrays have been used successfully with both action potential and impedance measurements with a variety of cell types.

The action potential measurement system (and associated fluidic and thermal systems) was shown to provide a stable means of monitoring the extracellular APs. Action potentials have been recorded from spontaneously beating chick myocardial cells cultured on the microelectrode arrays. Easily measurable quantities such as the beat rate and AP amplitude have been monitored and found to correlate well with biologically anticipated responses. For the first time, changes in the extracellular AP shape have been used to monitor the cellular response to the action of pharmaceuticals and toxins. The use of power spectral density analysis as a tool for classifying the action of a biologically active agent was investigated and found to offer promise if consistent cell populations can be developed.

The impedance system developed was capable of measuring impedances consistent with cellular membrane properties given a sufficiently high seal resistance. Experiments using two different cell types and a variety of channel specific agents were inconclusive due to cellular motility (which could not be inhibited) and presumed cellular swelling. It is possible that channel modulation was observed, but changes in the measured impedance could not be distinguished from changes in the seal resistance.

This work has examined new aspects of cell based sensors and attempted to monitor changes in cellular response that had previously been ignored. The action potential experiments successfully registered changes in the shape of the AP with addition of channel specific agents, even though the extracellular signal was a second derivative of the transmembrane potential. The derivative nature of the recorded signal means low frequency information is lost which could be useful for expanding the sensing capabilities and sensitivity when AP shape is examined. Thus, it is important that future work focus on improving the cell to substrate adhesion for increased seal resistance, since this has been shown to reduce the order of the derivative observed. The use of stimulation pulses to pace the cells would also allow better averaging to be performed. With sufficient averaging, it may be possible to observe the repolarization of the AP which would provide the desired low frequency information. As proposed by professor Edward Perl (UNC Chapel Hill), it is also possible to measure the fastest pacing rate possible, and deduce the refractory period of the cells. This would give an indication of the repolarization time and provide an

estimate of the low frequency signal. Both of these techniques should be fully investigated.

Alternative analog measurement techniques for real time analysis of the action potential should also be explored. It is possible the total rms power of the AP would be a better indicator of general shape than the simple peak to peak amplitude monitored in this work. Additionally, by examining the rms power in different frequency bands, it may be possible to approximate the power spectral density analysis performed numerically herein. The use of analog rms power measurements should be examined in detail.

Further work on the cell culture chamber is also required if quantitative dose response curves and response times are to be obtained with the cultured cell systems. The current packaging technology utilized a relatively large volume P35 dish to encapsulate the cell culture media. This large volume (approximately 4 ml) prevented fast exchange of the media in the dish, and the efficiency of mixing was unknown. To alleviate these problems, a flow through chamber should be designed with a small fluid volume (μl). This would facilitate rapid and efficient media exchange making quantitative measurements possible.

Consistency between cell populations is extremely important for any sensor application. Thus, future work focusing on engineered cell lines with more consistent characteristics is crucial if techniques such as PSD analysis are to be used to deduce the action of unknown agents. The use of frequency domain analysis of intracellular AP recordings would also be of significant interest, since much better sensitivity to the plateau and repolarization phases of the signal would be obtained (as compared to the extracellular recordings). It is possible this technique could expand the utility of classical analysis techniques, and allow more functional information to be obtained with fewer required experiments.

For measurement of cell membrane properties via impedance to be conclusively successful, a high and *constant* seal resistance must be maintained. Thus, either surface modifications that enhance the density of adhesion plaques, or an active method (such as suction) must be employed in the future to maintain a steady seal resistance. Another alternative suggested by Professor Steven Boyd (Stanford University) is to overdrive the cells to purposely open voltage-gated channels. Since the discrete opening of channels is a nonlinear process, harmonics would be present in the output signal. If the homodyning stage was changed to tune to harmonics rather than the fundamental, it is possible this channel conductance could be observed. Since changes in the seal resistance are linear in nature, they would not contribute to this harmonic signal. It is important to note that these harmonic signals would be extremely small as they result from current flow through the

opening ionic channels (and a current divider exists between the seal resistance and the channel conductance). Thus, a high seal resistance is required for this technique to be practical. However, given a sufficiently high seal resistance, this method could allow changes in membrane properties to be observed in the presence of a changing seal resistance. The only caveat is that a changing seal resistance would also change the effective voltage drop across the cellular membrane (recall the circuit model of Chapter 7). Thus, the gating drive on the channels would change, possibly resulting in a changing harmonic response. This technique should be tested to evaluate its utility. If it does not work, and an improved seal resistance cannot be obtained, then the use of extracellular microelectrodes for impedance studies will be limited to measurement of proliferation, cell / substrate separation, and motility.

Microelectrode based sensor technologies offer promising possibilities for the use of living cells as sensor elements. While more work is required to fully prove the utility of the techniques presented herein, there is clear evidence that cultured cells coupled to microelectrodes can be a powerful tool for analyzing the effects pharmacological and toxic agents on living cells. Further advances in cultured cell technologies, genetically engineered cell lines, and substrate structures will improve the power of these techniques, and undoubtedly permit the use of these technologies for pharmaceutical screening, drug discovery and environmental sensors.

Appendix A CHIP PACKAGING SCHEMATICS
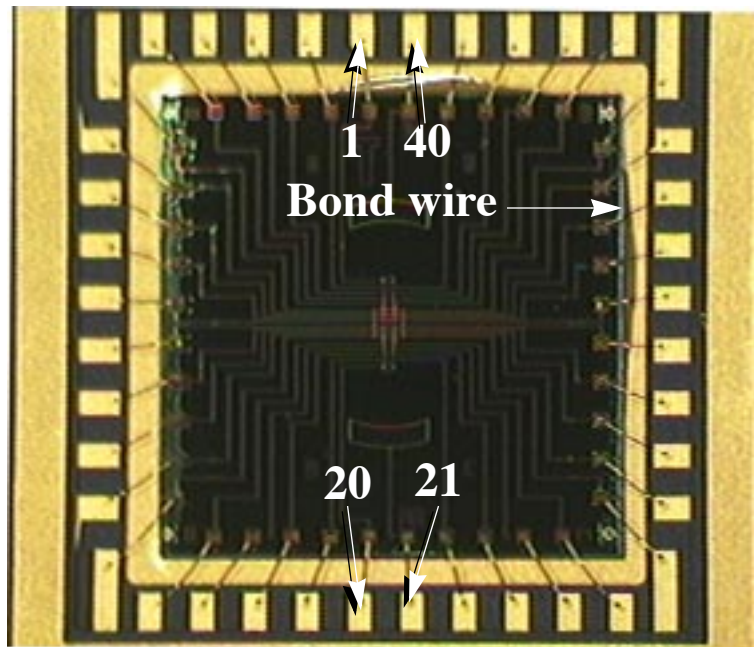
Figure A.1: Packaged electrode array showing the pads corresponding to pins 1, 20, 21 and 40 on the DIP package. The bond wires connecting the chip and package are clearly visible.

1
2
3
4
5
6
7
8
9
10
11
12
13
14
15
16
17
18
19
20

40
39
38
37
36
35
34
33
32
31
30
29
28
27
26
25
24
23
22
21

5 4 3 2 1 40 39 38 37 36
6   35
7   34
8   33
9   32
10   31
11   30
12   29
13   28
14   27
15   26
16 17 18 19 20 21 22 23 24 25

40 Pin DIP

40 S/B CAV.400

MFGP/N: KD-78302-C

Kyocera
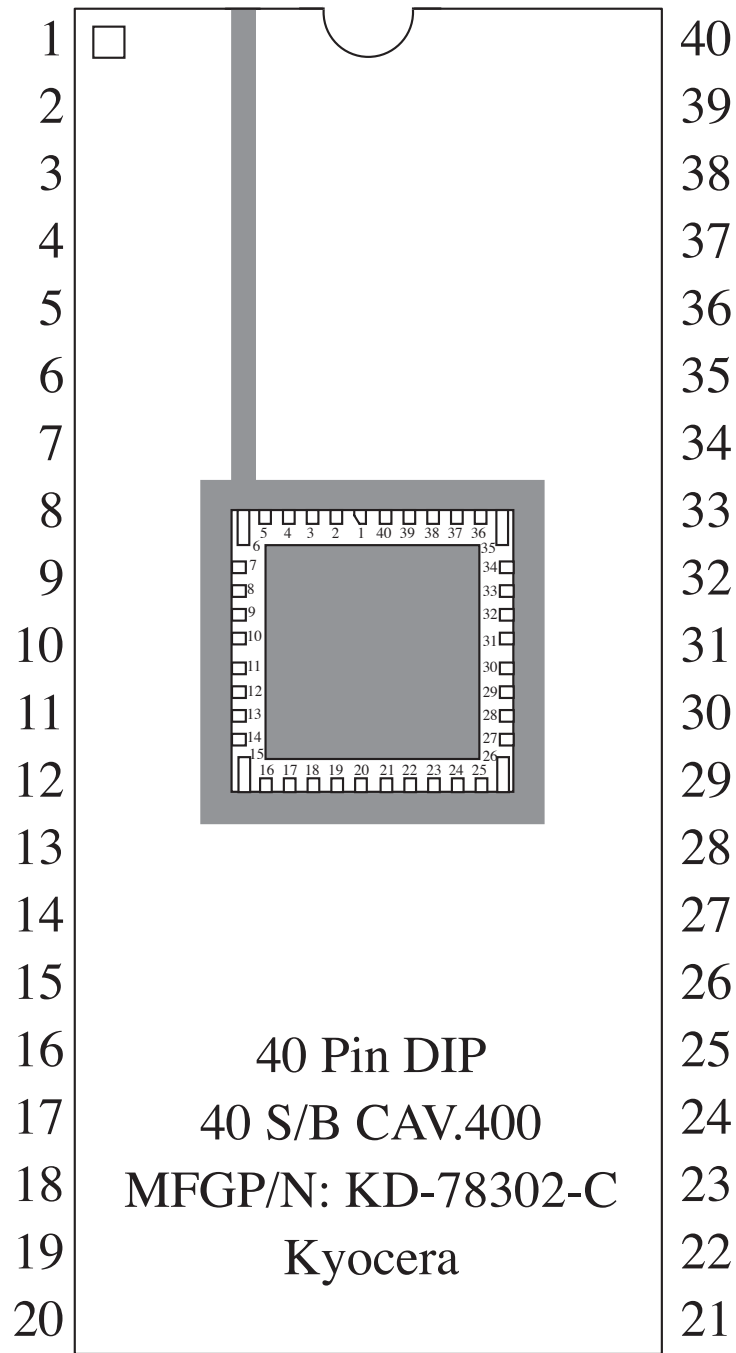
Figure A.2:   40 pin DIP showing the die cavity and package bond pads. The bond pads are electrically connected to the corresponding package lead.
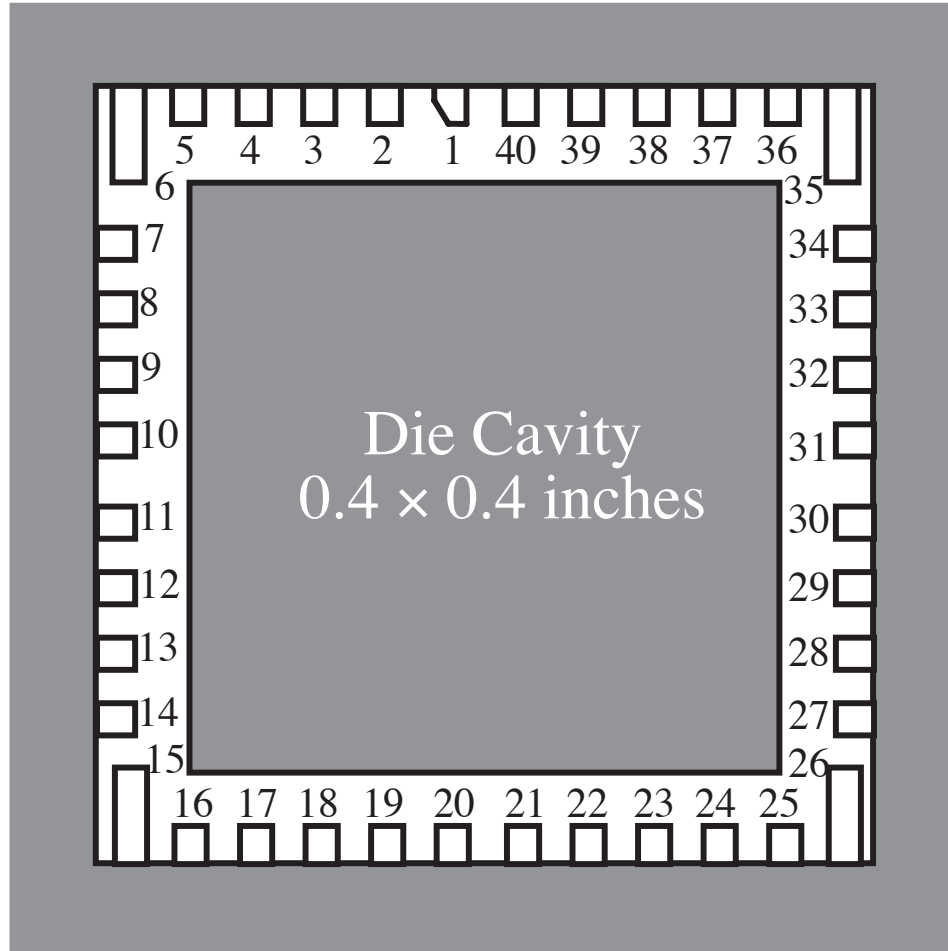
Figure A.3:   Close up of the DIP die cavity. The microelectrode array is bonded into this cavity and wire bond connections are made between the chip and package. The numbers correlate to the corresponding DIP lead.

Appendix B   ELECTRODE MODELING

B.1 Electrode Model Parameters

Area	C_I	R_t	C_w (Hz)$^{-.05}$	R_w (Hz)$^{0.5}$	R_s
480 μm^2	326 pF	6.8 MΩ	7.0 μF	22.9 kΩ	14.6 kΩ
240 μm^2	163 pF	13.5 MΩ	3.5 μF	45.8 kΩ	20.6 kΩ
120 μm^2	82 pF	27.1 MΩ	1.7 μF	91.7 kΩ	29.1 kΩ
60 μm^2	41 pF	54.2 MΩ	869 nF	183 kΩ	41.2 kΩ
30 μm^2	20 pF	108 MΩ	435 nF	367 kΩ	58.2 kΩ
150 μm^2	15 pF	217 MΩ	217 nF	733 kΩ	82.4 kΩ
Counter electrode	27 μF	80 Ω	590 mF	0.3 Ω	50 Ω

Table B.1:   Electrode model parameters for the six different electrode sizes on the electrode array. All electrodes were circular and bare platinum.

Pt wire used as counter electrode: 0.01 inches diameter by 3 inches long.

Diameter = 254 μm

Circumference = 800 μm

Length in solution approximately 2 inches = 50.8×10^3 μm

Total area in solution = Circumference * length = 40.5×10^6 μm^2

B.2 HSPICE Electrode Model

* Electrode models for Pt electrodes.
* Analysis
.PARAM plat=10   *scaling factor to account for platinization
.PARAM Area_start=15   *um^2
.param area_stop=480
.param Jo=1e-4   *default is 8e-4 A/cm^2
****
*Circuit Description

Vs in 0 ac 1
* Source voltage for impedance determination
* Reference electrode (coiled Pt wire). Assumed to be negligible compared to other Z

* electrode impedance
Cp in 0 0.92p
CI in S C='0.68p*area*plat' ctype=1
Rt in W R='0.0259/(Jo*1e-8)/(area*plat)'
Cw W S C='area*plat*sqrt(HERTZ)/15.5MEG/(2*3.14)' ctype=1
Rw W S R='15.5MEG/(area*plat)/sqrt(HERTZ)'
Rs S 0 R='319k/sqrt(area)'

Cpar in 0 10p

.AC dec 100 100 100k Sweep area oct 1 area_start area_stop
.net Vs
.options post=1
.PROBE AC ZIN(M) ZIN(P)
.print AC ZIN(M) ZIN(P)

.END

Appendix C CELL CULTURE PROTOCOLS

C.1 Mouse Astrocyte Cell Culure

C.1.1 Culture and Recording Media

Chemicals used

MEM with Earle's salts, without L-glutamine. (Gibco-BRL Cat # 11090-073)

FBS (certified) 500 ml. Aliquot 50 ml in 50 ml centrifuge tubes and freeze. (Gibco-BRL Cat # 16000-028)

Penicillin-Streptomycin Aliquot 25ml in 50ml centrifuge tubes and freeze. (Gibco-BRL Cat # 15140-122)

EDTA - (Gibco-BRL Cat # 15576-028)

L-cysteine (Sigma Cat # C-7755)

Papain (Worthington Biochemical Corp., 730 Vassar Ave., Lakewood, NJ 08701; 800-445-9603 Cat # PAP)

$CaCl_2$

Poly-d-lysine (Sigma Cat # P7405)

Disaggregation Medium

MEM - 20ml

$CaCl_2$ (100mM) - 500μl

EDTA (50mM) - 300μl

L-cysteine - 8mg

Papain - 500μl

Heat to 37°C and filter sterilize.

Growth Medium (MEM / 5% FBS / 2.5% Pen-Strep)

MEM 1 liter.

FBS 50 ml.

Pen-Strep 25ml.

Recording Medium

Isosmotic salt solution buffered with HEPES

In sterile distilled water prepare:

		For 1 liter solution
NaCl	137 mM	8.006 gm
KCl	5 mM	0.037 gm
$MgCl_2 \bullet 6H_2O$	1 mM	0.203 gm
$CaCl_2 \bullet 2H_2O$	3 mM	0.441 gm
D-Glucose	25 mM	4.504 gm
HEPES	10 mM	2.383 gm

Adjust pH to 7.4 at room temperature.

C.1.2   Astrocyte Culture Protocol

Disaggregation procedure

After obtaining embryonic mouse brains from the nice people in biology...

Remove the meninges and chop brain into pieces.

Rinse the tissue 3x with sterile media to help sterilize.

Rinse 1x with disaggregation media.

Transfer to a 15ml tube and add 10ml of dissaggregation media.

Put in water bath @ 37°C and let sit for 30 minutes.

Break up tissue with pastuer pipette

Cetrifuge 5 minutes at 1000 rpm.

Aspirate off supernatant and resuspend in 10ml of culture media. Break up pellet using pastuer pipette.

Two T75 flasks (for two brains) should have been treated with poly-d-lysine (1μg/ml) overnight.

Rinse these flasks 3x with sterile distilled water to remove the excess polylysine.

Plate cells in these two flasks with approximately 25ml of cell culture medium.

Place in CO2 incubator (5% CO2, 37°C, 98% Relative humidity).

Feed 50% once per week.

Culture procedure

Allow cells to plate to confluency (1 - 2 weeks).

Aspirate media from flask.

Add 10ml of disaggregation media to each flask.

Place in incubator for 10-30 minutes.

Use a cell scraper to remove cells from substrate (if necessary).

Centrifuge for 5 minutes at 1000 rpm.

Resuspend in 10ml culture medium.

Plate into T75 flasks... approximately 2ml cell suspension per flask with 25ml of culture medium. Note: it is not necessary to treat these flasks with poly-d-lysine.

Once the cells are confluent again, can repeat this procedure. Repeat till there are no neurons left in the culture (should occur at passage 2).

Cells can be passaged approximately 30 times with no problems.

C.2　Embryonic Chick Myocardial Cell Culture

C.2.1　Culture and Recording Media

#1: Balanced Salt Solution w/o Ca-Mg (1 liter)

NaCl　　　　　　6.80 gm/l

KCl　　　　　　0.40 gm/l

NaH_2PO_4　　　　0.06 gm/l

Na_2HPO_4　　　　0.27 gm/l

Dextrose (D-Glucose) 1.00 gm/l

Filter sterilize solution.

#2: Disaggregation Medium

In solution #1 put: 0.025% (wt/vol) Trypsin

　　　　　　　　0.05% (wt/vol) DNase I

Trypsin/EDTA 0.25% (SIGMA T4538):

　　Put 10ml in 90ml of sterile soln #1 (gives 100ml of 0.025% solution)

　　Aspirate off 0.767ml of 0.025% Trypsin solution.

DNase I (GIBCO-BRL 18047-019):

Have 20,000 units at 30,430 units/mg --> 0.657mg of DNase I

　　Dilute DNase I with 10ml of sterile Soln #1 (for 6.57% solution)

　　Add 0.767ml of 6.57% DNase I to 99.233ml of trypsin solution.

#3 Trypsin Inhibitor

50% heat inactivated bovine calf serum (SIGMA C5280)　27.8ml

50% sterile Solution #1　　　　　　　　　　　　　　27.8ml

#4 Cell Culture Media

6% Heat Inactivated bovine calf serum:　　　　　　22.2ml

40% Medium 199 10X (SIGMA M0650):　　　　　　13.32ml

Sterile Distilled Water: 133.2ml

L-Glutamine 200mM (SIGMA G7513): 1.48ml

(Effective total volume of 1X Medium 199 w/ L-glutamine is 148ml.)

0.1% Penicillin-Streptomycin (GIBCO-BRL 15140-122)   370μl

54% Low K Balanced Salt Solution:

Mix in 200 ml of distilled water.

NaCl	116 mM/l	1.356 gm (in 200ml DI water)
NaH$_2$PO$_4$°H2O	1.0 mM/l	0.0276 gm
MgSO$_4$	0.8 mM/l	0.0193 gm
KCl	1.18 mM/l	0.0176 gm
NaHCO$_3$	26.2 mM/l	0.440 gm
CaCl$_2$°2H$_2$O	0.87 mM/l	0.0256 gm
D-Glucose	5.5 mM/l	0.198 gm

Filter Sterilize.

Recording Media

Isosmotic salt solution buffered with HEPES

In sterile distilled water prepare:

NaCl	142.2mM	8.310 gm/l
KCl	5.4mM	0.403 gm/l
NaH$_2$PO$_4$*H$_2$O	1.0mM	0.138 gm/l
HEPES acid	4.49mM	1.070 gm/l
HEPES Na salt	5.51mM	1.434 gm/l
Dextrose (D-Glucose Anhydrous)	5.6mM	1.009 gm/l
MgSO$_4$ anhydrous	0.8mM	0.096 gm/l
CaCl$_2$*2H$_2$O	1.0mM	0.147 gm/l

Adjust pH to 7.45 at room temperature using 1N NaOH.

Filter sterilize solution.

C.2.2   Chick Myocardial Cell Culture Protocol

Bibliography

1- De Hann (1967) Devel.Biol. 16:216-249

2- Barry   (1975) Circ. Reser. 36:727-734

3- Polinger (1970) Exp. Cell Reser. 63:78-82

=================================

Note: This protocol was adapted from the above to work well with culture on the microelectrode arrays.

Use approximately 30 eggs (11 days old)

1. EMBRYO EXTRACTION PROCEDURE

1.1 Candle the eggs and select eggs with viable embryos.

1.2 Swab eggs with towel soaked in 70% ethanol. This cleans the egg but does not completely sterilize it.

1.3 Using a sharp probe, poke a hole through the shell at the blunt end.

1.4 Remove the egg shell down to the membrane using forceps. This should be done by holding the egg at an angle over a waste container and slowly nibbling away at the shell until the shell surrounding the air space is completely removed. The forceps may be re-sterilized in 70% ethanol.

1.5 Peel away the shell membrane using another set of forceps. This is done by gently grasping the membrane at the edge of the air space and gently pulling toward the other edge. The embryo surrounded by the chorioallantoic membrane is now exposed to view.

1.6 Gently pierce the chorioallantoic membrane with one tine of the curved forceps, and hook it around the neck of the embryo. Partially close the forceps and slowly lift the embryo out of the shell. As the embryo is lifted, the extraembryonic membranes will tear, thus freeing the embryo.

1.7 Place the embryo in a sterile 150mm petridish and sever the head.

1.8 Repeat 1.3 to 1.7 for all 30 eggs.

2. HEART REMOVAL / PREPARATION

2.1 Dissect out the hearts and place in a P100 dish with 20ml cold (directly out of fridge) solution #1. (Do for all 30 embryos)

2.2 Remove arteries and incise around edge of ventricle to release blood. Move around in solution to rinse blood away.

2.3 Transfer to another P60 dish with 10ml of cold solution #1 and cut into fragments small enough to fit into a 10ml pipet. It is best to leave fragments as large as possible to minimize the number of mechanically damaged cells.

2.4 Transfer all cells and media to the trypsinization flask. Remove media and replace with 10ml solution #2 at 37°C.

2.5 Agitate gently for 5 minutes. Remove media and discard. Repeat one time with 10ml solution #2 at 37°C. This removes the outer layer of cells which may be mechanically damaged.

3.**DISAGGREGATION PROCEDURE**

3.1 Add new solution #2 (10ml @ 37°C) and agitate gently for 8 minutes. Suck contents of flask up and down in a 10ml pipette several times to break up aggregates. Avoid air bubbles and foaming when you do this!

3.2 Aspirate off media in flask retaining large fragments of tissue in the flask. Add the 10ml of cell suspension to 20ml of cold solution #3 (trypsin inhibitor) through a 40μm cell strainer. The flask containing the cell suspension and trypsin inhibitor should be on ice. Discard the cell strainer.

3.3 Repeat 3.1 to 3.2 three to four times till all large tissue fragments are disaggregated. The cells from each passage can be placed in the same flask containing trypsin inhibitor. A new cell strainer should be used each time.

3.4 Transfer cell suspension / trypsin inhibitor solution to several centrifuge tubes and centrifuge for 10 minutes at 1000rpm.

4.**CULTURE PROCEDURE**

4.1 Discard the supernatant and resuspend cells in 5-8ml of solution #4 (culture medium) at 37°C. Plate the cells in a P100 dish and place in the CO2 incubator (5% CO2, 37°C) for 45 minutes. This is an important passage to separate the muscle cells from the fibroblasts in the cellular population based on their differential adhesion time to the polystyrene dish.

4.2 Remove the media form the P100 dish and place in a centrifuge tube. Gently rinse the dish one time with 2 ml of media #4 at 37°C. Add this to the centrifuge tube. Centrifuge for 10 minutes at 1000 rpm.

4.3 Discard the supernatant from the centrifuge tube and re suspend the myocardial cells in 1-2ml of media #4 (culture media). Count the cells using a hemocytometer and trypan blue exclusion and calculate the viability (viability = # live cells/total # cells). Viability should be greater than 90%)

4.4 Plate cells in P35 dish and on chips with 2ml of cell culture media (media #4).

P35 dish plate 1.5E6 cells.

Chips plate 5E5 to 1E6 cells.

4.5 Place in CO2 incubator (5% CO2, 37°C)

5. **NOTES**

5.1 Cells should be active by day 3-4. By day 7 the myocytes stop beating.

5.2 If cells are dividing and growing, but not beating, the concentrations of potassium and calcium are probably off.

5.3 Floating elliptical cells are red blood cells, not dead myocardial cells. These will not hurt anything. If wish to remove them, can rinse culture with culture media immediately before experiments.

C.3   NG108 Cell Culture

Note: This protocol was originally transferred from the laboratory of Dr. David Stenger at the Naval Research Laboratory, Washington, DC.

C.3.1   Culture and Recording Medium

Chemicals used (Gibco BRL)

D-MEM 1x, high glucose, with L-glutamine, with 110mg/l sodium pyruvate. (Cat # 11995-032)

Trypsin 10x. Aliquot 1ml in 15 ml centrifuge tubes and freeze. (Cat # 25095-019)

FBS (certified) 500 ml. Aliquot 50 ml in 50 ml centrifuge tubes and freeze. (Cat # 16000-028)

Hanks Balanced Salt Solution 1x. (Cat # 14170-021)

HAT supplement 100x. (Cat # 31062-037)

N2 supplement 1 ml vials. (Cat # 17502-014)

B-27 supplement 2 ml vials (50x). (Cat # 17504-010)

Growth Medium (DMEM / 10% FBS / 2% HAT)

DMEM 440 ml (Aspirate 60 ml from a new 500 ml bottle).

FBS 50 ml.

HAT 10ml.

Differentiation Medium (DMEM / 1% N2)

DMEM 99 ml.

N2 1 ml.

Filter sterilize solution.

Recording Medium

Isosmotic salt solution buffered with HEPES

In sterile distilled water prepare:

		For 1 liter solution
NaCl	120 mM/l	7.013 gm
KCl	3 mM/l	0.2237 gm
$MgCl_2 \cdot 6H_2O$	1.2 mM/l	0.244 gm
$CaCl_2 \cdot 2H_2O$	2.5 mM/l	0.3676 gm
$NaHCO_3$	22.6 mM/l	1.899 gm
D-Glucose	11.1 mM/l	2.000 gm
HEPES	5 mM/l	1.192 gm

C.3.2 NG108 Cell Culture Protocol

Culturing cells from a frozen vial

Heat DMEM / 10% FBS / 2% HAT to 37 °C.

Add 5 ml DMEM / 10% FBS / 2% HAT solution to vented T25 flask.

Thaw frozen vial of cells in 37 °C water bath for 2 minutes.

Add cells to T25 flask.

Place in incubator (5% CO2, 37 °C, 98% relative humidity).

Following day re-feed 100% with fresh DMEM / 10% FBS / 2% HAT at 37 °C to remove DMSO. Return to incubator.

Allow to grow till nearly confluent (4 - 5 days).

Trypsinization procedure

Heat HBSS (Hanks Balanced Salt Solution) to 37 °C.

Heat DMEM / 10% FBS / 2% HAT to 37 °C.

Thaw 1 ml of Trypsin (in 15 ml centrifuge tube).

Remove media from T75 (or T25) vented flask.

Add 10 ml (5 ml for T25) HBSS and rock gently to rinse off any FBS. FBS will inhibit the trypsin.

Aspirate off HBSS.

Add 9 ml of HBSS to 1 ml trypsin.

Add 10 ml (5 ml for T25) trypsin solution to flask and rock gently for 2 minutes. The cells will lift from the substrate during this time forming a cell suspension.

Remove cell suspension from the flask and put in 15 ml centrifuge tube.

Add 1 ml of DMEM / 10% FBS / 2% HAT to cell suspension. This inhibits the trypsin action.

Centrifuge at 1000 rpm for 5 minutes. After centrifuge, can keep in pellet form for 2-3 hours if necessary.

Discard the supernatant and hit end of tube until cell pellet is broken up.

Re-suspend cells in 1 ml of the desired cell culture media.

Cell growth in serum containing media

Heat DMEM / 10% FBS / 2% HAT to 37 °C.

Re-suspend cells in 1 ml DMEM / 10% FBS / 2% HAT.

Add 15 ml DMEM / 10% FBS / 2% HAT at 37 °C to vented T75 flask.

Add 0.1 to 0.2 ml of cell suspension to T75 flask.

Place in incubator (5% CO2, 37 °C, 98% relative humidity).

Allow to grow till nearly confluent and then repeat trypsinization procedure.

Should only use cells up to perhaps 50 passages since the cell population is assumed to change over time.

Cell Differentiation

Heat DMEM / 1% N2 to 37 °C.

Re-suspend cells in 1 ml DMEM / 1% N2. May use 40 μm cell strainer prior to performing cell count to remove any large clumps of cells.

Add 2 ml of DMEM / 1% N2 to P35 dish.

Plate cells at desired density in the dish.

Cryopreservation Procedure

Perform trypsinization procedure and re-suspend cells in 1 ml DMEM / 10% FBS / 2% HAT.

Count cells with hemocytometer using trypan blue exclusion. Use 50% trypan blue solution (0.4%) with 50% cell suspension.

In a 1.5 ml cryogenic freezing vial place:

Cell suspension for 3 x 104 cells

DMEM / 10% FBS / 2% HAT to make 1 ml total volume

10 μl of DMSO (Dimethyl Sulfoxide)

Check seal of vials using methylene blue (0.05% solution).

Place vials on dry ice OR in -80 °C freezer for 3-12 hours.

Transfer vials to liquid nitrogen.

Appendix D   HSPICE MODEL OF A BULLFROG ATRIAL CELL

*HSPICE model for APs based on a frog atrial cell model in:

Rasmusson, R.L., Clark, J.W., Giles, W.R., Robinson, K., Clark, R.B., Shibata, E.F. and Campbell, D.L., "A mathematical model of electrophysiological activity in a bullfrog atrial cell," American Journal of Physiology, 259(2):H370-H389 (1990).

```
** Constants:
.param F = 96486.7                          * C/mol
.param R = 8314.3                           * kJ/molK
.param T = 295.15                           * K = 22C
.param V_i = 0.0025                         * nl
.param tau_p = 10000                        * msec
.param K_b = 2.5                            * mM
.param Ca_b = 2.25                          * mM
.param Cm = 33                              * pF
.param V_c = 0.0004                         * nl
.param Na_b = 111                           * mM
.param Mg_i = 2.5                           * mM


.param Vmem_IC1 = -90.00                    * mV
.param Vmem_IC2 = -90.00                    * mV


.param R_gap_junction = 1                   *gap junction resistance
```

**extra variables for direct gating of ionic currents

```
.param bork_Na = 1          * modulation of I_Na
.param bork_Ca = 1          * modulation of I_Ca
.param bork_K  = 1          * modulation of I_K

**extra variables for modulation of channel gating variables
.param bork_alpha_n = 1     * modulation of I_K influx constant
.param bork_beta_n  = 1     * modulation of I_K efflux constant
.param bork_d_inf   = 1     * modulation of I_Ca activation
.param bork_f_inf   = 1     * modulation of I_Ca inactivation


.global GND  Extra

* Calculation of gating variables: m, h, d, f, and n
* These are the solution of a first order differential
* equation.
.SUBCKT FO_DEQ xx Alpha Beta
Cxx            xx             GND         1              *1F cap to calculate integral
Gxx            xx             GND CUR ='-1*(V(Alpha)*(1-V(xx))-V(Beta)*V(xx))'
.ENDS

**Inward and background currents

* Sodium current (I_Na)
.SUBCKT I_Na Intra Vmem Na_i Value
.IC v(m) = 0
.IC V(h) = 1

Ealpha_m alpha_m GND
VOL='0.757*(V(Vmem)-31.2)/(1-exp(-0.0617*(V(Vmem)-31.2)))'
Ebeta_m beta_m GND Vol='2.26*exp(-0.042*(V(Vmem)+52.85))'
Ealpha_h alpha_h GND VOL='0.051*exp(-0.124*(V(Vmem)+85.45))'
Ebeta_h beta_h GND VOL='1.27/(1+exp(-0.0764*(V(Vmem)+2.91)))'
Xm m alpha_m beta_m FO_DEQ
Xh h alpha_h beta_h FO_DEQ
EI_bar_Na I_bar_Na GND
VOL='bork_Na*1000*(0.0497*V(Na_i)*V(Vmem)*(exp(0.039*(V(Vmem)-V(V_Na)))-
1)/(exp(0.039*V(Vmem))-1))'
ENa V_Na GND VOL='R*T/F*log(Na_b/V(Na_i))'
Evalue value GND Vol='PWR(V(m),3)*V(h)*V(I_bar_Na)'
GI_Na Intra Extra CUR='V(value)'
.ENDS


*Calcium current (I_Ca)
.SUBCKT I_Ca Intra Vmem Ca_i value
```

.IC V(f) = 1
.IC V(d) = 0

Etau_d tau_d GND
VOL='V(d_inf)*(1-exp(-1*(V(Vmem)+10)/6.24))/(0.035*(V(Vmem)+10))'
Ed_inf d_inf GND VOL='bork_d_inf*1/(1+exp(-1*(V(Vmem)+10)/6.24))'
Ealpha_d alpha_d GND VOL='V(d_inf)/V(tau_d)'
Ebeta_d beta_d GND VOL='(1-V(d_inf))/V(tau_d)'
Xd d alpha_d beta_d FO_DEQ
Er r GND VOL='0.6/(1+exp((50-V(Vmem))/20))'
Etau_f tau_f GND VOL='1/(0.0197*exp(-1*PWR(0.0337*(V(Vmem)+10),2))+0.02)'
Ef_inf f_inf GND VOL='bork_f_inf*(V(r)+(1/(1+exp((V(Vmem)+35.06)/8.6))))'
Ealpha_f alpha_f GND VOL='V(f_inf)/V(tau_f)'
Ebeta_f beta_f GND VOL='(1-V(f_inf))/V(tau_f)'
Xf f alpha_f beta_f FO_DEQ
EI_bar_Ca I_bar_Ca GND
VOL='bork_Ca*1000*0.01174*V(Vmem)*(V(Ca_i)*exp(0.07792*V(Vmem))-Ca_b)/(e
xp(0.07792*V(Vmem))-1)'
Evalue value GND VOL='V(d)*V(f)*V(I_bar_Ca)'
GI_Ca Intra Extra CUR='V(value)'
.ENDS

*Time independent potassium current (I_K1)
.SUBCKT I_K1 intra Vmem K_c K_i value
EV_K V_K GND VOL='R*T/F*log(K_b/V(K_i))'
Evalue value GND
VOL='1000*(0.4*K_b/(K_b+210))*((V(Vmem)-V(V_K))/(1+exp(0.078*(V(Vmem)-V(
V_K)-20))))'
GI_K1 Intra Extra CUR='V(value)'
.ENDS

*Background currents
.SUBCKT I_b Intra Vmem Na_i Ca_i I_Na_b I_Ca_b value
ENa V_Na GND VOL='R*T/F*log(Na_b/V(Na_i))'
EI_Na_b I_Na_b GND VOL='1000*0.00015*(V(Vmem)-V(V_Na))'
ECa V_Ca GND VOL='R*T/2/F*log(Ca_b/V(Ca_i))'
EI_Ca_b I_Ca_b GND VOL='1000*0.000000216*(V(Vmem)-V(V_Ca))'
Evalue value GND VOL='V(I_Na_b)+V(I_Ca_B)'
GI_b intra extra CUR='V(Value)'
.ENDS

**outward currents
*Delayed rectifier (I_K)

225

.SUBCKT I_K Intra Vmem K_i value
.IC V(n) = 0

Ealpha_n alpha_n GND
VOL='bork_alpha_n*0.0000144*(V(Vmem)+26.6)/(1-exp(-0.128*(V(Vmem)+26.5)))'
Ebeta_n beta_n GND VOL='bork_beta_n*0.000286*exp(-0.0381*(V(Vmem)+26.5))'
Xn n alpha_n beta_n FO_DEQ
EV_K V_K GND VOL='R*T/F*log(K_b/V(K_i))'
Er_prime r_prime GND VOL='95/(1+exp((V(Vmem)-V(V_K)-78)/25))-95'
EI_bar_K I_bar_K GND
VOL='Bork_K*1000*0.0125*(V(Vmem)-V(V_K)+V(r_prime))'
Evalue value GND VOL='PWR(V(n),2)*V(I_bar_K)'
GI_K intra extra CUR='V(Value)'
.ENDS

**Pump and Exchanger currents
*Sodium-potassium pump (I_NaK)
.SUBCKT I_NaK Intra Vmem Na_i K_c value
Evalue value GND
VOL='1000*0.0772*PWR((V(Na_i)/(V(Na_i)+5.46)),3)*PWR((K_b/(K_b+0.621)),2)*(
V(Vmem)+150)/(V(Vmem)+200)'
GI_NaK intra extra CUR='V(Value)'
.ENDS

*Calcium pump (I_Ca_P)
.SUBCKT I_Ca_P Intra Ca_i value
Evalue value GND VOL='1000*0.00135*(V(Ca_i)/(V(Ca_i)+0.001))'
GI_Ca_P intra extra CUR='V(Value)'
.ENDS

*Sodium-calcium exchanger (I_NaCa)
.SUBCKT I_NaCa Intra Vmem Na_i Ca_c Na_c Ca_i value
Enum1 num1 GND VOL='0.0015*PWR(V(Na_i),3)*Ca_b*exp(0.0195*V(Vmem))'
Enum2 num2 GND VOL='0.0015*PWR(Na_b,3)*V(Ca_i)*exp(-.0195*V(Vmem))'

Eden Den GND
VOL='1+0.0001*V(Ca_i)*PWR(Na_b,3)+0.0001*Ca_b*PWR(V(Na_i),3)'
EValue Value GND VOL= '(V(num1)-V(num2))/V(den)'
GI_NaCa intra extra CUR='V(Value)'

.ENDS

**Extracellular Concentrations of ions (cleft)

*Sodium concentration in cleft (Na_c)
.SUBCKT Na_c I_NaK I_NaCa I_Na I_Na_b Na_c
.IC V(Na_c) = 111
CNa_c Na_c GND 1   *1F cap to calculate integral
GNa_c Na_c GND
CUR='-1*((Na_b-V(Na_c))/tau_p+(3*V(I_NaK)+3*V(I_NaCa)+V(I_Na)+V(I_Na_b))/F
/V_c)'
.ENDS

*Potassium concentration in cleft (K_c)
.SUBCKT K_c I_NaK I_K1 I_K K_c
.IC V(K_c) = 2.5
CK_c K_c GND 1   *1F cap tp calculate integral
GK_c K_c GND
CUR='-1*((K_b-V(K_c))/tau_p+(-2*V(I_NaK)+V(I_K1)+V(I_K))/F/V_c)'
.ENDS

*Calcium concentration in cleft (Ca_c)
.SUBCKT Ca_c I_NaCa I_Ca I_Ca_P I_Ca_b Ca_c
.IC V(Ca_c) = 2.25
CCa_c Ca_c GND 1   *1F cap tp calculate integral
GCa_c Ca_c GND
CUR='-1*((Ca_b-V(Ca_c))/tau_p+(-2*V(I_NaCa)+V(I_Ca)+V(I_Ca_P)+V(I_Ca_b))/2/
F/V_c)'
.ENDS

**Internal concentrations of ions
*Internal sodium concentration (Na_i)
.SUBCKT Na_i I_Na I_NaK I_NaCa I_Na_b Na_i
.IC V(Na_i) = 7.5
CNa_i Na_i GND 1   *1F cap for integral calculation
GNa_i Na_i GND
CUR='-1*(-1*V(I_Na)-3*V(I_NaK)-3*V(I_NaCa)-V(I_Na_b))/F/V_i/1000'
.ENDS

*Internal potassium concentration (K_i)
.SUBCKT K_i I_NaK I_K I_K1 K_i
.IC V(K_i) = 95
CK_i K_i GND 1   *1F cap to calculate integral
GK_i K_i GND CUR='-1*(2*V(I_NaK)-V(I_K)-V(I_K1))/F/V_i/1000'
.ENDS

*Internal Calcium concentration (Ca_i)
.SUBCKT Ca_i I_NaCa I_Ca I_Ca_P I_Ca_b Ca_i
.IC V(Ca_i) = 0.2m   *.2uM entered in mM
.IC V(O_c) = 0.7

.IC V(O_TC) = 0.05
.IC V(O_TMgC) = 0.75
.IC V(O_TMgM) = 0.24

CO_c O_c GND 1
GO_c O_c GND CUR='-1*(100*V(Ca_i)*(1-V(O_c))-0.238*V(O_c))'
CO_TC O_TC GND 1
GO_TC O_TC GND CUR='-1*(39*V(Ca_i)*(1-V(O_TC))-0.196*V(O_TC))'
CO_TMgC O_TMgC GND 1
GO_TMgC O_TMgC GND
cur='-1*(100*V(Ca_i)*(1-V(O_TMgC)-V(O_TMgM))-0.0033*V(O_TMgC))'
CO_TMgM O_TMgM GND 1
GO_TMgM O_TMgM GND
CUR='-1*(0.1*Mg_i*(1-V(O_TMgC)-V(O_TMgM))-0.333*V(O_TMgM))'

EO_B O_B GND
VOL='0.000045*(100*V(Ca_i)*(1-V(O_c))-0.238*V(O_c))+0.0000842*(39*V(Ca_i)*(
1-V(O_TC))-0.196*V(O_TC))+0.0001684*(100*V(Ca_i)*(1-V(O_TMgC)-V(O_TMgM
))-0.0033*V(O_TMgC))'

CCa_i Ca_i GND 1
GCa_i Ca_i GND
CUR='-1*((2*V(I_NaCa)-V(I_Ca)-V(I_Ca_P)-V(I_Ca_b))/2/V_i/F/1000-V(O_B)/V_i)'
.ENDS

**** HH MEMBRANE CHANNEL CURRENT MODEL ****
.SUBCKT HH Intra Extra Vmem I_Na Na_i Ca_i I_Ca K_i I_K1 I_Na_b I_Ca_b I_b
I_K I_NaK I_Ca_P I_NaCa

EVmem   Vmem   GND   VOL='V(intra,extra)'

XNa   Intra Vmem Na_i I_Na   I_Na
XCa   Intra Vmem Ca_i I_Ca   I_Ca
XK1   Intra Vmem K_c K_i I_K1   I_K1
Xb   Intra Vmem Na_i Ca_i I_Na_b I_Ca_b I_b   I_b
XK   Intra Vmem K_i I_K   I_K
XNaK   Intra Vmem Na_i K_c I_NaK   I_NaK
XCa_P   Intra Ca_i I_Ca_P   I_Ca_P
XNaCa   Intra Vmem Na_i Ca_c Na_c Ca_i I_NaCa   I_NaCa

XK_i   I_NaK I_K I_K1 K_i   K_i
XCa_i   I_NaCa I_Ca I_Ca_P I_Ca_b Ca_i   Ca_i
XNa_i   I_Na I_NaK I_NaCa I_Na_b Na_i   Na_i

*XNa_c   I_NaK I_NaCa I_Na I_Na_b Na_c   Na_c
*XK_c   I_NaK I_K1 I_K K_c   K_c

228

```
*XCa_c        I_NaCa I_Ca I_Ca_P I_Ca_b Ca_c                              Ca_c

.ENDS

**** TOP LEVEL CIRCUIT WITH MEMBRANE CAPACITANCE; STIMULUS ****
VREF          Extra         GND           0
XHH1          Intra1 Extra Vmem1 I_Na1 Na_i1 Ca_i1 I_Ca1 K_i1 I_K11 I_Na_b1
I_Ca_b1 I_b1 I_K1 I_NaK1 I_Ca_P1 I_NaCa1              HH
CMembr1       Intra1        Extra         Cm IC=Vmem_IC1

XHH2 Intra2 Extra Vmem2 I_Na2 Na_i2 Ca_i2 I_Ca2 K_i2 I_K12 I_Na_b2 I_Ca_b2
I_b2 I_K2 I_NaK2 I_Ca_P2 I_NaCa2 HH
Cmembr2 Intra2 Extra Cm   IC=Vmem_IC2

* Stimulate the first cell
VStim1 stim1 GND PULSE (0 -300 20 .1 .1 4 2000)
Rstim1  stim1 GND 1
Gstim1  Intra1 Extra CUR='V(stim1)'

* add gap junction resistance between the two cells so the first can
* initiate an AP in the second.
G_R_gj  Extra Intra2 Cur='V(intra1,intra2)/R_gap_junction/exp(V(Ca_i2)*752)'

**** Differentiation to simulate extracellular recordings ****
EDeriv1 Deriv1 GND VOL='I1(Cmembr1)/Cm'
Rfilter1 deriv1 filter1 10      * 100 Hz filter = 100 kHz (1 sec = 1 msec)
Cfilter1 filter1 GND 1m         * Filter HF noise out of first deriv

Gderiv1_2 Rnode1 GND CUR='-1*V(filter1)'
Rjunk1 Rnode1 deriv1_2 1    *Resistor to help convergence
Lderiv1_2 deriv1_2 GND 1   *Calculate second derivative

EDeriv2 Deriv2 GND VOL='I1(Cmembr2)/Cm'
Rfilter2 deriv2 filter2 10      * 100 Hz filter = 100 kHz (1 sec = 1 msec)
Cfilter2 filter2 GND 1m         * Filter HF noise out of first deriv

Gderiv2_2 Rnode2 GND CUR='-1*V(filter2)'
Rjunk2 Rnode2 deriv2_2 1    *Resistor to help convergence
Lderiv2_2 deriv2_2 GND 1   *Calculate second derivative

.PROBE V(deriv2_2)
.PRINT TRAN V(deriv2_2)

.options post=1 vntol=10m abstol=10m ingold=1
.TRAN STEP=10m STOP=3000 UIC
.END
```